



# NSTX-U FY2018 Year End Report

J. Menard, S. Kaye, S. Gerhardt, R. Feder, and the NSTX-U Team

Report editor: S. Horst

October 8, 2018 – Version 5

<b>Executive Summary of FY-18 NSTX-U Year-End Report</b>	<b>6</b>
Executive Summary for FY-18 Notable Outcomes	6
Executive Summary for the NSTX-U Recovery Project	7
Executive Summary for NSTX-U Maintenance and Run Prep	9
Maintenance Run and Preparation	9
Motor-Generator and Field Coil Power Conversion Systems	10
Executive Summary of Research Results – FY-18 Milestones	10
Executive Summary for Additional Research Highlights	13
Boundary Science	13
Summary of Research Highlights for Pedestal Structure and Control	13
Summary of Research Highlights for Divertor and Scrape-off Layer	14
Summary of Research Highlights for Materials and Plasma Facing Components	14
Core Science	15
Summary of Research Highlights for Macroscopic Stability	15
Summary of Research Highlights for Transport and Turbulence	17
Summary of Research Highlights for Energetic Particles	18
Integrated Scenarios	19
Summary of Research Highlights for Solenoid-Free Start-up and Ramp-up	19
Summary of Research Highlights for Wave Heating and Current Drive	20
Summary of Research Highlights for Advanced Scenarios and Control	21
<b>Performance of FY2018 Notable Outcomes</b>	<b>22</b>
<b>NSTX-U Recovery Project</b>	<b>26</b>
Magnets	28
Plasma Facing Components	33

Vacuum Vessel and In-Vacuum Hardware (VV+IH)	47
Cooling and Bakeout	55
Vacuum and Fueling	59
Diagnostics	63
Test Cell	70
Metrology and fit-up activities	75
<b>NSTX-U Engineering Operations</b>	<b>84</b>
Heating Systems	84
Power systems	85
Central I&C	86
Real-time Control and Protection	87
Procedures and Training	87
<b>NSTX-U Facility and Diagnostics</b>	<b>89</b>
F(18-1): Evaluate PFC operational limits and develop integrated diagnostic plans for operations	89
Mechanical Testing of CSFW pin-mounted tiles	90
Material Evaluation Experiments	93
Heat Flux Quantification and Tests of Integrated PFC Diagnostics	95
Prototype PFC Heat Flux Tests	98
(Incremental) Diagnostic Milestone ID (18-1): Install and commission Far Infrared Tangential Interferometer / Polarimeter diagnostic system.	99
<b>NSTX-U Research Program</b>	<b>100</b>
NSTX-U Research Results – FY-18 Milestones	100
R(18-1): Develop and benchmark reduced heat flux and thermo-mechanical models for PFC monitoring	100
R(18-2): Develop simulation framework for spherical tokamak breakdown and current ramp-up	112
Real-time control simulation framework	113
Time-dependent transport simulation framework	119
Inductive Startup Calculations	121
Summary and Future work	123
R(18-3): Validate and further develop reduced transport models for electron thermal transport in ST plasmas.	125
R(18-4): Optimize energetic particle distribution function for improved plasma performance	135

NSTX-U Research Results - Additional Research Highlights	139
I. Boundary Science	139
A. Pedestal Structure and Control	139
Low-to-high confinement	139
Beam emission spectroscopy using carbon	139
Enhanced Pedestal Physics	140
B. Divertor and Scrape-off Layer	145
Edge turbulence	145
Blob-hole correlation model	146
Filamentary instabilities in the edge, SOL and divertor legs	146
Connection of midplane turbulence to divertor target plate in NSTX L-mode discharges.	146
Divertor detachment optimization in an unfavorable open geometry horizontal target divertor configuration in NSTX and NSTX-U	148
M3D-C1 / TRIP3D modeling of divertor strike point splitting due to error fields	149
C. Materials and Plasma Facing Components	151
Fundamental surface science of PFCs for improved plasma performance in NSTX-U	151
Alternative PFC Concepts	152
Whole Machine Transport Processes	153
In vacuo material characterization with MAPP	153
II. Core Science Research Highlights	157
A. Macroscopic Stability TSG Research Highlights	157
1. Error Field Correction in NSTX-U	157
(a) Predicted Resonant and Non-resonant Error Field Effects	158
(b) Physics Recommendations for Coil Alignments	161
(c) Investigation of TF Error Field Effects	162
2. Simulations of Vertical Displacement Events in NSTX-U	165
3. Disruption Event Characterization, Forecasting, and Related Physics Analysis	166
(a) Disruptivity and General Event Diagrams from DECAF analysis	166
(b) Local Island Power Balance Theory for Density Limit	168
(c) Discrimination of Rotating MHD Instabilities and Related Disruption Forecasting by DECAF	170
(d) DECAF analysis of extended disruption event chains forecasting disruption	171
4. Spontaneous tearing modes in small island regimes	174
5. Study of Non-ideal and Kinetic Plasma Response to 3D Fields	175
(a) Magnetic Sensors for Kinetic 3D Plasma Response	175

(b) Observations of Internal Magnetic Island Bifurcations in Resistive MHD Simulations	176
6. Progress with the Electromagnetic Particle Injector (EPI)	178
7. Collaborations for error field physics	179
(a) Effects of high-field-side error fields	179
(b) Error field threshold scaling for $n=1$ and $n=2$	180
8. Collaboration with KSTAR on Ideal, Kinetic, and Resistive Stability Analysis Supporting DECAF	181
B. Transport and Turbulence	186
NSTX-U L-mode modeling	186
NSTX H-mode analysis and modeling	187
Impurity Transport Modeling	189
Collaborations	191
C. Energetic Particles	196
Improvements To Energetic Particle Analysis And Modeling Tools	196
Development of Reduced Models for Energetic Particle Transport	197
Analysis of Alfvénic Instabilities on NSTX and NSTX-U	198
Energetic Particle Transport by Low-Frequency MHD	200
III. Integrated Scenarios	203
A. Solenoid-Free Start-up and Ramp-up	203
A.1 CHI Experiment on QUEST and related Theory/Modeling	203
B. Wave Heating and Current Drive	206
B.1: Initial Modeling on the Impact of Hydrogen Species on High Harmonic Fast Wave Performance	206
B.2: Modeling on RF Edge Losses in NSTX/NSTX-U Plasmas by a Finite Element Code FW2D	208
B.3: RF studies on LAPD Device	211
B.4: ICRF Collaboration with EAST: ICRF Interactions with the SOL	211
B.5: EC/EBW Simulations on QUEST	211
B.6: RF SciDAC: “Center for Simulation of Fusion Relevant RF Actuators”	212
C. Advanced Scenarios and Control	214
C.1 Summary of R18-2 Milestone	214
C.2 Real-time Capable Neural Network Modeling of NUBEAM for Use on NSTX-U	214
C.3 Evolution of Wall Conditions on NSTX-U	218
C.4 MAST-U Collaboration on Scenario and Control Development	219
C.5 Reflective Memory Supporting Future PCS Expansion	220
C.6 Control System Design, Closed-Loop Simulation, Optimization for Snowflake Divertor	221

<b>NSTX-U Publications</b>	<b>226</b>
Papers Published by NSTX-U Researchers (Oct. 2017 - Sept. 2018)	226
Papers Recently Accepted for Publication	232
<b>NSTX-U Presentations</b>	<b>233</b>
Invited / Oral Talks at Scientific Conferences (Oct. 2017 - Sept. 2018)	233
<b>Seminars and Colloquia by NSTX-U Researchers</b>	<b>237</b>
<b>NSTX-U Awards and Leadership</b>	<b>238</b>
Major Awards by NSTX-U Researchers	238
Hosted / Organized Meetings and Workshops	238
NSTX-U PPPL Employee FY18 Leadership in Venues Outside of PPPL	240
NSTX-U PPPL Employee Membership and Participation in Scientific Groups and Meetings Outside of PPPL	241
<b>NSTX-U Collaborator Institutions</b>	<b>243</b>

# Executive Summary of FY-18 NSTX-U Year-End Report

## Executive Summary for FY-18 Notable Outcomes

The NSTX-U Recovery Project completed the five PEMP Notable Outcomes in FY-18. The following table summarizes the PEMP outcomes.

	<b>NSTX-U Recovery PEMP Notable Outcome</b>	<b>Defined Finish By Date</b>	<b>Status as of September 30, 2018</b>
2.1	Successful completion of the Inner PF Coil FDR	3/31/2018	Completed 3/31/2018
2.2.A	Complete mechanical and electrical testing of one Inner PF1 Prototype coil	7/15/2018	Completed 7/13/2018
2.2.B	Complete a PDR for the repair of the Passive Plate structures	7/31/2018	Completed 7/26/2018
2.2.C	Complete an FDR for the redesigned Plasma Facing Components (PFCs)	9/30/2018	Completed 9/28/2018
4.2	Successfully complete a Director's Review prior to CDE-2/3A	9/30/2018	Completed 9/7/2018

## Executive Summary for the NSTX-U Recovery Project

The Recovery Project held thirty preliminary design reviews (PDRs) and nine final design reviews (FDRs) in FY-18 in support of advancing the project in nine key areas:

1. Six redesigned Inner PF coils (PF1A,B,C-Upper, PF1A,B,C-Lower)
2. Redesigned upper and lower Polar Region structures for support of the new inner PF coils and enhanced NSTX-U vacuum performance
3. Repairs to the Passive Plate structures
4. Redesigned select Plasma Facing Components (PFCs)
5. Design and install improved Bakeout System
6. Design and install Coil and Structural Benchmark and Trending Instrumentation (Stress and Strain)
7. Improve NSTX-U Test Cell safety controls with enhanced test cell neutron shielding and improvements to the Access Control System (ACS)
8. Implement DOE Order 420.2C, "Safety of Accelerator Facilities"
9. Reassemble NSTX-U with alignment of magnets and structures that enable full experimental operating parameters

The most important engineering scope for the Recovery Project in FY-18 was the design and prototype fabrication of the replacement Inner PF Coils. A successful FDR for the redesign of the Inner PF1 coils was completed at the end of March 2018. The FDR showed that the revised Inner PF1 design provides reliable high performance coils that can be manufactured more easily than in the past. Four prototype PF1 coils were fabricated and qualified through electrical and mechanical testing. Prototype coils were built by PPPL as well as at subcontractors ETI, Tesla, and Sigma Phi. Procurement of the production Inner PF1 coils in FY-19 will be based on the prototype experience.

Important engineering advancements were also made in the redesigned Polar Region structures and upgrades to the Upper and Lower Center Stack Casing (CSC) structures. The Polar Region and CSC structures align and support the three inner PF1 coils under large static and transient electromagnetic and thermal loads. The CSC also supports important interfaces with PFCs and the heating and cooling components. Two PDRs were conducted for the Polar Region Inconel structures, and the team was working towards a CSC PDR at the end of FY-18. The design and function of the Inner PF1 coils and the Polar Region are tightly integrated on requirements and interfaces. The success of the Polar Region and CSC program in FY-18 is tied into the emphasis on Systems Engineering on the Recovery Project and strong interactions between the Polar Region and Coil design teams.

Plasma Facing Component design advanced to the FDR late in September 2018. The PPPL PFCs team, with important contributions from ORNL, worked on the design, material testing, and prototype fabrication of the engineered graphite tiles. Potential scarcity of the preferred graphite material grade forced the PFC team to evaluate tile performance for multiple grades. To mitigate this risk, procurement of bulk graphite was started in FY-18 to buy up preferred

graphite grades. When NSTX-U was initially assembled, the alignment of magnets and structures was not handled carefully, and there were issues with plasma performance during the ten week NSTX-U experimental campaign. The Recovery Project took several steps in FY-18 to plan for careful alignment of the magnets, structures, and PFCs to ensure high performance. Detailed accounting of the integrated stack up of component tolerances was used to size the magnets and polar region structures. A trial fit between the Center Stack Casing and the TF/OH (Toroidal Field/Ohmic Heating) bundle was performed to demonstrate there is sufficient clearance between the two to enable TF/OH alignment adjustments. At the end of FY-18, a metrology subcontractor was brought in to precisely measure the position of the Outer PF Coils with respect to vacuum vessel upper and lower flanges.

A key Recovery Project scope area is the implementation of DOE Order 420.2C, "Safety of Accelerator Facilities" (ASO). The Recovery Project ASO Implementation Plan document was issued in FY-18 to map out how PPPL would accomplish this. NSTX-U will be the first program at PPPL and first fusion facility in the U.S. that operates under the ASO, which made FY-18 a year of discovery and organization for the Recovery Project team in this regard. The team set in motion processes to gain an approved NSTX-U Accelerator Safety Envelope (ASE) and Safety Assessment Document (SAD) and to ensure NSTX-U had a responsive Un-Reviewed Safety Issues (USI) system. DOE ASO implementation specialists were brought to PPPL to consult with the team, and a two-part Accelerator Readiness Review (ARR) plan was established to transition the NSTX-U program from the Recovery Project to Operations. A full time ASO implementation specialist was hired at the end of FY-18 to manage the overall process.

Late in FY-18 the ASO team began to understand that additional work is needed to modernize the Access Control System (ACS). NSTX-U has a functional access control system but it is not up to a standard that will pass the Accelerator Readiness Review process for ASO implementation. At the end of FY-18, the team was working on refining ACS requirements and consolidating a new team to make progress on this important new Recovery scope.

FY-18 saw a large increase in the Recovery Project engineering and project office team. The Recovery Project scope is labor-intensive in design and assembly phases. Mechanical Engineering (ME) subcontractors were hired and other mechanical engineering labor was procured from Oak Ridge National Lab and other sources that brought the ME ranks up to nearly 50 full time employees. The size of the Project Management Office was also doubled in FY-18 to manage the project effectively and satisfy stakeholder reporting obligations.

There were a series of Project Reviews, Advisory Boards, and other project assessments in FY-18 to check on project management and the integration of PPPL lab-wide management initiatives in the Recovery Project. A CD-1 style PPPL Capability and Recovery Project OPA review was held Feb 6, 7, and 8 followed by a CD-0 style Mission Need review March 14-16, 2018. The Mission Need Review committee confirmed the NSTX-U science program as vital, and the OPA Capability Review recognized the performance of the Recovery Project and PPPL in transforming project culture and running a successful project.

FY-18 closed with the NSTX-U Recovery Project Director's Review. An experienced panel of DOE technical and management specialists was led by John Post from LLNL through a complete review of the project. The goal of the review was to assess Recovery Project readiness for a CDE-2/3A baseline. The Director's Review was preceded by a full Recovery Project Integration and Requirements Preliminary Design Review which set up the technical basis for the Director's Review. Technical progress based on strong systems engineering and completion of many reviews was highlighted by the DR panel. This technical progress created a strong foundation for baseline cost and schedule estimates and assessment of risk. The Director's Review panel recommended that the project continue to update cost and schedule estimates and bolster the detail of the basis of estimate before a CD-2 baseline review is held.

## **Executive Summary for NSTX-U Maintenance and Run Prep**

### **Maintenance Run and Preparation**

NSTX-U Maintenance and Run Preparation efforts continued to provide the management, oversight, maintenance, run preparation, reduction of obsolescence periodic testing, and repairs of the NSTX-U infrastructure at D site and the NSTX-U Test Cell during FY-18. Additionally, the M&RP scope provided the cost of D site electricity, Health Physics allocations for the HP technical staff support, and level of effort costs for responsible engineers for their subsystems. The M&RP scope delivered the safe operations of the D site facility infrastructure, including work planning and control functions for the NSTX-U Test Cell activities. M&RP maintained safe areas throughout the D site facilities, and responded to Management Safety Walkthrough action items.

M&RP performed maintenance and testing to ensure the long term viability of subsystems needed to support restart and research, maintained pre-operational test and operating procedures, and maintained training of staff, including the cost of maintaining the core capability of the operating team for restart. The subsystems maintained include the Motor-Generator set, Field Coil Power Conversion, Central Instrumentation and Control, Real-time Control and Protection, the Torus Pumping Vacuum System, Cooling Water System, and Heating Systems. Heating systems continued with the testing of the Electron Cyclotron Heating Pre-Ionization system, as well as Neutral Beam (NB) work. NB work included repairs of beamline components, refurbishment of ion sources, and electronics updates to manage down obsolescence in the NB power supplies and controls.

The NB Cryogenics system was refurbished and tested including compressor installation, alignment, and tests; the Cold Box was refurbished with replacement of old thermocouple wells with welded caps and diodes to eliminate a failure mode. The Cryogenics system performed a full system test and is considered back in service when needed for restart. Work continued on the Torus Vacuum Pumping System backing pump used to evacuate the turbomolecular pumps; work included AC Power, controls, and mechanical installation. M&RP also supported the inspection of Hoisting and Rigging equipment used at D site.

## **Motor-Generator and Field Coil Power Conversion Systems**

Significant maintenance activities for Motor-Generator Systems during FY-18 included the replacement of faulty Watt and VAR transducers, the replacement of malfunctioning thrust bearing oil pressure monitoring switches, and the installation of a new waste oil tank monitoring system. For the Field Coil Power Conversion (FCPC) systems, extensive maintenance activity was performed covering all of the rectifier double pole and double throw power switches including lubrication, mechanical operational adjustments for switch travel, and verification of contact pressure.

## **Executive Summary of Research Results – FY-18 Milestones**

### **Summary of R(18-1): Develop and benchmark reduced heat flux and thermo-mechanical models for PFC monitoring**

- PFC research activities during FY-18 centered on developing new analysis tools for understanding the near- and long-term behavior of PFCs to be deployed in NSTX-U. Heat and particle flux tools were developed by Oak Ridge National Laboratory to aid in predictive capabilities for the highly shaped tiles being designed within the Recovery Project. Erosion estimates based on the steady-state, ELM, and disruption plasmas contributed directly to the PFC System Requirements Document.
- Researchers developed probabilistic tools to assess the impact of physics uncertainties on the expected heat fluxes in the device. A conservative philosophy has, to date, been applied to the requirements for the PFCs, but this analysis indicated that the actual operation of the device is likely to have engineering margin.
- Options for PFC monitoring diagnostics were explored by NSTX-U collaborators from Oak Ridge National Laboratory and Lawrence Livermore National Laboratory that included both optical methods and embedded sensor methods. Ray tracing for several optical concepts indicated that spatial resolutions of 0.2-0.6 cm/pixel can be achieved with previously-developed periscopes. Neural network-based algorithms were also evaluated that showed it is possible to reconstruct heat flux widths from embedded thermocouples based on training data developed in this milestone.

### **Summary of R(18-2) Milestone: Develop simulation framework for spherical tokamak breakdown and current ramp-up**

- A simulation framework was developed in FY-18 to perform predictive closed-loop simulations of the discharge ramp-up on NSTX-U. This was done to accelerate the realization of high-performance discharges when operations resume.
- The framework builds upon the TOKSYS framework maintained by General Atomics and contains the necessary description of the NSTX-U actuators and conducting structures. A

control-oriented model reduction technique was used to simplify the conductor model from the EFIT description in order to increase computational speeds.

- The simulation framework has a simulink capability where the operational plasma control system (PCS) software is executed in a feed-forward or closed-loop simulation. Additionally, the PCS control algorithms are mirrored within the SIMULINK environment to enable rapid development and functional testing of new control schemes.
- The linear plasma model within TOKSYS was extended to a linear time-varying (LTV) model. This was a critical element for completing fast, time-dependent simulations when the current distribution and plasma boundary are evolving, such as during ramp-up.
- The LTV model was employed to examine the vertical growth rates and the effectiveness of the vertical controller for the ramp-up phase on NSTX-U.
- Predictive TRANSP calculations completed for this milestone identified suitable choices of models and free-parameters. These choices and models reproduced the evolution of the global equilibrium parameters for a range of different ramp-up scenarios realized in NSTX-U plasmas.
- Criteria were established to evaluate time dependent vacuum field calculations of the magnetic field evolution during the startup phase. Calculations were completed using the LRDFIT code to develop and optimize startup scenarios for the MAST-U commissioning campaign.

### **Summary of R(18-3) Milestone: Validate and further develop reduced transport models for electron thermal transport in ST plasmas**

- Multiple transport models were tested using TRANSP and TGYRO solvers to predict electron temperature profiles over a wide database of NSTX L-mode and H-mode discharges.
- The Lehigh microtearing mode model, incorporated into the multi-mode model (MMM), was shown to successfully predict  $T_e$  profiles in high collisionality NSTX H-modes, but over predicted transport for low collisionality discharges. Comparisons were made between the model and first-principles gyrokinetic simulations, linear and nonlinear, that identified a few shortcomings in the model scaling. Two upgrades to the model were identified that should partially address these issues. Once implemented, model profile predictions will be retested to clarify the new limits of applicability.
- The TGLF model was found to provide many reasonable NSTX  $T_e$  predictions when applied in the electrostatic limit. In particular,  $T_e$  predictions for low beta NSTX L-modes agreed well with data, specifically when using the “SAT1” saturation rule that accounts for cross-scale, ITG/TEM-ETG coupling. Similar electrostatic TGLF-SAT1 predictions in an NSTX H-mode,

unstable to ETG, were also found to be in good alignment with  $T_e$  measurements. Furthermore, the TGLF flux-gradient relationship in the H-mode was found to agree well with nonlinear gyrokinetic simulations of ETG turbulence. These results confirmed that the TGLF ETG model may be sufficient for modeling electron-scale transport in spherical tokamaks. It also hinted at the possible need for multi-scale gyrokinetic simulations to account for cross-scale coupling. (See additional discussion in the Transport & Turbulence Additional Research Highlights.) Work will continue to compare the flux-gradient relationship predicted by TGLF with nonlinear gyrokinetic for the L-mode plasma.

- Linear stability comparisons between TGLF and the GYRO/CGYRO gyrokinetic codes illustrated that TGLF can capture many of the key scalings relevant to low-beta, electrostatic modes at a low aspect ratio, consistent with the agreement in the above model profile predictions.
- Irregular flux-gradient behavior predicted by TGLF when including electromagnetic effects appropriate for high-beta H-modes made it challenging to obtain converged profile predictions, especially in TRANSP. To address these issues, a number of potential upgrades to TGLF were discussed with Gary Staebler of General Atomics. However, these upgrades will likely necessitate development of a newer version of the model which is outside the scope of FY-18 milestone activity.
- The core of a high- $\beta_{pol}$  NSTX H-mode, with a large fraction of non-inductive current, has been calculated by gyrokinetic simulations to be near the kinetic ballooning mode/energetic particle mode (KBM/EPM) thresholds. Work continues to test whether the electromagnetic TGLF model with “hand-tweaked,” non-default settings can recover these thresholds and scalings. If successful, profile predictions will be attempted to determine whether KBM/EPM modes set the ultimate limit on  $T_e$  profiles in the high beta plasmas envisioned for 100% non-inductive scenarios.

## **Summary of R(18-4): Optimize energetic particle distribution function for improved plasma performance**

- Analysis and simulations during FY-18 of NSTX-U experiments from the FY-16 run confirmed the strong dependence of Energetic Particle (EP) driven instabilities on details of the fast ion distribution function.
- A connection was established between the regime of Alfvénic instabilities (e.g. quasi-stationary vs chirping/bursting) and thermal plasma turbulence. A criterion that predicts the regime of instabilities for given background plasma parameters was developed and validated.
- Reduced EP transport models were used to develop NSTX-U scenarios with optimized NB injection parameters to reduce or suppress Alfvénic instabilities.
- Suppression/mitigation of high-frequency Global Alfvénic instabilities (GAEs) was demonstrated on NSTX-U when the second, more tangential NB sources were used. Results were confirmed through simulations with the HYM code.
- Work continued in FY-18 to extend the use of reduced EP transport models to scenarios that feature multiple types of instabilities, including Alfvénic modes and low-frequency magneto-hydrodynamic (MHD) modes such as kinks, fishbones, and sawteeth.

## **Executive Summary for Additional Research Highlights**

### **Boundary Science**

#### **Summary of Research Highlights for Pedestal Structure and Control**

- A velocimetry algorithm was developed in FY-18 to extract accurate velocity field measurements from several diagnostic data, e.g. gas-puff imaging and possibly beam emission spectroscopy. This approach utilized averaging techniques that annihilate the invisible part of the velocity field for the case of incompressible flow, relevant to tokamaks.
- An initial development to extend BES measurement capabilities using carbon emission was successful. This development opens new scientific opportunities for multi-field, fast two-dimensional measurements of turbulence, instabilities, and impurities for NSTX-U.
- Continuing analysis into Enhanced Pedestal (EP) H-mode, an attractive operating regime discovered in NSTX, showed that the large ion temperature gradients achieved surpass the maximum gradients predicted from neoclassical codes such as NCLASS and GTC-NEO. The present analysis supports that the increased gradients in the edge temperature are consistent with the scaling derived from the leading terms of neoclassical transport theory, but quantitative agreement between theory and measurements has yet to be established.

## Summary of Research Highlights for Divertor and Scrape-off Layer

- Analysis of the divertor geometry effects in NSTX relevant to high-triangularity NSTX-U divertor configurations continued in FY-18. The standard divertor configurations with lower X-point height, higher connection length, and low poloidal separatrix angle in NSTX appeared favorable for divertor detachment; inherently high flux expansion lead to reduced peak heat flux, and plasma plugging and higher recycling lead to lower divertor temperature and higher density. Such configurations overcome unfavorable effects created by open horizontal plate divertor configuration, and are naturally created in NSTX-U with the planned divertor coil layout.
- Divertor strike point splitting in NSTX-U in the presence of error fields was calculated with the M3D-C1 and TRIP3D codes. Splitting due to misalignments in poloidal field coils was found to be small, but splitting up to 10 cm was found to be possible for 5 mm / 5 mrad misalignment of the TF inner leg.

## Summary of Research Highlights for Materials and Plasma Facing Components

- Progress was made in FY-18 on fundamental surface science studies of Li films on plasma facing components (PFCs) for improved plasma performance in tokamaks. Energetic  $D_2^+$  incident on thin Li films was shown to readily form LiD, which lead to a lower Li sputtering yield than the sputtering yield of pure Li. Measured sputtering yields for thin LiD films agreed with previous simulations and bulk erosion measurements.
- Elemental images of graphite samples from NSTX-U were obtained with a Scanning Auger Microprobe (SAM) at sub-micron resolution. The samples showed strong microscopic variations in deposition, and correlated with 3D topographical maps of surface irregularities. The NSTX-U samples were boronized and exposed to D plasmas. Topographical maps of the samples were performed with a 3D confocal optical microscope and compared to the elemental deposition pattern. The results revealed localized deposition concentrated in areas shadowed from the ion flux.

## Core Science

### Summary of Research Highlights for Macroscopic Stability

The potential effects of non-axisymmetric magnetic error fields due to PF/TF coil misalignments were investigated in various scenarios using the IPEC and M3D-C1 simulations. Both simulations identified PF4&5 and TF inner legs as the dominant source of error fields that could drive considerable 2/1 resonant fields, as well as neoclassical toroidal viscous damping of rotation in H-mode scenarios. Higher tolerances were recommended for TF inner legs than the others, as an error field from the inboard side is not easily correctable by RWMEF coils located at the outboard midplane.

- Further analysis of NSTX-U error field experiments in FY-18 suggested that large TF errors can also induce catastrophic locking of 1/1 modes in sawtoothed plasmas. This is an important multi-mode error field effect that the next-step device may also have to consider, depending on scenarios.
- Three-dimensional simulations of a vertically unstable NSTX discharge were carried out using M3D-C1 in order to investigate the formation of non-axisymmetric halo currents. A conclusion of this work is that unmitigated vertical displacement events are subject to secondary instabilities in the plasma edge that result in a fast thermal quench and localized non-axisymmetric halo currents.
- Axisymmetric M3D-C1 simulations were carried out for an NSTX-U model equilibrium with  $I_p=2$  MA in order to estimate axisymmetric forces on coils during vertical displacement events. These calculations found that the maximum force on the coils is modestly reduced by the presence of a resistive wall, and is essentially independent of the drift time.
- Disruption prediction and avoidance research has expanded in several ways. The disruption event characterization and forecasting (DECAF) code produced analysis of large databases that were thousands of shot seconds and upwards of one half million tested sample times per database for NSTX, MAST, and KSTAR for a small set of disruption characterization events. Analysis of the current quench event produced the equivalent of “disruptivity diagrams.” This analysis continues to support the relatively unappreciated conclusion that plasma disruptivity does not increase with plasma normalized beta.
- A local island power balance model to explain the density limit in tokamaks was tested in FY-18 with NSTX data and is being evaluated as a potential disruption forecaster in the DECAF code, presently showing similarities to the global Greenwald density evolution and limit.
- The DECAF code development has significantly increased capability by automatically identifying rotating MHD instabilities, their bifurcation, and their locking. Toroidal mode number is also automatically discriminated for an arbitrary number of modes that occur simultaneously. The information analyzed for these modes, along with plasma rotation

profile and other plasma measurements (15 criteria presently used), produces predictive warning signals for the modes, along with a total MHD event warning signal showing initial success as a disruption forecaster.

- DECAF analysis of NSTX plasmas demonstrated that disruption forecasting analysis should start in areas of the parameter space of the larger disruptivity database that are non-intuitive, and that usual areas of disruption investigation from human processing of disruption databases, or black-box machine learning, are not targeting the correct plasma conditions. DECAF disruption event chains for relatively long and relatively slow evolution toward the current quench (which often occur) provide the understanding of the disruption event evolution in such cases.
- The study of resistive MHD activities in NSTX discharges revealed spontaneously growing but saturated modes at very low amplitudes. The precursors of these small-island activities were also identified. Resistive DCON showed that the modes are classically unstable even with stabilizing effects expected by strong curvature and pressure gradients in NSTX, although the rotation shear could stabilize the modes as predicted by M3D-C1 simulations.
- MARS-F/K simulations were carried out to investigate the poloidal structure of the plasma response to magnetic perturbations applied with the NCCs. The study aimed at identifying optimal locations where new toroidal arrays of magnetic probes could be installed to improve the measurement of quasi-stationary, non-axisymmetric magnetic fields. The study highlighted how the addition of 12 toroidal arrays of probes, equally distributed between the top and the bottom of the machine as well as between poloidal and radial sensors, would provide adequate measurements to discriminate the poloidal structure of 3D fields up to  $n \leq 6$ .
- Resistive M3D-C1 MHD simulations of magnetic islands driven by the proposed Non-axisymmetric Control Coil (NCC) in NSTX-U, with different normalized pressures, have shown that the internal island structure bifurcates before they overlap with neighboring islands. These internal bifurcations produce new sets of X- and O-points that result in an internal island stochastization, which is expected to locally alter the heat and particle transport across the islands prior to the onset of global stochasticity.
- Based on successful tests with the Electromagnetic Particle Injector (EPI-1) system for fast time response disruption mitigation in tokamaks, which was able to verify the critical EPI parameters of fast response time and velocity consistent with the projected values, the much upgraded EPI-2 has been designed and built with field augmenting coils with a capability of  $>2T$ . EPI-2 will be fully characterized during 2019.
- The collaboration with COMPASS on error field physics showed that the conventional single-mode approximation is still valid to avoid a locking from high-field-side error fields, but the effects of the residual resonant fields are still under investigation. NSTX-U and

COMPASS results both indicated the multi-mode effects of the high-field-side error fields can be more significant than other source of error fields.

- The collaboration with DIII-D/KSTAR/EAST on error field physics was also successfully extended. The parametric dependences of the  $n=2$  scaling on density,  $B_T$ , rotation were investigated and shown to be similar to one of the  $n=1$  as expected. The  $n=1$  and  $n=2$  scaling could be combined accordingly, using the overlap resonant field as a threshold metric, although the relevance of power scaling for rotation and stability index must be further investigated.
- The collaboration with KSTAR on disruption prediction and avoidance produced steady evolution of both linear ideal and resistive MHD analysis for long-pulse KSTAR plasmas. A critical part of this analysis has been extensive kinetic equilibrium reconstruction analysis including motional Stark effect (MSE) data. The analysis concluded that the classical resistive  $\Delta'$  does not accurately describe the experimental plasma stability. Kinetic MHD analysis of global MHD modes (resistive wall modes) using the MISK code found stability of high beta KSTAR plasmas, consistent with the experiment.

### Summary of Research Highlights for Transport and Turbulence

- NSTX-U L-mode discharges have been used to validate local, nonlinear gyrokinetic simulations. Separate ion-scale and electron-scale simulations predict comparable electron thermal transport ( $Q_{e,low-k} \sim Q_{e,high-k}$ ), whose sum is close to experiment. However, cross-scale coupling are likely to be important under these conditions ( $Q_{e,low-k} \sim Q_{e,high-k}$ ), which would require multi-scale simulations to accurately predict. Such simulations are being considered for the NSTX-U L-mode plasmas.
- Electron-scale electron temperature gradient (ETG) simulations can predict electron heat fluxes that match experiments for two different levels of ETG drive (that depend on density gradient) in an NSTX H-mode. Synthetically generated spectra using a new analysis technique can reproduce the qualitative change of measured high-k microwave scattering fluctuations with changing density gradient and corresponding ETG drive. However, in the weak ETG-drive case, ion scale turbulence is predicted to be near marginal such that  $Q_{e,low-k} \sim Q_{e,high-k}$  and cross-scale coupling effects cannot be ruled out without multi-scale simulations.
- The NSTX and NSTX-U discharges referenced above, in addition to discussion in the R18-3 Milestone summary, have been identified as potential targets for future multi-scale simulations to investigate cross-scale coupling. Such multi-scale simulations would complement recent simulations at conventional aspect ratio (e.g. Alcator C-Mod, ITER) and would contribute to efforts to improve predictive modeling capabilities in all tokamaks.
- Analysis of the DIII-D FY17 NSTX-U campaign experiment “study of collisionality dependence of ion- and electron-scale turbulence in advanced inductive hybrid scenario with ST-relevant  $q_{95}$  on DIII-D” has progressed. Initial analysis found dimensionless confinement scaling of  $B\tau_E \sim v_e^{-0.5}$  in  $q_{95}=6.5$  hybrid discharges that were similar to DIII-D H-

modes. Density fluctuations at low wavenumber measured by Doppler backscattering have lower fluctuation power with decreasing collisionality consistent with improved confinement. Transport analysis found the dominant energy losses to be through the electron channel. While TGLF modeling predicts the correct change in  $T_i$  profiles with  $v_*$ , it only captures  $T_e$  changes at the lowest collisionalities and underpredicts transport at high  $v_*$ . However, cross-scale coupling was not included in the model and may be important in the low  $v_*$  cases. Global gyrokinetic GTS simulations also predict reasonable ion thermal fluxes, but significantly under predict electron fluxes, further suggesting electron-scale/cross-scale coupling may be important.

- Analysis of the DIII-D FY17 NSTX-U campaign experiment “Validating electromagnetic effects in high performance plasmas” has also progressed. Initial analysis of the QH-mode discharges indicated that the ratio of scattered powers measured by cross polarization scattering (CPS, expected to be proportional to  $\sim\delta B$ ) and DBS ( $\sim\delta n$ ) increased with increasing beta, as expected from theory. To analyze the QH-modes with very large impurity content (run  $\sim 6$  weeks after boronization), the impurity transport code STRAHL was used to estimate impurity content, constrained by soft x-ray and bolometer measurements. The results were included in TRANSP analysis to produce transport and equilibrium solutions most consistent with neutron and stored energy measurements. These will provide the basis for future gyrokinetic simulations.
- Gyrokinetic simulations have been used to analyze microtearing mode stability in high  $\beta\sim 100\%$  Pegasus plasmas that complement  $\beta\sim 40\%$  NSTX plasmas. The influence of  $\nabla B$  drift reversal is found to be stabilizing to  $k_{\theta}\rho_s \sim 1$  modes, illustrating the importance of understanding the impact of a deep magnetic well on electromagnetic drift modes.
- Analysis of impurity transport in NSTX H-modes using 3D fields for ELM pacing has moved forward in FY-18. Quasi-linear gyrokinetic simulations were used to predict theoretical turbulent carbon flux profiles resulting from a mix of unstable electrostatic ballooning modes and micro-tearing modes. Initial tests of centrifugal effects using the CGYRO code indicate they are not critical to include for carbon transport in these particular cases.

### Summary of Research Highlights for Energetic Particles

- A correction to the scattered light signal from cold  $D_{\alpha}$  was developed during FY-18 to reduce uncertainty in the interpretation of the FIDA signal. The correction is based on results from measurements made both in the laboratory and during plasma operation.
- Processing of experimental and simulation data as inputs to the “kick model” were streamlined by developing a multi-processor procedure. The time required to compute kick model inputs using this procedure was reduced from several hours to 5-30 min.
- Good progress was made in developing the Resonance-broadened Quasi-linear model (RBQ1D) by implementing self-consistent multi-mode simulation capabilities. An important

development was the capability to describe transport induced by multiple Alfvén modes acting simultaneously on the fast ion population.

- Experimental scaling of Global Alfvén Eigenmode frequencies and toroidal mode numbers with toroidal field was found to be qualitatively consistent with that from analytic theory. HYM simulations confirmed that fast ions with high parallel velocity from the more tangential beam line in NSTX-U are effective in suppressing the GAEs, opening up a path to scenario optimization through selective neutral beam injection.
- Fully self-consistent HYM simulations revealed strong energetic particle modifications of GAE mode. Large changes in GAE mode frequency through changes in beam injection velocity and in accordance with Doppler-shifted cyclotron resonances, without accompanying changes in mode spectrum, were largely unexpected.
- Repetitive drops in neutron production observed in conjunction with sawteeth were studied using data from FIDA and the ssNPA, and they suggested fast ion redistribution and/or loss. Modeling showed that neither the Kadomtsev full, or Porcelli partial reconnection models were consistent with the observations. The more comprehensive kick model, however, which determines the redistribution in energy, pitch, and radial location, showed agreement with observations.

## **Integrated Scenarios**

### **Summary of Research Highlights for Solenoid-Free Start-up and Ramp-up**

- Three dimensional MHD NIMROD simulations were carried out in FY-18 to examine whether maximum closure during transient CHI is feasible in the presence of non-axisymmetric 3-D magnetic fluctuations. The simulations were extended to numerically investigate two major effects: 1) the role of three-dimensional magnetic fluctuations on the plasmoid-mediated flux closure, and 2) the effect of the toroidal field on 3-D stability during transient CHI. Closed flux current of about 220kA and large-volume flux closure were obtained even in the presence of non-axisymmetric edge magnetic fluctuations. It was also found that the 3-D physics response was drastically different for simulations at higher toroidal field, and complete stabilization of non-axisymmetric fluctuations were achieved at higher toroidal flux. (A paper covering this is in preparation for presentation at a later date.) Further simulations will be carried out for prediction and accessibility to the regimes of maximum start-up with increased toroidal and injector fluxes in larger STs.
- The CHI systems on QUEST were operated reliably and up to 45 kA of toroidal current was generated by transient CHI.
- Initial scoping studies for a biased divertor CHI configuration for Pegasus were conducted, and the power supply requirements identified.

## Summary of Research Highlights for Wave Heating and Current Drive

- Initial modeling on the impact of hydrogen (H) species on High Harmonic Fast Wave was performed for NSTX-U plasmas by the use of the full wave code AORSA. Different H concentrations from 2% to 10% with and without NBI were considered. Furthermore, two wave frequency regimes have initially been considered: 30 MHz, which corresponds to the frequency of the current HHFW heating system, and 60 MHz. These wave frequency regimes have different D & H cyclotron resonances in the plasma.
- Modeling on RF edge losses in NSTX/NSTX-U plasmas by a finite element code FW2D was performed. In particular, two aspects have been considered: the impact of the realistic vacuum vessel boundary conditions on the wave propagation in the SOL, including the evaluation of SOL losses, and the evaluation of the HHFW losses in the FW2D code. This type of numerical study shows that wave propagation in the SOL strongly depends on the boundary shape and the density in front of the antenna.
- RF studies on Large Plasma Device (LAPD) were conducted. To assess the relationship between rectified currents and rectified voltages, detailed experiments have been performed on LAPD, where an electron current was measured flowing out of the antenna and into the limiters, consistent with RF rectification.
- A study on the effect of ICRF heating on triple-probe signals was carried out as part of an ICRF collaboration with the Experimental Advanced Superconducting Tokamak (EAST). EAST has two ICRF antennas and twelve megawatts of ICRF source power in support of high-power and long-pulse operation. A comparison between EAST and NSTX results was made. It was discovered that in both cases, probes which do not connect to the antenna but whose field lines pass just in front of it experience a negative shift in floating potential. This is consistent with RF rectification occurring in the divertors.
- Electron cyclotron (EC) and electron Bernstein waves (EBW) numerical simulations were performed on QUEST plasmas. Graduate student Ryota Yoneda from Kyushu University (Japan) worked in collaboration with Nicola Bertelli and Masa Ono on EC/EBW modelling for QUEST plasmas employing ray tracing. Numerical simulations of high energy electrons by mean of the Fokker-Planck code CQL3D coupled to the ray tracing code GENRAY were also performed and presented at the annual QUEST workshop. Finally, a grid-based start-up code was developed where plasma parameters, generated plasma currents, and resulting poloidal magnetic fields evolved from the vacuum fields.

## Summary of Research Highlights for Advanced Scenarios and Control

- Research milestone R18-2: “Develop simulation framework for spherical tokamak breakdown and current ramp-up” was completed, providing a significant advance for developing and testing scenario and control solutions for realizing high-performance discharges on NSTX-U.
- A high-fidelity neutral beam neural network model, suitable for use in real-time applications, was developed in FY-18 to enable rapid evaluation of the beam heating, torque, and current drive profiles based on measured equilibrium profiles. The model is able to generalize and accurately reproduce NUBEAM calculated profiles and scalar quantities.
- Results of processor-in-the-loop simulations of the NUBEAM neural network model within the NSTX-U plasma control system demonstrated the suitability of the approach for real-time use and accelerated offline analysis.
- The rapid accrual of oxygen impurities over the course of H-mode operations during the NSTX-U commissioning campaign was correlated with vertical disruption events (VDEs) that put considerable power on the inner divertor surfaces. The results supported the thesis that inboard divertor tiles that were not sufficiently baked prior to the start of operations contained the largest source of water trapped in the graphite tiles.
- Collaboration with the Mega Amp Spherical Tokamak Upgrade (MAST-U) advanced the development of common tools for developing scenarios and control on the two complementary ST experiments. Members of the NSTX-U team are actively consulting on the development of the MAST-U commissioning procedures and a planned expansion of the real-time control system.
- Extensive tests with the Dolphin Interconnect Solutions demonstrated that this technology is a suitable reflective memory solution for expanding the computational power of the real-time plasma control system (PCS) in support of future PCS development, such as disruption prediction and avoidance.
- A physics-based multiple-input-multiple-output algorithm was developed for real-time feedback control of the snowflake divertor (SFD). Reduced models for the response of an X-point to changes in poloidal field and for the plasma response to changes in the PF coil currents are used to design a Linear-Quadratic Regulator for the SFD based upon a set of user-defined weights specifying the relative importance of the controlled variables.
- The SFD control algorithm was implemented in the NSTX-U and DIII-D Plasma Control System (PCS). The algorithm was commissioned at DIII-D in March 2018.

- A simple analytical model was derived that describes the partitioning of scrape-off layer power and particle exhaust in the SFD due to diffusive transport to multiple activated strike points (SPs). The model was validated against simulation results from the multi-fluid edge transport code UEDGE and used to analyze a database of 70 SFD-minus equilibria to determine optimal SFDs for heat flux mitigation and particle control.

### **Performance of FY2018 Notable Outcomes**

**FES:** For the NSTX-U recovery project, complete final design reviews for six inner poloidal magnetic field coils (viz., PF1A-upper, PF1A-lower, PF1B-upper, PF1B-lower, PF1C-upper, and PF1C-lower) by March 31, 2018 (Objective 2.1).

- A Final Design Review (FDR) for the Inner PF Coil Production coils was conducted on March 30, 2018 in order to satisfy milestone requirements. The FDR covered all six inner PF coils: PF1A-upper, PF1A-lower, PF1B-upper, PF1B-lower, PF1C-upper, and PF1C-lower. The design and analysis of the interfaces and coils was presented, in addition to cost, schedule, risks, and fabrication plans and strategies that included PPPL and external vendors. The review was attended by both PPPL staff and external coil subject matter experts (SMEs) and was deemed successful.

**FES:** For the NSTX-U recovery project, build at least one prototype PF1A inner poloidal magnetic field coil. Qualify the coil by operating it at both the maximum required current and at maximum joule heating. Verify the quality of the coil's insulation system through electrical testing followed by destructive sectioning and inspection. Submit a final report documenting the results by July 15, 2018 (Objective 2.2).

- Inner PF Coil Prototype Technical Evaluation Procedure (PTEP) C/D-PTP-NSTX-CL-063 was applied to two prototype coils delivered to PPPL during FY-18. This procedure involved physical inspections, sectioning of the coil for internal inspection, low- and high-voltage testing, power testing, and turn-to-turn insulation electrical testing.

The PTEP generated the following results:

- PF-1a prototype coils from Everson Tesla, Incorporated (ETI) and PPPL were evaluated and passed basic dimensional inspections, low power electrical tests, and mechanical evaluation before and after they were sectioned. The coils also successfully passed high power tests on the Field Coil Power Conversion (FCPC) test stand. The low power electrical tests were repeated, and there was no change in the coil's electrical insulation properties.
- The ETI and PPPL prototype coils were successfully sectioned and visually examined to confirm the quality of the Vacuum Pressure Impregnation (VPI). The ETI coil displayed 2-3 continuous voids along toroidal channels near the turn corners at section ends, and the PPPL coil showed 4-6 small non-continuous voids.

- Turn-to-turn and turn-to-ground insulation of both halves of the sectioned coils was successfully tested using insulation resistance and hi-pot tests. Samples of the fully cured resin material properties were confirmed by a Differential Scanning Calorimetry (DSC) test.
- The NSTX-U Recovery project will get prototype inner PF coils from four suppliers. The technical evaluation of the remaining two prototypes will begin as soon as they are received by the coil test team. The information obtained in the technical evaluation process, along with other factors, will be considered part of the Source Selection Procedure for production coil suppliers. PPPL will continue to use the PTEP procedure on all four coil sections, with the exclusion of the high power test. A complete report will be written to cap this milestone summary once testing is finished.
- The two coils successfully passed all tests, although neither coil was entirely void-free. Since the NSTX-U Recovery project has obtained and evaluated two prototype inner PF coils, one supplied by ETI and another supplied by PPPL, it is concluded, based on test results, that the DOE Notable Outcome Objective 2.2 requirements have been met. These results are also now key elements in the vendor evaluation process.

**FES:** For the NSTX-U recovery project, complete a preliminary design review (PDR) for the passive plates and helium bake-out line supports by July 31, 2018. (Objective 2.2)

- A PDR was conducted on July 26, 2018. The PDR scope covered a review of the as-built condition of the passive plates, passive plate support structures, and the hot helium bake piping. The loads on these components and current finite element analysis stress were also reviewed. A design was proposed that would relieve the high stress components and minimize the motion in passive plates. An electrical strap was also proposed to reducing the variation in resistances across the passive plates. The review was deemed successful.

**FES:** For the NSTX-U recovery project, complete a final design review (FDR) for improved and re-designed plasma facing components by September 30, 2018. (Objective 2.2)

- The full scope of tiles (WBS 1.1.1.1 thru 1.1.1.7 inclusive) was reviewed at the Final Design Review held on September 28<sup>th</sup>. This work encompasses as much 1400 graphite tiles protecting the machine from the plasma and vice versa. The FDR was chaired by Valeria Riccardo and included two external reviewers. The FDR was determined to be successful pending resolution of final CHITs.
- All areas of the project were reviewed at a Preliminary Design Review (PDR) as of November 2017. In the time since, a major WAF revision was undertaken to reflect uncovered scope in the PFC WBS areas due to the large number of variants and other procurement challenges associated with the graphite industry.

- Tile designs will meet physics requirements as listed in the PFC SRD and enable high power operations when the NSTX-U Recovery Project concludes. This includes operations and physics diagnostics embedded within the PFCs.
- As part of the FDR, the PFC team produced six design reports, 23 calculation reports (and check reports), eight test, metrology, or other reports, closed approximately 200 CHITs from previous reviews dating back to the Design Verification and Validation Review (DVVR) process, and produced 65 drawings.

## **Goal 4.0 - Contractor Leadership/ Stewardship**

**SC/FES:** The University, in concert with PPPL leadership, shall ensure that the necessary support is provided for efficient and effective management of the NSTX-U Recovery effort, such that this project will have completed a Director's Review by September 30, 2018. (Objective 4.2)

- A Director's Review and Independent Cost Evaluation was held on September 5-7, 2018 and was chaired by John Post of Lawrence Livermore National Laboratory. The first day of the review was for plenary presentations, the second day of the review consisted of parallel subcommittee sessions devoted to in-depth exploration of topics, and the third day was for report generation and debrief to the NSTX-U Recovery Team.
- The review committee was requested to address the following charge questions A, B, C:
  - A.** Please address the draft DOE CDE-2/3A OPA baselining review charge questions 1 through 8 enumerated below:
    - 1A. Are designs supporting the Recovery Project technically sound and likely to meet performance specifications?
    - 1B. Are all design interfaces appropriately defined?
    - 1C. Is the CDE-3A scope appropriate?
    - 1D. Is the design sufficiently mature to establish the baseline and initiate CDE-3A long-lead procurement?
  - 2. Are project risks properly identified and are appropriate mitigation strategies in place?
  - 3A. Are the cost and schedule estimates credible and realistic to support establishment of the baseline?
  - 3B. Do they include adequate contingency based on project risk and uncertainty analysis?
  - 3C. Are the cost estimates traceable and appropriately integrated with the project schedule?

4A. Is the project being managed (i.e., properly organized and adequately staffed) as needed to complete final design and support the project through construction to successful completion?

4B. Is the risk management process being effectively managed?

4C. Are project assumptions (technical/cost/schedule) appropriately documented?

5A. Are environmental, safety & health aspects being properly addressed given the project's current stage of development?

5B. Are integrated safety management principles being followed?

6. Have the recommendations from previous reviews been appropriately addressed?

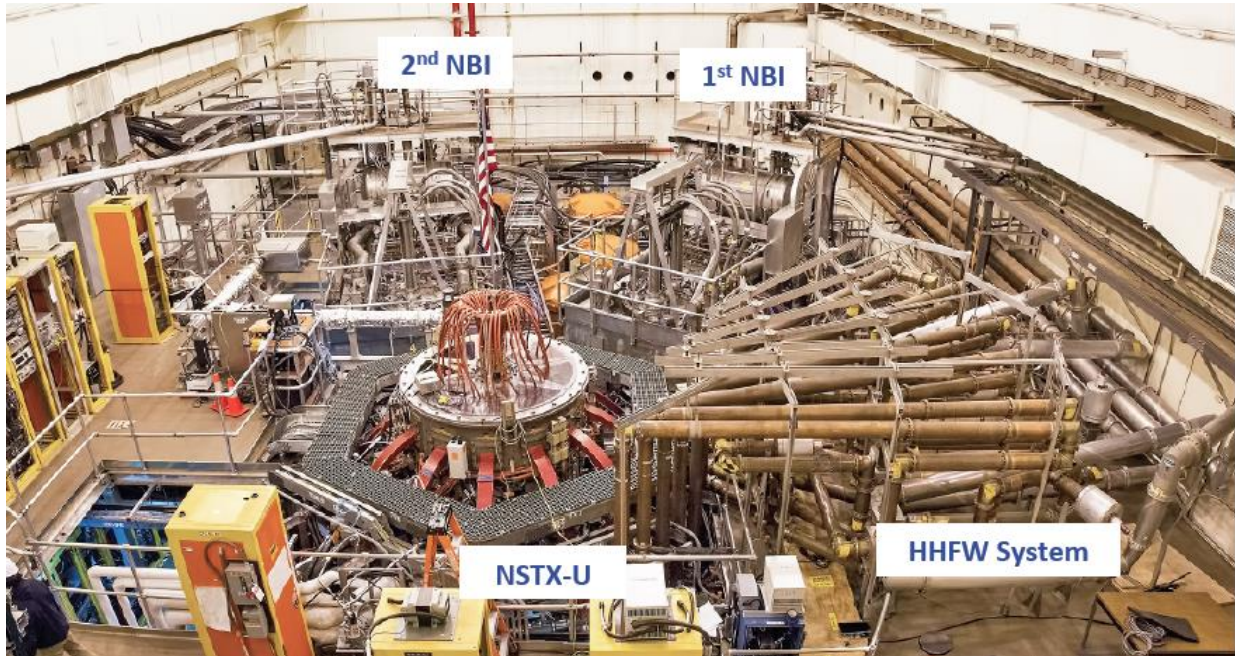
7. Is the project documentation (e.g., PEP, HAR) complete and ready for approval?

8. Is the project ready for CDE-2/3a approval?

**B.** Please provide your assessment of whether the Recovery project scope has appropriate QA/QC oversight and staffing. Similarly, please provide your assessment of whether PPPL engineering policies and procedures adequately support the NSTX-U Recovery project.

**C.** The project has been asked to consider options to shorten the project duration by deferring (and/or possibly accelerating) scope required to meet the ultimate performance objectives of the facility. Please provide your assessment of the Recovery team's proposals for these options.

# NSTX-U Recovery Project



During the spring of 2018, the DOE SC Office of Project Assessment (OPA) carried out two major assessments of NSTX-U. The first assessment evaluated PPPL's capability to design, estimate costs and schedule, and execute repair activities. The second assessment evaluated the continued mission need for the NSTX-U program and facility. Both assessments were sufficiently successful to warrant continuation of the program. Furthermore, during FY2018, more than 40 conceptual, preliminary, and final design reviews were carried out to develop component cost and schedule estimates and to prepare for fabrication and installation of improved components. Substantial progress has been made in many Recovery Project areas, but the most substantial hardware development progress has been made in the PF1 coil development area. Key FY-18 PF1 coil progress includes:

- A "straight log" created and manufactured at PPPL that used vacuum pressure impregnation (VPI) to bond a 4x6 pack of conductors as a test of the VPI process. The process was successful as evidenced by lack of voids in the VPI epoxy, good mechanical integrity of the log, and turn-to-turn voltage stand-off results.
- A final design review for production coils was successfully completed in March 2018 and accomplished a Notable Outcome for FY 2018.
- Prototype PF1 coil fabrication was initiated at PPPL and 3 external vendors: PPPL, Everson Tesla (PA USA), Tesla (UK), and Sigma Phi (France). The prototype program was completed in August, 2018, and the results from prototype coil mechanical and electrical testing will be used to select vendor(s) for PF-1 production magnets.

- Copper conductor for the PF-1A, B, and C production coils was successfully fabricated and fully inspected via ultrasound at Luvata in Finland. By the end of FY-18 all of the production copper conductor was at a facility in Italy for grit blast and priming surface treatment.

During FY2018, PPPL and FES developed criteria for sorting NSTX-U scope into 2 categories:

- Recovery Project scope - for repair and/or redesign of deficient components including components that (a) are very difficult to access in the event of component failure, (b) directly impact a Key Performance Parameter in the Preliminary Project Execution Plan (PPEP), or (c) are related to a safety order, safety issue, or a safety system. (This is an abridged list of the actual criteria used.)
- Facility Operations scope – this covers primarily routine maintenance of previously functional systems, and/or ongoing support for systems necessary for commissioning activities in the Recovery Project.

The NSTX-U team is preparing for a Project baselining review tentatively planned for winter 2018. Assuming baselining is successful, all Recovery Project scope is planned to undergo final design review during FY 2019 for subsequent execution and/or fabrication/installation in FY 2019-2020.

Recovery Project scope titles and FY2018 progress highlights are described below organized by WBS and Level 2 WBS / Job Number / Description.

# Magnets

## 1.1 / 4015 Inner PF Coil Replacement

The inner PF replacement scope includes the redesign of the PF1a, PF1b, and PF1c coils. A Final Design Review (FDR) for the Inner PF Coils was conducted on March 30, 2018. Major design changes were made throughout all the coils. These changes included mandrel-free coils, increasing insulation, and a softer single length of copper conductor. The final design of PF1a is shown in Fig. 1.1.1.

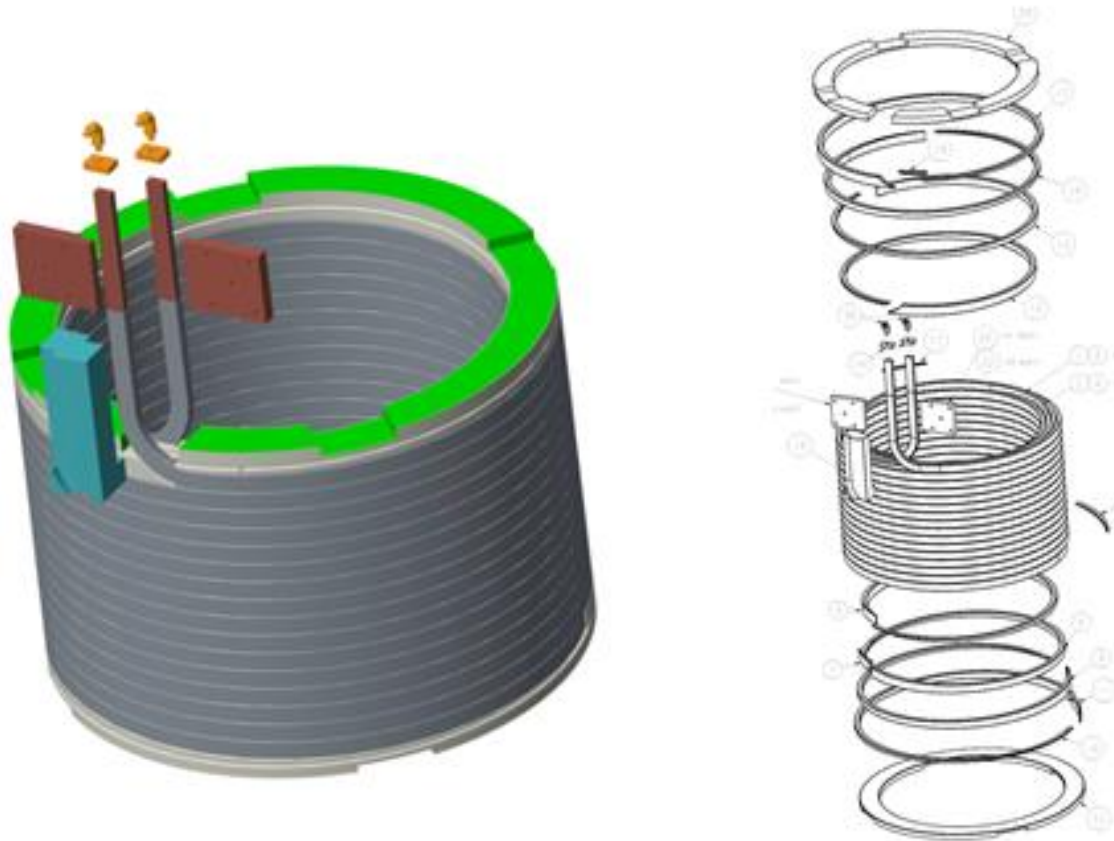


**Fig. 1.1.1:** Upgraded PF1a Coil, final design.

The old coil design consisted of individual turns of copper that were brazed together with joggles. Having a single length of copper conductor allows for a continuous manufacturing process and eliminates the risks associated with brazing. The increased insulation scheme was designed to increase the dielectric strength of the coil. The insulation scheme is shown in Fig. 1.1.2.

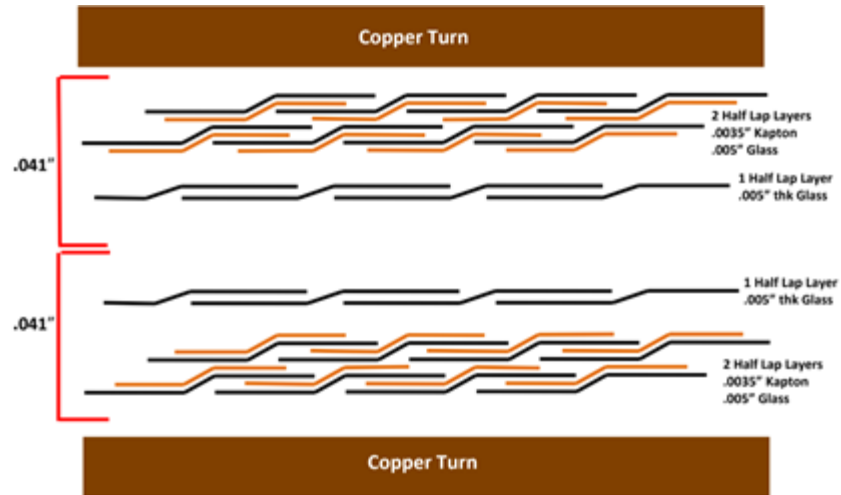


**Fig. 1.1.2:** Inner PF Coil insulation scheme.

Also presented at the FDR was the procurement plan for the inner PF coils which included procuring prototype coils, testing the coils, and procuring production coils from vendors who completed a successful prototype. To ensure that the replacement coils were of the highest quality, prototype coils were fabricated to confirm the manufacturing process and to qualify suppliers. In June 2018, two of the prototypes were completed and tested by PPPL. In August 2018, the remaining two coils were delivered to PPPL and will be tested by the end of the fiscal year. The testing and evaluation includes dimensional inspection, DC megger tests, AC impedance scan, surge tests, and full power pulse tests. The prototype coils will then be milled into two sections, and the sectioned coil will undergo a series of tests including the physical examination of sectioned coil, as well as turn-to-turn breakdown testing. Fig. 1.1.3 shows a prototype coil configured for full power testing. An FDR for the Inner PF Coil Power Test Plan for the prototype coil was held on May 9, 2018.



**Fig. 1.1.3:** PF1A Prototype test setup.

By the end of the calendar year, all the prototype coils will be evaluated and compared. Contracts to fabricate the inner PF coils will be awarded to the chosen subcontractors.

### 1.1 / 4020 PF Bus Support

The inner PF BUS bars and terminal supports were updated in FY-18 to match the as-built condition first, and were further modified based on the new PF coil design and the updated polar region design. Design models were given to the analysis group to evaluate the design for EM and structural loads satisfaction. Fig. 1.1.4 shows the updated design of the PF inner hard and flex bus; Fig. 1.1.5 shows the coil terminal support design for top and bottom PF1 coils.

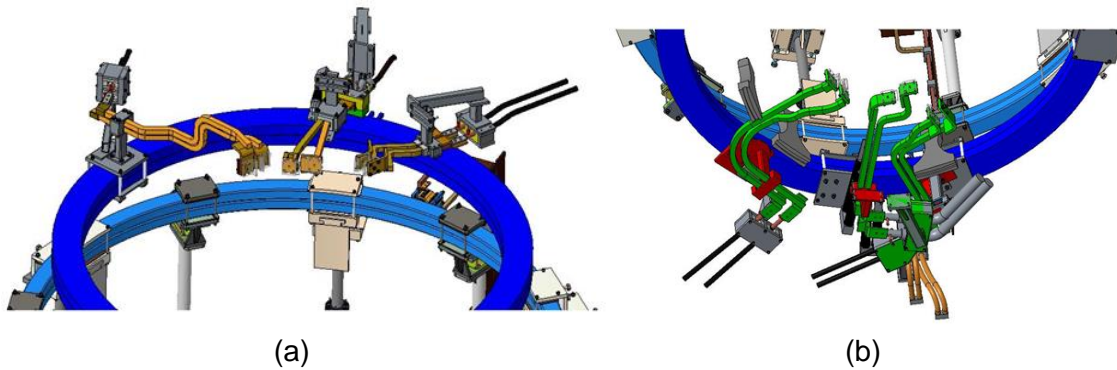


**Fig. 1.1.4:** (a) PF inner hard and flex BUS, top, and (b) PF inner hard and flex bus, bottom.

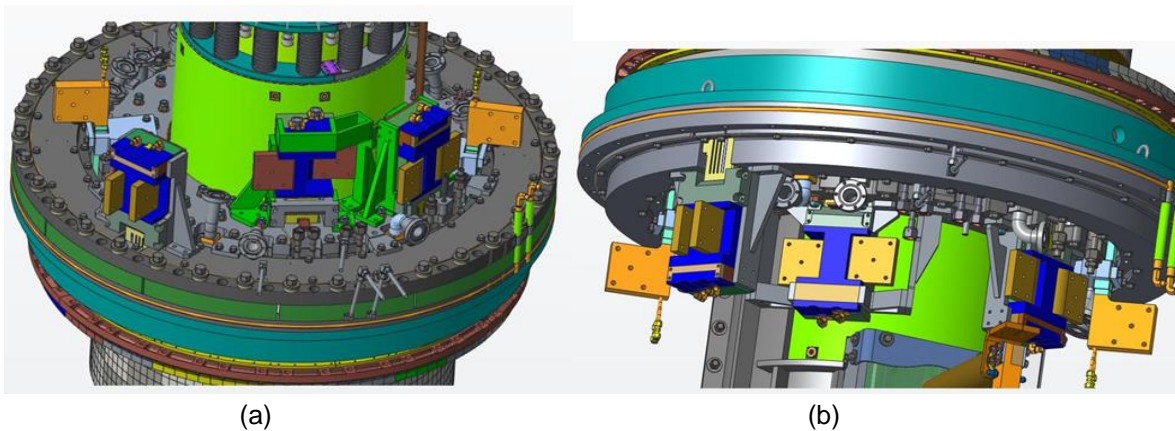


**Fig. 1.1.5:** (a) PF inner coil terminal supports, top, and (b) PF inner coil terminal supports, bottom.

The design of the PF1B power supply from PCTS to PF1B hard BUS was modified to PDR specifications. Water cooled power supply cable was quoted and the interconnection between flex cable and PCTS hard connection was designed. Fig. 1.1.6 shows the drawing for the interconnection design.

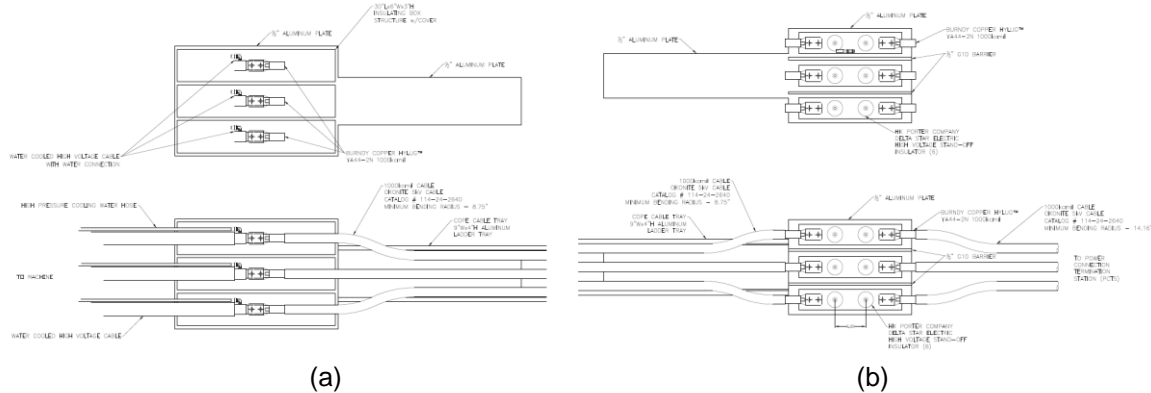


**Fig. 1.1.6:** PF1B coil (a) machine end transition connection, and (b) PCTS end transition connection.

Hard supports for outer PF coils were field verified in FY-18, and the design of the reinforcement for PF4 flex BUS support was completed. Fig. 1.1.7 shows the design of the PF4 BUS supports. The design model was passed to the analysis group for EM, thermal, and structural analysis. The analysis work is ongoing.

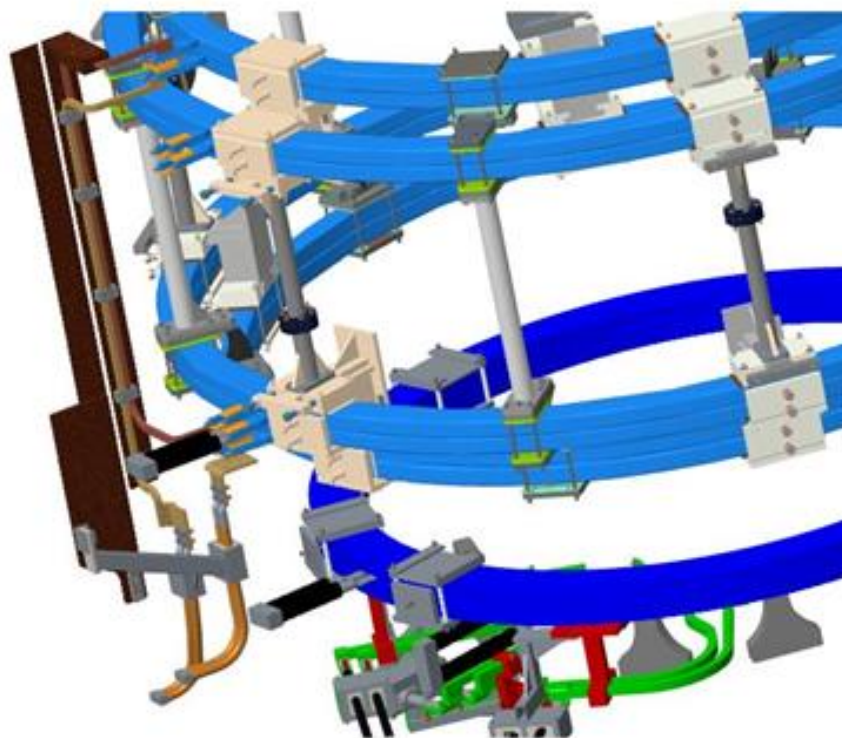


**Fig. 1.1.7:** Reinforcement design for PF4 flex BUS.

The last part of the work scope was to modify the CHI bus to accommodate the new bake-out scheme for CS casing. The bottom ceramic break was removed in the polar region, and the power supply and return for center stack baking are now on top of the vacuum vessel. The design of the top and bottom bakeout BUS bars was finished, and EM and structural analysis continues. Fig. 1.1.8 shows the new bakeout BUS design top and bottom.

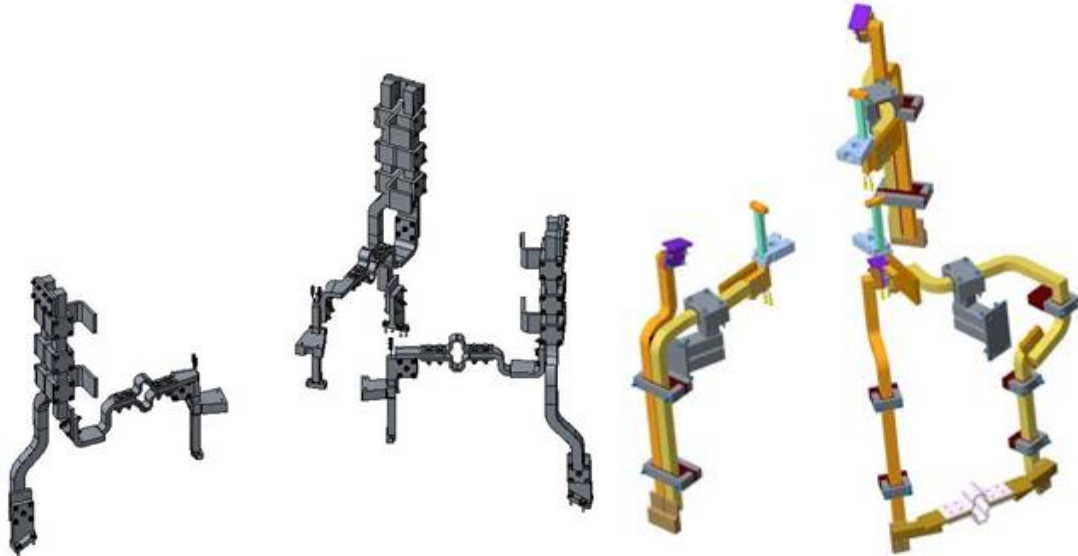


**Fig. 1.1.8:** (a) New top bakeout bus design and (b) new bottom bakeout bus design.

## 1.1 / 4025 Magnet Recovery Project Scope

The 4025 magnet control account recovery project scope focuses on work scope related to resolving miscellaneous CHITs generated during the magnet DVVR process. The work is mainly divided into three areas: modification of the coil cooling water interlock, inspection of the Torodial Field/Ohmic Heating (TF/OH) bundle and its reliability, and inspection/repair of the outer PF coils.

The modification of the coil cooling water interlock was reviewed at a preliminary design review (PDR) on February 22, 2018. The modification primarily consisted of interlocking detected loss of coil cooling flow with the supplying pumps. This new embodiment ensures that a detected leak disables the water flow supply to mitigate excessive water damage.

The inspection of the TF/OH bundle and reliability was reviewed at a PDR on April 3, 2018. The proposed improvements included methods to harden the bundle against water leaks, managing the pre-existing aquapour-embedded removal wires, and water leak detection. Proposed reliability assessment consists of electrical testing of the TF/OH bundle.

The outer PF coils were identified as a concern at the magnet design, validation, and verification review (DVVR) due to their age and pedigree. Electrical testing was reviewed at a PDR held on March 13, 2018. *In-situ* power testing the coils is not considered viable due to the *in-situ* installation of the coils and the current disassembled state of the overall machine. Accordingly, the proposed electrical testing involves verifying the coil insulation integrity over temperature to simulate thermal stresses imparted on the insulation system during coil energization.

## 1.1 / 4030 Magnet Operations Scope

Due to other ongoing Recovery efforts, Operations resources have been reassigned to other Project areas.

## Plasma Facing Components

Plasma facing components (PFCs) are the first surface to come in contact with the plasmas produced within fusion experimental devices. As such, these components are sometimes called “armor” as they protect other parts of the machine from the harmful damage caused by unmitigated plasmas. In the NSTX-U Recovery Project, the PFCs also present a benign material surface that has a lower atomic number ( $Z$ ) than the steel vacuum vessel.

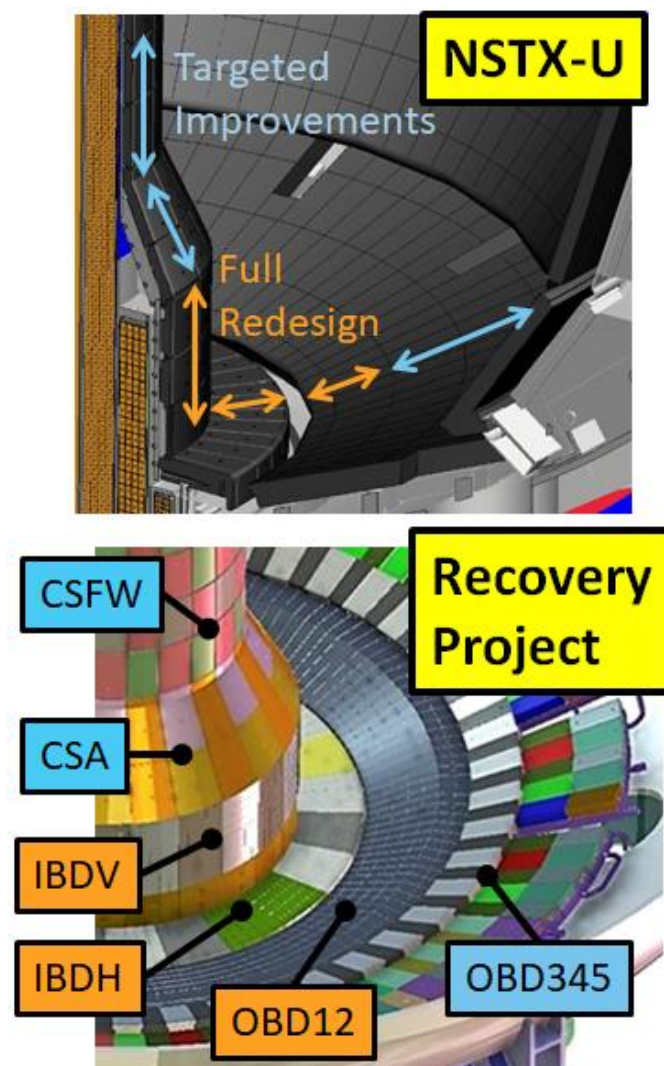


*Fig. 1.1.9: Modification areas and work breakdown areas for PFCs.*

The DVVR and Extent of Condition processes at PPPL throughout FY 2017 identified several problems with the current set of PFCs. In response, the Recovery Project has undertaken the

redesign and improvement of several key areas of PFCs. The regions of NSTX-U that require modification, as well as the Recovery Project work breakdown area, are identified in Fig. 1.1.9 below. The Recovery Project has divided the tiles to be replaced into two categories: full redesign and targeted improvements. These categories are largely defined by how much heat-flux is expected in these regions. These general categories are described further below.

Regions that are expected to receive significant heat fluxes during plasma operations are denoted “high heat-flux” or HHF. The significant thermo-mechanical loading that occurs from absorbing the NSTX-U plasmas led to an early decision to completely change the tile design, and so these areas have “full redesign.” In low heat flux (LHF) regions, it was found that the existing tile designs could be modified to handle the combined thermomechanical and electromagnetic loads expected during operations. The tiles in these regions are denoted as “targeted improvements.”

The requirements driving the design of these tiles are itself, an accomplishment of the project. The combined efforts of project management, the Plasma Facing Components Requirements Working Group, and the PFC Recovery Project team have co-developed the current system requirements document NSTX-U-RQMT-SRD-003-01. Together with other requirements documents for the NSTX-U Recovery Project, the PFC team has implemented a set of tiles that will meet physics requirements and not require extremes of manufacturing precision and cost. The systems requirement document (SRD) prescribes load conditions that must be met by the PFCs identified for modification. In addition, the PFC Diagnostics Requirements Document delineates the diagnostics that are integral to the PFCs themselves for operating the machine and conducting research. Both the PFC SRD and PFC Diagnostics RD were developed jointly by PPPL and ORNL with input from the wider NSTX-U team. This effort helped to ensure the requirements reflected an up-to-date physics basis and included a conservative means for PFC monitoring - embedded thermocouples - both of which were identified in the FY17 Extent of Condition report through CHITs at associated DVVRs.

Highlights for FY2018 from each work breakdown structure (WBS) area within the PFC Recovery Project are listed below. All areas of the PFC scope of work successfully completed PDRs as of November 15th, 2017, and an FDR on Friday, September 28<sup>th</sup>. Oak Ridge National Lab engineering support was crucial for achieving the FDR and, in general, for the PFCs program.

## **1.1 / PFC1 CSFW**

WBS item 1.1.1.1 refers to the Center Stack First-Wall (CSFW) set of tiles and is designated as the “PFC1” control account. Tiles in this region are designated as “targeted improvements.” Heat fluxes on these tiles are dominated by plasma radiation and experience at most 1 MW/m<sup>2</sup> of heating during full power operations. More challenging are the electro expected during disruptions of the plasmas. Induced eddy currents and absorbed halo currents both react with the magnetic field in the machine to generate loads on the PFCs. These must be resisted by the tile fixturing system.

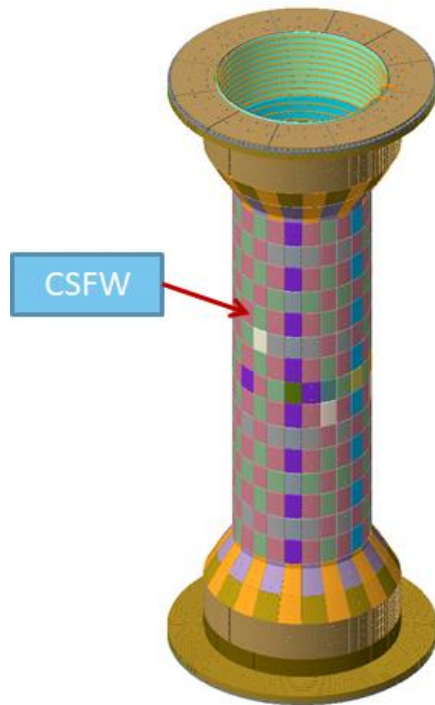


**Fig. 1.1.10:** Center Stack, First Wall tiles (CSFW).

The set of tiles associated with the CSFW are shown in Fig. 1.1.10 above. An assembly of the two primary tiles for the CSFW is shown in the Fig. 1.1.11. The CSFW tiles consist of a pair of tiles: one bolted and one “floating”. In fact, the floating tile is held in place by a set of pins that are held in place by an inconel rail or backing plate. The backing plate is fixed directly to the casing by a pair of nut-caps that attach to welded studs.

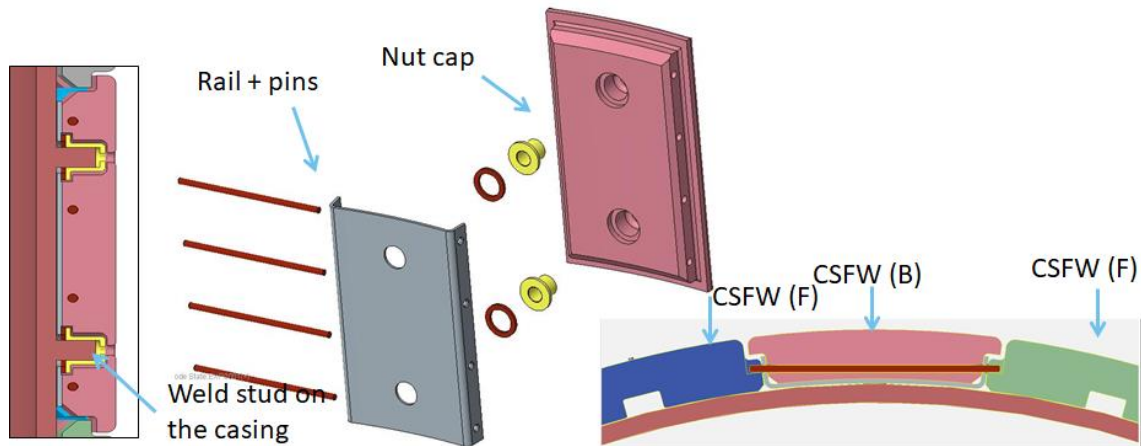


**Fig 1.1.11:** CSFW primary tile pair assembly, one pair bolted and the other “floating.” The floating tile is held in place with pins that are held in place with an inconel rail or backing plate.

At the time of the PDR, the contact between pins and the graphite PFC material was a known problem for analysis. The round contact between components produces a local stress concentration that is difficult to analyze with FEA software. Instead, the decision was made to

qualify these tile designs by testing the pin-tile contact limits. These tests are described in detail elsewhere in this report in the section on the facility milestone F18-1.

Additional testing was carried out on prototype casing studs to verify their performance. A replica center-stack sector was created with a set of studs welded on with the same procedure and equipment as the current weld-studs on the casing. These were then subjected to torque and shear tests according to ASTM standards. In the event that some studs have to be removed and re-welded, a similar procedure was carried out on the replica sector. Studs were ground off and then re-welded on the same metal as before and re-tested. All were found to be acceptable.

The scope of work in this area included two base tile types: one floating and one bolted. The bolted tiles include a single design variant to accommodate an embedded thermocouple. The floating tile includes seven variants to accommodate the following: thermocouples, shunt probes, Langmuir probes, Mirnov probes (both 1D and 2D), and gas injection tubes.

### 1.1 / PFC2 IBDH Tiles

WBS item 1.1.1.2 refers to the Inboard Divertor Horizontal (IBDH) set of tiles and is designated as the “PFC2” control account. Tiles in this region are designated as “full redesign.” Heat fluxes on these tiles are dominated by plasma impingement at low angles of incidence with nominal axisymmetric heat fluxes of about 6 MW/m<sup>2</sup> of heating during full power operations. Eddy and halo currents act on these tiles as well.

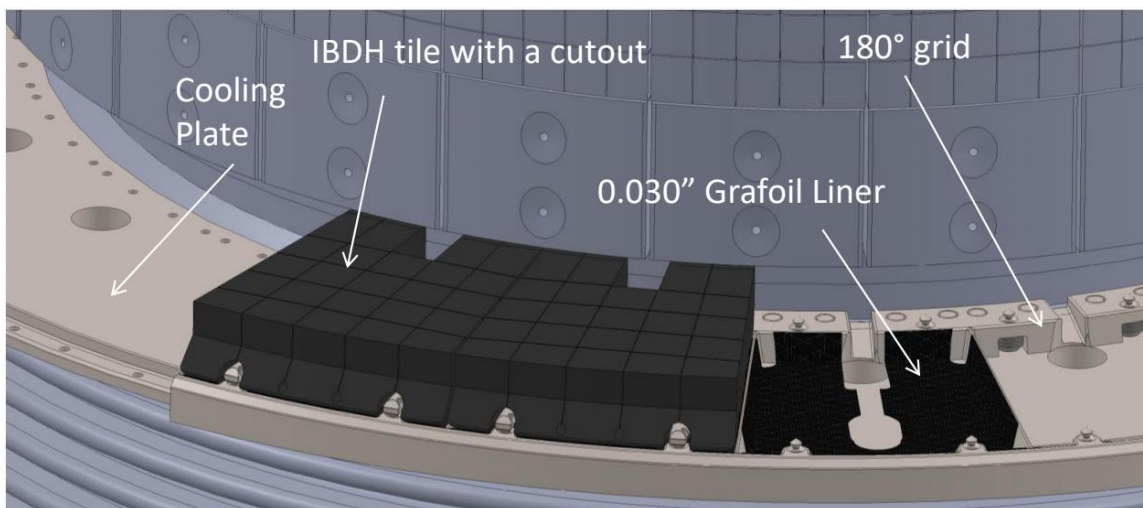


**Fig. 1.1.12:** Inboard Divertor Horizontal (IBDH) set of tiles with castellated surface features. Tile castellations relieve surface stresses during plasma bombardment periods of intense heat.

The tiles consist of segments with castellated surface features. This design was selected at the close of the 2017 fiscal year and developed to a PDR that was conducted in November 2018. The design consists of the graphite tile, a grafoil liner, a grid structure that provides lateral positioning of the tiles, and a mounting location for a set of pins that interface with the tiles via a

cam-action locking bar. The entire scheme was prototyped with a 3D plastic printer for the PDR, and a graphite prototype is under construction.

The castellations in the tile serve to relieve surface stresses that develop under the intense heat fluxes during plasma bombardment. This allows the tiles to achieve nearly ideal thermal performance that approximates a semi-infinite solid reaching sublimation temperatures prior to reaching stress limits. An end-of-pulse contour plot of the compressive and tensile stresses developed in these tiles is shown in Fig 1.1.13 below.

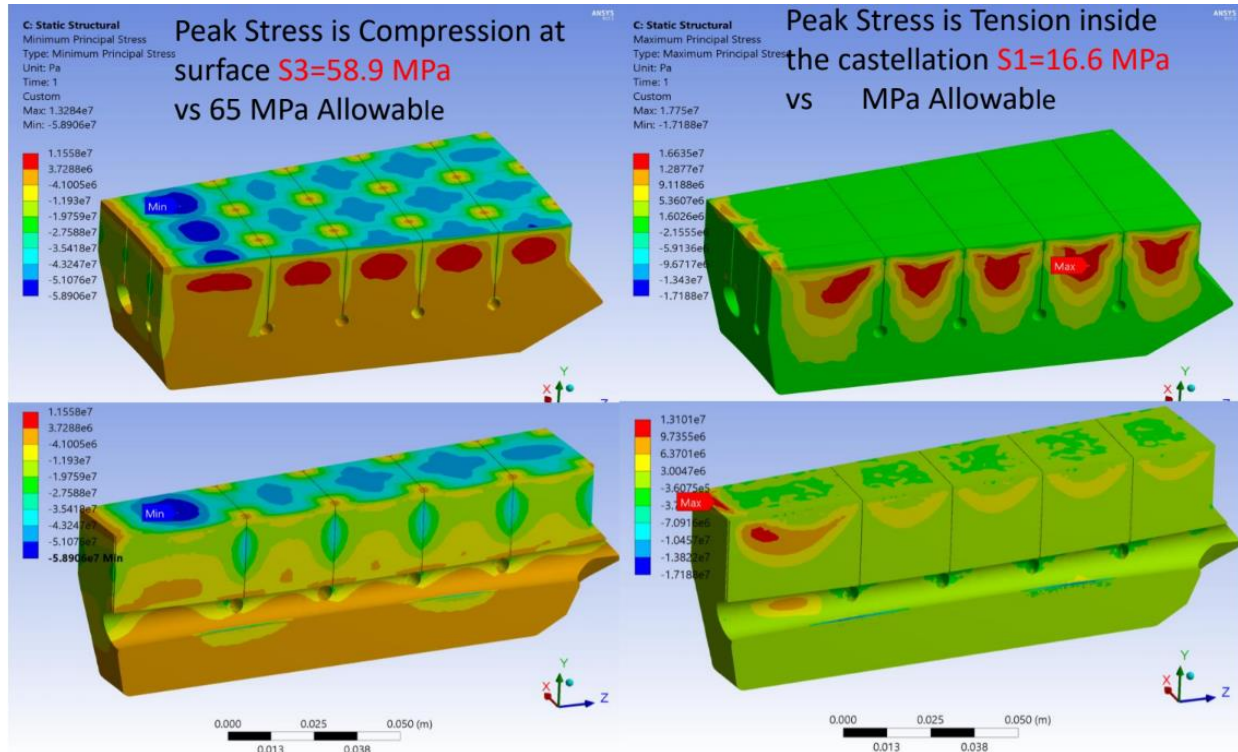


*Fig 1.1.13: An end-of-pulse contour plot of the compressive and tensile stresses on tiles.*

The scope of work in this area includes one base tile type and the mounting hardware. The diagnostic variants include the following: thermocouples, Langmuir probes, mirnov probes, and optical access through the organ pipes of the vessel.

## 1.1 / PFC3 IBDV Tiles

WBS item 1.1.1.3 refers to the Inboard Divertor Vertical (IBDV) set of tiles and is designated as the “PFC3” control account. Tiles in this region are designated as “full redesign.” Heat fluxes on these tiles are dominated by plasma impingement at low angles of incidence with nominal axisymmetric heat fluxes of about 6 MW/m<sup>2</sup> of heating during full power operations. Eddy and halo currents act on these tiles as well. The tiles in assembly are shown in Fig. 1.1.14 below.

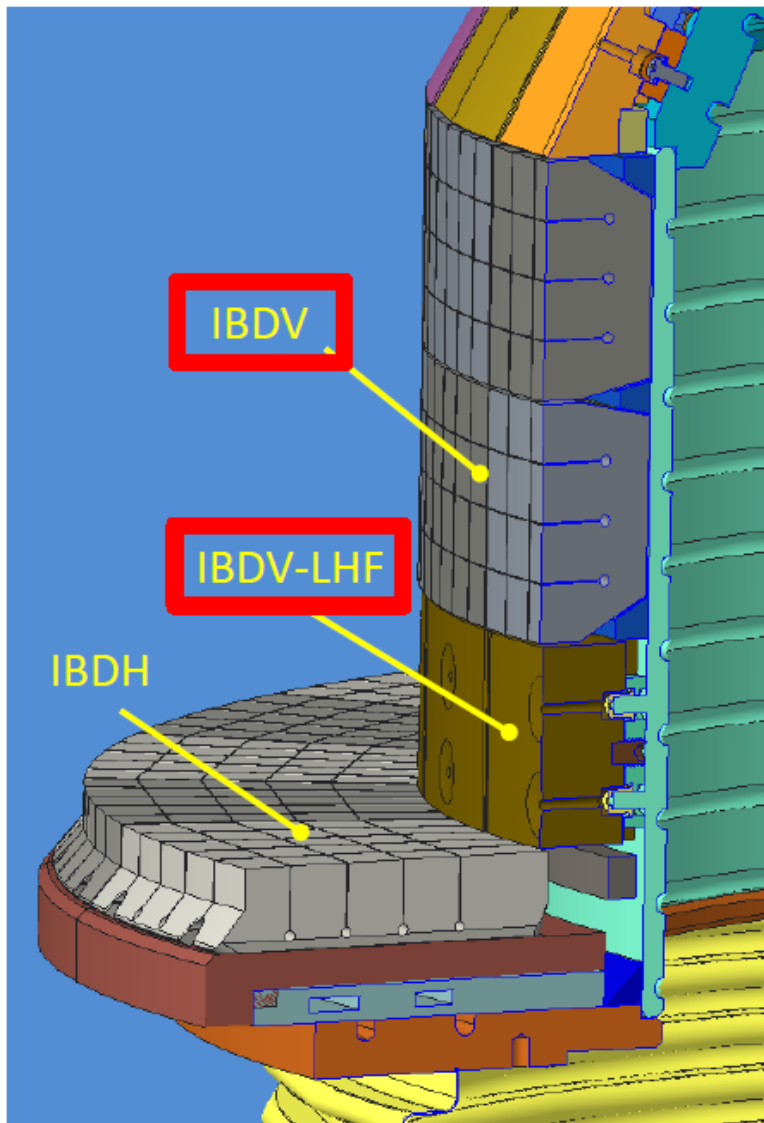


**Fig. 1.1.14:** Inboard Divertor Vertical (IBDV) tiles, in assembly. These tiles have been fully redesigned.

Noted in the figure are a row of tiles that include front-access holes and a T-bar system. These are denoted “IBDV-LHF” for Low Heat Flux. Due to the inner PF coil placements, it is not expected inner or outer strike points will be placed at the innermost corner of the NSTX-U Center Stack, and the revised SRD specifies lower heat fluxes in this region compared to the IBDH and the rest of the IBDV. As such, these tiles retain front-access and serve to shadow the mounting hardware of the castellated tiles on either side.

As with the IBDH tiles, these PFCs have a castellated front surface to relieve surface compressive stresses. They also have the same grid and cam-action lockbars to hold the tile onto the lower surface. The design was prototyped with a 3D printer for the PDR in November 2017 and this prototype is shown in Fig. 1.1.15 below.

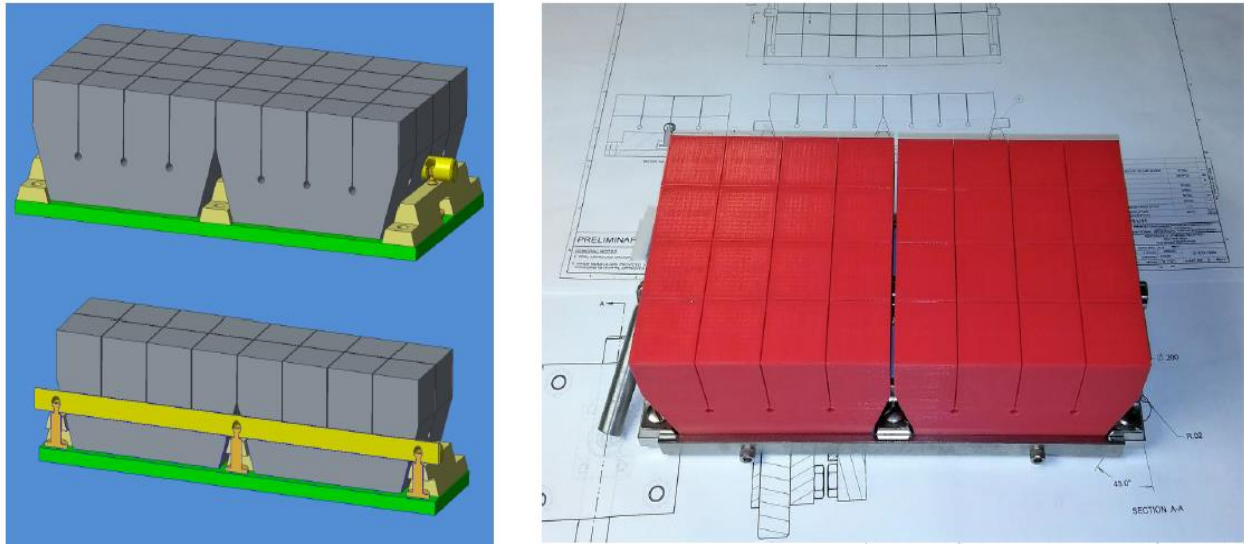


**Fig. 1.1.15:** Castletailed Inboard Divertor Vertical (IBDV) tiles (left), 3-D prototype (right). These PFCs have a castellated front surface to relieve surface compressive stresses.

There are two base tiles and the associated grid and mounting hardware as well as diagnostic variants for thermocouples and Langmuir probes.

### 1.1 / PFC4 OBD 1, 2 Tiles

WBS item 1.1.1.4 refers to Outboard Divertor rows 1&2 set of tiles and is designated as the “PFC4” control account. Tiles in this region are designated as “full redesign.” Heat fluxes on these tiles are dominated by plasma impingement at low angles of incidence with nominal axisymmetric heat fluxes of about 6 MW/m<sup>2</sup> of heating during full power operations. Eddy and halo currents act on these tiles as well. The tiles in assembly are shown in Fig. 1.1.16 below.

The high-heat flux region of the outboard divertor extends over the region that was previously occupied by rows 1 and 2 in NSTX and NSTX-U. Instead of two distinct tiles, it was decided to combine two tiles in poloidal extent and two tiles in toroidal extent to cover this same part of the machine. The result reduces the number of graphite components that need to be fabricated. The essential components of the design are shown in Fig. 1.1.16 below.

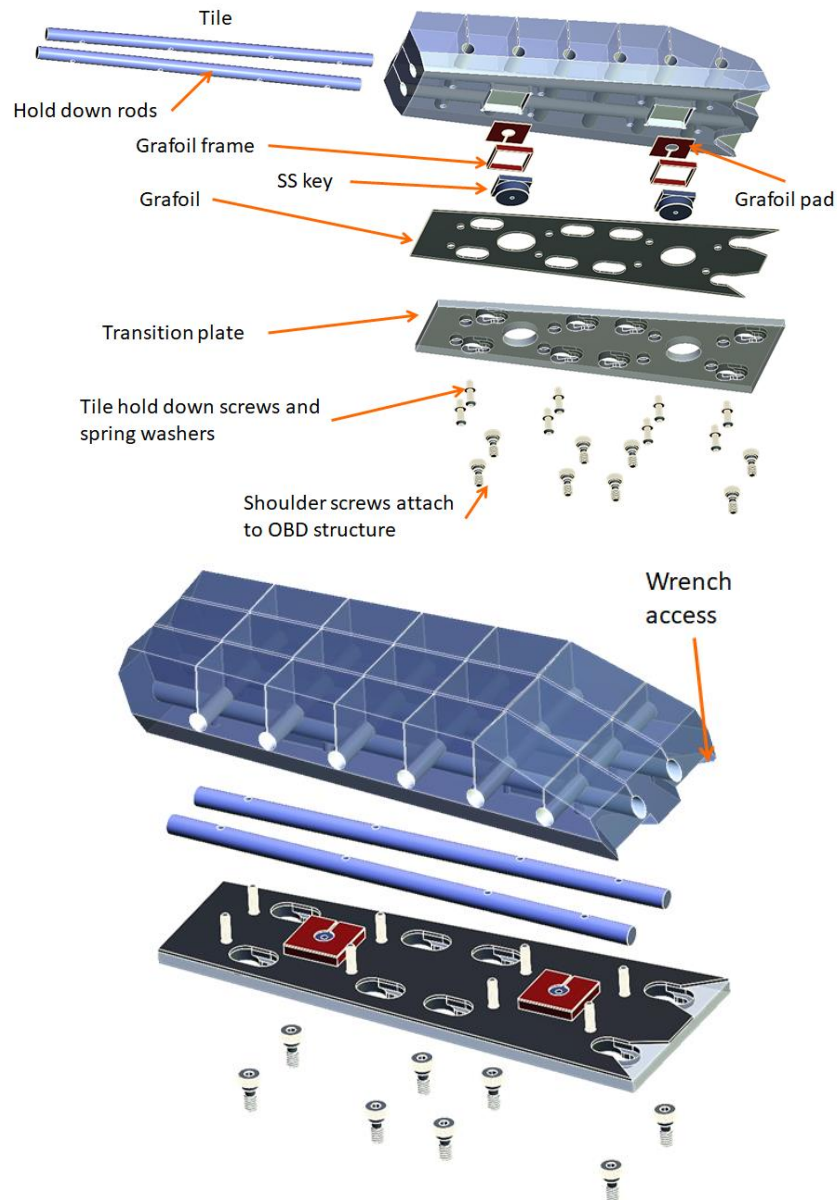


**Fig. 1.1.16:** Outboard Divertor rows 1&2 tiles have been redesigned with a tile that spans both rows and replaces two styles in each row.

One particular challenge for this region of the NSTX-U project is the as-built condition of the underlying divertor structures. The outboard divertor structures consist of a set of copper “slats” with embedded helium lines for bake-out. Each copper component has finite misalignments with respect to the vessel flanges. Due to the low angle of incidence, these misalignments would make meeting the heat flux requirements a challenge. As a result, the OBD 1, 2 designs include a “transition plate” component which is unique to each location in the vessel. This plate corrects out misalignments in the underlying copper structures and provides a means to create an axisymmetric surface without unique graphite parts. In order to accomplish this design, detailed in-vessel metrology of the copper plates was conducted to build the design table defining each transition plate, upper and lower.

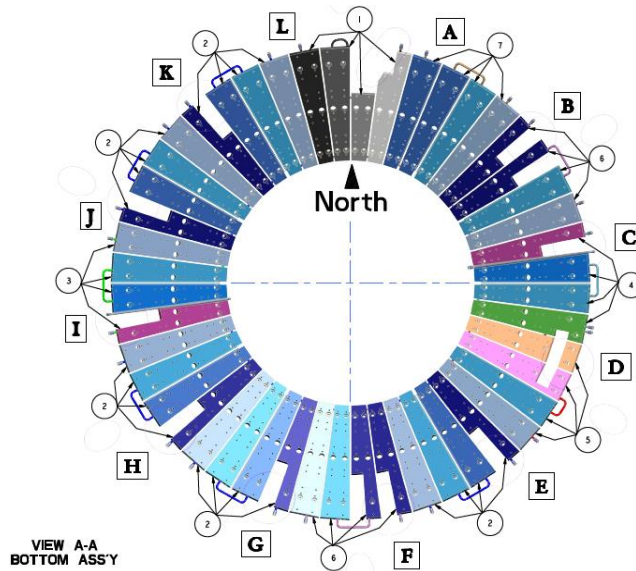


**Fig. 1.1.15:** Plan view of the lower outboard divertor plates which carry helium cooling lines and support PFCs.

Similar to the IBDH and IBDV designs, these tiles are castellated. At the time of the PDR, it was again found that the tile was achieving near-ideal performance of the material by reaching SRD-defined temperature limits before reaching stress allowables. A thermal simulation is shown in Fig. 1.1.16. In particular, this figure also indicates that at the lowest angles of incidence, surface shaping is expected to shadow parts of the surface as the design angle is the steepest required.

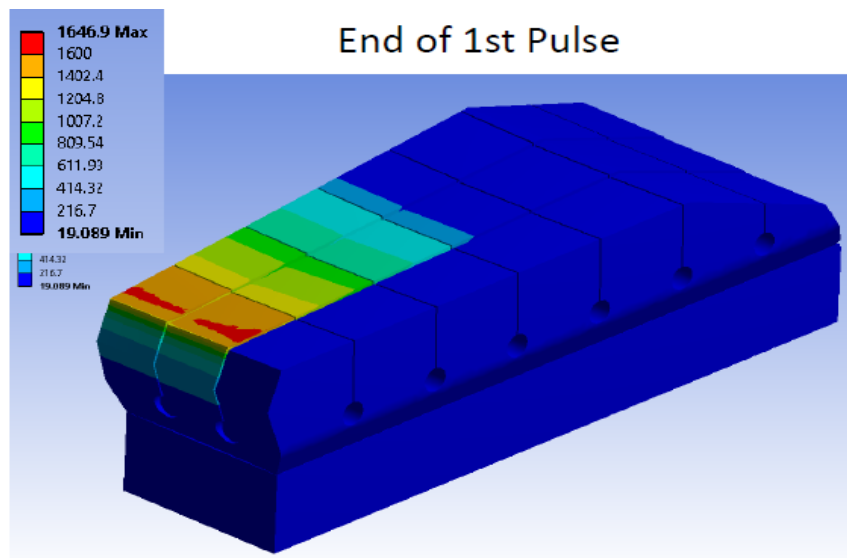


**Fig. 1.1.16:** Thermal simulation, Outboard Divertor tiles rows 1 & 2. At the lowest angles of incidence, surface shaping is expected to shadow parts of the surface as the design angle is the steepest required.

Like other areas of the machine, there are a number of modifications made to accommodate diagnostics. These include the following: thermocouples, Langmuir probes, and Mirnov sensors. The scope of work delivered a successful PDR in November 2017.

## 1.1 / PFC5 OBD 3, 4, 5 Tiles

WBS item 1.1.1.5 refers to the Outboard Divertor rows 3, 4, and 5 sets of tiles and is designated as the “PFC5” control account. Tiles in this region are designated “targeted improvements.” Heat fluxes on these tiles are dominated by plasma impingement at low angles of incidence with nominal axisymmetric heat fluxes of about 10 MW/m<sup>2</sup> of heating (for 1s) during full power operations. Eddy and halo currents act on these tiles as well. The tiles in assembly are shown in Fig. 1.1.17.

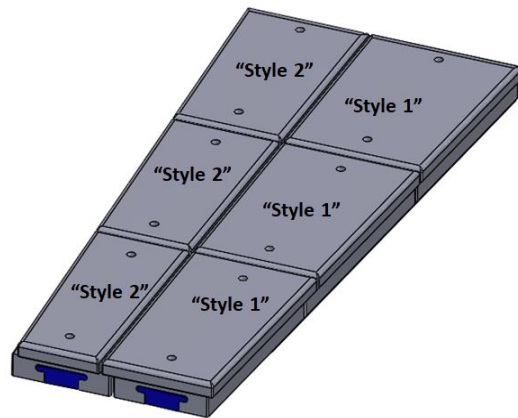


*Fig. 1.1.17: Outboard Divertor Rows 3,4 and 5, in assembly.*

Early in the project, it was decided to retain the previous design, including a T-bar feature and front-access fasteners. These features create leading edges that receive larger heat-fluxes than does the front surface. Two elements were modified to qualify these tiles for full-power operations: the T-bar was modified to be more compliant and thereby reduce thermomechanical stresses during heating, and locating pin in the center of the tile was modified to a full-size shear pin that will resist poloidal motion induced by eddy and halo currents. The redesigned locating pin is shown in Fig. 1.1.18 below.

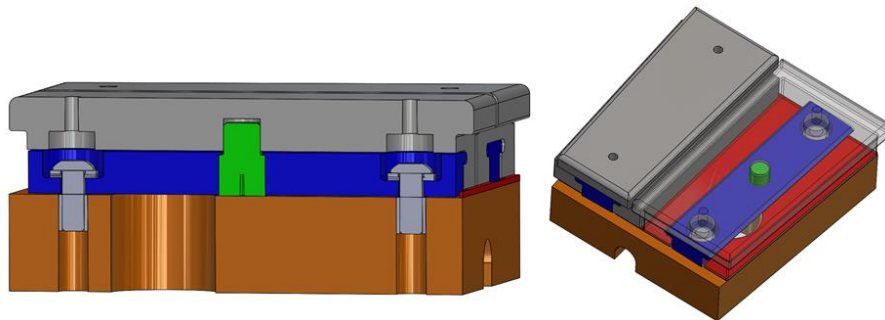


*Fig. 1.1.18: T-Bar modification with modified, full-sized shear pin.*

Each row of tiles features two “base” tile designs. Style 1 and style 2 tiles feature an overlapping interface to eliminate direct line of sight to the underlying copper structure. In addition, this region of tiles features the largest number of variant tiles due to the embedded diagnostics (thermocouples, Langmuir probes, mirnov 1D and 2D, and shunt probes), but also

the need for optical access in the outer-most rows of the machine. In all, there are 36 variants in this region.

Significant effort was spent ensuring optical access to the vessel for diagnostics. This included in-vessel metrology and efforts by the diagnostics involved. Revision of the divertor structural drawings was undertaken to provide a comprehensive survey of the as-built condition as well.

To manage the heavy design and analysis load in this region, analysis templates were developed. These analysis templates were critical in the ability to coordinate analysis tasks with ORNL and contractor analysts.

A successful PDR for OBD 3, 4, 5 was held in late September 2017.

### 1.1 / PFC6 PFC Integration/Support

Team organization for the PFC scope of work is handled within WBS 1.1.1.6, which is referred to as the “PFC6” control account. Mike Jaworski and Jonathan Klabacha interface with external resources such as procurement division, the project management office, and other work breakdown structure (WBS) areas of the project. An organizational diagram of the PFC scope of work is shown in Fig. 1.1.19 below.

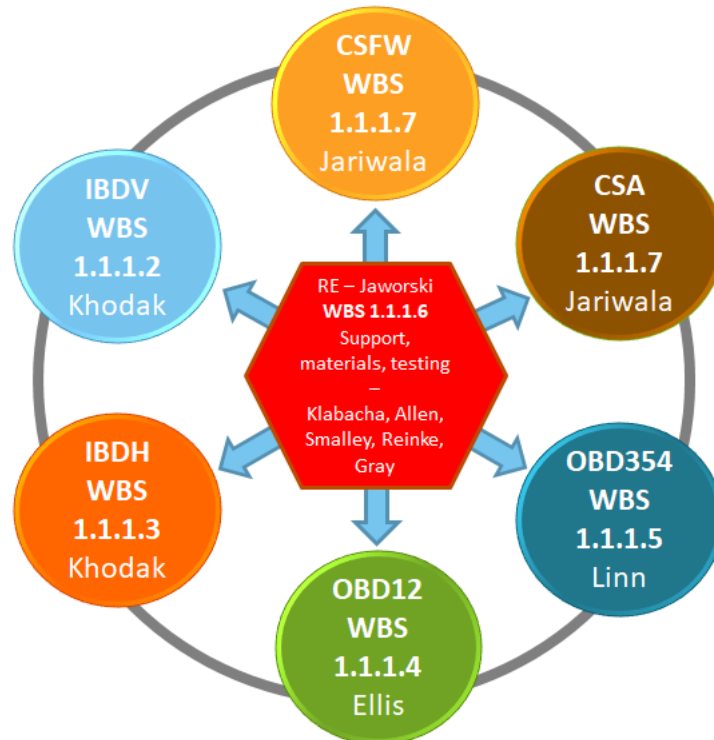


**Fig. 1.1.19:** PFC scope of organization diagram and work breakdown structure elements (WBS).

The WBS areas are indicated alongside their control account designations for each of the 7 control accounts in the PFC Recovery Project. Project management and support occurs in the central section and helps coordinate activities in the other control accounts.

A major activity was revision of the work authorization forms (WAFs) associated with the PFC Recovery project. An updated WAF was reviewed in April 2018 to refine the scope definitions and move the project to a 50/50 reporting model. While overall cost estimates increased, they were still within the expected range as reported in August 2017 at the Cost and Schedule Review. The new, combined WAF includes some 800 activities in the 7 control accounts in order to manage this scope of work.

WAF cost comparison		Uncertainty			Cost \$M					
		C&SR \$M	Min	Max	Min	Max	Today's Cost \$M	Variance \$M	% variance	Justification
PFC Overall		10.284			8.227	14.398	12.084	1.800	17.5	
PFC1	CSFW	1.498	0.8	1.4	1.198	2.097	1.975	0.477	31.9	Quantity of components, fabrication cost
PFC2	IBDV	1.861	0.8	1.4	1.489	2.605	1.538	-0.323	-17.3	Updated tile costs
PFC3	IBDH	1.817	0.8	1.4	1.454	2.544	2.028	0.211	11.6	Updated tile costs, variant designs
PFC4	OBD12	1.738	0.8	1.4	1.390	2.433	1.514	-0.224	-12.9	Updated tile costs
PFC5	OBD345	1.352	0.8	1.4	1.082	1.893	2.755	1.403	103.7	Expanded design, tile costs, installation
PFC6	Integration	2.018	0.8	1.4	1.614	2.825	1.215	-0.803	-39.8	Converted to 100% LOE
PFC7	CSA	0					1.059	1.059	***	Split from CSFW

**Fig. 1.1.20:** Overall cost changes to the PFC Control Accounts as of the April WAF review.

Material selection and testing has been coordinated within the PFC6 control account. In November, difficulties in procuring graphite were identified and a plan of action was developed. Graphite is a specialty material without any single specification as one may expect when procuring common alloys. Instead, each grade of graphite is formulated by the manufacturer and methods and results are trade secrets. It was decided to undertake material certification testing within the PFC project to indicate the properties of the graphites that were available to the project. PPPL procured a subcontract to test three candidate graphites in order to verify the datasheet values for these materials. A Material Peer Review meeting was held in June 2018 and authorization to purchase materials was obtained (MEMO PFC-180628-MAJ-03).

Prototype activities were coordinated within PFC6 that yielded both technical information for the project and improvements to the basis of estimate. Prototype HHF tiles were procured to determine if the originally budgeted cost for tiles and hardware required revision. Minor revisions to the M&S estimates for the PFC scope of work were included in the April WAF review. The current estimates cover the range of bids received for the prototype tiles.

Technical scope for prototypes has been formalized into a procedure for Cognizant Individual (COGs) and PFC personnel to follow. A PPPL engineer is charged with coordinating prototype tests on-site after COGs issue technical requirements that establish the need and desired outcomes of the tests. High heat flux testing was identified as part of the prototype testing scope, which required improvements to an off-site electron beam facility located at Penn State University's Applied Research Laboratory. Following a joint PPPL/ORNL activity to use the ARL e-beam to inform material selection in early FY18, Oak Ridge National Laboratory researchers led work to enhance the facility and demonstrate methods for quantitative testing of castellated graphite tiles in February 2018. A more detailed discussion on this work is included in the F(18-1) milestone. The end report of each prototype test will be filed according to the NSTX-U

Planning documents and PPPL policies and procedures. After the WAF revision, all prototype activities were moved out from PFC6 and into the relevant control accounts associated with the tests. Coordination is still maintained within PFC6.

In mid-FY-18, there was a shortfall of thermomechanical engineering analysis support within PPPL to meet design verification requirements in time for the PFC final design review in late FY-18. The PFC Responsible Engineer (RE) worked with the Project Manager and ORNL staff on- and off-site to identify and organize spare capacity at ORNL that could support Recovery in a timely manner. COGs in WBS 1.1.1.2-1.1.1.5 streamlined analysis tasks using templates that could be easily transferred to off-site ORNL collaborators. A team of six ORNL staff (working part-time) coordinated activities directly with COGs and attended weekly PFC engineering and design meetings via teleconference.

### 1.1 / PFC7 CSA IBA

WBS item 1.1.1.7 refers to the Center Stack Angle (CSA) sets of tiles and is designated as the “PFC7” control account. Tiles in this region are designated as “targeted improvements.” Heat fluxes on these tiles are dominated by plasma impingement at low angles of incidence with nominal axisymmetric heat fluxes of about  $5 \text{ MW/m}^2$  of heating (for 2s) during full power operations. Eddy and halo currents act on these tiles as well. The tiles in assembly are shown in Figure 1.1.21. As targeted improvements, these tiles retain the T-bar mounting feature and front-access holes. A rendering of one of the tiles fastener hardware is shown in the figure below. As in the OBD 3, 4, 5 designs, the locating pin feature has been redesigned into a full shear pin to resist eddy and halo current-driven loads.

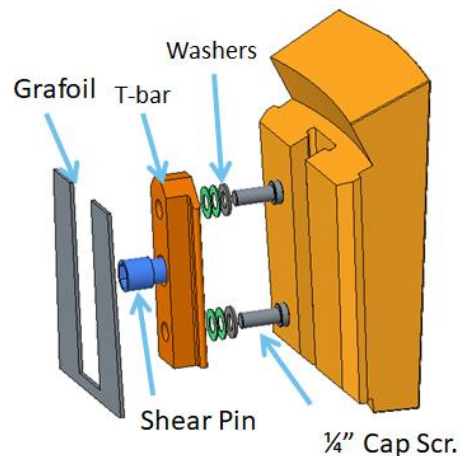


**Fig. 1.1.21:** Center Stack Angle (CSA) tile featuring tile fastener hardware with full shear pin.

A cross section of the two-tile assembly for the CSA is shown in Fig. 1.1.22. Redesign work has been minimized by retaining the NSTX-U interface between CSA and CSFW. The full redesign of the IBDV tiles has required significant modification to the CSA tile 5 interface. An added benefit of the new transition piece is the accommodation of the Rogowski current sensor at the transition between CSA and IBDV.

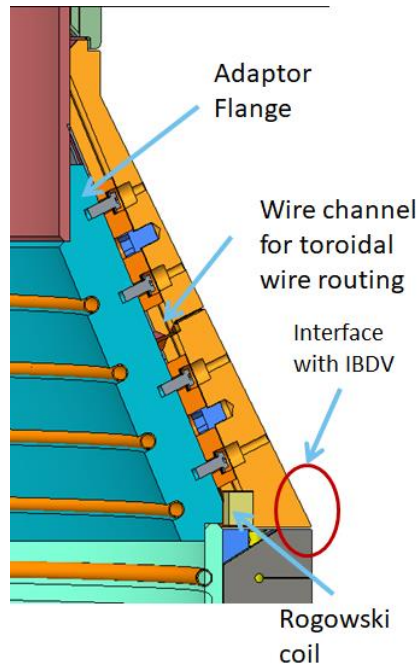


**Fig. 1.1.22:** Cross section of the two-tile assembly for the CSA tile.

While lower than the requirements in IBDH, IBDV, and OBD1-2, the heat fluxes on the CSA tiles are still significant. At the time of the PDR, however, both tiles were found to meet requirements, though also with added surface ramps to mitigate leading edges. A thermal simulation is shown in Fig. 1.1.23 below.

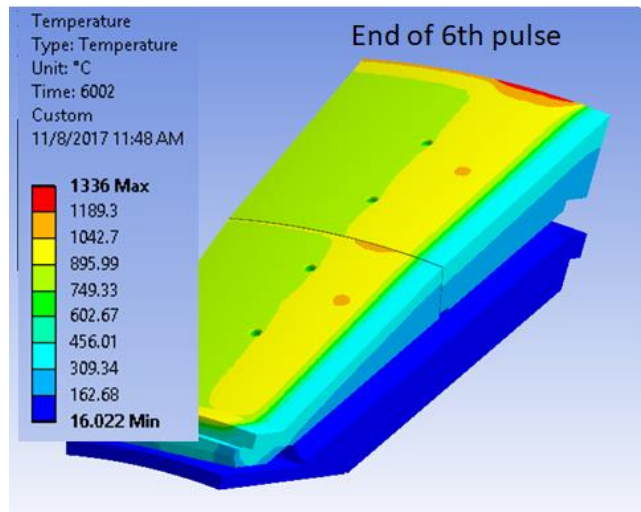


**Fig. 1.1.23:** Thermal simulation of heat fluxes on Center Stack Angle (CSA) tiles.

A successful PDR of these designs was held in November 2017. Progress has continued to refine the design and accommodate diagnostic access and wire ways. These tiles include only thermocouple variants, but all diagnostics through the center section and center-stack gas injection lines pass through this region of the casing and require smooth transitions.

# Vacuum Vessel and In-Vacuum Hardware (VV+IH)

## 1.1 / 6010 Polar Region

During FY 2018, the Polar Region's systems, structures, and components (SSCs) underwent significant redesign and analysis. The Polar Region is a combination of three WBS elements that support the Recovery Project and consists of regions within the upper and lower core section of the NSTX-U device. The Polar Region (Fig. 1.1.24) encompasses SSCs between the vacuum vessel's upper and lower dome main flanges and the center stack case divertor flange.

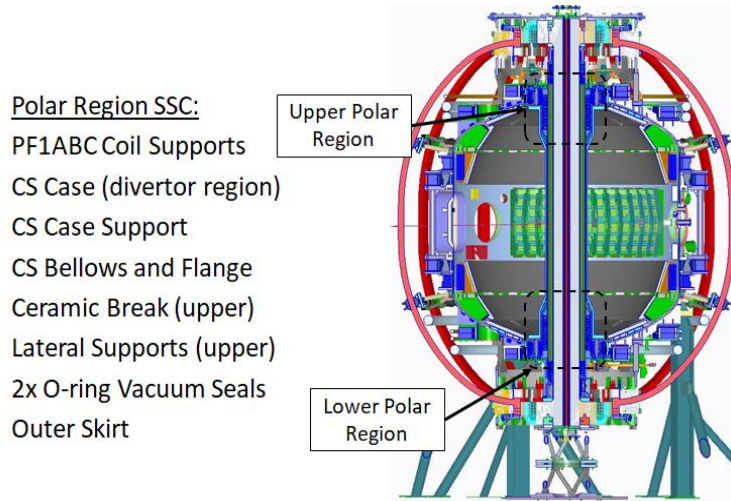


**Fig. 1.1.24:** Upper and Lower Polar Region, NSTX-U.

Cross-sectional images of the upper/lower polar region components are depicted in Fig. 1.1.25. The PF1A coil support and the PF1B coil support are depicted in Fig. 1.1.26. The upper PF1C coil support is integrated in the Ceramic Break and is depicted in Fig. 1.1.27, along with the lower PF1C coil support.

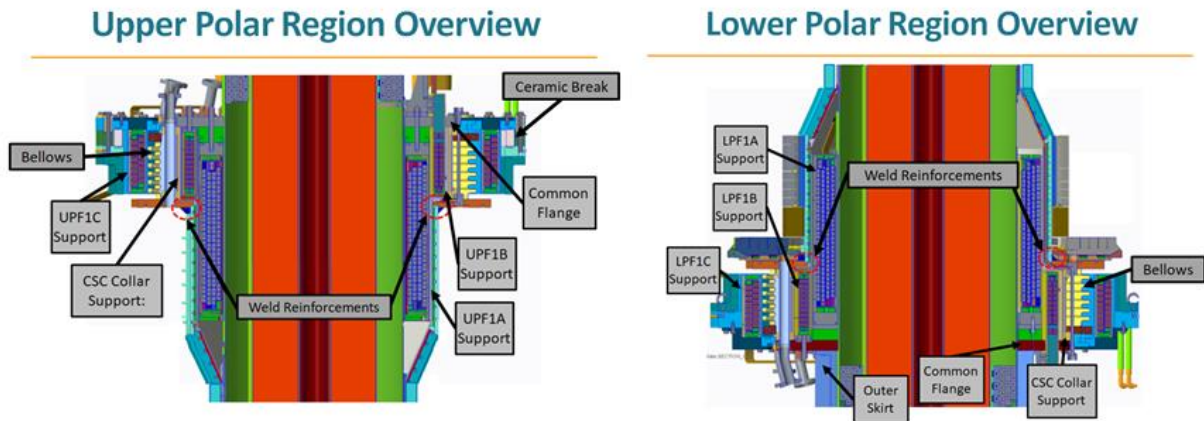


**Fig. 1.1.25:** Cross-section views of the Upper and Lower Polar Regions.

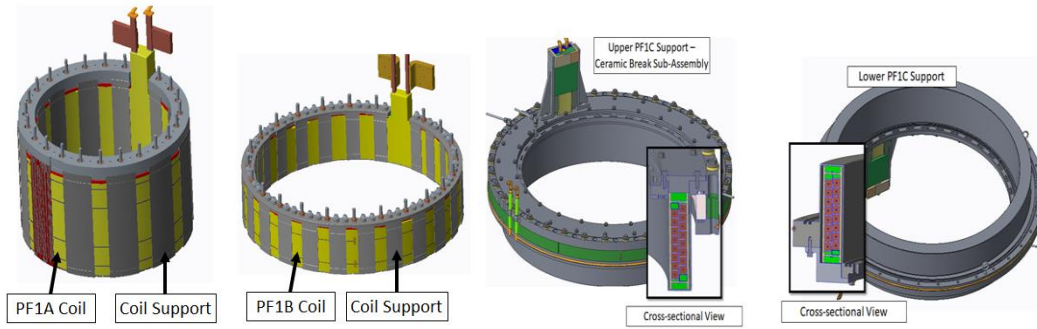


**Fig. 1.1.26:** left to right: PF1A and PF1B coil support assembly; Upper PF1C coil support and ceramic break, Lower PF1C coil support.

The ceramic break integrated into the upper PF1C support was redesigned to allow for the new Recovery requirements. In the event of a water leak, the new requirements specify water egress into the ceramic break must be prevented. The ceramic break design details can be seen in Fig. 1.1.27.

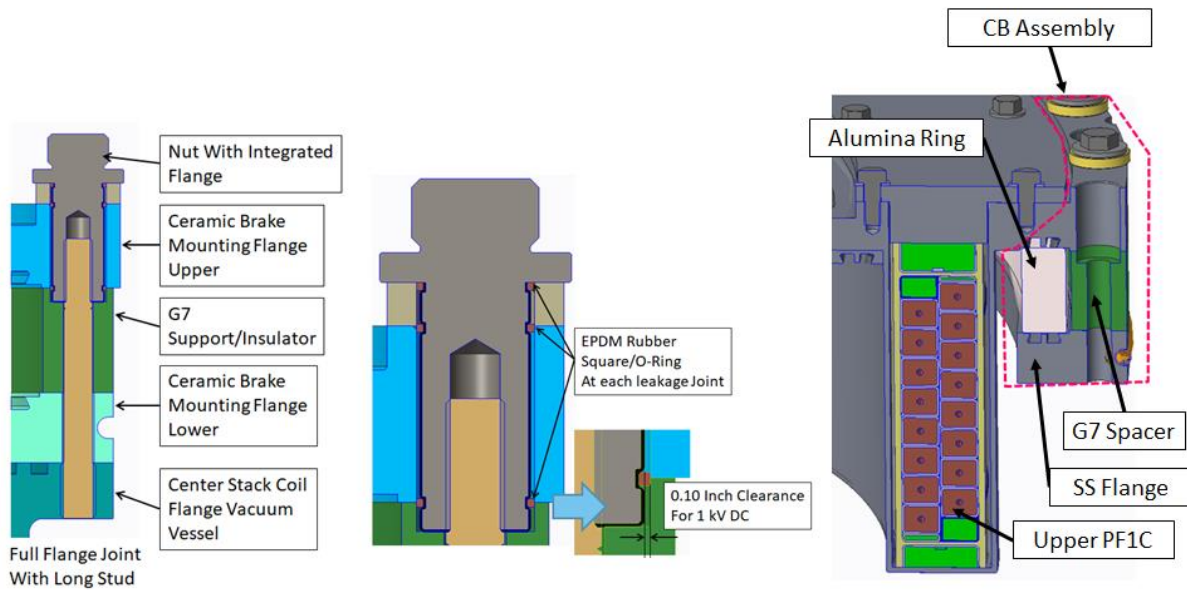


**Fig. 1.1.27:** Ceramic break design details. In the event of a water leak, new requirements specify water egress into the ceramic break must be prevented.

The vacuum sealing interfaces within the Polar region were redesigned to address new recovery requirements and various chits from prior DVVR and extent of condition (EOC) reviews. The new seal design uses double Viton O-rings with a vacuum pumped guard vac interspaced between them. There are six locations (Fig. 1.1.28) within the polar region that required this new seal design.

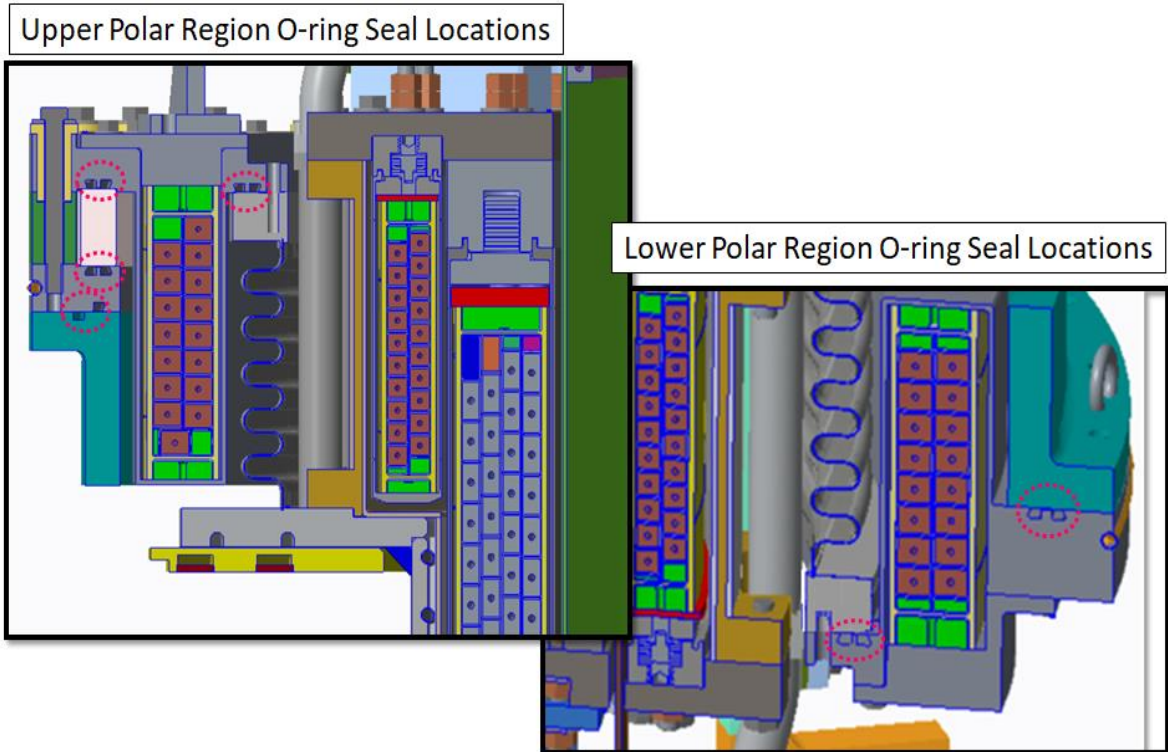


*Fig. 1.1.28: New Polar Region O-ring seal designs.*

A number of PDRs were held during FY 2018. An Inner PF Coil Supports PDR was held on March 27, 2018, and the Polar Region team PDR was held on August 2, 2018. The Polar Region team was also involved in several peer and design reviews during FY 2018, including the Inner PF Coil final design review (FDR) on March 30, 2018 and the NSTX-U Alignment peer review in February of 2018.

### **1.1 / 6000 Passive Plates**

The Recovery Project scope for the Passive Plates includes a review of the as-built condition of the passive plates, passive plate support structures, the hot helium bake piping, and upgrades to the structures as necessary to meet the project requirements. A successful conceptual design review (CDR) was held on June 8, 2018, and a successful PDR was held on July 26, 2018. Prior to the PDR an effort was made to analyze the maximum displacement that could be observed in the passive plates. Results uncovered the displacement was caused by field fit modification made to thermal expansion joints, resulting in too much additional clearance. Displacement in the plates was seen as a potential issue, and the Recovery Project presented the opportunity to address this concern. The total measured motion of the passive plates is shown below in Fig. 1.1.29.

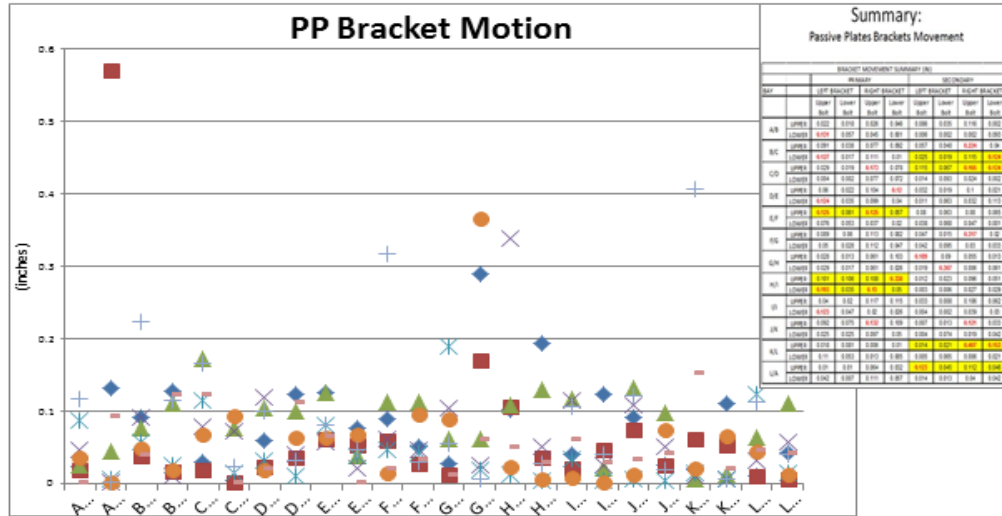


Fig.1.1.29: Measured motion in Passive Plates.

Because of this motion, a design was proposed at the PDR that would limit it. The proposed design does not modify the current expansion joints due to time constraints and limited access to the area, but it does add additional brackets to the primary passive plates (PPP) and secondary passive plates (SPP). These brackets have an expansion joint with less clearance so that the plates can still expand without the unnecessary motion. The proposed brackets were prototyped using a 3D printer, and a trial fit was conducted to check the feasibility of the design. The trial fit showed that the design is feasible and requires a few small modifications to accommodate it for as-built conditions. The proposed brackets are shown below in blue in Fig. 1.1.30.

Analysis done on the passive plate assembly determined that both the PPP and the SPP were experiencing bending loads during operation, and high stresses were found on the passive plate bracket welds. Additional stiffeners were proposed at the PDR that would mitigate these stresses and redistribute the loads. The proposed stiffeners are shown in green in Fig. 1.1.31.

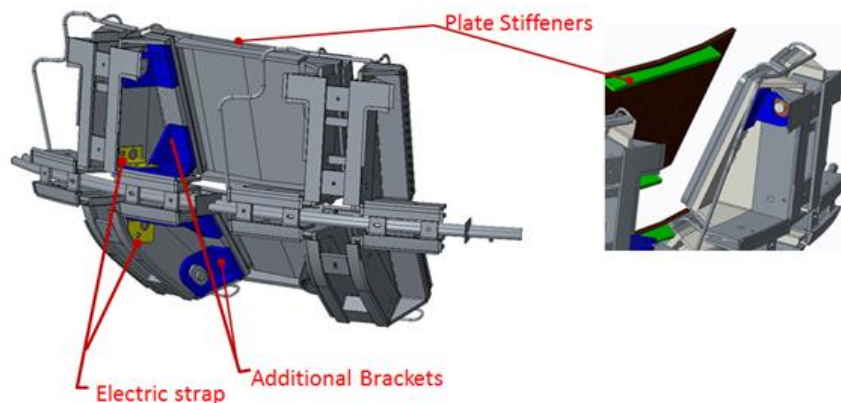
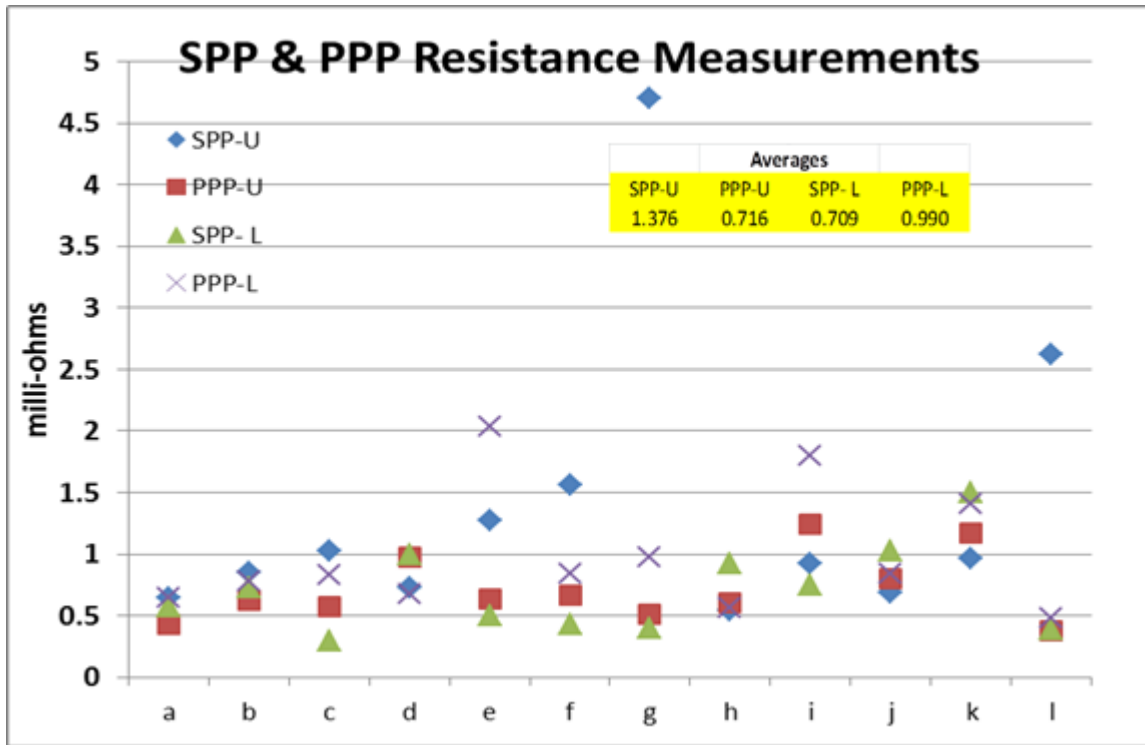


Fig.1.1.31: Proposed Passive Plate upgrades.

The passive plate scope also included reducing the variation in resistances across the passive plate supports. Fig. 1.1.32 shows the measured variation in the resistance. To minimize the difference between the actual and desired resistance, an electrical strap was designed to provide a reliable electrical connection across the passive plate supports. This electrical strap is shown in yellow in Fig 1.1.31.



**Fig.1.1.32:** Passive Plate resistance measurements.

Another concern addressed under the passive plate scope is support for the helium bakeout lines. Currently, the helium tubes used to bakeout the passive plates provide a parallel path for induced toroidal currents. These IXB forces combine with forces from the motion of the passive plates and produce high stresses on the helium bakeout lines. For these reasons, a cooling helium tube support was designed to both alleviate the high stresses and increase the connection's electrical resistance. The design is shown in Fig. 1.1.33.

This design activity continues into the final design stage with a scheduled review before the end of the calendar year.

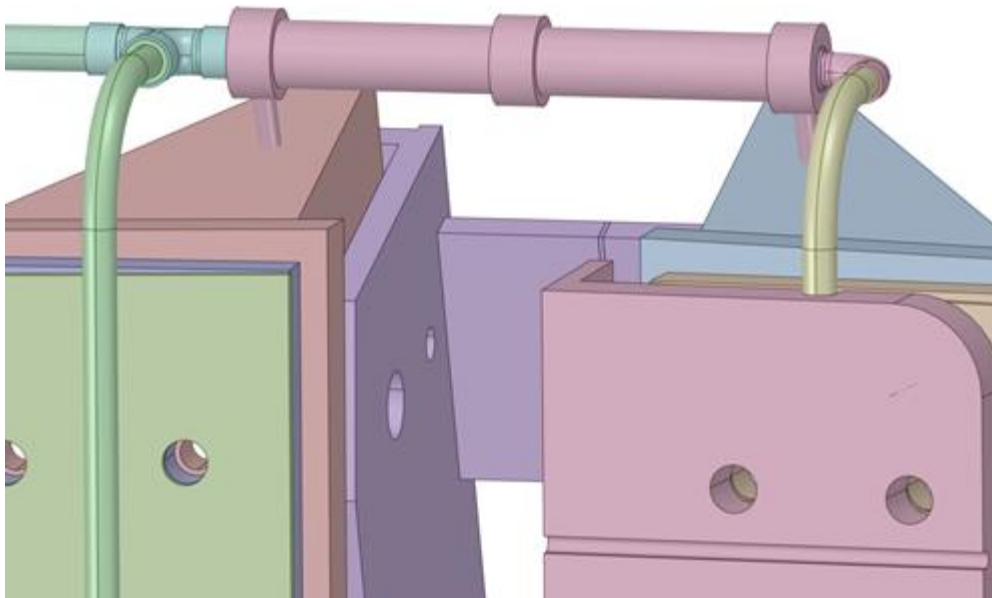


*Fig. 1.1.33: Helium Tube Support design.*

## **1.1 / 6015 VV+IH Field Scope**

Vacuum Vessel and In-Vacuum Hardware Field Scope Recovery (FSR) is a selection of specific assessments, field modifications, and document checks gathered from DVVR chits, that apply to current as-built NSTX-U conditions in the field.

FSR and its eleven tasks were defined in FY-17 following a DVVR assessment. Work activity for carrying out the tasks was undertaken over FY-18. The activity can be broadly summarized as assessments of mechanical and electrical machine conditions, including possible interference between structural pieces during thermal movement or adequacy of electrical grounding and arcing potential.

Re-assessment of the friction performance of mechanical joints, specifically the friction performance repeatability of those clamped structural joint assemblies that utilize Carbinite surface treatment, must be better characterized for the Recovery phase. In light of this, future analysis is planned.

- Re-design of threaded components to improve adjustability/positioning and to prevent mechanical loosening.
- Additional hardware design is an outcome.
- Documentation verification and improvement of prior mechanical and thermal analysis is also planned.

A CDR for VV+IH FSR was deemed unnecessary after considering that tasks were relatively small in scope and, with one or two exceptions, did not involve a complete design cycle or fabrication.

A successful PDR was held in February 2018 summarizing VV+IH FSR with progress details on each of the eleven tasks. The PDR conclusions arranged the tasks into four groups:

- 1) Tasks completed (assessments) with no future work required.
- 2) Tasks completed (assessments) with future work recommended.
- 3) Tasks remaining in work - testing and design.
- 4) Tasks not yet started - assessments and documentation.

### **1.1 / 6005 Cooling Tubes**

The cooling tube scope for the Recovery Project covers the replacement of the heating/cooling tube located on both the air side and the vacuum vessel side of the center stack casing that provides the heating and cooling to the casing and the PFC tiles on the Inboard divertor section during bakeout and operations. The conclusion gathered during the conceptual design review (CDR) was that the current design for IBD cooling during operation is not sufficient in removing heat due to the damage in the tubes.

A successful PDR was held on November 30, 2017. The PDR proposed a new design based on the updated PFC heat flux requirements and a requirement that there will be no water cooling in the vacuum vessel during operations with lithium wall conditioning. The new design also proposed that the material to be used for the cooling tubes located in the Center Stack casing (air side) would be Inconel 625 to match the Center Stack casing material and to minimize thermal stresses. Fig. 1.1.34 shows the air side cooling tubes that are being replaced.

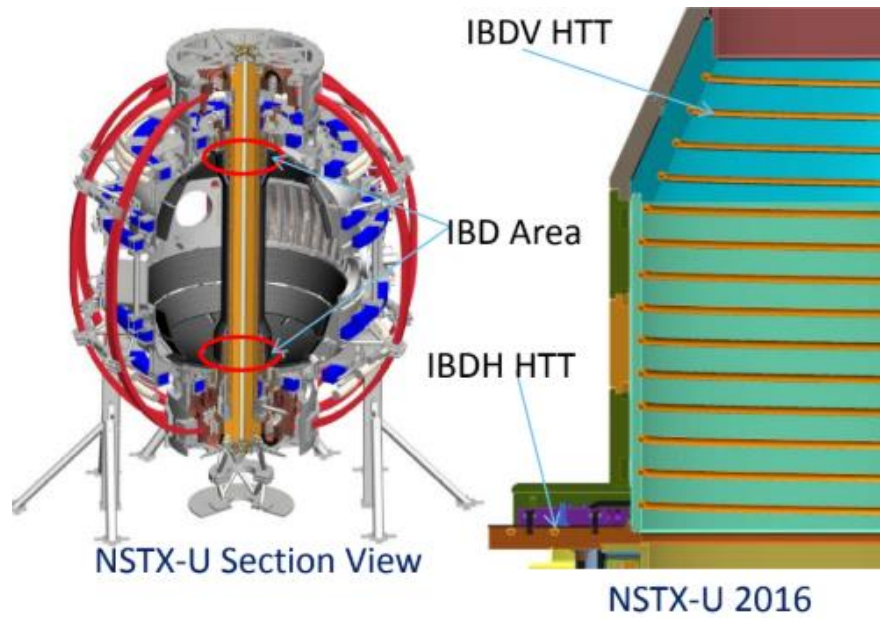


**Fig. 1.1.34:** Center Stack cooling tubes.

A heat transfer plate is being designed to supplement the heating and cooling of the inboard divertor horizontal area. The plate will be made of Inconel and will use helium as a heat transfer medium. Fig. 1.1.35 shows the heat transfer plate incorporated onto the inboard divertor.

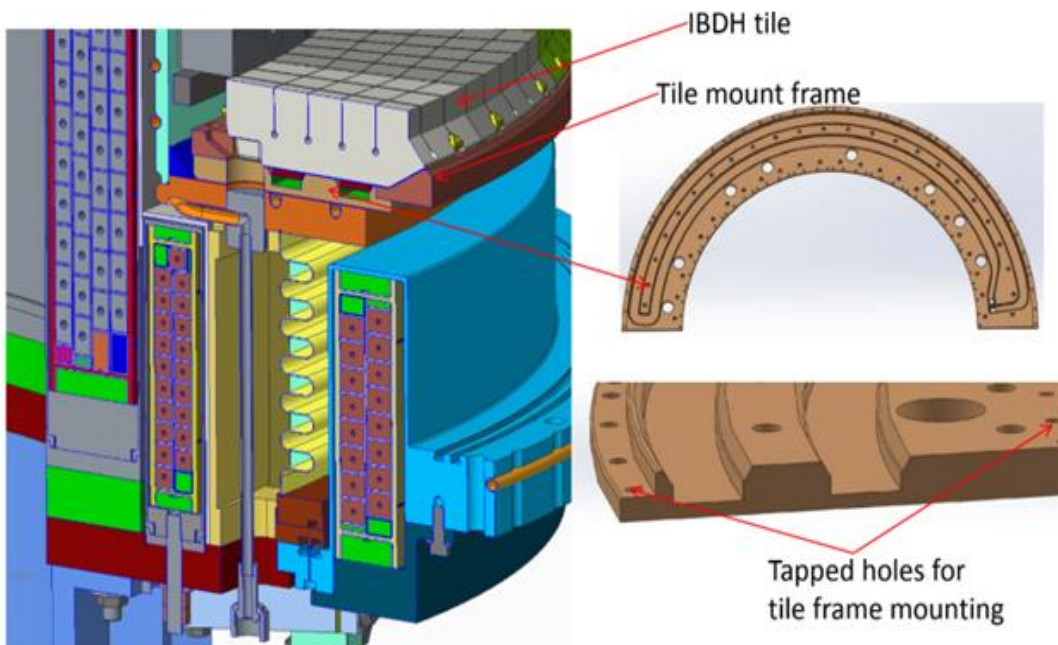


**Fig. 1.1.35:** Heat Transfer plate.

An FDR will be held later this year. Procurement and manufacturing will start once the FDR is successfully completed.

## 1.1 / 6025 VV+IH Integration

All the various components that comprise the vacuum vessel will be integrated as components are fabricated. Based on assembly procedures, there is a specific order of component parts. After this integration takes place, other components will be integrated. For example, magnet integration will be included as part of the Polar Region sub-assembly, and PFCs on the OBD assembly. This will happen during FY-19 or FY-20.

## Cooling and Bakeout

### 1.3 / B100 Helium Bake System

The Recovery scope for the High Temperature Helium System (HTHS) included analysis and redesign of the feed-through ports and improvements to the gas circulation piping. This scope was divided into two separate PDRs after completion of the recovery scope conceptual design review held the previous fiscal year. A PDR was held December 1, 2017 for the feed-through port redesign and reviewed calculations were presented of the existing design and a new, improved design (Fig. 1.3.1). The existing feed-through design was found through analysis to not meet the NSTX-U structural design criteria. The new design meets NSTX-U structural design criteria and features double re-entrant ports to segregate the high temperatures of the helium gas supply/return piping from the comparatively low temperature of the vacuum vessel wall. The addition of two electrical feedthroughs to the port takes advantage of the redesign to add a value engineered feature.

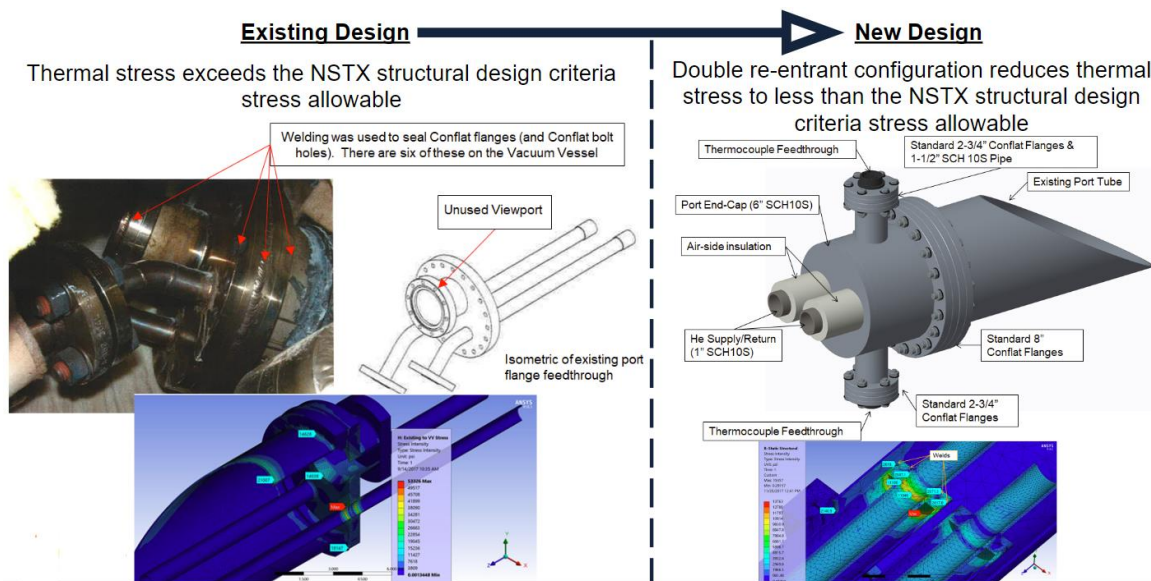


Fig. 1.3.1: Helium feed-through redesign.

A second HTHS PDR was held on January 11, 2018 to review proposed designs for mitigating excessive HTHS piping insulation jacket temperatures and helium flow control. Analysis indicated that the existing insulation system exceeded the rated jacket temperature during operation. This analysis was verified through observing charred insulation surfaces on the in-

situ insulation system. A new design was proposed that added insulation depth to the existing insulation system whereby the outer jacket temperature was reduced below the rated jacket temperature (Fig. 1.3.2).

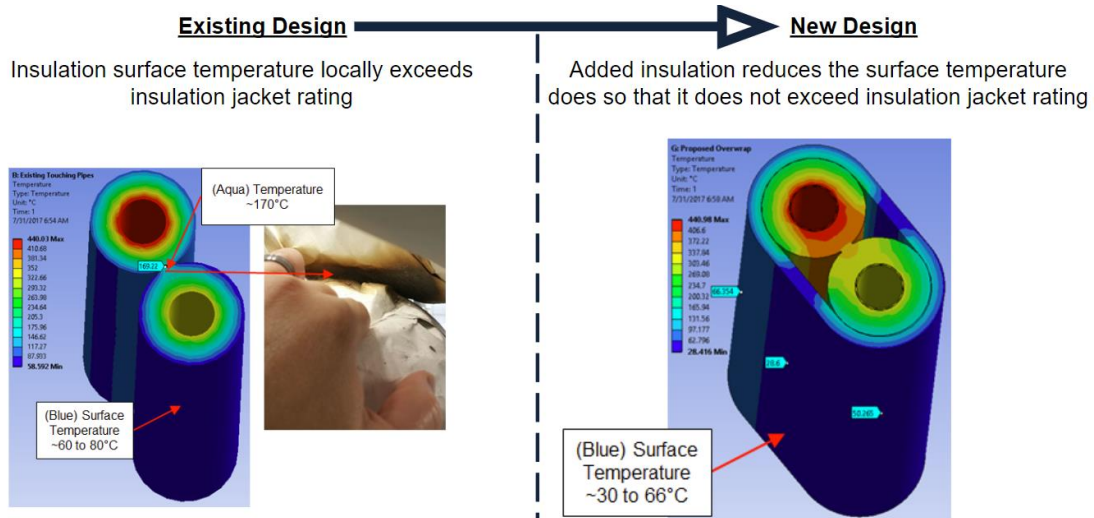


Fig. 1.3.2: Helium piping insulation redesign.

Asymmetry was historically noted in the imparted heating of plasma facing components (PFCs) located in the Primary Passive Plates (PPPs), Secondary Passive Plates (SPPs), and Outboard Diverters (OBDs) during the 2015 NSTX-U bakeout. The existing HTHS gas distribution system lacks the ability to balance the distribution of imparted heating to the PPPs, SPPs, and OBDs. A new design in the PDR held on January 11, 2018 proposed installation of throttling valves to permit on-the-fly balancing of the system imparted heating (Fig. 1.3.3).

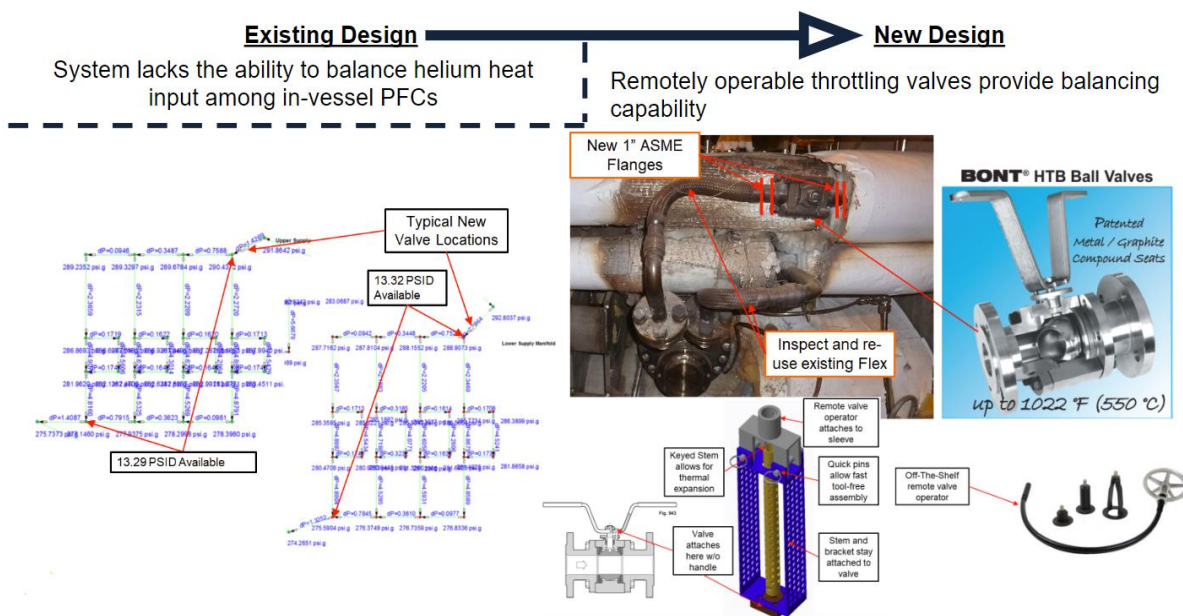


Fig. 1.3.3: HTHS gas piping balanced design.

### 1.3 / B105 exVessel Heating System

The recovery scope for the Ex-Vacuum Vessel Heating System (ExVVHS) included the redesign of a commercial heating skid to comply with industry standards and practices. The commercial heating skid was originally designed with Dowtherm A® as the working fluid and was subsequently repurposed to work with pressurized medium-temperature water, circa 1999. In order to update and upgrade this skid, additional instruments, interlocks, and controls were needed to safely operate the commercial skid as a Medium Temperature Water System (MTWS). A conceptual design review (CDR) of the improvements to update the skid was held the previous fiscal year, and a PDR was held for this scope on February 1, 2018. The PDR level design eliminated unnecessary pressurized volumes, created a redundant pumping configuration using existing pumps, and added instrumentation, controls, and interlocks to conform to industrial standards (Fig. 1.3.4).

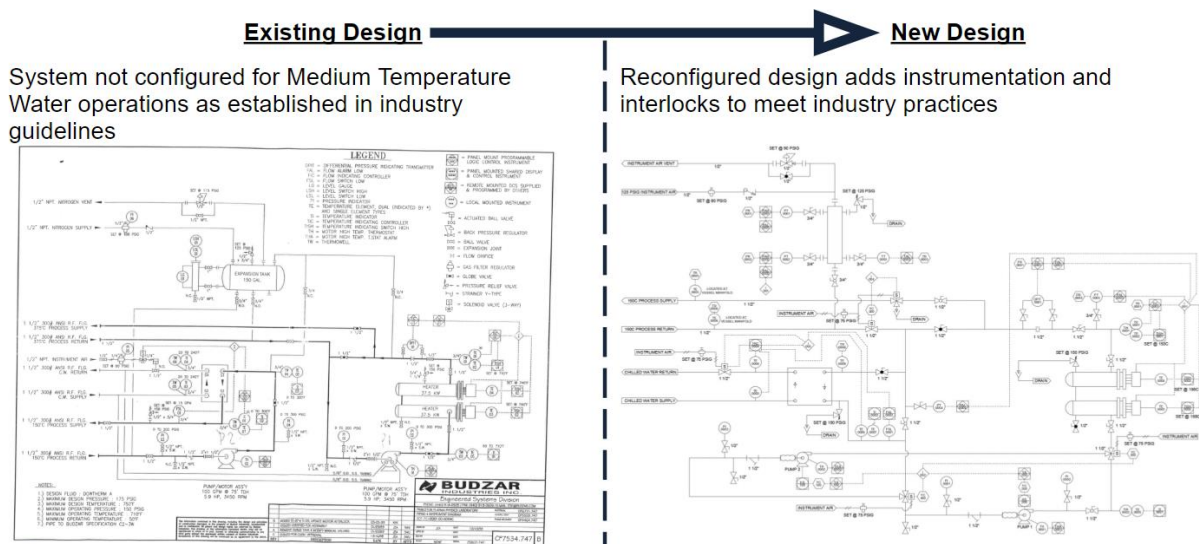


Fig. 1.3.4: ExVVHS PDR Design.

### 1.3 / B115 Bake Requirements/Limits

The recovery scope for bakeout requirement/limits revised and aligned documentation to meet physics requirements for bakeout while preserving engineering feasibility. Concurrence was reached through iteration with physics and engineering. New documentation was developed in the form of a System Requirements Document (SRD) and the General Requirements Document (GRD) was revised. The alignment is illustrated in Fig. 1.3.5.

<b>Existing Design</b>				<b>New Design</b>			
Conflicting/mutually exclusive requirement flow through from GRD to SAD regarding bakeout temperatures				Reworked GRD and SRD matches requirements with SAD limits			
	<u>PFCs</u>	<u>Vacuum Vessel</u>	<u>Ceramic Break</u>		<u>PFCs</u>	<u>Vacuum Vessel</u>	<u>Ceramic Break</u>
NSTX-SRD-3X-Rev2_8-7-98 NSTX-CSU-RQMT-GRD	=350°C >300°C	=150°C >110°C	N/A	NSTX-U-RQMT-SRD-005-01 NSTX-CSU-RQMT-GRD	>300°C ≤350°C	>115°C ≤160°C	N/A
NSTX-U Safety Certificate NSTX-U Safety Assessment Document	≤350°C	≤150°C	N/A	NSTX-U Safety Certificate NSTX-U Safety Assessment Document	≤350°C	≤150°C	N/A
NSTX-OP-G-156 Rev 4	>360°C notify >350°C average notify	>190°C notify >150°C average notify	>175°C notify >150°C average notify	NSTX-OP-G-156 Rev 4	>360°C notify >350°C average notify	>190°C notify >150°C average notify	>175°C notify >150°C average notify

**Fig. 1.3.5:** Bakeout system requirements alignment.

### 1.3 / B120 DC current to top of NSTX-U

The Recovery Project scope for the Ohmic Heating System (OHS) primarily consists of moving the existing ohmic heating power supply connections from the bottom of NSTX-U to the top of NSTX-U. The Center Stack (CS) plasma facing components are indirectly heated by passing low voltage DC current through the CS casing. The existing DC feedpoints at the bottom of the machine must be moved due to the elimination of the lower ceramic break. A CDR of the improvements was held the previous fiscal year, and a PDR was held for this scope on April 5, 2018. The PDR level design moved the DC power supplies to a permanent location on the 118-foot platform and created semi-permanent connections up to the upper umbrella (Fig. 1.3.6).

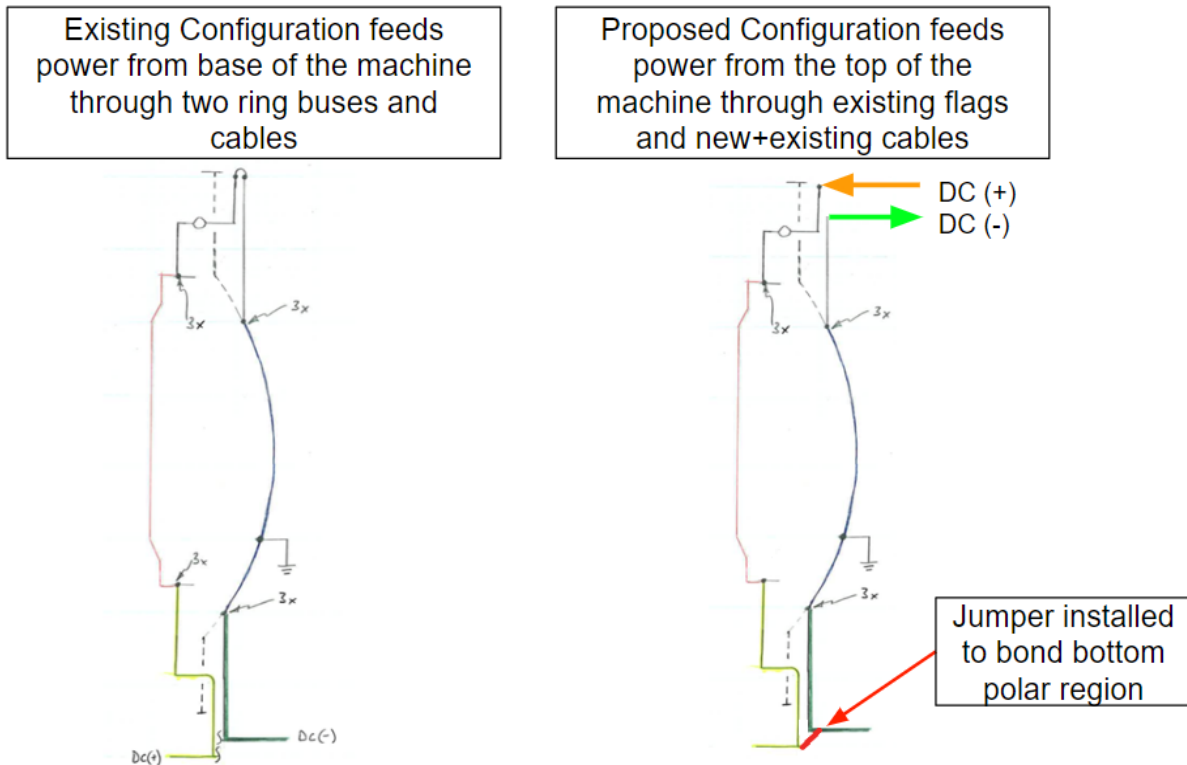


Fig. 1.3.6: DCCHS design premise.

## Vacuum and Fueling

### 1.3 / 3010 Interspace Pumping

Six sets of double Viton O-rings and pumped interspaces will be incorporated into the design of the large flanges and ceramic insulator in the upper and lower polar regions of NSTX-U vessel. The design of the six interspaces (4 upper and 2 lower) will be configured with a pump-out port. The Interspace Vacuum Pumping System (IVPS) will be connected to the pump-out ports and maintain the interspaces at vacuum during NSTX-U operations in order to greatly ameliorate the permeation through the O-rings and to provide an additional guard for leaks that may develop at the O-rings. The preliminary design review meeting of the IVPS was successfully completed in FY-18. The design work accomplished is detailed by the following paragraphs.

The system consists of a dry vacuum pump, 1" OD pump-out line, 2 manifolds with 3/8" OD tubulation, ceramic breaks gauging and associated valving (Fig. 1.3.7).

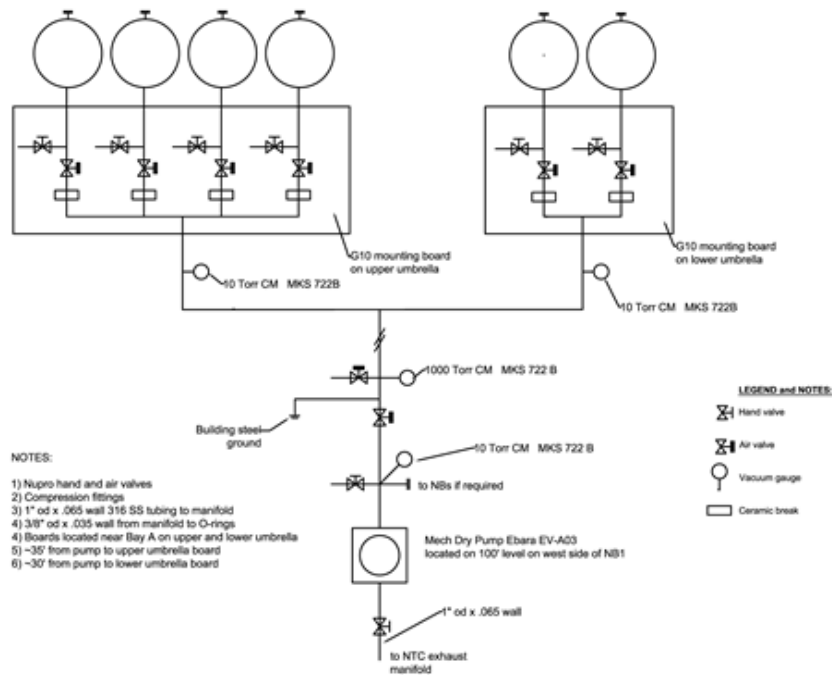


**Fig. 1.3.7:** Schematic diagram of the Interspace Pumping System.

The vacuum pump is an Ebara EV-A03 compact dry pump (Fig. 1.3.8) with a maximum pumping speed of 4.2 l/s. The pump is located at the 100' level on the west side of Neutral Beam 1. The inlet of the pump is configured with an isolation valve, vacuum gauge, vent valve, capped port for future expansion and the outlet is connected to the test cell exhaust ring manifold.

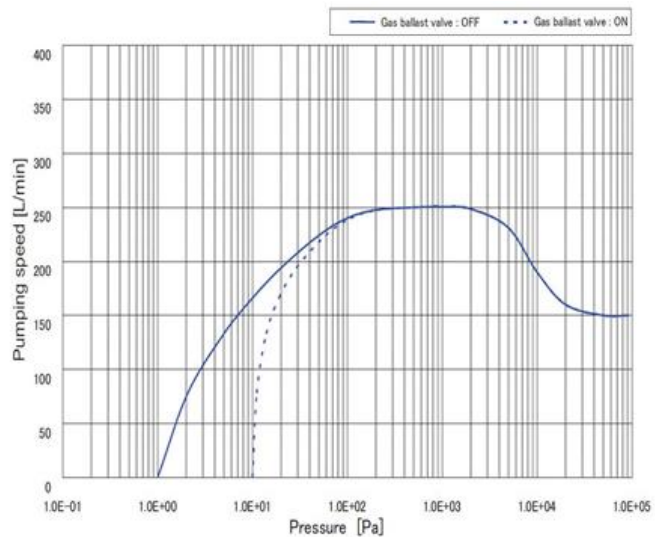


**Fig. 1.3.8:** Compact dry pump (8.3"W x 15.2"D x 9.8") and graph of pumping speed.

The pump-out line consists of a 1" OD (.065" wall) that runs along the west side of NB1 to the north side of the vacuum, and splits out to two manifolds for the upper and lower polar regions

located on the upper umbrella at Bay A and the lower umbrella at Bay D. The pump-out line joint connections are made using compression fittings. The pump-out line has an air actuated vent valve and the system is grounded to building steel.

The upper manifold at Bay A consists of 4 pump-out lines, and the lower has 2 pump-out lines. Each of the manifolds is mounted on G10 boards and consists of NuPro isolation air valves, hand valves for leak checking, ceramic breaks for electrical isolation and a 10 torr capacitance manometer vacuum gauge.

The system is monitored and controlled using the TVPS PLC (Fig. 1.3.9). During operations and prior to each shot, the manifold isolation valves and the pump inlet valve will be closed and the pump-out line backfilled with air. This will preclude arcing across the ceramic breaks in the event that elevated voltage is impressed on the vacuum vessel. The line will then be pumped out directly after the discharge, and the isolation valves will be opened when the pump-out line reaches a satisfactory vacuum. The pressure at the pump-out ports welded on the O-ring flanges will be 50 millitorr or lower.

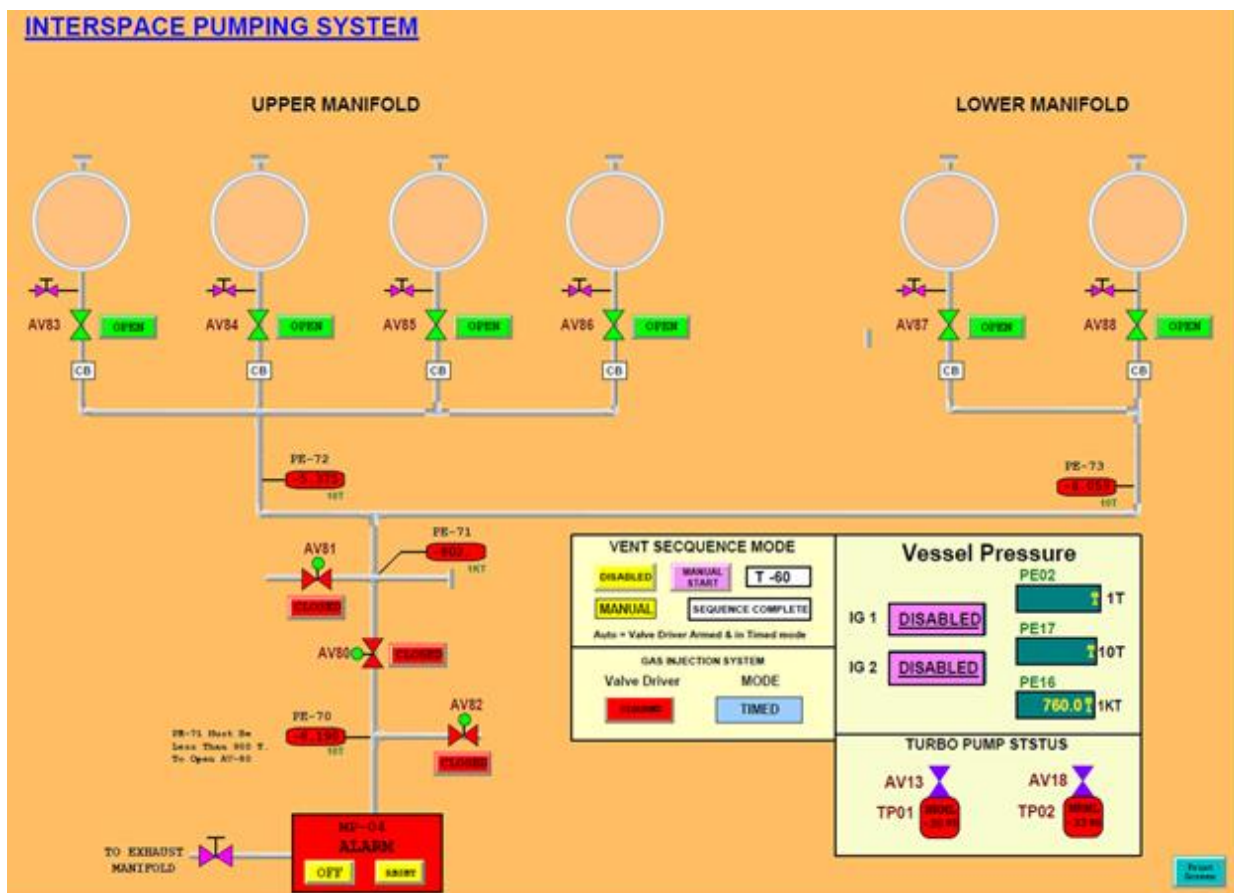


Fig. 1.3.9: PLC display for monitoring and control of the Interspace Pumping System.

### 1.3 / 3020 PFR Fuel Injectors

The Private Flux Region (PFR) injection systems will be used to inject deuterium or impurity gases to mitigate heat flux to plasma facing components.

The detail of this job was planned in FY-18, and is described as follows. There will be two injection systems. Each injection system consists of a torus interface valve, piezoelectric valve, fill volume, gauging on the fill volume, and a fill valve. Each injection system will be mounted on a G-10 board which will be mounted on studs welded to the upper and lower umbrella of NSTX-U, with the upper injection system located near 285° and the lower near 155° (Bay F). The outputs of the injectors will be to organ pipes in Bay J upper and Bay F lower, and the two injection systems will have a common gas delivery line (previously CHI gas delivery line). Flow restrictors will be installed to provide the ability to fill the plena to within 50 Torr of the requested value up to 5000 Torr.

In FY-18, the preliminary design of the gas injection systems was completed (see Fig. 1.3.10) and locations for mounting the systems were identified. This job is currently on hold and may be deferred until 2021.

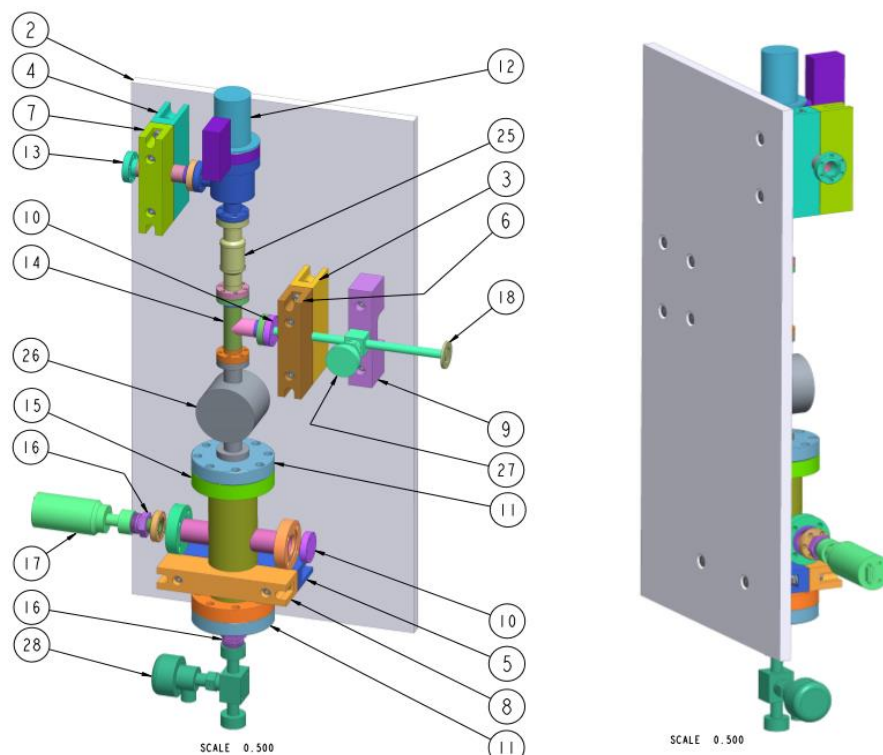


**Fig. 1.3.10:** PFR gas injector assembly.

# Diagnostics

## 1.4 / 8000 Vessel/Coil Instrumentation

Recommendations from the DVVR and EOC process led the NSTX-U Recovery Project to adopt a more extensive instrumentation system. Originally, strain and displacement instrumentation was used on important vessel components such as the TF coil outer legs and the OH solenoid preload assembly. The components to be measured are listed in Fig. 1.4.1.

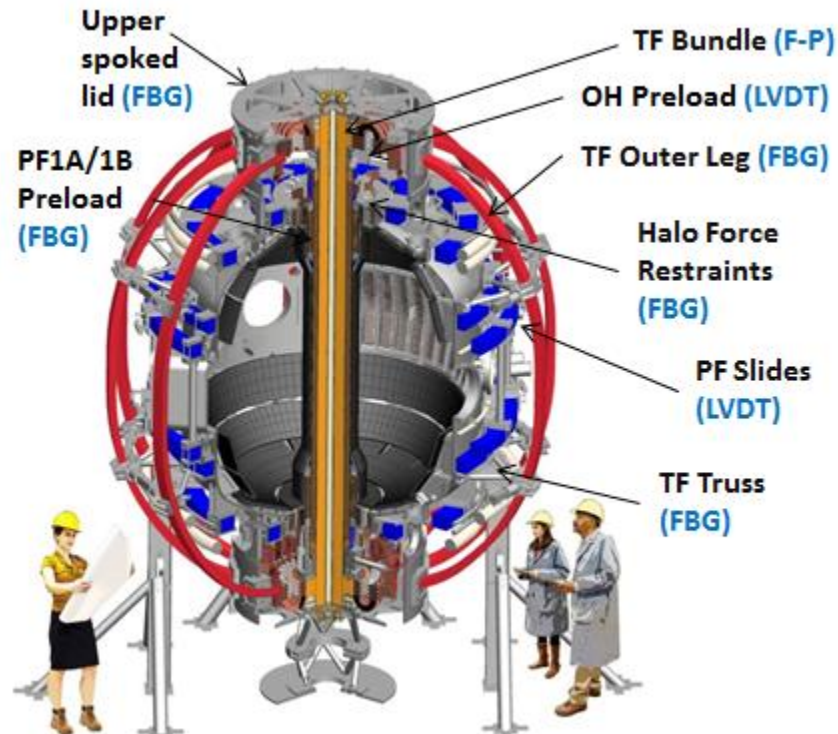


*Fig. 1.4.1: Components to be instrumented.*

- The TF (Toroidal Force) outer legs, because they are legacy components considered to be at risk for delamination;
- The TF trusses, to verify that they are distributing load uniformly to all coils;
- The spoked lids, in order to determine their flex due to center stack expansion;
- The strain, and therefore the force, in the halo current force restraints at the top of the center stack;
- The OH solenoid preload assembly, to verify that the preload exceeds launch forces;
- The twist of the TF center bundle;
- The displacements at the PF4 and PF5 coil slides;
- The preload on PF1A and PF1B coils to verify that launch forces do not exceed preload.

The instrumentation system will serve to verify that the machine components are behaving as predicted by analysis, and trending data from the system may help to detect incipient problems.

Strains are measured by two fiber-optic techniques: Fiber-Bragg sensors and Fabry-Perot sensors. Fiber optics was used because the fibers and sensors are not electrical conductors. Multiple Fiber-Bragg sensors can be attached to the same fiber, minimizing the number of fiber runs and electrical chassis required for the system. The drawbacks are a slightly greater sensor size than for Fabry-Perot, and compensation for temperature sensitivity. Fabry-Perot sensors are more compact and not sensitive to temperature, but one fiber and electrical chassis is required for each sensor.

Displacements will be measured by LVDT Fabry-Perot transducers, which use the same electronics as the Fabry-Perot strain gauges. As with the strain gauges, the signal travels on an optical fiber. Implementation of the system is straightforward: selection of the sensor location based on analysis results, installation of sensors, and routing and installation of optical fibers and electronics.

Fig. 1.4.2 shows the locations of the Fiber-Bragg sensors on the TF outer legs and truss structure. The sensors on the TF legs are clearly at the locations of high stress and strain. Stress and strain do not vary greatly over the trusses, which are nominally in tension or compression, so the sensors are located near the middle. All of the sensors on one TF leg and its associated truss belong to the same fiber strand.

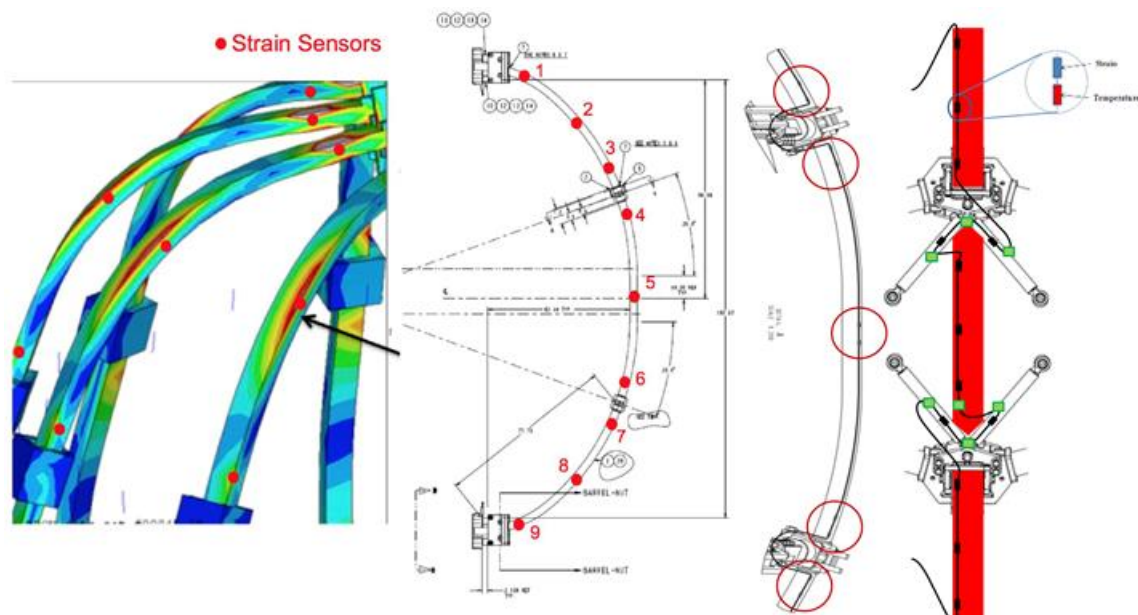


**Fig. 1.4.2:** Locations of strain sensors on the TF outer legs and trusses.

The primary technical risks in developing the vessel instrumentation system were development of a technique for attaching sensors to coils and obtaining meaningful data from the Fiber-Bragg sensors during a fast thermal transient.

Attachment of Fiber-Bragg sensors to a surface like a magnet that can heat up can be challenging. The curing temperature for the epoxy must exceed the maximum operating temperature by 15 degrees Celsius in order to raise the glass transition temperature of the epoxy above the maximum coil temperature. A procedure for properly curing the epoxy was developed and used for the tests of the old PF-1A coil (Fig. 1.4.3).

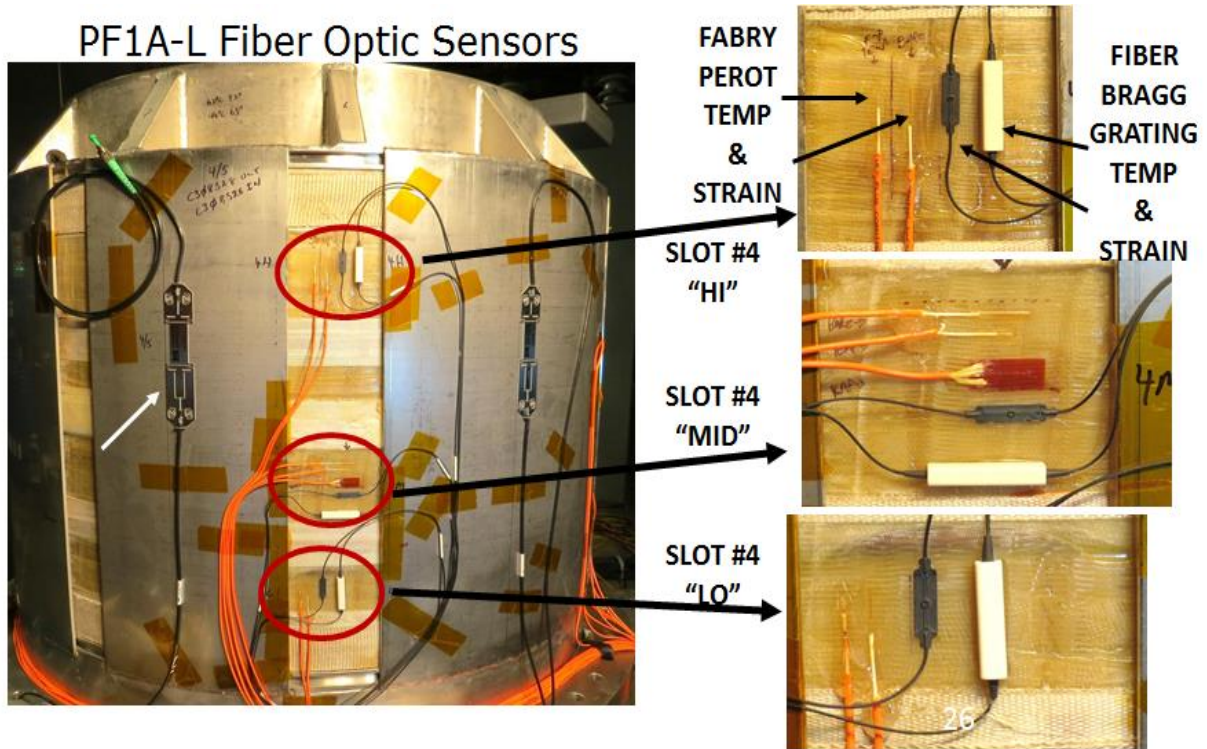


**Fig. 1.4.3:** Strain sensors installed on the old PF1A-L coil.

The PF1A test also verified that meaningful data could be obtained from the Fiber-Bragg sensors during a fast thermal transient. As mentioned above, Fiber-Bragg strain sensors are sensitive to temperatures. Typically, a Fiber-Bragg strain sensor placed near the strain gauge measures temperature, which is used to compensate the strain measurement. During a fast thermal transient, the temperature sensor cannot track the temperature accurately. Tests on the PF1A coil showed that, for a fast transient, the heat does not have time to soak into the Fiber-Bragg strain sensor, and compensation is only required during the much slower cooldown of the coil where it functions properly (Fig. 1.4.4).

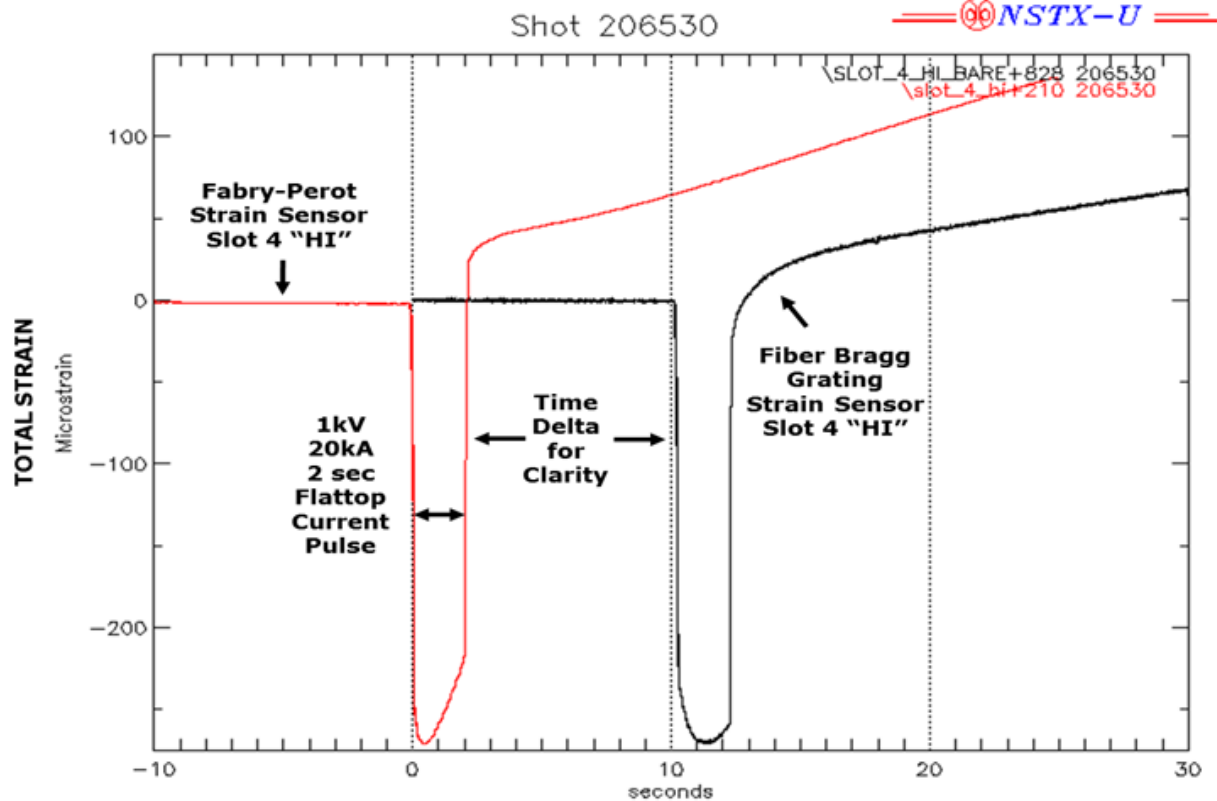


**Fig. 1.4.4:** Comparison of Fiber-Bragg and Fabry-Perot measurements on PF1A. The Fiber-Bragg measurements are displaced 10 seconds for clarity.

Structural components, such as the TF trusses and spoked lids, are not expected to experience fast thermal transients. The instrumentation system had a successful preliminary design review on March 22, 2018.

### 1.4 / 8035 Plasma Facing Component (PFC) Diagnostics

Five types of diagnostic sensors - Mirnov coils, Langmuir probes, thermocouples, halo current shunts, and center stack halo current Rogowski coils - are embedded in the plasma facing component tiles in the center stack and outboard divertors. Redesign of the PFCs as part of the NSTX-U Recovery Project required updated designs for some of the sensors and wire routing. This effort utilized existing designs wherever possible. Plasma facing components are grouped into several categories: Outboard divertor rows 1-2 (OBD12), inboard divertor horizontal and vertical (IBDH, IBDV) that are exposed to high heat flux, outboard divertor rows 3-5 and the Center Stack Angled and first wall sections (OBD305, CSA, CSFW) that receive low heat flux (Fig. 1.4.5).

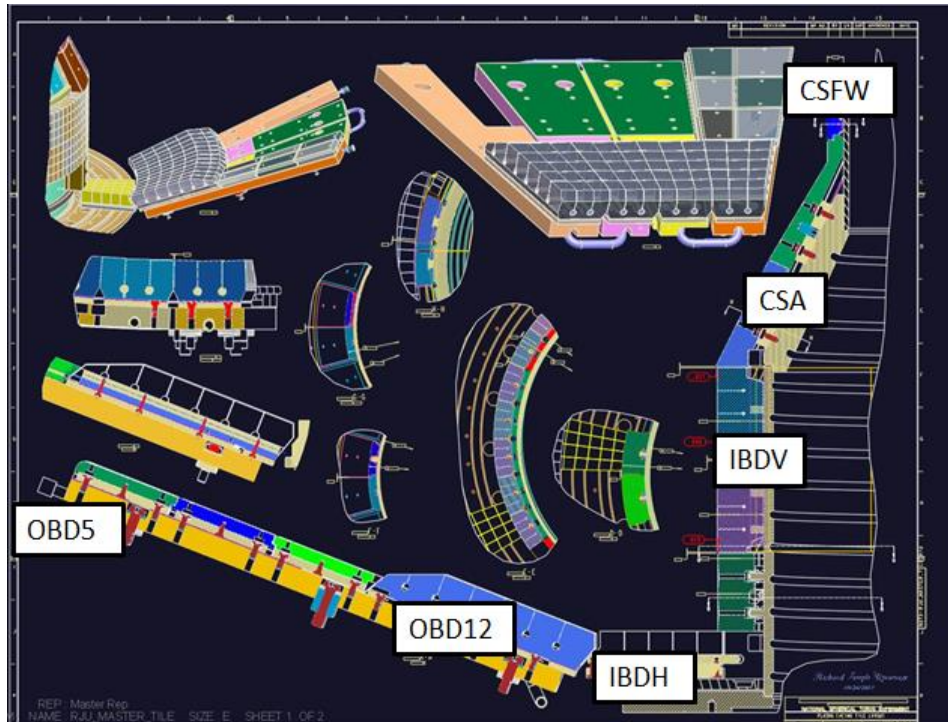


**Fig. 1.4.5:** Locations of plasma facing components.

Mirnov sensors consist of one or two orthogonal solenoids on a mandrel and are used to measure radial and vertical fields (Fig. 1.4.6). It is planned to use the existing design on the new PFCs and incorporate them into the tile designs.

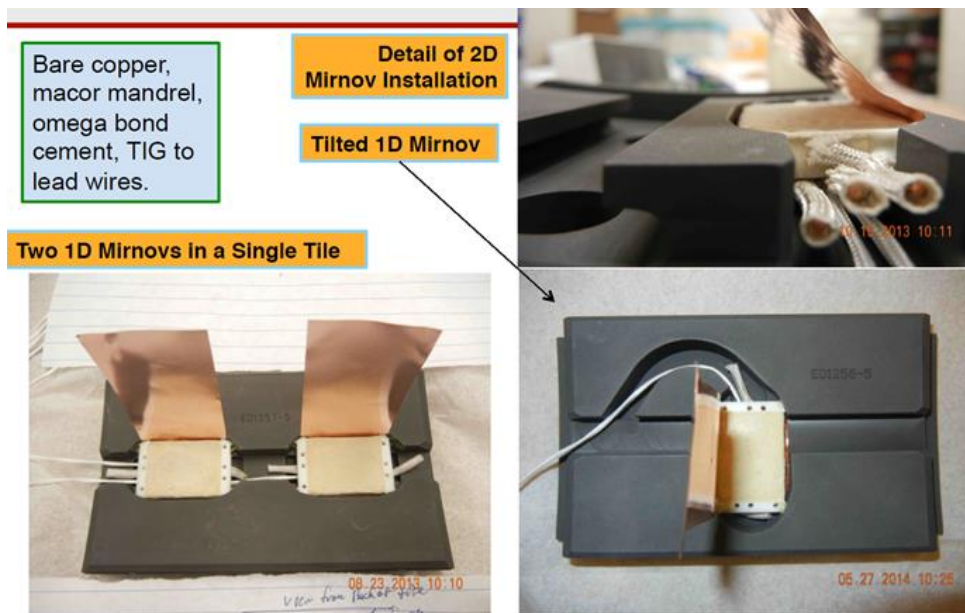


**Fig. 1.4.6:** Mirnov sensors.

Langmuir probes provide local measurements of electron temperature, electron density, and floating potential. A new design is required for the Langmuir probes in the high heat flux tiles. This new design is based on a rail probe design used on Alcator C-Mod (Fig.1.4.7).

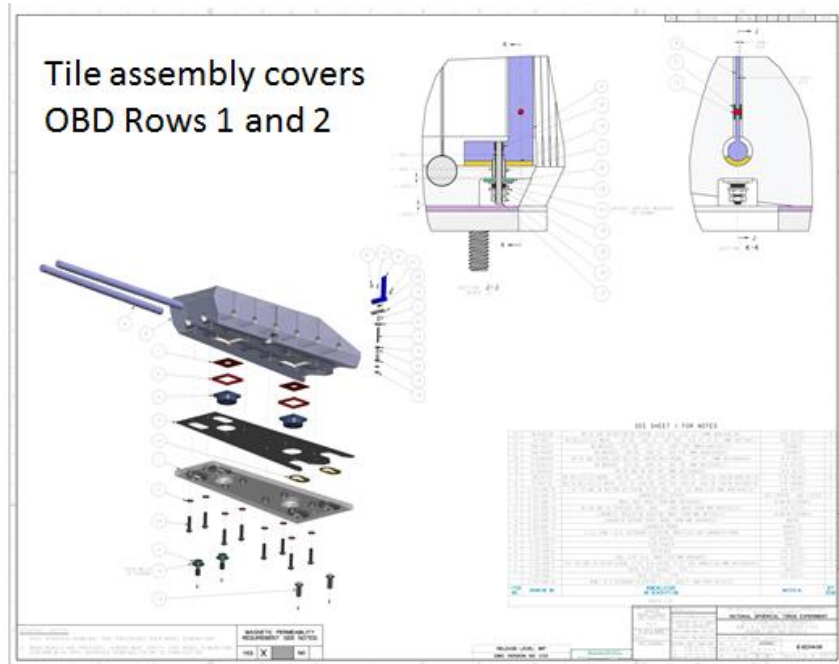


**Fig. 1.4.7:** New Langmuir probe incorporated into OBD rows 1-2.

The existing Langmuir probe design will be used in the low heat flux tiles (Fig. 1.4.8).

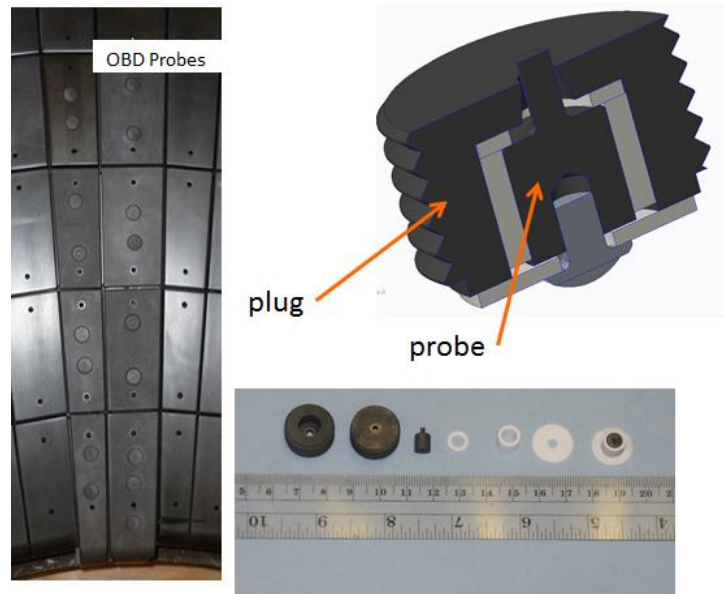


**Fig. 1.4.8:** NSTX Langmuir probes.

Thermocouples measure the temperature of the tiles, and will be used to monitor bakeout performance, thermal transients, and energy deposition during experiments.

Shunt tiles measure the distribution of halo currents during a disruption. They will only be used in low heat flux areas CSFW and OBD345. The principle of a shunt tile is to insulate the tile from its support structure so that all of the current in the tile passes through a resistive shunt. Current is obtained by measuring the voltage across the shunt. The existing design will be used again on the CSFW tiles (Fig.1.4.9).

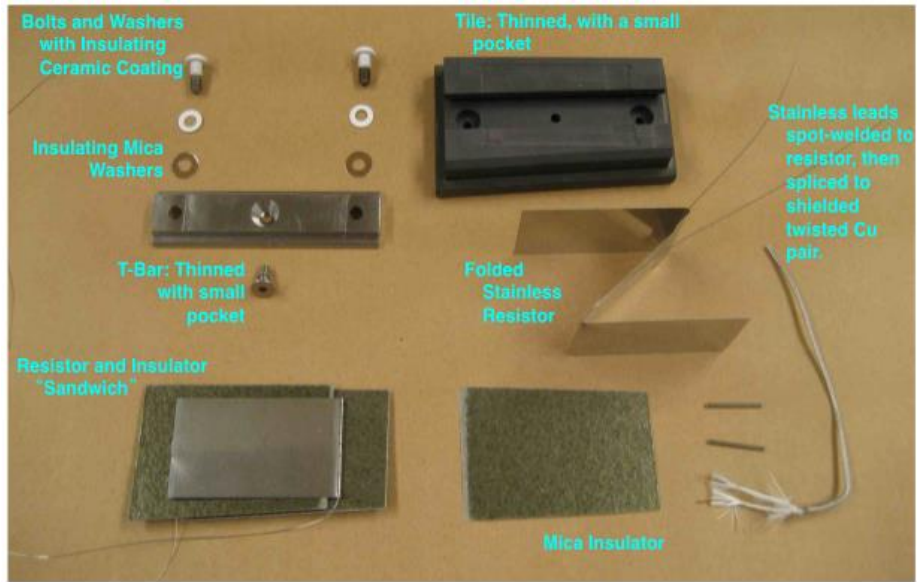


Fig. 1.4.9: Halo current shunt tile.

Changes to the design of the OBD345 tiles require a new shunt design. The operating principle is the same, but the configuration is different; the Z-folded shunt is replaced with a resistive leaf spring inside the T-bar (Fig. 1.4.10).



Fig. 1.4.10: Shunt tile for OBD 3,4,5.

Rogowski coils are used to measure halo currents in the Center Stack. Four coils are installed: two each on the upper and lower IBDV. For the NSTX-U recovery, slight repositioning, and improvements to the design aimed at enhancing reliability are planned.

The PFC diagnostics had a successful preliminary design review on January 4, 2018. Work continues on integration with the PFC tile assemblies, wire routing, and prototypes.

1.4 / 8010 Aerodag Replacement - this task was deferred to FY19 because of resource limits.

1.4 / 8015 Ip Rogowski Repair - this task was deferred to FY19 because of resource limits.

1.4 / 8020 Field Seal Repairs - this task was deferred to FY19 because of resource limits.

1.4 / 8025 Halo/Flux Loops and Diagnostic Compatibility - this task was deferred to FY19 because of resource limits.

1.4 / 8030 BES Shutter - this task was deferred to FY19 because of resource limits.

## **Test Cell**

The NSTX-U Test Cell and South High Bay have served the NSTX and NSTX-U program well throughout its 20 year existence. The NTC houses the machine, both neutral beams, and supporting equipment and services. Radiation surveys during the 2016 run period and subsequently using a DT Generator indicate that changes to the NTC shielding are required to comply with site boundary dose limits, and permit access to surrounding areas to the NTC when the machine is operating. In 2018, a design effort was undertaken to improve shielding during a PDR in August 2018.

The test cell work scope also includes plans for an oxygen monitoring and radiation annunciation system. The oxygen monitoring will be used to monitor oxygen deficiency in selected areas where there is a potential for gas leaks, and alarm personnel entering into the test cell, or who are already in the test cell, to leave the area. The radiation annunciation will be used to alarm personnel entering into the test cell if the radiation levels in the test cell are above the allowable limit.

### **1.8 / 5000 NTC Shielding**

The NTC shielding will be improved in several key ways in anticipation of neutron flux from the full performance enhancement of the NSTX Upgrade. The South High Bay door to the gallery will be shielded with the addition of a concrete labyrinth. The labyrinth walls will be constructed by pouring concrete mix in place. Fig. 1.8.1 shows a draft drawing for the poured concrete wall. The roof of the labyrinth will be made using existing concrete blocks from TFTR. The labyrinth wall and roof will be dressed with 1-inch thick borated polyethylene sheathing.

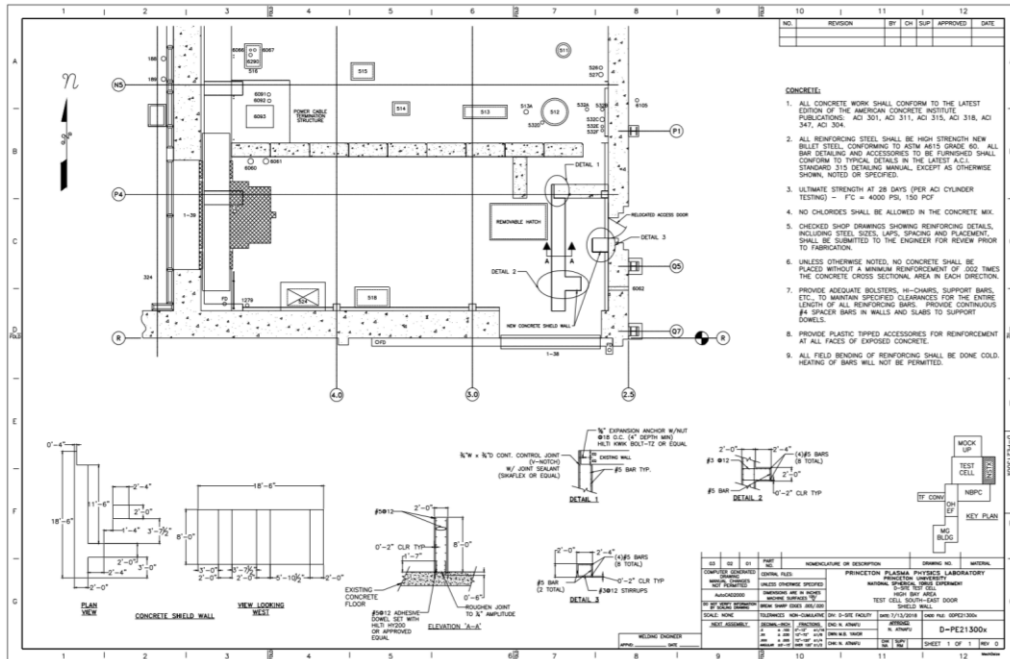


Fig. 1.8.1: Draft drawing for constructing the poured concrete shield wall.

The movable shield door to the Neutral Beam Power Conversion (NBPC) building will also be augmented with the boronated polyethylene sheathing. The north door access will make use of the legacy “battleship” door with additional boronated polyethylene sheathing. Existing penetrations in the shield walls from prior usage of the NSTX-U Test Cell (NTC) area dating back to TFTR will be augmented with additional boronated polyethylene beads or concrete. Fig. 1.8.2 shows a draft drawing with the specifications for shielding each penetration.

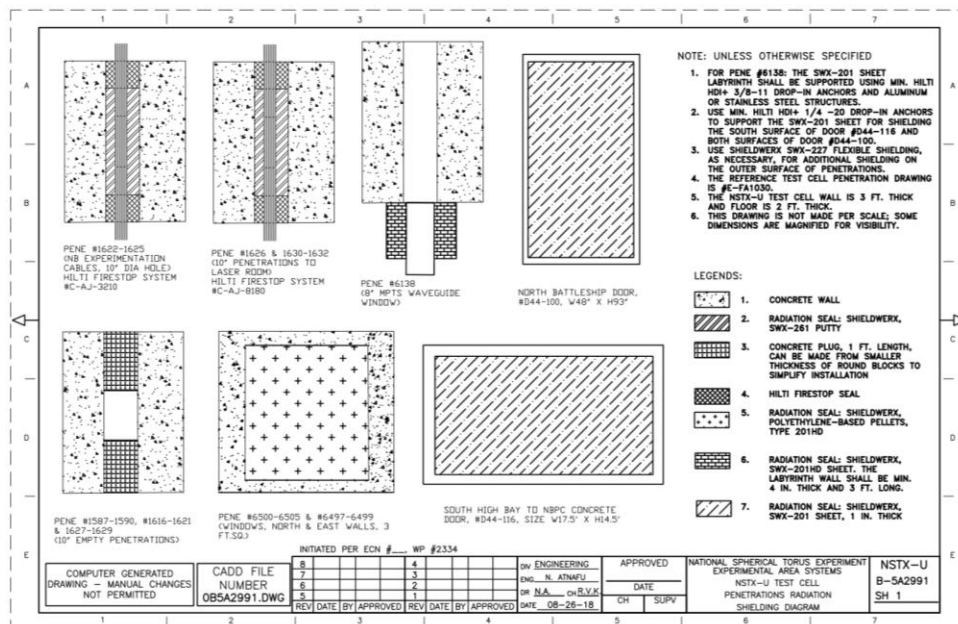
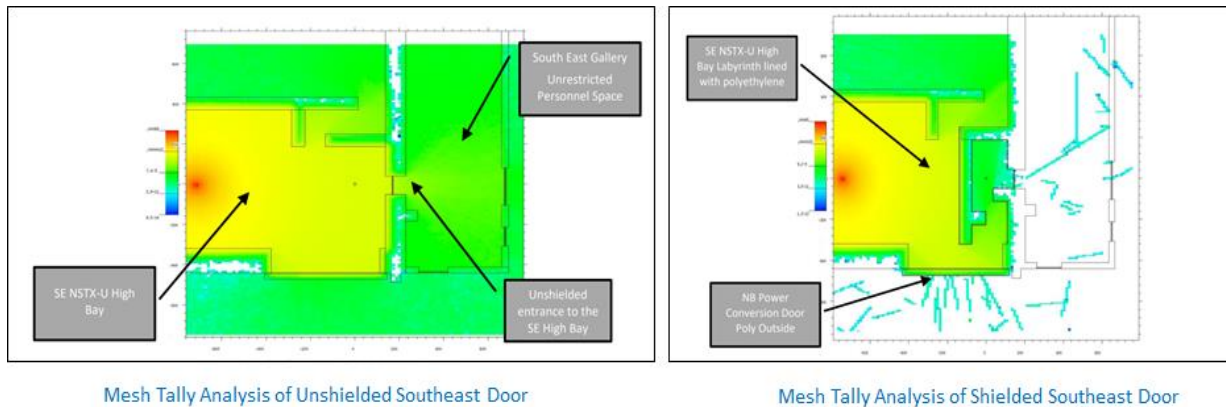


Fig. 1.8.2: Draft drawing of the penetrations shielding specifications.

Finally, due to penetrations in the NTC floor that pose major difficulties or are impossible to shield, the subterranean Mechanical Equipment Room will become access controlled with no entry during operations. The design effort for this improvement produced layouts which were then compared with existing shielding using the well-known MCNP code; these calculations indicate that 99.9% of neutrons produced (the limit of the code) in the NTC will be attenuated. Fig. 1.8.3 shows an image from the neutronics calculation (Document #NSTXU-CALC-81-02-00) of the mesh tally analyses with and without the labyrinth shielding.



**Fig. 1.8.3:** Comparisons of the MCNP Mesh Tally Analysis of the southeast door with and without the labyrinth shielding.

The cost of the shielding changes has been captured in a cost estimate for project baselining. Major risks to the project have been analyzed and added into the project risk registry. Because of the changes to the access in the South High Bay and Mechanical Equipment Room (MER), an effort was started to modify and extend the Access Control System and Hardwired Interlock System.

### 1.8 / 5005 Rad Monitor Compliance

There is an existing radiation monitoring system which is being used by the PPPL Radiological Control group to read radiation sensors and send signals to a control unit. The work scope included in the Recovery Project expands the capability of the existing radiation monitoring system by adding posts and alarm signs in order to comply with applicable regulations. Fig. 1.8.4 shows the configuration of the existing radiation monitoring system in the test cell. There are four instrumentation sets installed in the test cell in all four dimensions at the midplane elevation. Each instrumentation set includes neutron and gamma sensors. All of the instrumentations (a total of 8) are networked to a server through a fiber optics link and monitored via a web page tool. The controller will be replaced with a more advanced control unit as part of this project. The Project also posts signs at the entrance doors both in the north and south side of the NSTX-U Test Cell. When high radiation level is detected in the test cell, the LED signs will display a “Danger High Radiation Area” warning. Complying with DOE title 10 part 835 regarding radiation area control guideline, the warning signs will have a trefoil symbol with black and yellow background. Under normal conditions, the signs will be blacked out with no text. The control panel provides switching capability to turn on and off the signs.

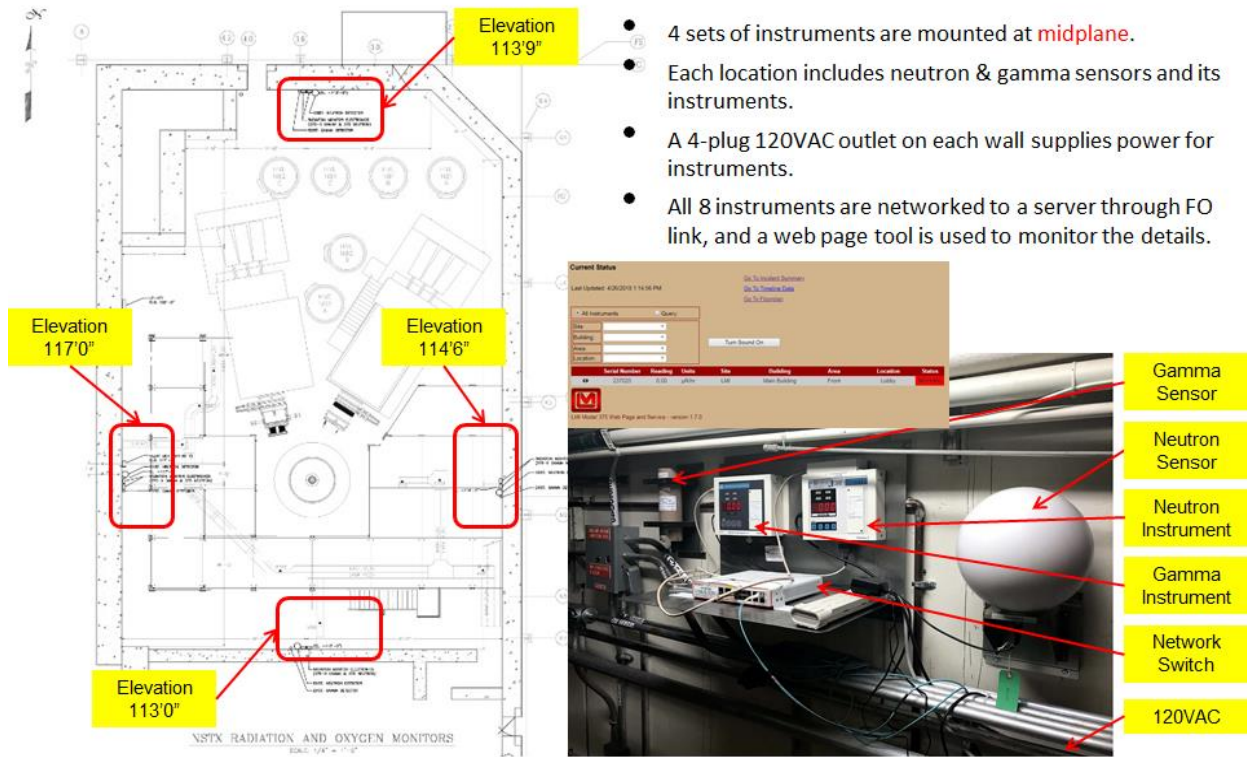
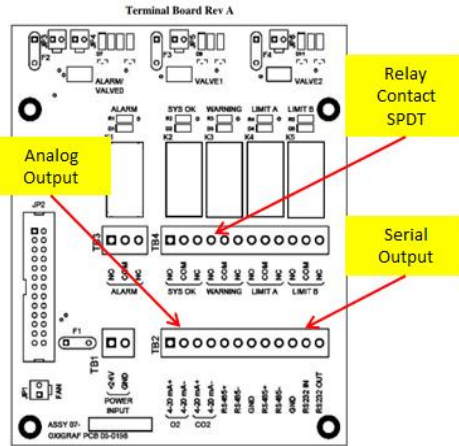


**Fig. 1.8.4:** Configuration of the existing radiation monitoring system in the test cell.

### 1.8 / 5010 Oxygen Monitor

The new installation of an oxygen deficiency monitoring system will be used to provide a siren in the test cell and an alarm indicator at the entrances of the test cell to alert personnel to leave the area in case of an oxygen deficiency emergency. Fig. 1.8.5 shows the design for the oxygen monitor and indicator. Fig. 1.8.6 and 1.8.7 show the current design and related cable routing for indicator installation at the north and south doors.

Measurement Performance	
Sample Ports	Standard: One (1), Optional: Up to Four (4)
Measurement Range	5-100%
Accuracy	±0.5%
Cross Sensitivity	0.2% (XC mode)
Response Time	500 ms at 200 ml/min flow rate, additional low pass filtering programmable.
Ambient Temperature (Operating)	-10 to 50 °C 14 to 122 °F
Ambient Temperature (Storage)	-20 to 60 °C -2 to 140 °F
Gas Inlet Temperature	-10 to 50 °C 14 to 122 °F
Gas Pressure	750 to 1150 mbar
Humidity	0 to 95%, non-condensing
Warm-up for Full Accuracy	5 minutes
Filter (Inlet)	4 micron hydrophobic PTFE inlet filter blocks any condensates.
Pump Sampling Rate	Diaphragm pump up to 250 ml/min at 1010 mbar
User Interface	
Display Resolution	0.1% O2
Display	16 x 2 character YFD, 8 mm character size
Strobe	Red lens flashing strobe
Horn	100 dB
Enclosure	NEMA 4X rated non-metallic box with Lexan window, wall mounted



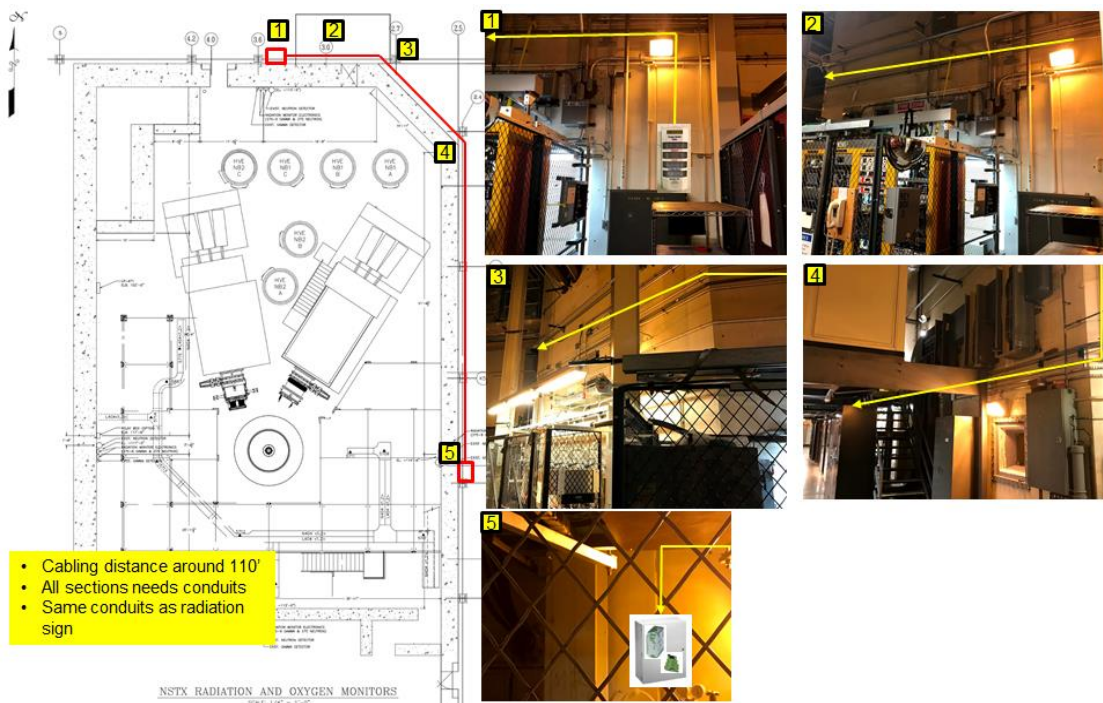
O2 MONITOR



REM. INDICATOR

- Oxygen O2IM main display shows the O2 level (%) and flow rate (ml/m).
- It has a local alarm strobe and 100dB horn.
- The on-board electrical interface provides serial output, analog output, and fail-safe SPDT contact output. Only the relay contacts are used this scope of the work.
- The NO relay contact sends signal to the alarm control panel.

Fig. 1.8.5: Current design of the oxygen monitor and indicator.



- Cabling distance around 110'
- All sections needs conduits
- Same conduits as radiation sign

NSTX RADIATION AND OXYGEN MONITORS  
SCALE: 1/4" = 1'-0"

Fig. 1.8.6: Design of the north door indicator and cable routing.

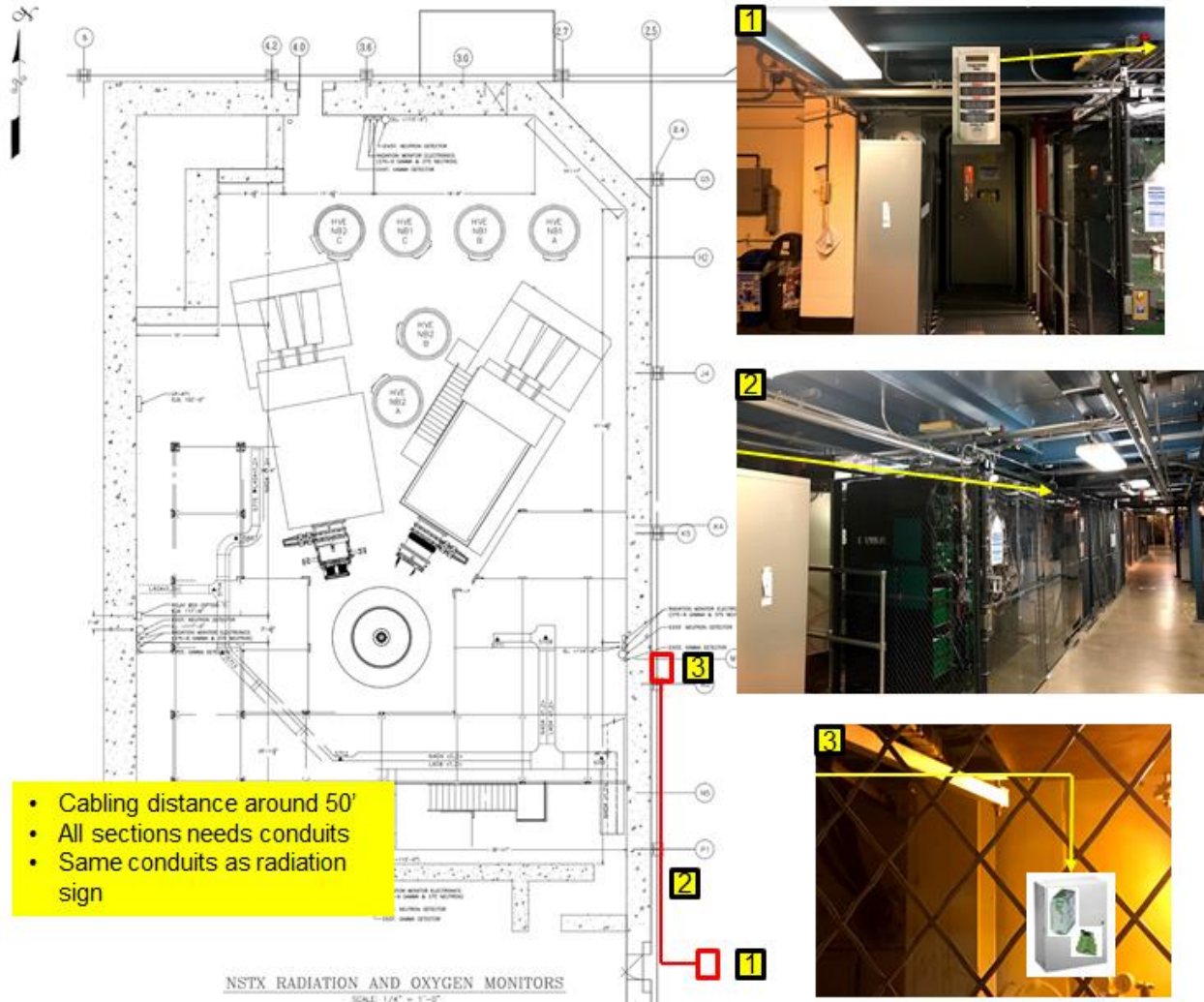


Fig. 1.8.7: Design of the south door indicator and cable routing.

## Metrology and fit-up activities

There is a desire for the NSTX-U Recovery Project to improve the relative alignment of specific components, for reasons fundamentally driven by the underlying physics. In particular, the relative location of the Inner Poloidal Field (PF) Coils and Toroidal Field (TF) Bundle to the Inboard Divertor (IBD) PFCs strongly influences the local heat flux to the tiles. Moreover, the Inner TF Bundle must be well-aligned to the Outer PF4 and PF5 Coils to minimize magnetic error fields. These high-level goals involve “action at a distance” effects between magnets and magnets, and magnets and PFCs. In reality, the location and alignment of such components is governed by assembly chains or tolerance stack of many interstitial components. Therefore, achieving machine-level alignment goals requires a two pronged approach:

- 1) Defining a framework to determine the requirements at the component level, which in aggregate support the high-level goals;

- 2) Developing the capability to perform integrated measure-align-install assembly work packages.

The first component of this scope, the definition of alignment requirements, is an ongoing activity. It first began with weekly meetings between all tokamak core responsible engineers (REs), in addition to stakeholders from assembly and machine integration. These meetings resulted in the defining an overarching strategy for how to align the machine:

- Identify which components need to be aligned to which other components;
- Define coordinate systems and the critical sequence of alignment operations;
- Identify several specific risks.

This effort continued to evolve, eventually resulting in the development of requirements document NSTX-U-RQMT-RD-011 and several qualitative analyses of machine-alignment chains (Fig. MET-1). Recently, these qualitative alignment chains are being incorporated into a quantitative tool to model the results of machine assembly (Fig. MET-2). This tool allows for the assignment of specific values to each alignment relationship between individual components, varying in both phase and magnitude, to compute the possible aggregate resulting alignment relationships for the high level requirements. Re-running many different ensembles of this “simulated assembly” through a Monte Carlo analysis, without corrective rework, provides probabilistic information on the risk that specific, project-level alignment goals will be reached on the first attempt. Continuation of these analyses, in a way that minimizes total project risk, will allow for the assignment of machine-level tolerance into buckets for each individual component. These can be updated as the project progresses, and “as built” values become known during the fabrication and assembly process to shift tolerances back and forth.

# Simplified Alignment Flow Chart

## Dimensional Control Strategy NSTX-U Recovery Project

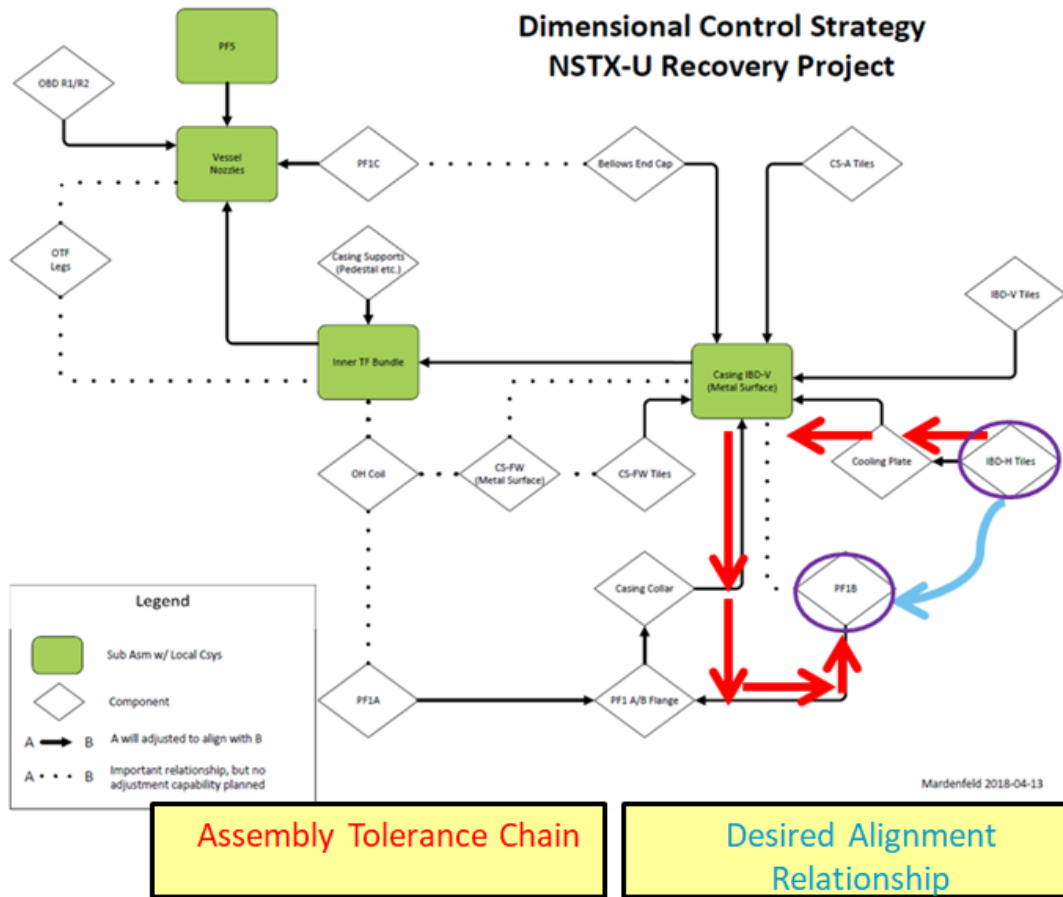
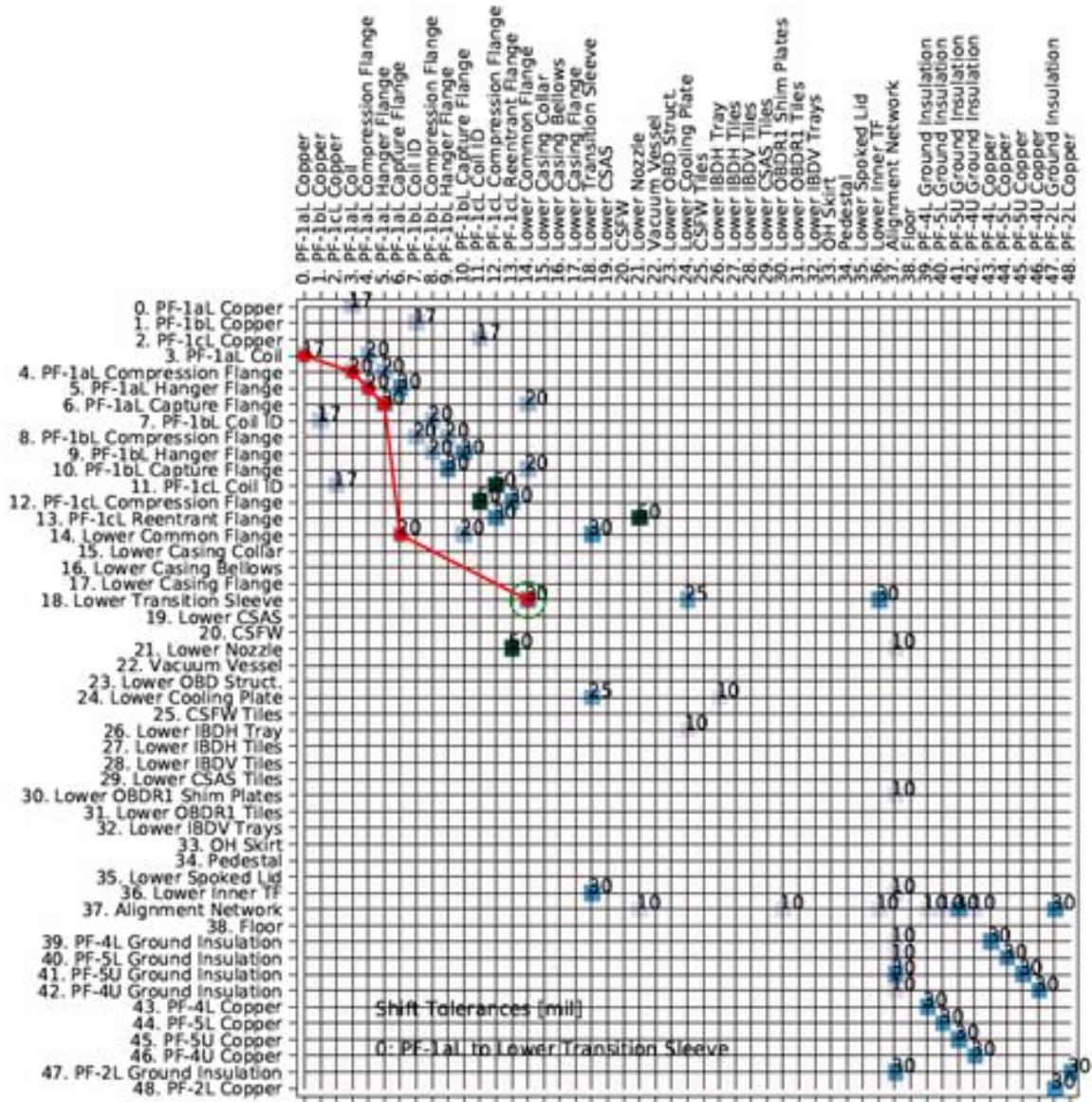


Fig. MET-1: Simple alignment flow chart.



**Fig. MET-2:** Adjacency matrix augmented with shift or tilt tolerances with alignment chain.

The second component of this scope involves developing the capability to achieve these individual component-level alignments. More specifically, it means the ability to measure geometry in the field, post process those measurements into useful data, design any special tooling or handling fixtures, physically install/manipulate the components as desired, and verify that alignment objectives have been achieved. During the course of the Dimensional Control meetings, one risk in particular was identified as potentially problematic: the ability to align the Center Stack (CS) Casing to the TF Bundle while preserving sufficient space for interspace diagnostics and thermal insulation. The recent, successfully completed Trial-Fit Assembly resulted from this identified risk.

Prior to the Trial-Fit Assembly, the CS Casing and TF/OH Bundle underwent individual metrology characterization in the staging area of the South High Bay (Fig. MET-3). The results

were then individually analyzed and virtually combined in the desired alignment (Fig. MET-4). This was done to map the variation in radial clearance due to eccentricities and deviations from roundness. This analysis identified potentially advantageous relocations of the TF Rogowski Coils to a different toroidal angle (Fig. MET-5).



**Fig. MET-3:** Machine Tech Scott Gifford with horizontally-mounted laser tracker atop CS Casing.

## OH and CS-FW Clearance: Flattened 2D Analysis Bounding Lines for Measured Radii vs Toroidal Angle

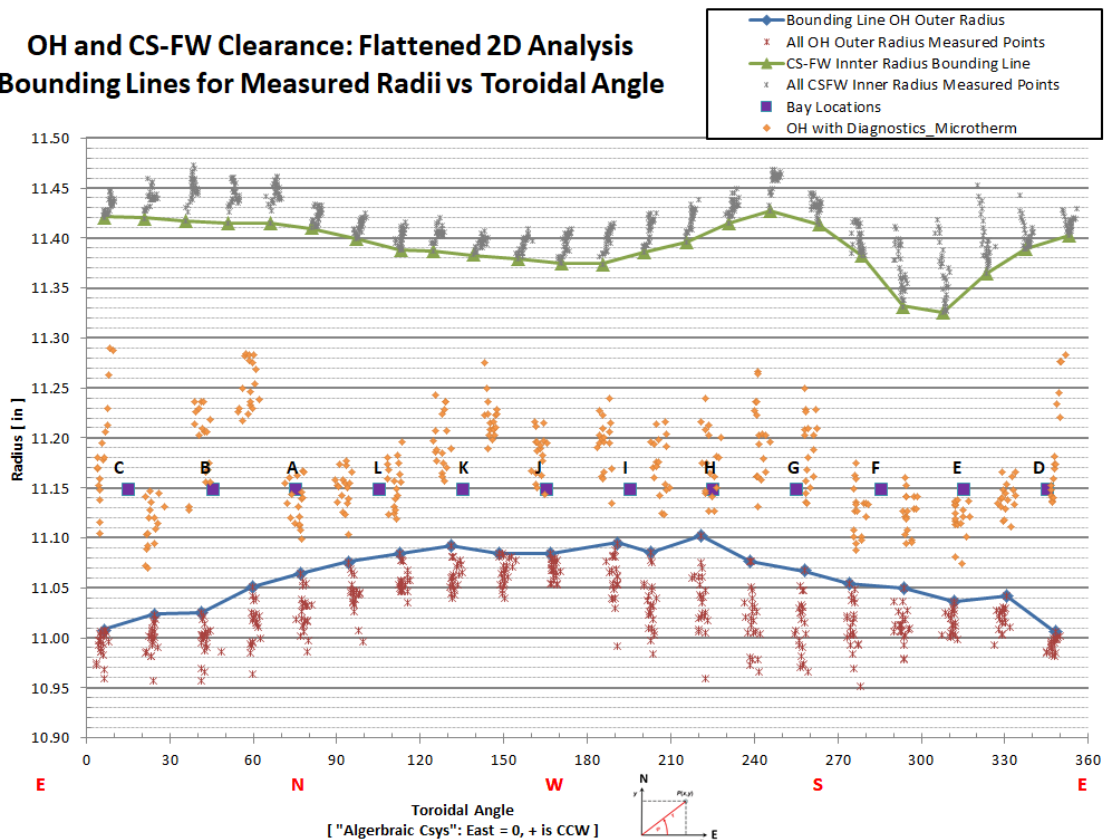


**Fig. MET-4:** Flattened 2D analysis of “Virtual Assembly” between the OH and CSFW.

- This plot represents a “perfect” alignment, because the TF and Center Stack First Wall (CSFW) axes were “exactly” aligned when the data was combined.
- Each cluster of points (red and grey) represents the variations of radius at a single toroidal angle as a function of elevation for the OH and CSFW.
- The bounding lines are a conservative estimate of the constricting radii of the OH and CSFW at each angle.
- The orange points represent the as-installed interspace components, as measured by laser tracker after installation on the OH Coils. The distance between the orange point cloud and the CS-FW bounding lines indicates an expected radial clearance of approximately 0.100”.
- Note the definition of “Algebraic Coordinate System” in the inset picture.

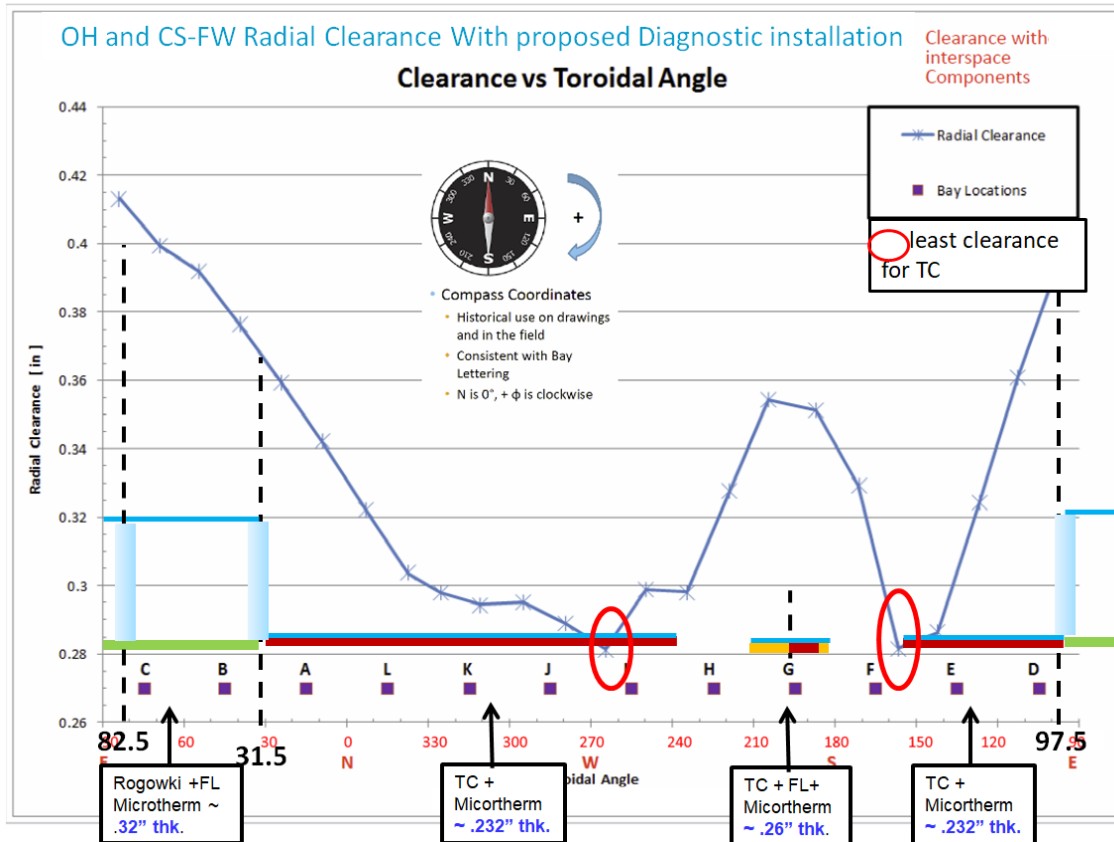


**Fig. MET-5:** Flattened 2D Analysis, radial clearance vs angle w/ planned diagnostic build.

- This plot is a subtraction of the two bounding lines from the previous plot to show the conservative estimate of radial clearance as a function of angle.
- The schematic overlay represents the expected radial build of the interspace components. This overlay is not to scale.  
 FL = Flux Loops  
 TC = Thermocouples  
 This schematic is not to scale
- The red circles represent areas of least clearance between the CS Casing and the TF/OH Bundle.
- Two of the Rogowski Coils and the TC/Flux loop leads were relocated to areas of greater clearance: “peaks” as shown in the plot.
- Note the definition of the “Compass Coordinate System” in the inset picture.

During the Trial-Fit Assembly, the actual TF Rogowski Coils, along with other interspace diagnostics and the Microtherm insulation blanket, were installed on the TF Bundle. The CS Casing was then hoisted onto the TF/OH Bundle and then physically manipulated into the desired alignment using custom built tooling fixtures. This ultimately proved the desired alignment could be achieved and showed that a space envelope of clearance existed around this alignment (Fig. MET-6).

## Upper and Lower IBD-V Cylinder Centers for Various Casing Positions

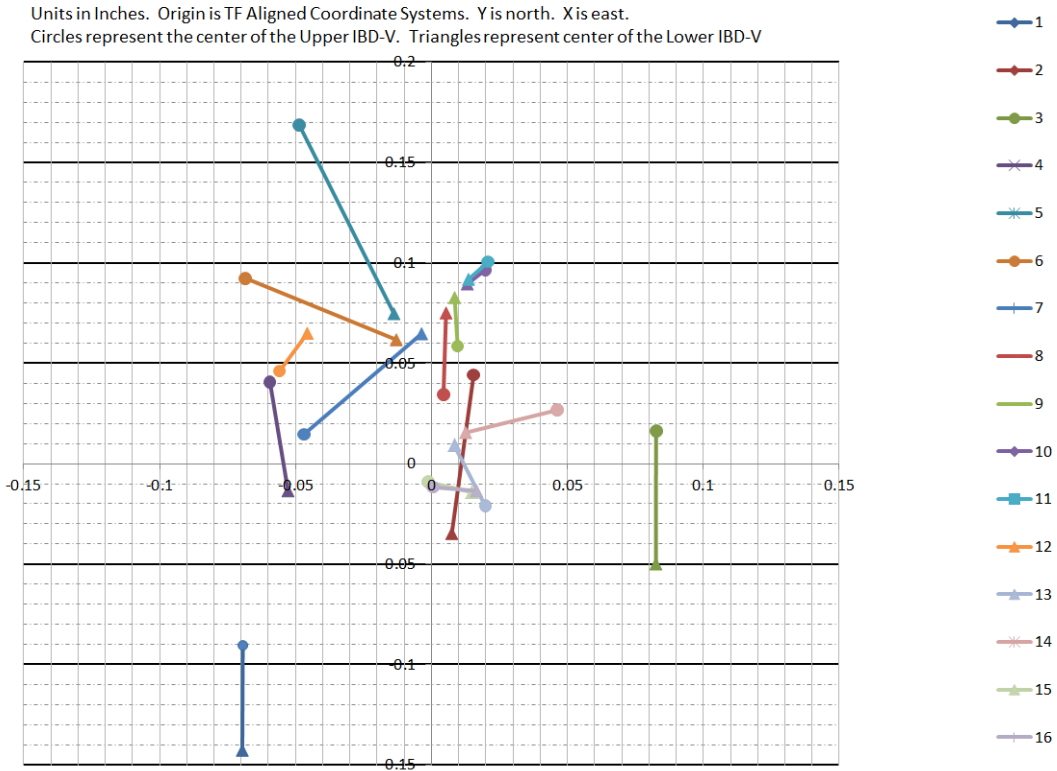


**Fig. MET-6:** Summary plot of the relative position of the Casing to the TF Bundle for 16 positions.

In the process of retiring alignment concerns through the Trial-Fit, PPPL developed various techniques to work through these types of integrated assembly workflows. New techniques, like using two laser trackers simultaneously, reducing as-built data to geometric primitives, and performing virtual assemblies were learned and validated. In addition, critical feedback was gained on how to design and actuate custom tooling mechanisms.

Although the trial fit was the most extensive metrology and alignment activity undertaken in FY-18, several other notable tasks were also completed. These included:

- Characterization of the Outboard Divertor (OBD) in preparation for the OBD R1/R2 shim plates;
- Measurement of the CS casing, and post processing to support the PFC and Polar Region designs;
- Measurement of the “skirt” component and its interface with the base of the TF/OH Bundle (Fig. MET-7);
- Resurrection and testing of PPPL’s photogrammetry equipment;
- Reprocessing and combination of several legacy metrology datasets to get a snapshot in time of the past relationships between the Vessel Nozzles, CS Casing, TF/OH Bundle, and PF4/5 Coils.



**Fig. MET-7:** Custom threaded gauge made to measure Keensert locations in bottom support (E-DC1482).

# NSTX-U Engineering Operations

Engineering Operations continued to provide coverage to maintain D site with minimum staff coverage for safe operations, maintenance and run preparation, routine inspections, and management of obsolescence. The NTC was maintained as an active work area using the Work Control Center and Work Permit system and also supported numerous public and outreach tours. Coverage for these activities also included ongoing safety training and maintenance of procedures. As part of ASO implementation, Unreviewed Safety Issue screening has been added to all work activities using a new procedure OP-AD-131. Engineering Operations level of effort included HP support for the NTC surveys, associated HP allocations, electricity for D site, and supplies.

## Heating Systems

### FY-18 Progress in Heating Systems - NBI

At the end of FY 2016 plasma operations, all six Neutral Beam Injection (NBI) ion sources were operating at 90 kV injection energy. There were, however, no spare sources left, as the spares that had been present at the beginning of the 2016 campaign were used to replace failed sources during the run period. Furthermore, an ion source from beam-line #2 was found to have an internal water leak and had to be removed for repair. Recently, a BL#1 source hose was identified as end of life (EOL) since it has been in use for over a decade and must be refurbished. During FY-18, one spare source was refurbished and tested and will fill the N2A open position for the next run. Two other source refurbishments have been started, with arc chamber assembly and accelerator alignments in progress. The present plan is to prepare 4 sources during the recovery outage in order to both replace the outdated source and to have three spares when operations resume.

During FY-18, the grid alignment machine was replaced and a grid rail alignment jig was developed to improve accuracy and maintain critical reference points. Source parts, including new Langmuir probes, were decontaminated and refurbished.

After plasma operations in 2016, both calorimeters were removed for repair and maintenance. In FY-17, both BL#1 and BL#2 calorimeter bellows systems were repaired and both drives were realigned. Repair of the BL#1 exit scraper began in FY-18, including removal, water line machining, and manufacture of new tubing to install on the plate. Prototyping of the brazing of the water lines is in progress. The calorimeters will await movement of the machine Center Stack so they can be staged in the South High Bay for lifts into position in the beamlines.

Repair of the damaged NBI #1-A source isolation valve (SIV) was completed, as well as inspection of the B and C SIVs. Repair of a spare SIV was also completed.

Three helium screw compressors were rebuilt in FY-17, and they were re-installed and tested in FY-18. Also in 2018, replacement of all the helium refrigerator Cold Box thermocouple wells with diodes was completed, and the Cold Box was pumped down to verify that it is without leaks. Subsequently, the newly rebuilt compressor skid was used to pressurize the helium process lines to further test the diode welds. The test was successful.

Progress in FY-18 for other Neutral Beam work includes:

- Used auto-transformers will be tested in FY-18. The auto-transformer that was damaged during the FY 2016 run was repaired and returned to the site in FY-18.
- The NBI armor was leak tested. The quadrant with the leak has been removed and awaits replacement. This job started in FY-18 and will be completed in FY-19.
- Replacement of outdated electronic turbine controllers will begin, with some work to be completed in FY-19.
- Replacement of EOL fiber optic transmitters will begin in FY 2018 with some work to be completed in FY-19.
- Updating of the armor thermocouple scanner boards for higher voltage isolation will begin in FY 2018, with some work to be completed in FY-19.
- Maintenance and repair of power supplies and related electronics and spares will be performed in FY 2018, with some work being completed in FY-19.

## **2018 Progress in Heating Systems - RF**

Based on preliminary assessments of the budget requirement to support the NSTX-U recovery effort, only essential HHFW (High Harmonic Fast Wave) maintenance and documentation activities were carried out during FY2018. The HHFW control systems were recalibrated and numerous electronics repairs were performed to ensure the system can be recovered if future funding becomes available. Evaluation and testing of the ECH-PI system also took place during FY-18.

## **Power systems**

The NSTX-U experimental power systems are from the TFTR era, and many components are 30 to 40 years old. The Field Coil Power Conversion (FCPC) systems include 68 identical rectifiers (Transrex AC/DC Converters), and provide a total pulsed power capability of 1650 MVA for 6 seconds every 300 seconds. Similarly, the NSTX-U motor generators (MG) #1 and #2 are of the TFTR vintage, roughly 40 years old, and significant maintenance and refurbishments are needed to ensure the highest possible reliability.

### **FY-18 Progress in Power Systems - Motor Generator Systems**

The MG#1 set was maintained during FY-18 and supported FCPC coil test shots. Several problems arose and were corrected. The most significant problem consisted of the inability of the MG to switch to doubly-fed mode. An extensive troubleshooting campaign was undertaken that consisted of testing and performance verification of multiple cyclo-converter (CCV) circuit boards and input sensors. The problem was found to be faulty switch connections that caused a loss of the reference signal for one of the two series drives of the C phase cyclo-converter.

## **FY-18 Progress in Power Systems - Field Coil Power Conversion**

The Field Coil Power Conversion coil test facility was designed to accommodate the power, water cooling, and instrumentation needs for testing the prototype and all of the production coils. The FCPC performed coil testing using the machine divertor coil PF1A Lower used during the 2016 run period. This coil was pulsed to full parameters without any issues. This work also verified the test facility's capability to perform the power tests of the prototype coils. The prototype coil power testing of the ETI and PPPL coils was completed in June 2018 utilizing this test facility. The test stand for mounting the coil was reused with minor hardware additions to allow for fastening of mandrel-less coils. An extensive maintenance activity has started on rectifier mechanical Pringle switches, used to connect individual converters into the coil power circuit or to bypass the converter from the circuit. Mechanical operational adjustments will be performed for switch travel and contact pressure with contact resistance measurements.

## **Central I&C**

The central instrumentation and control (CI&C) systems provide key functions for plant control, data acquisition, and data archival. These systems are critical for the synchronization of all NSTX-U functions during the shot cycle, as well as support for data users.

## **FY-18 Progress in Central Instrumentation and Control**

Central Instrumentation and Control continued to support testing and other activities where timing, data archiving, and display were required. These efforts included PF coil testing, motor generator testing, and general software and hardware development efforts. NSTX and NSTX-U data availability was maintained 99% of the time, which allowed the review of coil testing data and analysis of existing data by NSTX-U scientists and collaborators.

A facility upgrade to accommodate the forthcoming NSTX-U instrumentation system and diagnostic systems was completed in the diagnostic Data Acquisition Room (DARM). A new networking technology, Course Wave Division Multiplexing (CWDM) was tested and is now undergoing long term testing by PPPL network engineers. This equipment will enable the use of a single existing fiber for up to 16 Ethernet connections in the test cell.

Plans were reviewed and made to replace obsolete Computer Automated Measurement and Control (CAMAC) hardware in the D-Site pump house and in the two Radio Frequency (RF) areas still using existing hardware or common Programmable Logic Controllers (PLCs). The additional effort to design, test, and procure a prototype CAMAC replacement system and subject it to conditions present in the NSTX-U test cell was successful, and the replacement will be available for off-site radiation and field testing by the end of FY-18. Plans to replace obsolete Experiment Physics and Industrial Control System (EPICS) servers and software began in FY-18, and the preliminary design work will be completed before the end of the fiscal year.

## Real-time Control and Protection

The Real-time Control and Protection (RTCP) systems provide functionality for controlling NSTX-U during operation, and protects the experiment from substantial failures. Broadly speaking, this is achieved by measuring a large number of system parameters using data acquisition hardware. The measured data are sent via a specific data network to separate real-time computers that execute software for control and protection. For the control functions, the results of the performed control calculations are sent back to actuators in the system, e.g., the rectifiers that drive the plasma shaping coils. For the protection functions, the performed calculations result in issuing a fault signal that safely stops an ongoing plasma shot and prevents any further shots until the fault has been reset following strict operational procedures.

### FY-18 Progress in Real-time Control and Protection

Work for RTCP during FY-18 was mostly centered on design and implementation of hardware components that perform data acquisition and data transmission. It had been previously determined that three of the main acquisition components required more spare components than were available. Because of component obsolescence, changed technical requirements, and the more stringent Quality Assurance Program Description (QAPD), providing spares could not be accomplished simply by purchasing more modules. Redesign of all components was required.

Design work for one of the components was completed, had its FDR in August, and will be followed by prototyping. Work for the other two main components and one minor component was scheduled and is underway. The engineers working on the data acquisition hardware also performed a detailed hand-over of the related design documentation, operating procedures, and other related documents. This was triggered by the fact that two very senior electronics engineers left the lab.

In addition to reasonably well defined electronic design work for existing systems, investigation of an additional protection system to prevent damage through arching on the coils or turn-to-turn faults within the coils began in FY-18. The investigation is ongoing, and it is not clear at this point if protection can be achieved with a real-time system that determines failure during a shot, or if a system that performs trending of measured electrical parameters over the series of shots is sufficient and more cost-effective.

Finally, work began to update existing manuals for the control and protection systems. The reason for the update was to satisfy the new set of laboratory procedures, to mitigate the effects of personnel changes, and to prepare for the upcoming commissioning phase.

## Procedures and Training

During the assessment and initial planning for the implementation of DOE O 420.2c *Safety of Accelerator Facilities*, it became clear that a large scope of technical procedure updates and operator training will be required before operations. The procedure updates are, in some cases,

related to new requirements imposed by the Accelerator Safety Order (ASO). Other updates are motivated by technical changes to systems during the Recovery outage or by changes associated with the new Quality Assurance Program Description (QAPD). Updates to operator training are motivated by the same set of change drivers; new staff brought onto the project to return the operations team to full coverage will need a complete regimen of training. Further, or both procedures and training, the mandatory 3 year review cycle will pass from when NSTX-U last ran so full revisions and retraining are required.

### **FY-18 Progress in Procedures and Training**

During FY-18, the list of procedures that need updating was completed and triaged. The larger procedures and training programs will be revisited in the context of the larger ASO implementation. Some initial procedures began the update process at the end of the fiscal year.

# NSTX-U Facility and Diagnostics

NSTX-U had two facility and diagnostic milestones in FY2018:

- F(18-1): Evaluate PFC operational limits and develop integrated diagnostic plans for operations
- (Incremental) Diagnostic Milestone ID (18-1): Install and commission Far Infrared Tangential Interferometer / Polarimeter diagnostic system.

Summaries of these milestones are provided below:

## **F(18-1): Evaluate PFC operational limits and develop integrated diagnostic plans for operations**

*Description: The NSTX-U Recovery Project is developing new plasma-facing components (PFCs) for use in the divertor of NSTX-U. The extreme conditions of the NSTX-U divertor make it possible to stress even graphite surfaces to the material limits, leading to the possibility of component failures. In addition, the complex, mixed-material environment of the NSTX-U due to the use of boron and lithium wall conditioning techniques creates significant uncertainties in the monitoring of the PFCs. To assist in planning for initial and high-performance operations, it is advantageous to determine the design limits that will ensure reliable operation. It is also necessary to assess and redesign several edge-plasma diagnostic systems that must integrate with the new PFC designs. The goals of this milestone are three-fold:*

- *Test stress-limited PFC design features (potentially to destruction) and test high-temperature plasma-surface interactions that might result in operational temperature limits using e-beam and linear plasma-materials test facilities, respectively;*
- *Redesign boundary diagnostics and actuators affected by PFC design modifications (e.g. Langmuir probes, gas injection, spectroscopic views, or IR thermography);*
- *Assess and develop the technical and engineering basis needed to effectively measure and monitor the performance of the PFCs, based on experimental test results.*

*Status:* In FY-18, several different sets of tests were carried out to evaluate the type of graphite to be used in each area of NSTX-U. High heat flux (HHF) regions such as the Inboard Divertor Horizontal (IBDH) and rows 1 and 2 of the Outboard Divertor (OBD 1,2) will be exposed to high heat fluxes via an Electron Beam (EB) facility located at Penn State University. These HHF tiles were designed to be surface temperature limited such that graphite would sublime from the surface of the tile rather than the tiles cracking due to internal stresses. Other tile variants such as the far outer divertor (OBD 3,4,5), angled Center Stack (CSA) tiles, and the Center Stack First Wall (CSFW) tiles were limited to “minor modifications” of the NSTX-U or NSTX design. These do not attain the same level of thermal performance as HHF tiles. In certain cases, it is not possible to qualify the design by analysis due to complex contact between dissimilar materials. Mechanical testing is conducted in these cases such as the CSFW described below.

## Mechanical Testing of CSFW pin-mounted tiles

A design was proposed for mounting the CSFW (Center Stack First Wall) tiles to the casing using Inconel brackets, nut caps and 4 pins. At the PDR, it was recognized that CSFW tile should be qualified with testing prior to FDR, as "contact stresses" reported for tiles did not meet NSTX allowable. Worst case load for these tiles are EM loads that cause the tile to slide up and down on the casing due to halo current strike event. Thermal-Mechanical analysis reported stresses at the tile and pin interfaces were higher than  $\frac{1}{2}$  x ultimate strength of material selected. As graphite is a brittle material, per NSTX criteria the stresses should be below half of ultimate strength of the material. These stresses are due to temperature gradient in tile and long pin bending making a small, localized contact with tile. These contact stresses are "Hertzian Contact stress," and it is difficult to report a FEA solution that has converged. This testing relates to building a full scale tile prototype and testing a tile under operational loads.

This testing, if successful, gives us assurance the tile would not fail during operation, even though the FEA results reported are higher than allowable. These results will be presented at the FDR to qualify the tile for the operational loads and also to predict the failure load and mechanism.

The existing tile material POCO<sup>TM</sup> was used to make 10 tiles to load in tension, first under static and then under fatigue load. Five tiles were taken from billet K3255 and five from billet K324. The tiles from billet K324 include a taper at the pin holes. The tile fixture is shown in Fig. F18-1.1 and a loaded sample is shown in Fig. F18-1.2.

Combined thermomechanical and electromagnetic analysis in ANSYS was used to determine the maximum pin loading that would be expected during NSTX-U operation. Use of all four pins in a test, as would directly mimic the ultimate design, represents an over-constrained problem, and finite manufacturing tolerances would not allow direct comparison of any test to a reasonable analysis. Instead, the maximum pin stress was applied using the minimum number of pins to hold a tile in place as shown in the fixture of Fig. F18-1.1. this eliminated uncertainty in the applied load due to manufacturing tolerances.

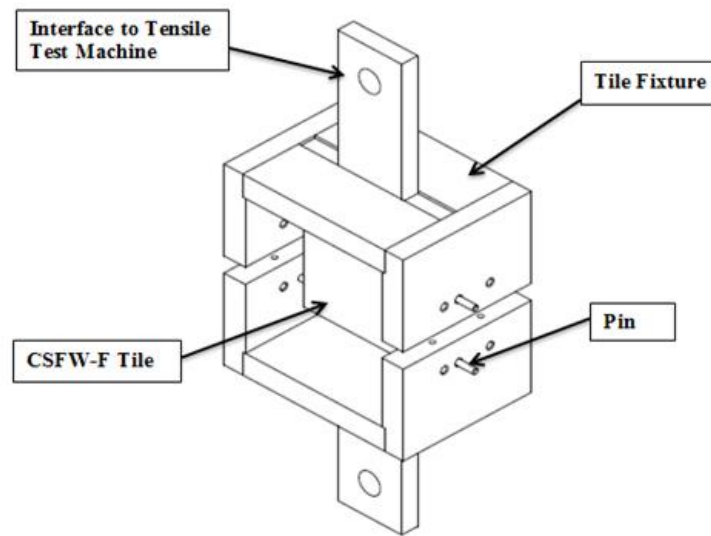


**Fig. F18-1.1:** Pin-test fixturing system with labels on key components. Ref. Drawing EDC11069.

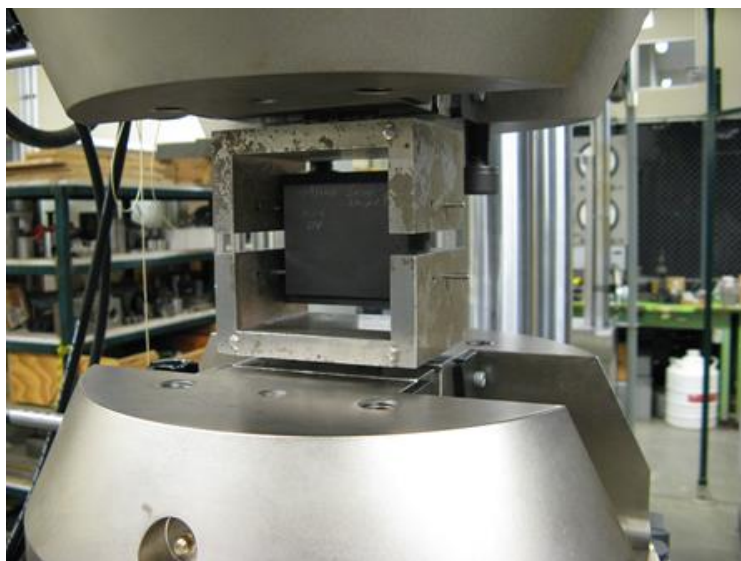


**Fig. F18-1.2:** Static test setup with tile sample 1 mounted in fixture.

Static and cyclic loading was conducted on the samples, originally, up to 22000 cycles. (An example is shown in Fig. F18-1.3.) It was later determined in NSTX-U-RQMT-RD-003-01 that a full test to 22000 cycles is very conservative. This was counterbalanced by a revised analysis that showed the original test load was 14% lower than the latest analysis indicated. The new maximum load of 350N was experienced on pin 5 of the bolted tiles as shown in figures F18-1.4 and F18-1.5, respectively. In addition, the test fixture allowed a significant amount of flex between the metal “yoke” and the graphite test specimen whereas the actual design had a metal frame component very near to the graphite that would limit flexure. As a result, tests will be repeated to the new shot spectrum with the upgraded load and with the modified test fixture.

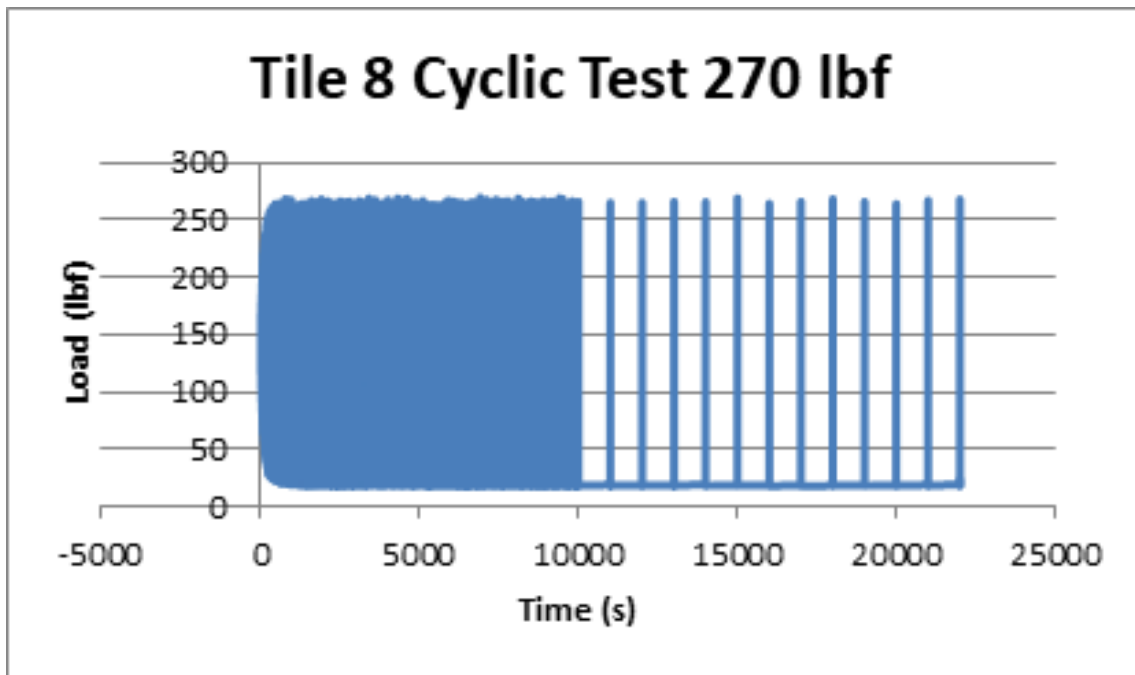


Fig. F18-1.3: Example cyclic testing data output showing survival of the component to 22000 cycles at 270 lbf load.

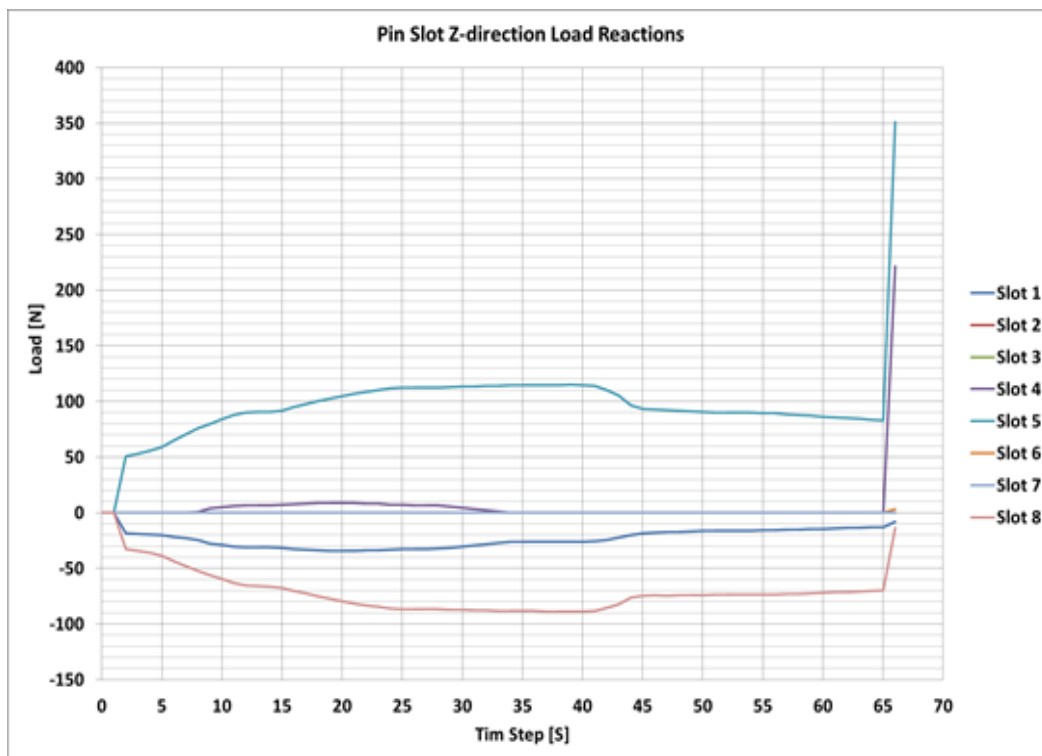
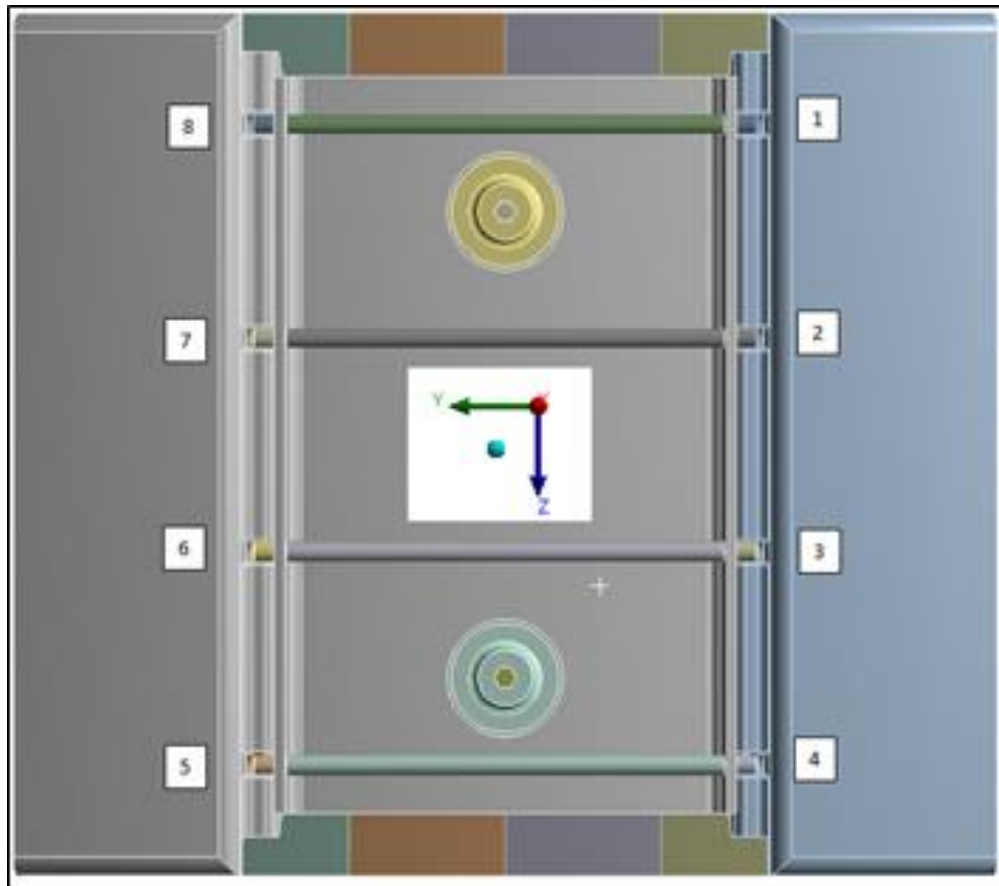


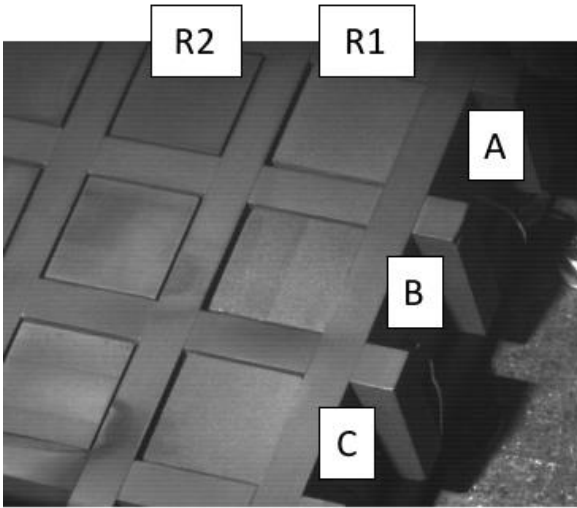
Fig. F18-1.4: Combined thermomechanical and electromagnetic analysis indicating the maximum pin contact force is 350N.



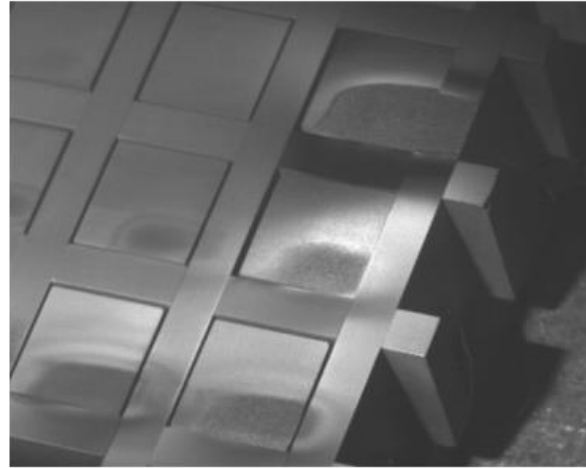
**Fig. F18-1.5:** Pin contact location reference. Data in figure F18-1-4 shows that the contact stress is greatest in pin 5 (lower left corner).

## Material Evaluation Experiments

A set of experiments were designed to expose specific blocks of graphite in a graphite test rig to the 17 kV electron beam available in the EB facility. (A portion of the test rig is shown in Fig. F18-1.6.) The electron beam was positioned onto each graphite block at low current. The graphite test rig, which was made of POCO™ graphite, contained three samples of six different types of graphite. Each graphite sample was cut to 1" x 1" x 1.5" to fit in the test rig. Each grade of graphite was placed in a row of the test fixture (R1, R2, and up to R6) while each column in the test rig was exposed to different electron beam currents,  $I_{\text{beam}}$  ranging from 380 mA up to 1235 mA. Figure F18-1.6 shows images of the individual graphite blocks installed in the test rig before and after exposure to the electron beam. The six grades of graphite tested were POCO™, R6510, R6710, ATJ, Mersen 2124 and FMI CFC. Each graphite sample was only exposed to the electron beam once. Full details on the material evaluation experiments can be found in MEMO: PFC-171113-MAJ-02[F18-1-1].



20171107\_1501\_Row1\_Before



20171107\_1752\_f04\_Row1\_After

**Fig. F18-1.6:** Before and after images of the first row of samples. The before images are annotated to indicate the column (A, B, or C) of the sample. In the image on the right (after), the beam currents applied were C) 593 mA, B) 486 mA, and A) 433 mA. In this particular test, an additional high-power pulse was applied to Column A to test the thermocouple calorimetry. This last step was not repeated on any other material samples.

Only half of the exposed graphite face was exposed to the electron beam, as seen in the after image in Fig. F18-1.6. This was done to increase the internal stress of the graphite during electron beam exposure. The intended goal was for the graphite blocks to fail mechanically due to internal compressive stress. However, even at 1235 mA of beam current, which corresponds to approximately  $65 \text{ MW/m}^2$  of incident heat flux, no large-scale fracture was observed in any of the graphite samples tested. Instead, ablation of graphite from the surface was observed, as seen in Fig. 18-1.6. The ablation damage was ordered for each grade of graphite and incident beam current. This data is summarized in Table F18-1.1. It should be noted that every graphite sample ablated for  $I_{\text{beam}} \geq 486 \text{ mA}$ , while no ablation was observed at the lowest beam current tested of 380 mA. Based on these experiments, R6510 and the FMI CFC samples showed the best qualitative performance since they showed no ablation at  $I_{\text{beam}} = 433 \text{ mA}$ , when all the other graphite grades showed ablation at similar  $I_{\text{beam}}$ .

Based on this testing, R6510 remained the material of choice for further engineering analysis and further high heat flux testing. While FMI CFC also performed as well as the R6510, it was ruled out as a candidate material due to the long lead time needed to manufacture and the substantially higher cost than isotropic graphite. Further, the experience of material testing showed that the EB facility at Penn State University could, in fact, be used for high heat flux testing of prototype PFC tiles as long as sufficient instrumentation was used to quantify the incident electron beam power deposited into the graphite.

Material	1235 mA (65 MW m <sup>-2</sup> )	806 mA (43 MW m <sup>-2</sup> )	593 mA (31 MW m <sup>-2</sup> )	486 mA (26 MW m <sup>-2</sup> )	433 mA (23 MW m <sup>-2</sup> )	380 mA (20 MW m <sup>-2</sup> )
POCO	Red	Red	Red	Red	Red	Green
R6510	Red	Red	Red	Red	Green	Green
R6710	Red	Red	Red	Red	Yellow	Green
ATJ	Red	Red	Red	Red	Yellow	Green
Mersen 2124	Red	Red	Red	Red	Yellow	Green
FMI CFC	Red	Red	Red	Red	Green	Green

**Table F18-1.1:** Summary of observed damage to material samples for given beam currents after 8s exposure. Red indicates visible, serious damage to the front-surface, orange indicates minor blemishes, and green indicates no visible damage after exposure. The requested beam current is shown and the nominal heat flux for this beam current over a 12x25mm surface area is shown in parenthesis.

## Heat Flux Quantification and Tests of Integrated PFC Diagnostics

To determine if the EB facility would be suited for quantitative HHF testing, collaborators from Oak Ridge National Laboratory led a second experimental campaign. A castellated POCO™ graphite target, shown in Fig. F18-1.7b, was designed with each castellation instrumented with a type-K thermocouple at either 0.24” or 0.48” below the surface. While the prototype NSTX-U PFC tiles were castellated as well, this target design was de-optimized for stress handling for the purposes of testing: castellation surface areas are nearly twice as large and ~70% the thickness compared to NSTX-U designs. The target is shown installed in the EB facility in Fig. F18-1.7a with a POCO™ graphite shield to protect thermocouple wires as they exited the target, and a copper baseplate for structural support of the target/shield and to increase the thermal mass and heat transfer out of the graphite. This assembly was placed on alumina stand-offs and the copper plate was grounded to the EB facility ground.

To quantitatively measure the incident heat flux from the electron beam, an IR camera (FLIR SC4000 350x256 pixels, 30 Hz) was installed on top of the EB facility with a perpendicular view of the instrumented target. The IR camera was calibrated ex-situ using a blackbody source and the ZnSe viewport that was later installed on the EB chamber. To determine surface temperature,  $T_{surf}$ , an emissivity of 0.77 was assumed as specified by the manufacturer. The calibration was limited since the blackbody calibration source was limited to temperatures < 1200°C, and an in-situ calibration wasn’t possible. However, during experiments, surface temperatures exceeding 1200°C were measured. In these cases, the blackbody calibration was linearly extrapolated and assumed to be valid.

It was desired to deposit heat flux onto the target similar to what is expected under normal operating conditions in NSTX-U. Therefore, the instrumented target shown in Fig. F18-1.7b was exposed to an electron beam current,  $I_{beam} \sim 100$  mA to manually adjust the beam positioning

and develop the desired heat flux pattern to be deposited while minimizing target heating. Two deposition patterns were developed in accordance with NSTX-U heat flux requirements. Similar to use on DIII-D[F18-1-2], a straightforward means to specify requirements is to use a heat flux that decreases linearly over a radial extent. One with a larger extent of ~ 15 cm represents high performance discharges in NSTX-U with large poloidal magnetic flux expansion,  $f_{exp}$ . Another deposition pattern was developed with an extent of ~ 4 cm for NSTX-U scenarios with low  $f_{exp}$ . Once the deposition pattern was established at low current,  $I_{beam}$  was scanned up to 1500 mA in 250 mA intervals. The diagnostics were triggered manually 1.0 sec before the electron beam was initiated. The timing of the electron beam exposure time was also controlled manually. For these experiments, 10 sec exposures were used for all e-beam shots in contrast to an expected 5 sec maximum for NSTX-U plasmas.

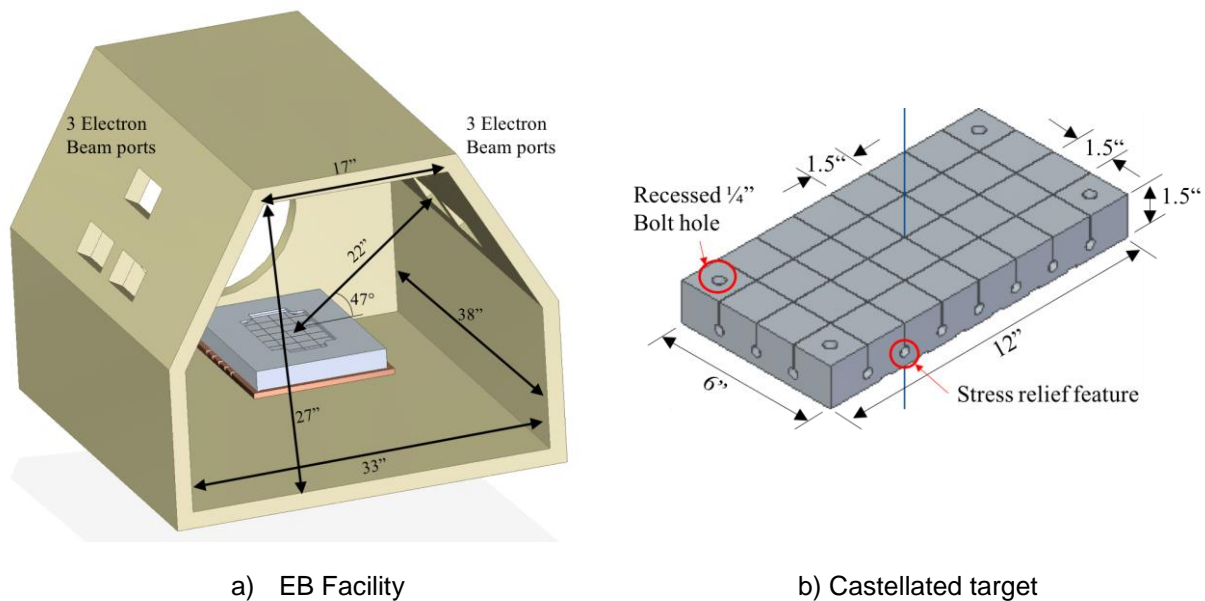


**Fig. F18-1.7:** a) CAD model of the Electron Beam (EB) Facility showing ports for the electron beams and the placement of the instrumented target for exposure. b) CAD rendering of the instrumented, castellated POCO™ target.

The thermocouple response ( $\Delta T_{TC} = T_{TC}(t) - T_{TC}(t = 0)$ ) to a 15 cm extent exposure is shown in Fig. F18-1-8a, along with the castellation averaged surface temperature measured by IR. A 6 Hz beat frequency between the IR camera frame rate (30 Hz) and the electron beam raster rate of 10 Hz is apparent in the raw IR measurement. A moving average is used to smooth the data, also shown in Fig. F18-1.8a, before direct comparison to the thermocouple data. Given the assumptions made and the limitations of the calibration discussed earlier, the error in the filtered IR measurement of  $T_{surf}$  is assumed to be linearly related to the peak-to-peak variation in  $T_{surf}$  of the unfiltered IR estimation of  $T_{surf}$ . This assumption results in estimated error in  $T_{surf}$  of  $\pm 10^\circ\text{C}$  based, on the variation in the unfiltered IR measurement.

Excluding data where there is indirect evidence of the target was ablating [F18-1-3] – therefore not all of the incident electron beam energy being deposited into the target – a comparison

between the  $\Delta T_{TC}$  and  $\Delta T_{surf}$  is shown in Fig. F18-1.8b. Here it is shown that all thermocouples, regardless of depth below the surface, behave linearly with respect to  $\Delta T_{surf}$ . This indicates that individual castellations can be treated as semi-infinite solids for the spatial and time scales of these experiments, which are expected to reflect NSTX-U operational conditions. This is a positive result for PFC monitoring approaches that rely on model validation using subsurface temperature measurements as described in the R(18-1) milestone.

Using the  $\Delta T_{surf}$  measurements to determine the incident heat flux, the energy deposited  $E_{dep}$  into each castellation can be found by integrating over the area of the castellation and in time. Required operational use on NSTX-U conservatively assumes that the TC signal will be polluted by electromagnetic interference during the plasma discharge, but the total  $\Delta T_{TC}$  can be accurately determined.  $E_{dep}$  is linear with respect to  $\Delta T_{surf}$  since the duration of each exposure was constant at 10 sec. Therefore,  $\Delta T_{TC}$  is also linear with respect to  $E_{dep}$ . A linear fit – with the constraint of a zero intercept – of  $\Delta T_{TC}$  to  $E_{dep}$  yields:

$$\Delta T_{TC} [^{\circ}C] = 14.3 E_{dep} [kJ],$$

where  $\Delta T_{TC}$  is given in  $^{\circ}C$  and  $E_{dep}$  in kJ. This gives a sensitivity of the thermocouple to deposited energy of  $70 J/^{\circ}C$  regardless of thermocouple depth below the surface of the target for  $0 < E_{dep} \leq 30$  kJ. This implicitly assumes that the thermocouple is located higher in the target than the stress relief feature.

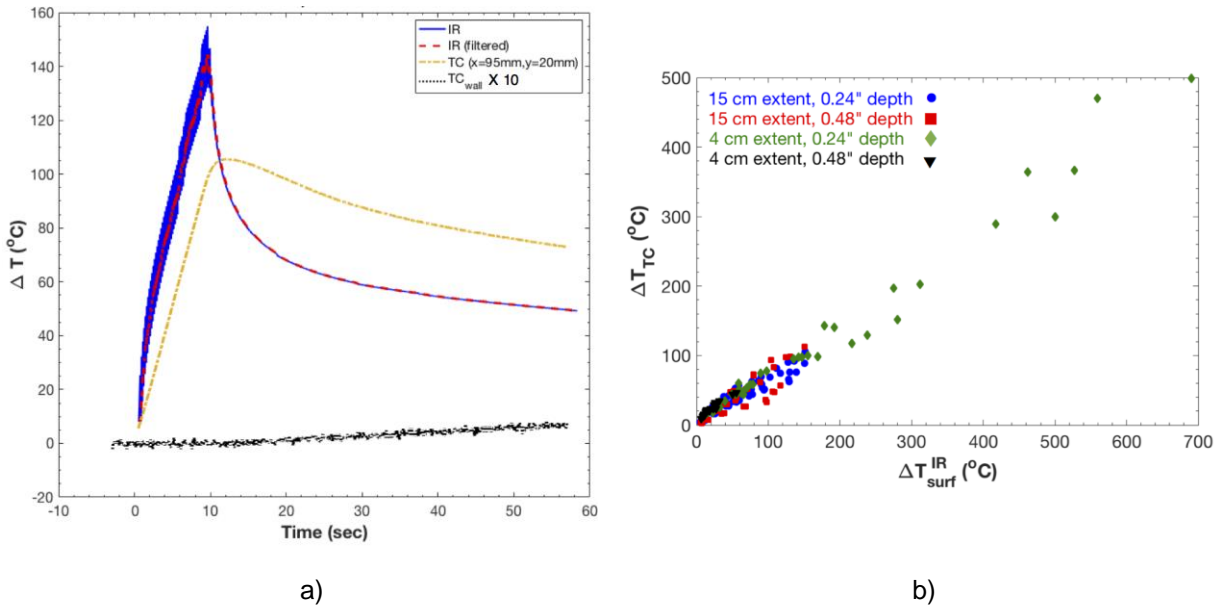


**Fig. F18-1.8:** a) Shows the typical time trace of the change in temperature,  $\Delta T$  for an embedded thermocouple and  $\Delta T_{surf}$  measured by IR camera for a given castellation and b)  $\Delta T_{TC}$  versus  $\Delta T_{surf}^{IR}$  for  $0 \leq E_{dep} \leq 30$  kJ for all deposition patterns and thermocouple depths.

Measurements of  $\Delta T_{TC}$  show a linear relationship with  $\Delta T_{surf}$ , when the shots with ablation were discounted. This linear relationship, regardless of thermocouple depth below the target surface, indicates that a semi-infinite heat conduction model for individual castellations is appropriate on time scales of interest, assuming the thermocouple is above the stress relief feature of the castellated target. It also indicates that individual castellations can be used as calorimeters to measure incident energy deposited by the plasma. When used as calorimeters, individual castellations have a sensitivity of 70 J for every 1°C of temperature rise measured. This was verified for a range of deposited energy up to 30 kJ on an individual castellation.

## Prototype PFC Heat Flux Tests

Plans have been made to expose prototype PFC tile variants of the IBDH and OBD12 designs in the EB Facility at Penn State University in September 2018 using the diagnostics described above. The prototype tiles will be made out of POCO™ graphite, which is the engineer's second choice material, since insufficient quantities of Sigratine R6510 will be available to manufacture prototype tiles. Both the IBDH and OBD12 tile variants will be heated by the electron beam with a range of heat fluxes and deposition patterns. The thermal performance of the prototype tiles will be compared to ANSYS simulations to verify the design assumptions and analysis of the prototypes. Unlike previous experiments, these tests will include a high temperature ( $T_{surf} \geq 2000$  °C) in-situ calibration in the EB facility with POCO™ and R6510 graphite calibration targets to match the viewing geometry, material properties, and emissivity of the graphite to be tested.

## References

[F18-1-1] MA Jaworski and TK Gray, "HIGH-HEAT FLUX TESTING REPORT 1: MATERIAL SURVEY RESULTS." NSTX-U MEMO: PFC-171113-MAJ-02 (2017).

[F18-1-2] C. J. Murphy, et al., Fus. Sci. and Technol. **52:3**, (2007) 539-543, DOI: 10.13182/FST07-A1544.

[F18-1-3] TK Gray, et al., "Integrated plasma facing component calorimetry for measurement of shot integrated deposited energy in NSTX-U Spherical Torus." Accepted for Rev. Sci. Instrum. (2018).

## **(Incremental) Diagnostic Milestone ID (18-1): Install and commission Far Infrared Tangential Interferometer / Polarimeter diagnostic system.**

*Description: A new Far Infrared Tangential Interferometer / Polarimeter (FIReTIP) will be installed on NSTX-U and commissioned. The FIReTIP system was developed by UC Davis to measure line-averaged plasma densities. This system uses a carbon dioxide laser to pump a methanol laser to create the far infrared beam needed for NSTX-U plasma densities. The system includes a new real-time vibration compensation capability to enable the FIReTIP signals from a central chord to be used for future real-time density feedback control. Commissioning activities will include insuring that the lasers and data acquisition capabilities are operational for the FIReTIP diagnostic, and testing of the vibration compensation system. This milestone will only be carried out if sufficient resources are available.*

Installation of the FIReTIP diagnostic was partially completed and then suspended to allow the resources to be used on higher priority recovery project work. The waveguide was installed over most of its length, leaving only a short run to the optics box to be completed. The optics box was prepared for installation and an installation package of procedure and drawings was prepared, but the optics box was not installed. Fabrication of the mixer table was completed, and an installation package of procedure and drawings was also prepared. The mixer table was not installed. It should be straightforward to complete installation of the optics box and mixer table in FY2019 if the required resources are available at UC Davis and PPPL.

# NSTX-U Research Program

In FY2018, the NSTX-U research team contributed experimental data, analysis, and leadership in support of the 2018 DOE Joint Research Target (JRT) milestone:

*Conduct research to test predictive models of fast ion transport by multiple Alfvén eigenmodes.*

*Fusion alphas and injection of energetic neutral particle beams provide an important source of heating and current drive in advanced tokamak operating scenarios and burning plasma regimes. Alfvén eigenmode (AE) instabilities can cause the redistribution or loss of fast ions and driven currents, as well as potentially decreasing fusion performance and leading to localized losses. Measured fast ion fluxes in DIII-D and NSTX-U plasmas with different levels of AE activity will be used to determine the threshold for significant fast ion transport, assess mechanisms and models for such transport, and quantify the impact on beam power deposition and current drive. Measurements will be compared with theoretical predictions, including quantitative fluctuation data and fast ion density, in order to validate models and improve understanding of underlying mechanisms. Model predictions will guide the development of attractive operating regimes.*

## NSTX-U Research Results – FY-18 Milestones

### **R(18-1): Develop and benchmark reduced heat flux and thermo-mechanical models for PFC monitoring**

*Description: The NSTX-U Recovery Project will deploy new plasma facing components (PFCs) to meet updated heat exhaust requirements driven by narrower scrape-off-layer widths, increased heating power, and longer pulse durations relative to NSTX. Inter-shot monitoring or intra-shot control of heat flux to PFCs is anticipated for a range NSTX-U operating space, necessitating reduced models that can be run between shots or even in real-time. Monitoring requires a reliable instrumentation suite which can support or contradict model predictions and confirm PFC integrity. The goals of this milestone are three-fold: (1) Develop tools for pre-shot planning and confirmation of post-shot PFC thermal observations which use reduced models to predict time-evolving heat fluxes to shaped PFCs and estimate distances from engineering limits. Assess additional effort needed for implementation of reduced models in PCS. (2) Where feasible, benchmark reduced models against boundary physics (e.g. SOLPS, UEDGE) and finite element analysis (e.g. ANSYS) tools, and validate using experimental data from relevant tokamaks and results from Facility Milestone F(18-1). (3) Evaluate examples of discrete monitoring systems that are sufficient to capture the evolution of the PFCs relative to engineering limits. Compare the ability for different techniques (e.g. thermocouples vs. imaging) and technologies (e.g. near vs. long-wave infrared cameras) to achieve NSTX-U PFC monitoring objectives.*

The work completed under this milestone was organized and executed as part of NSTX-U's PFC Performance and Monitoring Requirements Working Group (PFCR-WG). This resulted in resource availability and research needs being linked to the evolution of the Recovery project during FY-18. More detailed information regarding work completed is available on the Working

Group [website](#), and will be summarized in a Milestone Report to be completed at the end of FY-18. Achievements are summarized within the three goal areas in the text.

*R(18-1) - Goal 1: Develop tools for pre-shot planning and post-shot confirmation*

One of the primary means for pre-shot planning is predictive modeling of stationary or time-evolving heat flux on the PFCs. This has previously been done using individually created equilibria from GEQDSK files and a model for surface heat flux assuming axisymmetric plasma and axisymmetric wall structures. These tools were combined in an IDL GUI environment as the [W\\_PFC](#) widget, which was used in late FY-17 to scope the initial PFC heat flux requirements. More detailed designs of the PFCs revealed that non-axisymmetric structures are expected, both from intentional shaping to avoid leading edges, e.g. fish-scaling, or from having an axisymmetric surface approximated as multiple planar surfaces; e.g. faceting, similar to the outer divertors of NSTX-U. These are known to create 3D variation of heat flux, even from an axisymmetric plasma, and a goal was to evaluate software options for NSTX-U. Two existing codes were considered: PFCFlux [M. Firdouss, JNM v438 pgS536 (2013)], and SMARDDA [W. Arter IEEE Trans. Plasma Sci. v42 pg1932 (2014)]. Another was developed internally as part of this milestone by Andreas Wingen of Oak Ridge National Laboratory that exploited the existing MAFOT field line tracing code [A. Wingen, NF v49 pg055027 (2009)]. In early FY-19, the PFCR-WG will make a recommendation on which tool(s) to use to further support post-Recovery operations. Investigations using SMARDDA are still underway and are expected to be completed by the end of FY-18. In December 2017, the CEA team (M. Firdouss) volunteered to generate PFCFlux output for the NSTX-U case to demonstrate the code. This successfully showed this tool is capable of providing the needed 3D heat flux prediction, although further usage at PPPL would require a collaborative agreement between the two labs.

There is a more detailed description of ORNL's MAFOT-based code, which helps to demonstrate some of the challenges associated with this class of tools. The CAD model, exported from the NSTX-U design group, is imported as an STL. It is shown in Fig. R18-1.1 with hundreds of thousands of faces, so the initial challenge is identifying which are of interest for heat loading. While the "top" surface of the PFCs can be found reliably, in some cases edges at toroidal and poloidally running gaps are more difficult to identify and this hasn't been implemented in the ORNL tool yet. A GUI interface could be developed, but this type of task has already been completed in codes like PFCFlux. Once the surfaces are identified and further discretized, field line tracing is initiated from each sub-domain of the PFC surface. If the field line intersects another PFC surface, the area will have zero heat flux. (See the shadowed regions as shown in Figure R18-1.1. Otherwise, the field line is traced to find its minimum poloidal flux and is assigned a parallel heat flux. The surface heat flux is determined by the local calculation of the surface normal with the field line angle,  $q_{surf} = q_{\parallel}(\hat{n} \cdot \hat{B})$ .

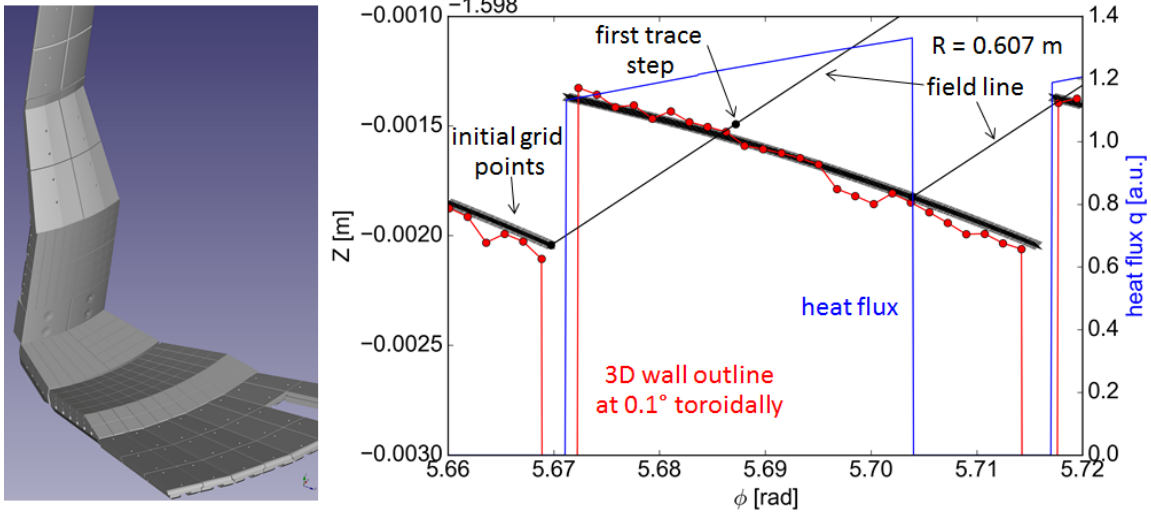


**Fig. R18-1.1:** The 30-degree sub-sector of the NSTX-U CAD geometry (left) and an example of how the field line tracing is completed to find shadowed regions of the PFCs (right).

Example outputs of this code are shown in Fig. R18-1.1 and R18-1.2 which highlight important non-axisymmetric heat flux features. R18-1.2 shows the outer target in a LSN L-mode with weak flux expansion, resulting in a poloidally narrow footprint. These types of scenarios will require strike point sweeping. The CAD tool shows a toroidally varying heat flux resulting from the faceting of the OBDR4 surface that caused ~33% increase in heat flux from one side of the facet to the other. Also noticeable are the white “holes,” both for fasteners and for a gap near  $\phi = 5.9$  rad which is used for diagnostics. There will be heat flux enhancements in this location, but it requires a more sophisticated code which can identify the relevant sides of various features.

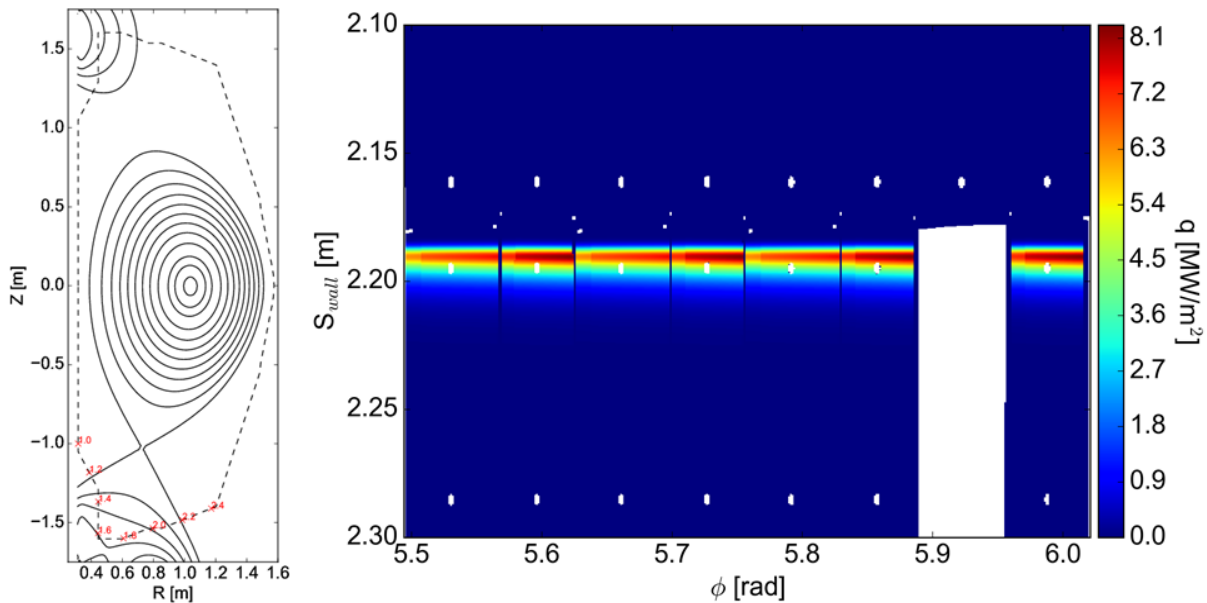


**Fig. R18-1.2:** Example of the output of ORNL's 3D heat flux code for the outer divertor for a LSN L-mode shot.

An H-mode shot, which heats the interface between the IBDH and OBDR1, is shown in Fig. R18-1.3. In this model, the IBDH does not have any surface features and, therefore, is axisymmetric, while the OBDR1 has both the facing effect as well as inter-castellation fishscaling. This leads to a complex surface heat flux profile which varies toroidally within a castellation and has shadowed areas between them. Future work will be needed to connect the output of these types of simulations with the input of ANSYS or other thermal simulation tools.

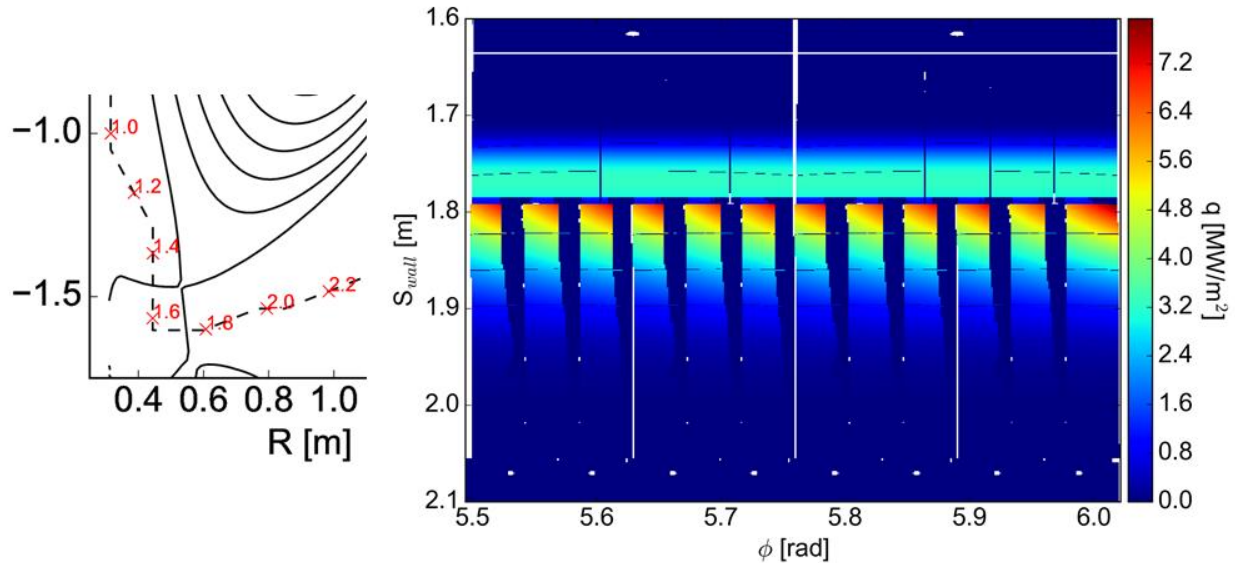


**Fig. R18-1.3:** Example output of ORNL's 3D heat flux code for the outer divertor for a DN H-mode shot.

To respond to a Recovery need to determine if leading edges should be eliminated on castellated tiles, a simplified model to estimate steady and transient (e.g. ELM, disruption) erosion was developed by ORNL (Reinke). For steady-state erosion of graphite, information from DIII-D [D. Whyte, JNM v266-269 pg 67 (1999)] coupled with JET data showed experimentally that erosion rates varied from 10-100 cm/ey (ey is an exposure year = 3.15e7 sec) for heat fluxes in the range of NSTX-U operation (~1-10 MW/m<sup>2</sup>). An admittedly crude estimate could be formed from the NSTX-U GRD shot spectrum which scaled the DIII-D results, indicating NSTX-U would erode graphite at (5,15,30,60) cm/ey for operation at (60,75,90,100) % of its peak performance. Treating this exposure as a “beam” that will be swept over the high heat flux area results in ~50 microns of erosion after completing 30% of the shot spectrum. While the total PFC thickness is large (> 5 cm), the feature sizes due to fishscaling can be small, of order 100-200 microns. If the tiles are worn unevenly, the leading edge avoidance could be compromised.

The effects of ELM-induced erosion were estimated to be sub-dominant to disruption induced erosion by using a recent multi-machine scaling (MAST, AUG, JET) [T. Eich, NME v12 pg 84 (2017)] for the peak parallel energy flux for an ELM:

$$\varepsilon_{\parallel} = 0.28 \pm 0.14 \frac{\text{MJ}}{\text{m}^2} \times n_{e,\text{ped}}^{0.75 \pm 0.15} \times T_{e,\text{ped}}^{0.98 \pm 0.1} \times \Delta E_{\text{ELM}}^{0.52 \pm 0.16} \times R_{\text{geo}}^{1 \pm 0.4}$$

where  $n_{e,ped}$  is in [ $10^{20} \text{ m}^{-3}$ ],  $T_{e,ped}$  is in [keV],  $\Delta E_{ELM}$  is in [%] and  $R_{geo}$  is in [m]. By taking a maximum NSTX-U pedestal pressure to be 25 kPa, results in  $p_{e,ped} = 0.78 [10^{20} \text{ m}^{-3} \text{ keV}]$  and taking the high end of the MAST-U observations of  $\Delta E_{ELM} = 6.6 \%$ , then a conservative estimate of  $\varepsilon_{||}$  that scales like  $p_{e,ped}$  would result in the parallel energy flux of  $0.58 \text{ MJ/m}^2$ . Assuming this impinges at the highest angle of incidence,  $\alpha = 5\text{deg}$  and  $0.1 \text{ ms} < \Delta t < 0.5 \text{ ms}$  durations, this would result in only 0.1-1.0 nm/ELM per the erosion scaling used below for disruptions. For 100 shots at this (very) high pressure with 100 ELMs/shot, this only amounts to 1-10 micron erosion.

The estimates for disruption erosion are strongly dependant on the transient energy pulse to the target, where the erosion rate (micron/shot) scales non-linearly with the plasma load, in  $\text{MJ/m}^2/\text{sec}^{1/2}$ . At values exceeding  $\sim 50 \text{ MJ/m}^2/\text{sec}^{1/2}$ , brittle destruction can occur resulting in loss of small particles (binder and grains in graphite [J. Linke, FED v66-68 pg 395 (2003)]), which also corresponds to short-duration,  $\sim 30 \text{ ms}$ , leading edge heat loading at high  $q_{||} \sim 300 \text{ MW/m}^2$ . For lower short pulse energy fluxes there is still a finite erosion loss according to laboratory plasma ELM simulation experiments. A substantial body of work from the 1990's and 2000's exists (when CFCs were still in consideration for ITER and ELM energy scalings were not yet known) which can be used to estimate the impact of disruptions on NSTX-U graphite PFCs. Experimental data of microns/event taken from [I.E. Garkusah, Phys. Scr. vT138 pg 014054 (2009)] for CFC were extrapolated smoothly down to from their reported lower bound of  $8.9 \text{ MJ/m}^2/\text{sec}^{1/2}$  where 0.01 microns/event were observed. This allowed an arbitrarily small NSTX-U disruption to still lead to an accumulation of loss of PFC.

A model was developed to estimate the  $\text{MJ/m}^2/\text{sec}^{1/2}$  from an NSTX-U disruption by using probability distributions for the amount of thermal and magnetic energy deposited on the target over an area and duration that can vary between events. This is described in more detail in PCFR-MEMO-22 (forthcoming), but requires a Monte-Carlo sampling of different run campaigns comprised of a defined number of discharges at different  $I_p$  and  $W_{TH}$ . Fig. R18-1.4 shows the probability of completing this campaign while being able to survive a certain level of erosion, indicating that somewhere  $\sim 100$  microns could be expected for a shot spectrum that is  $\sim 30\%$  of the expected NSTX-U lifetime.

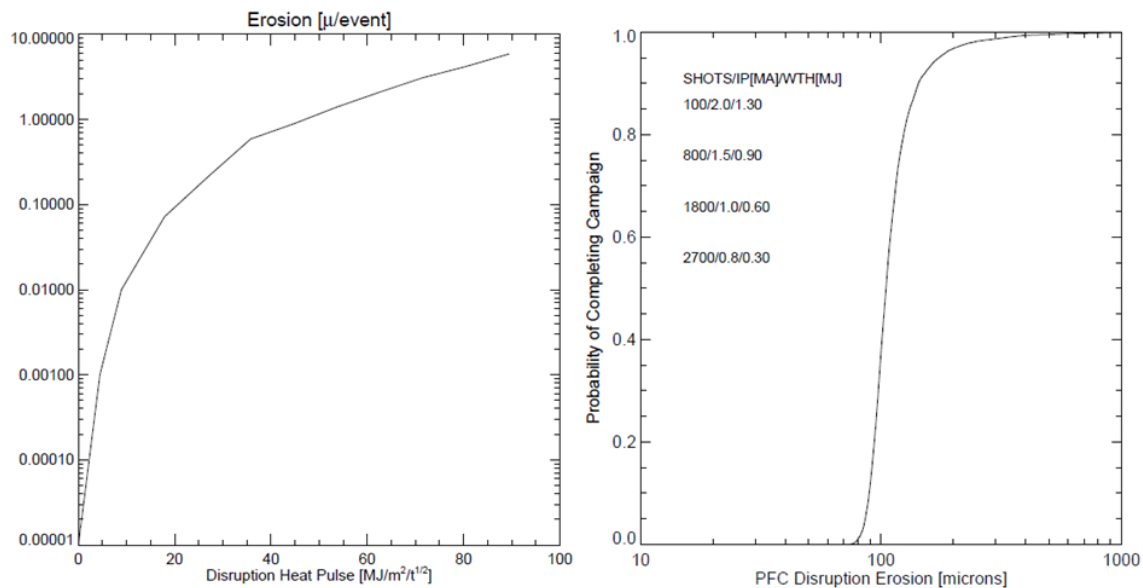


**Fig. R18-1.4:** The assumed erosion rate (left) and the estimated cumulative disruption induced erosion from the model described in the text (right).

Combined this erosion/ablation analysis resulted in a requirement of adding 0.003” (or 76.2 microns) to castellations, which was added to the most recent revision of the PFC Requirements. This was expected to be sufficient to make it through early campaigns after which experimental data would allow for direct evaluation as large uncertainties are present in all these calculations. This suggests an important early science and operations task of the NSTX-U Boundary Science team should be to catalog the achieved wear-rate of the high heat flux PFCs through metrology or more advanced techniques like surface holography. Discussions within the WG and with Recovery also identified the importance of studying the heat loads at toroidal gaps which will not be avoided in some areas by fish-scaling. Particle in Cell (PIC) codes have been identified as one means to explore these as discussed in [M. Komm, PPCF v55 pg 025006 (2013)].

The Simulink-based shape control simulation framework developed for R(18-2) was further developed for use as a tool to study strike point sweeping capabilities for heat flux management in long, high power discharges on NSTX-U. The simulation framework allows design of a linearized plasma response model around a selected equilibrium, which can come from EFIT for existing shots, or from the output of a TRANSP simulation for planning scenarios. A series of equilibria can also be chosen, resulting in a time-varying linearized plasma response model. Existing coil control algorithms, including the vertical control and ISOFLUX boundary control algorithms used on NSTX-U in FY16 were implemented as part of the ASC milestone work. In FY16, X-point radial and vertical position control was commissioned, along with control of the X-point height and position of the outer strike point. However, for heat flux management, it is desired to simultaneously sweep both the inner and outer strike points and to control the flux expansion at the strike point locations. Furthermore, the ability to simultaneously control the locations and flux expansion of each strike point requires simultaneous use of all four divertor coils (PF1A, PF1B, PF1C, and PF2), whereas only two were used for control in 2016. A multi-

variable control algorithm was developed to handle the coupled effect of the divertor coils on the strike point locations and flux expansion. In the algorithm, a constrained optimization algorithm is used to find the feasible combination of divertor coil currents (within current magnitude limits) that best matches the flux at the strike point targets to the reference values. Individual current feedback loops are then used to track the requests' divertor coil currents. Initial simulations of the approach have demonstrated strike point tracking concurrent with control of other shaping parameters, like midplane outer gap, and  $dr_{sep}$ . As evident in Fig. R18-1.5, strike point sweeping can introduce significant variation in the inner gap size. This variation can be controlled through selection of phasing and amplitude of the inner and outer strike point sweeping patterns. While the amplitude of the sweeps may be dictated by heat flux considerations, the phasing should be a free parameter to optimize in the design of the sweeping pattern.

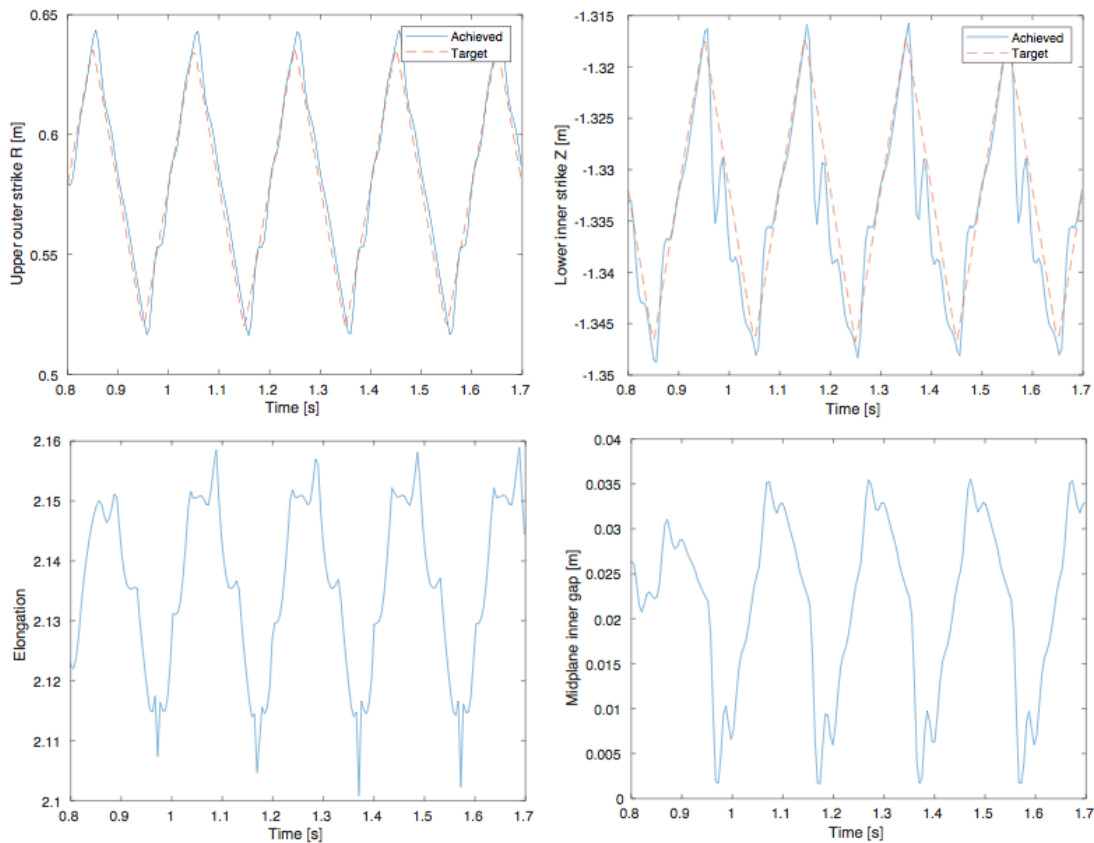


**Fig. R18-1.5:** Results of a strike point sweeping simulation showing tracking of the upper outer strike point  $R$  position and lower inner strike point  $Z$  position, as well as the effect of the sweeping pattern on elongation and midplane inner gap.

Once gains and sweeping targets have been found that satisfy shape control requirements, the simulated closed-loop evolution of the plasma equilibrium can be exported in standard formats for use in other tools. This developed as part of the milestone to evaluate the effectiveness of strike point sweeping strategies at mitigating the heat flux evolution. Iteration of this analysis could be used to develop optimized sweeping strategies for high heat flux scenarios.

An analysis of the real-time requirements of a possible future monitoring system is underway. Given that existing similar systems at other experiments were designed and implemented on computing hardware that predates NSTX-U's real-time control system, the current computational hardware is sufficient to perform algorithmic calculations. However, it is more advantageous to leverage advancements in technology to develop a modular system that is isolated from the primary control system and connected via a modern switched fabric. The expectation is to conduct initial processing on a dedicated computer or FPGA, and send reduced, processed data to the control computer in real-time. Additionally, the use of Camera Link and the micro-TCA form factor to interface to the imaging sensors aligns NSTX-U with recent developments at other experiments such as W7-X.

### R(18-1) - Goal 2: Benchmark reduced physics and engineering models

Limited progress was made under this goal due to changes in the needs and schedule of the Recovery Project. The original mission was to validate a physics model and analysis tool for predicting heat fluxes ( $W_{PFC}$ ), but this has been de-emphasized as the basis for setting the heat flux requirements for the IBDV, IBDH and OBD12. Presently, in NSTX-U-RQMT-SRD-003-01, the heat flux requirements for these regions are set by material properties of procurable graphite and manufacturing tolerances, assuming the PFCs are temperature limited with  $\Delta T = 1600\text{degC}$ . This would demonstrate that quantitative accuracy of the reduced physics and heat flux models was deemphasized. Further, following an initial Monte-Carlo style analysis of the impact of coil alignment in NSTX-U-DOC-101-00, it became clear that a conservative approach for the multiple parameters defining the heat loading is likely to be excessively conservative. If it is assumed that there is a probability distribution to quantities like the temperature limit ( $T_{lim}$ ), private flux spreading ( $S$ ), heat flux width ( $\lambda_q$ ), and radiated power fraction ( $f_{rad}$ ) - which in the original requirements were simultaneously set to be conservative - then the probability distribution of predicted heat fluxes is rather wide and has a very small likelihood of achieving the peak heat flux used in the original draft of the PFC heat flux requirements. An example is shown in Fig. R18-1-6 which shows a histogram of peak heat flux at the outer target for 10,000 different simulations where the physics parameters have an even probability distribution over  $0.14 < S/\lambda_q < 0.16$ ,  $2.0 < \lambda_q[\text{mm}] < 3.0$  and  $0.30 < f_{rad} < 0.40$ . For a high poloidal flux expansion 2.0 MA, 10 MW input power equilibrium (g116313.00851.NfHz0+\_0), the heat flux at the lower end of each of these bounds would be  $6.5 \text{ MW/m}^2$ . As shown in the figure, the variation, when these parameters are relaxed lead to a wider range of peak values, from  $3.6$  to  $6.5 \text{ MW/m}^2$ . This physics uncertainty translates into an engineering safety factor or margin to allow for misalignments of coils and/or PFCs or reduced material performance parameters. This has yet to be practically realized within Recovery planning as it is difficult to assign a risk factor extending the probability distribution of the physics parameters away from their original conservative starting point.

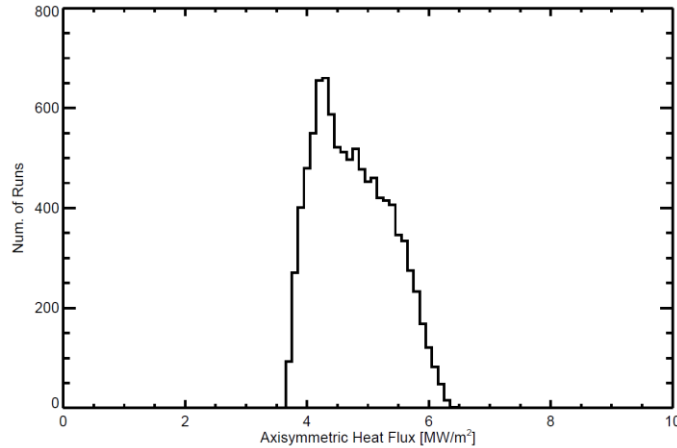


**Fig. R18-1.6:** Histogram of a 10,000 Monte-Carlo simulations of the peak outer divertor heat flux for a 2 MA, 10 MW high poloidal flux expansion equilibrium ( $g116313.00851.NfHz0+_0$ ) where the  $S/\lambda_q$ ,  $\lambda_q$  and radiated power fraction are allowed to vary independently over narrow ranges, as discussed in the text.

Activities developing and validating reduced engineering limit models from more detailed ANSYS analysis were also deferred due to Recovery. The mechanical analysis expertise remains a critical resource for Recovery, and in April 2018, ORNL increased its effort to support mainline PFC analysis at the expense of supporting this milestone. The PFC FDR originally scheduled for mid-FY-19 was pushed until late FY-19, and so support will be marginal until mid-September 2018. Initial progress was demonstrated to connect spatio-temporal varying heat flux predictions from physics-based predictions as to inputs to finite element simulations. An ACT script in ANSYS was developed to automate the breakup of a PFC surface into discrete subdomains, apply separate time-evolving heat fluxes from XML files, and execute and store results of transient thermal simulations. This was done to support automation of neural network training data set generation as discussed under Goal 3, but this will also be useful in connecting the time-evolving output of 2D and 3D PFC heat flux tools explored under Goal 1.

*R(18-1) - Goal 3: Evaluate options for PFC monitoring systems*

Two types of PFC monitoring approaches were considered that could be options for NSTX-U. Many devices ([JET](#), [WEST](#), [AUG](#), [W7-X](#)) use NIR/IR imaging to measure PFC surface temperature, generally in real-time, and interlock against overheating. While the technology has been demonstrated in the community, the specifics of adapting this approach to NSTX-U needs to be investigated, i.e., such as number and placement of cameras. LLNL (F. Scotti, V. Soukhanovskii) evaluated an imaging system that allows a wide-angle tangential view of the full poloidal cross-section of the tokamak in simultaneous infrared and visible light, drawing on experience with similar LLNL tools in operation on DIII-D [C. Lasnier, RSI v85, pg11D855 (2014)]. The IR/visible periscope would enable imaging of the plasma facing components and edge plasmas before, during, and after the discharge, as well as in real time. This would support a variety of operational tasks. FY-18 activities explored field of view and spatial resolution for potential NSTX-U locations using the DIII-D imaging solution and using POV-ray.

Fig. R18-1.7 shows a variety of simulations from a low-resolution (LR) system characteristic of the 640 x 501 IR sensors and a high-resolution (HR) visible camera with a 1200 x 940 pixel sensor. These are from achievable positions at Bay-I and Bay-G. The IR view could be considered for plasma facing component monitoring applications while the visible view could be used for after discharge plasma facing component inspection or general plasma monitoring (i.e., Plasma TV). In the visible view, the lighting from the in-vessel filaments is used and approximates the existing lighting configuration used in NSTX-U. In both renderings, three separatrices are also overlaid (from L-mode discharge 205020) toroidally centered at three consecutive bays (i.e., each separated by 30 degrees). The simulated views generally show that even the existing DIII-D optics layout would provide excellent imaging and spatial coverage characteristics for IR and visible imaging on NSTX-U.

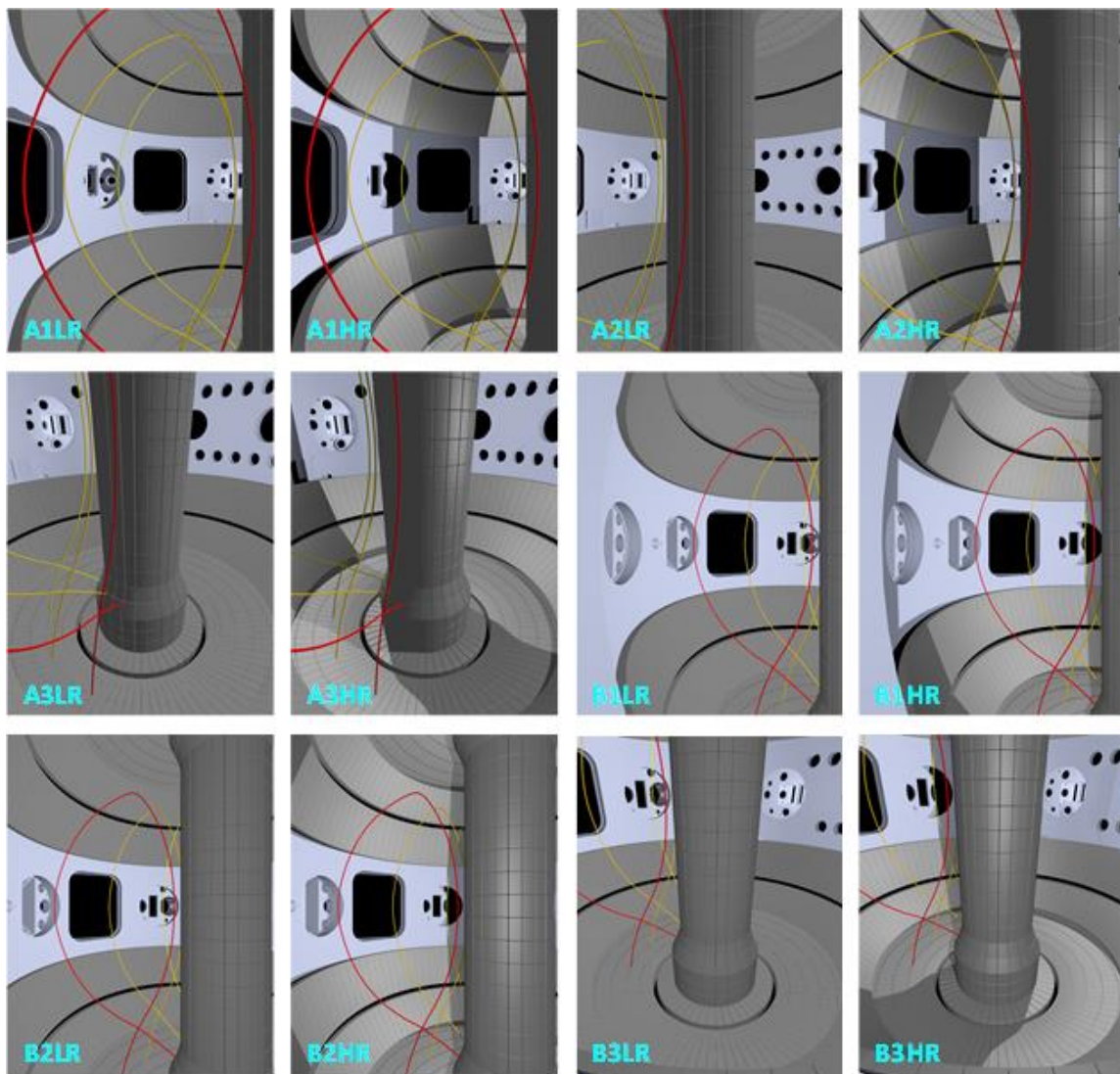
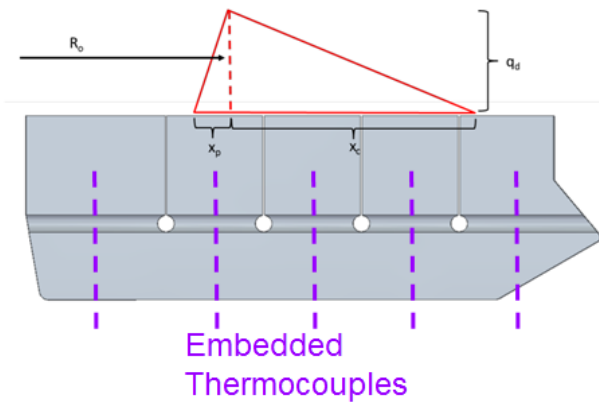


**Fig. R18-1.7:** Simulated periscope views and plasma outlines for the 6 periscope configurations (two ports, three view orientations) in low resolution, IR (LR) and high resolution, visible (HR). All BXXX views are from Bay-G while AXXX vies are from Bay-I.

The spatial resolution of the simulated imaging views was evaluated for several periscope options. Periscope view B3 (centered at Bay G and with a view of the lower divertor) was considered to determine the resolution per pixel (in cm/pixel) for [visible, IR] on various divertor surfaces: IBDH [0.23, 0.43], IBDV [0.32, 0.60], CSAS [0.25, 0.46], and OBD [0.23, 0.43]. This is demonstrated to be sufficient to observe large-scale tile or castellation failures/loss, but as castellations will be ~2.5 cm and feature intra-castellation structure due to faceting and shadowing as discussed above, additional zoom optics may be required to support detailed strike point profile measurements.

Effort was also devoted to exploring the feasibility of embedded, sub-surface temperature measurements, with strong contributions from UT-Knoxville (T. Looby). In this approach, no direct measure of the temperature during the shot would be completed, but the surface temperature would be computed by PCS using real-time knowledge of the input power, the total radiated power, and the time-evolving magnetic equilibrium. Also required is a physics model that partitions power to divertors, such as the  $dr_{sep}/\lambda_q$  model used in W\_PFC, and engineering scalings for  $S$  and  $\lambda_q$  that are inputs into the standard Eich model. If the physics model is accurate, PCS should have sufficient information to predict the PFC surface temperature and avoid operational limits. To validate the physics model requires shot-to-shot measurements, and the milestone explored whether the new suite of PFC thermocouples (TCs), outlined in NSTX-U-RQMT-RD-004, would be sufficient. To exploit this approach, PFC designs need to have limits that can be correlated to surface temperature, such as carbon blooms or surface compressive stress, as well as be able to predict temperature for axisymmetric heat flux. This requires avoiding leading edges near small gaps where it is difficult to quantify heat loads. Present designs for the high heat flux regions are expected to be temperature limited and avoid leading edges at poloidal gaps.

To explore the use of embedded TCs, a scoping problem was developed that could be used to demonstrate proof-of-concept for neural network methods to derive physics model parameter from TC time histories. Fig. R18-1.8 shows the simplified model where a heat flux footprint with a distinct private ( $x_p$ ) and common ( $x_c$ ) flux region is defined, which scale with a known flux expansion,  $f_x$ , unknown physics parameters,  $S$  and  $\lambda_q$ . The latter have unknown scaling coefficients,  $C_1 - C_4$ , that are functions of known engineering parameters  $B_p$ ,  $P_{heat}$ ,  $f_x$  and  $R_o$ . The question to be answered is: given the engineering parameters and measurements from the sub-surface TCs, can the physics scaling parameters  $C_1 - C_4$  be derived? TC measurements 0.75" from the surface were taken, but no noise or systematic error has yet been included. It has been shown previously on JET [V. Riccardo, PPCF v32 pg 881 (2001)] that TCs deposition profiles can be estimated, and NSTX-U's new high heat flux PFC design would improve the ability as the castellations have been shown numerically and experimentally to act as natural calorimeters. (See the F(18-1) milestone work.) The use of neural networks instead of using more conventional inverse heat conduction techniques [J.A. Myric, IJHMT v111 pg 982 (2017)] is being explored as means to decrease computation time while also allowing a direct connection between TC measurements and physics model parameters.



### Simplified Eich Model:

$$x_p = S f_x$$

$$x_c = \lambda_q f_x$$

$$P_{heat} = \int_{R_o - x_p}^{R_o + x_c} q(R) 2\pi R dR$$

$$\frac{S}{\lambda_q} = C_1$$

$$\lambda_q [mm] = C_2 P_{heat}^{C_3} B_p^{C_4}$$

$$0.1 < C_1 < 0.3$$

$$1.0 < C_2 < 2.5$$

$$-0.1 < C_3 < 0.25$$

$$-1.2 < C_4 < -0.5$$

$$0.2 < B_p [T] < 0.6$$

$$0.5 < P_{heat} [MW] < 4.9$$

$$4 < f_x < 30$$

$$46.0 < R_o [cm] < 57.5$$

$$1 < \Delta t [sec] < 5$$

**Fig. R18-1.8:** A schematic of the scoping problem where an asymmetric heat flux footprint is applied to a sub-domain of the graphite PFCs (left) while the heat flux model and simulation domain is described (right).

The open source TensorFlow (<https://www.tensorflow.org/>) library was used to construct the neural network, which required generation of training and demonstration datasets. As a means of creating these datasets ~5000 simulations were run in ANSYS, in which  $C_1 - C_4$  and the engineering parameters were varied. These simulations output temperature profiles that provide coverage of a myriad of the NSTX-U operational / physics domains. Demonstration datasets consisted of fixed  $C_1 - C_4$  values with varying engineering parameters, representing a fixed physics model that could be investigated by various combinations of NSTX-U “shots,” or “discharges.” A convolution neural network (CNN), the details of which will be described in depth in the final R(18-1) Milestone Report, was first trained to interpret  $C_1 - C_4$  from a single discharge. As shown in Fig. R18-1-9,  $S$  and  $\lambda_q$  could be reliably reconstructed from the CNN, but large variations in predicted  $C_2$  and  $C_4$  values were found using the demonstration dataset. While a CNN trained to predict  $C_2 - C_4$  from a single shot can resolve  $\lambda_q$  with relative ease, it cannot resolve the degeneracy between the  $C$ -variables that define  $\lambda_q$ . Analytically, it can be shown that three “shots,” with varying  $B_p$  and  $P_{heat}$ , are necessary to resolve  $C_2 - C_4$ . A new approach is being developed in which the CNN is trained to make predictions given three input shots (a “triplet”), which would resolve this degeneracy. Initial results indicate that increased accuracy in CNN predictions for  $C_2 - C_4$  are possible with this triplet method, but the neural network is still being optimized. If successful, this would indicate an increase in the amount of training data and training complexity as unknown parameters are added to the scaling. This work will continue into at least the end of CY-18 where the results will be summarized in a UT-K Master’s Thesis. Initial results show that CNN interpretation of embedded TC data could be helpful in supporting NSTX-U operations, but further numerical and experimental (using e-beam) investigation is required.

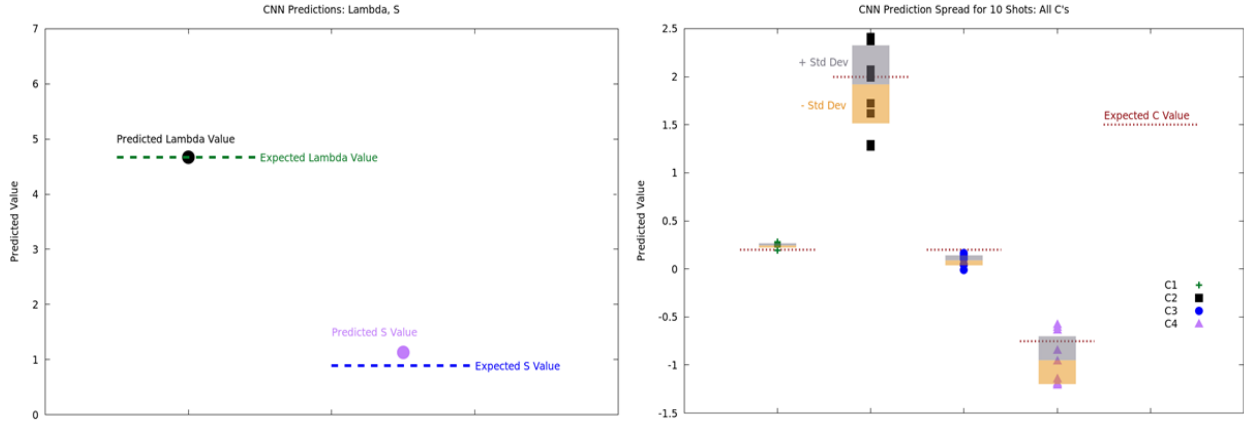


**Fig. R18-1.9:** Initial CNN results on computing  $S$  and  $\lambda_q$  (left) and  $C_1 - C_4$  (right) using a training method based on a single simulation.

## R(18-2): Develop simulation framework for spherical tokamak breakdown and current ramp-up

*Description: Access to high-performance discharges in spherical tokamaks (STs) is sensitive to the first phase of the plasma discharge, including the initial generation of the plasma discharge (i.e. breakdown) and the increase of the plasma current, temperature and density to the target value (i.e. ramp-up). An optimized ramp-up scenario would minimize the internal inductance ( $I_i$ ) and flux consumption while exhibiting reasonable resilience to expected variations in the experimental conditions. This milestone aims to develop computational tools that enable the optimization of the breakdown and ramp-up phase on NSTX-U and MAST-U. A reduced model computational framework, such as TOKSYS, will be developed in order to connect the real-time plasma control algorithms with a time-dependent model including the power supply capabilities, toroidal currents induced in the vessel structures and a free-boundary plasma equilibrium. This model will be used to gain insight into the vertical stability limits during ramp-up and the impact of power supply, wall structures and plasma parameters on the maximum stable elongation in STs. This framework will also be used to develop, test and optimize the real-time shape control algorithms in the ramp-up phase. A second framework approach will use comprehensive transport simulation, such as TRANSP, to investigate the evolution of the kinetic profiles during ramp-up as a function of the free parameters. The initial goal is to optimize the outer gap, density and neutral beam heating in the L- and H-mode phases of the ramp-up that minimize  $I_i$  and flux consumption while remaining within MHD and fast-ion stability limits. The results from the first reduced model framework will provide guidance on the target high-elongation shapes, while the second transport model framework will provide guidance on the evolution of equilibrium parameters such as  $I_i$  and  $\beta_N$ . This milestone also aims to develop a simulation framework for optimizing aspects of the inductive plasma breakdown, such as the null formation and the initial increase of the vertical fields, over the range of expected ohmic solenoid pre-charge and toroidal field currents. The proposed development of simulation frameworks described in this milestone will reduce the experimental time required to achieve a suitable optimization of the breakdown and ramp-up scenarios for accessing high-performance scenarios on NSTX-U and MAST-U.*

The scientific mission of NSTX-U and MAST-U benefits from the optimization of the initial phase of discharge. Highly shaped (large elongation and high triangularity) discharges are critical for maximizing performance and are more easily realized at low internal inductance (i.e., low- $I_i$  or a broad current profile). Low- $I_i$  operation was realized on NSTX by diverting, entering H-mode

with strong NBI heating and achieving large elongation early in the  $I_p$  ramp up to slow the diffusion of edge current to the core. NSTX-U and MAST-U plan to pursue a similar strategy for accessing the highest performance discharges. This report describes advances in the computational framework that will be used for optimizing the startup scenario on NSTX-U in the next fiscal year (R19-2), with the aim of accelerating the achievement of highly-shaped H-mode discharges when NSTX-U and MAST-U operations resume.

The initial phase of an NSTX discharge contains three sub-phases with unique challenges. The first phase, known as startup, must generate a plasma with closed field lines. The plasma is inner-wall limited, and the actuators (magnetic field coils, gas fueling, etc.) are in feed-forward control. The primary challenge in this phase is to achieve robust direct induction startup that satisfies the unique operational constraints of the tokamak and the specifics of the experiment. The second phase of ramp-up requires the active control of the plasma shape to transition from an inner-wall limited (IWL) shape to a diverted shape while increasing  $I_p$ . The primary challenge is achieving a control scheme that executes a reproducible diverting time and diverting shape that is resilient to the expected variation in the plasma parameters such as  $I_i$ ,  $\beta$  and the nature of the “seed” IWL discharge. The final phase encompasses the rapid increase in the neutral beam heating to induce the L-H transition. The primary challenge in this phase is achieving a reproducible L-H timing and optimizing self-consistent scenarios that achieve broad, current profiles while avoiding MHD and fast-ion instabilities.

This report describes progress on a simulation framework that addresses the control and scenario challenges of the three sub-phases. A closed-loop real-time control simulation framework was developed in close collaboration with General Atomics. The closed-loop model allows the control algorithms within the NSTX plasma control system (PCS) to be tested using reduced models for the actuators (e.g. coil power supplies) and measurements (e.g. magnetics) using the TokSys model. This framework enables the testing and optimization of control algorithms that address the rapid plasma boundary shape change while remaining resilient to variations in equilibrium parameters. TRANSP analyses focusing on the ramp-up phase were completed in order to establish the implications of various free parameters and assumptions within the transport model. The results identified suitable transport models for predictive TRANSP calculations of global equilibrium parameters in the ramp-up phase on NSTX-U. Finally, predictive calculations using LRDFIT were performed for NSTX-U and MAST-U to develop viable startup scenarios for a range of operational conditions. A set of criteria were developed based on NSTX and NSTX-U inductive startup to evaluate and constrain the proposed scenarios.

### ***Real-time control simulation framework***

Active real-time control of the plasma boundary shape is critical for optimizing tokamak performance. This is especially crucial during the ramp-up phase when the plasma boundary rapidly changes from an inner-wall limited, low elongation shape to a diverted, high elongation shape. Access to high-performance discharges is enabled by maximizing the elongation and shaping of the plasma early in the ramp-up phase. This is especially critical for STs where the

unique regime of high normalized pressure ( $\beta_N$ ) and broad current profiles (low- $I_i$ ) is enabled at high shaping. The challenge for real-time control systems is realizing the desired ramp-up scenarios over a broad range of experimental conditions and actuator performance.

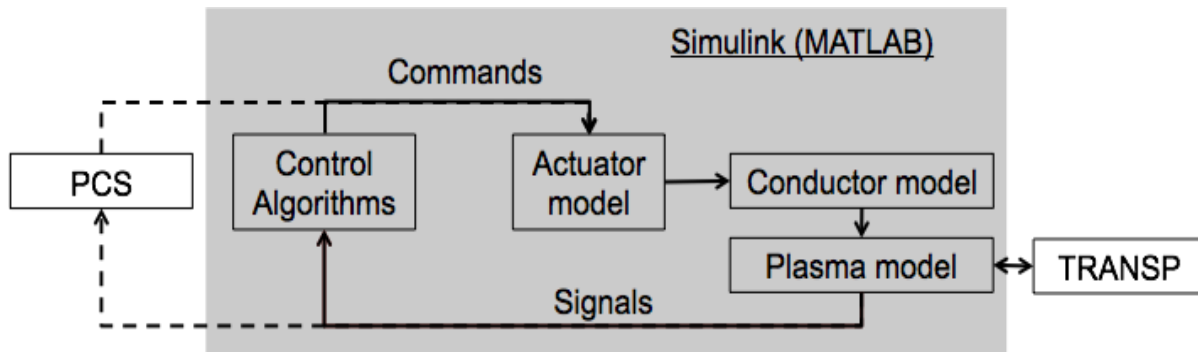


**Fig. R18-2.1:** Simulation framework for developing and testing real-time control solutions.

Work completed toward this milestone builds upon a simulation framework developed by General Atomics aimed at developing and testing the real-time control system. Fig. R18-2.1 shows the general elements of the simulation framework. The gray box indicates the elements within the TokSys model library [R18-2-1], written in the SIMULINK environment using the MATLAB language. The actuator model includes models specific to NSTX-U where commands from a plasma control system (PCS) are converted into the required inputs to the plasma model. For example, the power supply firing angle command output from the PCS is converted into a voltage that is applied to a poloidal field coil. The conductor model describes the axisymmetric conducting structures in order to account for induced toroidal currents.

One element of the framework is that the control algorithms can be written within TokSys, or a direct connection can be made with the NSTX-U PCS. The direct connection to the PCS system provides a “flight-simulator” capability where the PCS approved for operations can be tested and new scenarios can be developed. The software enabling this connection is the “Simulation Simeserver” and is represented as the dashed lines in Fig. R18-2.1. Mirroring the control algorithms in the PCS in SIMULINK provides a platform for fast and flexible development of control algorithms that can be tested before modifying the PCS.

Details of the elements of the simulation framework are provided in the following subsections.

## Control algorithms and PCS

The plasma control system (PCS) includes a library of control algorithms that interpret signals generated at the tokamak and issue commands to actuators such as power supplies, neutral beam injectors, and gas injection systems. The development and testing of new algorithms or new applications of existing algorithms was traditionally accomplished through targeted calculations and dedicated experimental time on the tokamak

The simulation framework has a “flight simulator” capability where the operational PCS code is executed in a feed-forward or closed-loop simulation. This capability enables the rapid testing and tuning of the PCS prior to running an experiment; it is a significant advance toward increasing the efficiency of NSTX-U operations. The interface between the PCS software and the SIMULINK environment (“Simulation simserver”) was developed for the NSTX-U PCS with the assistance of Mike Walker at General Atomics. The feed-forward calculations mimic the capabilities of the existing Data Simserver where archived signals are provided to the PCS and the command output transmitted to SIMULINK is compared to the archived commands. This model provides the capability to verify the simulation interface is configured correctly and a fast evaluation of the impact of changes within the PCS control algorithms. The closed-loop calculations provide an opportunity to plan future discharges. For example, one expected application is verification that a strike-point sweep satisfies heat flux requirements on the divertor tiles prior to running an experiment (see R18-1 report).

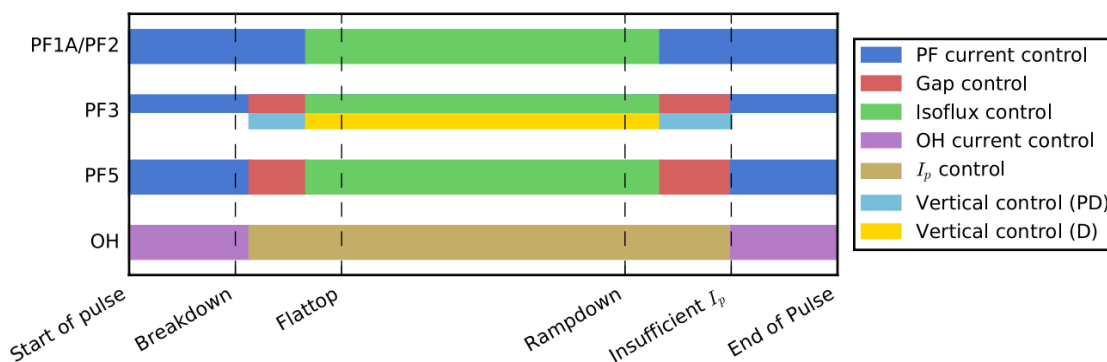


**Fig. R18-2.2:** Schematic of the PCS algorithms used in different phases of a typical NSTX-U discharge used to control the current in the coil sets.

The PCS control algorithms are mirrored within the SIMULINK environment to enable rapid development and functional testing of new control schemes. This allows control algorithms to be developed on a fast and flexible platform before starting the process of gaining approval to modify the PCS software, completing the modification, and completing functional testing with the “flight simulator” capabilities. Fig. R18-2.2 shows a typical timeline of the control algorithms used to control the voltage on each coil set in the present PCS. Implementation of the coil current, gap, ISOFLUX, and vertical control algorithms in TOKSYS were developed in FY-18. The ISOFLUX algorithm includes the latest developments of the shape control algorithms from the 2016 NSTX-U campaign, including the X-point and touch point locator, multi-input multi-

output (MIMO) inner gap control, and the  $d_{\text{rsep}}$  segment adjustments [R18-2-2]. These algorithms were developed to improve control during the ramp-up phase and were undergoing commissioning and tuning when operations ended in 2016. The simulation framework will be used prior to the restart of operations to make further progress on testing and tuning these algorithms for the ramp-up phase.

### Actuator model

The simulation framework includes a power supply model to convert a firing angle command from the PCS to a voltage applied to each coil. The model aims to capture both the logic of the power-supply control software and the specifics of the power supply hardware. The simplest and fastest power supply model (“Simple”) defines the latency, rate limits, and magnitude limits for each power supply. A more comprehensive model captures the details of the voltage modulations (“Switching”) of each power supply, but requires more computational time. Typically, the “simple” model is adequate since the timescale of interest is much longer than the voltage modulations of the power supplies.

The framework also has a simple actuator model for the neutral beam system to accept commands from PCS and to produce a beam current, voltage, and power output. Other actuator models, such as gas valve response, will be developed at a later date.

### Conductor model

The toroidal current induced in the conducting structures is comparable to the plasma current in the ramp-up phase and must be consistently self-included in time-dependent calculations. A model for the conducting structures was developed using the EFIT definitions for the conductor geometries and resistances. The device model also includes definitions of the magnetic probe diagnostics. To assess the accuracy of the conductor model, the model-generated magnetics signals were compared to measured signals from several single-coil and multi-coil vacuum test shots. Control-oriented model reduction techniques were used to increase simulation speeds by removing high-order vessel modes that were determined to have little influence on model fidelity.

Induced image currents, especially in the segmented passive plates on NSTX-U, play a significant role in the passive vertical stability of highly shaped discharges. Reconstruction codes, such as EFIT, use magnetic measurements to constrain the induced current in a simplified circuit model for the passive plates. The predictive calculations required a passive plate model that captures the more complicated geometry of different current paths through the segmented plates. The circuit includes a parallel path, representing currents flowing through the plates and mounting brackets, and an anti-series path, representing the net axisymmetric effect of eddy currents in the plates. The resistance of the toroidal path is augmented by an approximate ‘gap’ resistance representing the effective resistance of the path through mounting brackets and the vessel. Fig. R18-2.3 shows the effect of varying the gap resistance on the vertical growth rate for several times during the ramp-up of discharge 204118 on NSTX-U. The

active vertical control system is capable of maintaining the vertical position of the plasma with vertical growth rates below 120 Hz.

### Plasma model

The simulation framework is designed to provide flexibility in the complexity and fidelity of the plasma model. Linear models provide a fast solution but require that the target plasma equilibria are known prior to the simulation. Non-linear models solve for the self-consistent plasma equilibria within the time-dependent simulation. At present, parameterized profiles for  $p'$  and  $FF'$  are defined to be consistent with scalar inputs for  $I_p$ ,  $\beta_p$  and  $I_i$ . In the future, the framework can be coupled with reduced models or a flux-driven transport model, such as TRANSP, in order to evolve the kinetic profiles self-consistently.

The linear plasma model in TOKSYS computes a plasma response matrix using perturbations around a given equilibrium with the choice of a fixed, rigid or non-rigid solutions for the current distribution. A fixed solution does not include the plasma response; it only calculates the vacuum field response to the coils. Rigid models fix the plasma current distribution and assume the current distribution has two degrees of freedom (radial and vertical). Non-rigid models solve the perturbed Grad-Shafranov equation to allow the current distribution to change in response to small perturbations.

Simulations using linear models are fast (~ 1 minute) but are only valid for small perturbations from the equilibrium used to develop the linear model. The linear models provide the means for designing, analyzing and rapidly testing and tuning shape control algorithms for a predetermined evolution of the discharge. Nonlinear simulations provide higher fidelity testing of the resulting closed-loop system and support predictive solutions where the shot evolution is not constrained.

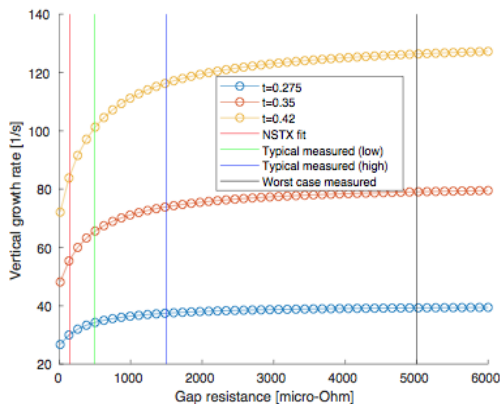


**Fig. R18-2.3:** Vertical growth rate versus the passive plate gap resistance at different times in the ramp-up: 0.275s (blue), 0.35s (orange) and 0.42s (yellow) for discharge 204118. The vertical lines show the expected gap resistance (red), a typical range for the measured gap resistance (green to blue) and the largest gap resistance measured on NSTX-U (black).

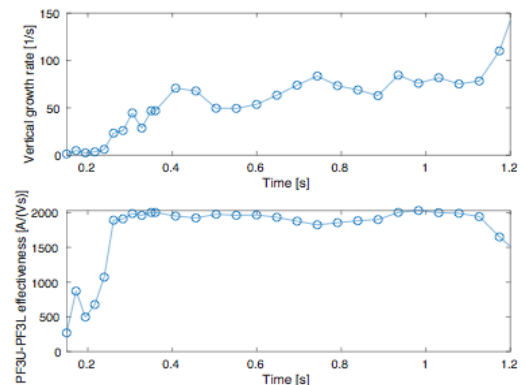


**Fig. R18-2.4:** Vertical growth rate (top) and effectiveness of the PF3 coil set to control the vertical position (bottom) versus time for discharge 204118.

The linear model within TOKSYS was extended to a linear time-varying (LTV) model to enable time-dependent simulations for periods where the current distribution and plasma boundary are evolving, such as during ramp-up. The new LTV model maintains the speed of the linear model while providing a necessary tool for completing control simulations of the entire discharge. The calculation shown in Fig. R18-2.3 uses the LTV model to explore the impact of varying the resistance of the mounting bracket for the passive plates on the vertical growth rate at different times in the ramp-up. These calculations support the design of a new passive plate mounting bracket pursued in FY-18.

Fig. R18-2.4 shows the vertical growth rate and effectiveness of the vertical control coils as a function of time for a simulation of an NSTX-U discharge (204118) using the LTV model. The simulation captures the rapid evolution of these parameters during the ramp-up phase (before 0.4s), which is important for testing the active vertical control system. Prior to implementing the LTV model, these values would be a fixed value for the duration of the simulation. LTV development also supports efforts to implement time-varying, model-based control to improve robustness to changes in operating conditions.

The Grad-Shafranov (GS) solver within TOKSYS was implemented to enable predictive calculations for NSTX-U where the equilibrium evolution is not predetermined. Support for this effort was provided by Anders Welander at General Atomics. Non-linear calculations require more time (~ 1 hour) compared to linear plasma models, but a non-linear model provides increased fidelity for predictive calculations when validating control solutions. The evolution of the plasma current and kinetic properties ( $\beta_p$ ,  $I_i$ ) are prescribed. In the future, these parameters could come from separate models such as reduced models like the neural net models described in IS-ASC C.1 section or flux-driven transport models (TRANSP). Results described in IS-ASC C.4 section use time-dependent, free-boundary solver in a closed-loop simulation to demonstrate the real-time control of a snowflake divertor boundary shape on NSTX-U.

Recent work toward developing neural net reduced models will provide a mechanism for evolving the kinetic parameters of the equilibrium in a fast simulation. The development of neural net reduced models for the fast ion pressure and beam current drive are described in the IS-ASC section C.1. The reduced models provide an avenue for evolving the kinetic parameters of the equilibrium self-consistently with very little impact on the speed of the calculation. Objectives within the FY-19 milestone will work toward developing neural net models for additional kinetic parameters (current profile, pressure, density) and integrating these models into the plasma model.

Additionally, the SIMULINK framework can interface with TRANSP in order to provide a self-consistent flux-driven calculation of the kinetic properties. Previous control simulation results wrote general control logic into the TRANSP code [R18-2-3]. The connection between TRANSP and SIMULINK allows for closed-loop simulations where machine-specific control algorithms can be tested with some or all of the equilibrium properties derived from a time-dependent TRANSP calculation. The development of this capability is discussed further in the next section.

### ***Time-dependent transport simulation framework***

The TRANSP code provides a free-boundary, time-dependent, simulation using 1.5D transport models for interpretative and predictive calculations. One application of TRANSP is to complete interpretive analysis of discharges where the models are constrained using experimental measurements. A database of interpretive analysis completed for NSTX and NSTX-U is used to develop and evaluate reduced models for the required kinetic equilibrium profiles such as the neural net model development. A second application of TRANSP is to complete predictive flux-driven calculations. The predictive calculations provide a rigorous plasma model within the simulation framework for developing and validating faster calculations using reduced physics. Within the simulation framework, TRANSP can provide some or all of the self-consistent, time-dependent plasma parameters required to evaluate the plasma equilibrium and, in the future, the plasma stability.

The work completed toward this milestone focuses on an assessment of the fidelity of the models in TRANSP for predicting the global equilibrium parameters in the ramp-up phase. The goal of this work is to identify both the applicability of, and sensitivity to, the choice of models and free parameters within TRANSP. The predictive calculations are evaluated by their ability to reproduce the global parameters, such as stored energy and  $I_i$ . Kinetic profiles (e.g., temperature profiles) are also considered to evaluate the agreement with the different transport channels.

The assessment of the predictive TRANSP calculations applied a variety of transport models over a range of ramp-up conditions on NSTX-U. An L-mode NSTX-U discharge (204202) with temperature and density measurements from Thomson and CHERS is used to identify the impact of the model choices. Further tests were conducted with three other NSTX-U H-mode discharges: 202946, 203679, and 204112. These discharges, like most other NSTX-U H-mode discharges, do not have dependable measurements for ion temperature and carbon density from CHERS when using the second neutral beamline. The three comparison discharges provide a wide range of ramp-up scenarios explored in the first campaign of NSTX-U [R18-2-4].

The thermal transport model used for these calculations is the Multi-Mode Module (MMM) version 7.2 [R18-2-5]. Among applicable modules within MMM, the Weiland model, and Electron Temperature Gradient (ETG) modes are considered. A generalized neoclassical transport model (Chang-Hinton [R18-2-6]) is used for ion thermal transport. The fixed-boundary equilibrium solver in TRANSP uses the EFIT equilibrium boundary shape and evolves the poloidal field diffusion to estimate current and  $q$  profiles; it does this by using the Sauter model [R18-2-7] for the resistivity and bootstrap current. The plasma current evolution that constrains the current profile is taken from the measurement. Similarly, the electron and carbon density profiles are determined from measurements since the necessary physics required for a predictive density evolution requires is not yet developed. (This is a proposed task for FY-19.) When carbon density is not available, a constant  $Z_{\text{eff}} = 2.5$  is assumed. A flat fixed anomalous fast ion anomalous diffusion coefficient of  $1 \text{ m}^2/\text{s}$  is used.

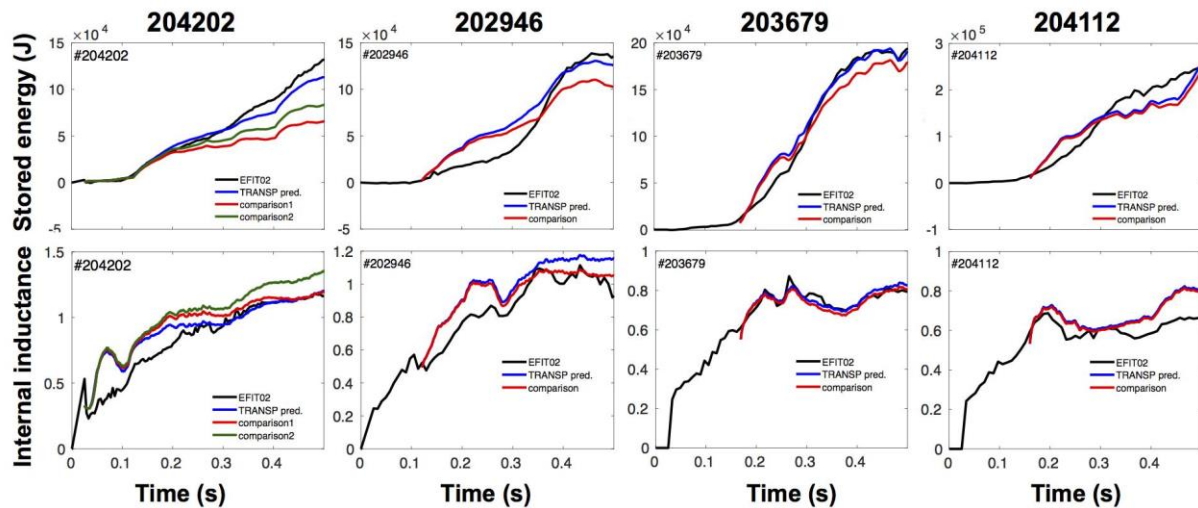


**Fig. R18-2.5:** Predictive TRANSP calculations using different model parameters (blue, red, green) compared to the values derived from EFIT reconstructions.

Fig. R18-2.5 shows a comparison between the predictions for stored energy, and  $I_i$  with the experimentally realized values (black lines) and the cases using different model settings. The best agreement for discharge 204202 (left column) is found using MMM7.2 with the Weiland and ETG model for electron thermal transport and the neoclassical model for the ion thermal transport. Adding the MTM module in MMM7.2 and switching the ion thermal transport model from neoclassical to Weiland (comparison 1, red lines) significantly under-predicts the stored energy. Switching just the neoclassical model to the Weiland model (comparison 2, green lines) compared to the blue lines results in the worst agreement with  $I_i$ .

The average deviation between 0.15 - 0.5s of the predicted values using the best settings (blue line) and the derived EFIT for all discharges considered is less than 20% for all cases except 202946 when there is significant MHD activity between 0.1 - 0.3 s. The 20% error level is reasonable considering the uncertainties in the measurement and the lack of a  $q$ -profile constraint in the EFIT solution.

The temperature profiles produced by the predictive TRANSP calculations were compared to the experimental measurements to gain insight into the drivers of the global parameters and identify avenues for improved model settings for the ramp-up phase. The global parameters are well reproduced using Weiland and ETG model for electron temperature evolution. However, the best agreement with the profiles requires the model settings to evolve during the ramp-up period. For the discharges with the largest NBI heating (203679 and 204112), the Microtearing Mode (MTM) model needs to be included to match the reference electron temperature profile, although the global parameters are similar with or without MTM module. In the future, the criterion for applying the MTM model (e.g.  $\beta_e$  from [R18-2-8]) could be predicted. In addition, for ETG mode the electrostatic or electromagnetic threshold [R18-2-5] that impacts the electron temperature profile (not as much as MTM but still effective in the central region) could be added

to the model. As typical of NSTX discharges, neoclassical transport was found to be a good approximation for the ion temperature profile [R18-2-9]. Since no measurement is available for the current and the safety factor profiles in NSTX-U, direct comparison of the simulated profiles cannot be done.

The results obtained in FY-18 establish that models currently available in TRANSP can predict the evolution of the stored energy and  $I_i$  within 20%, provided the discharge does not have large-scale global MHD activity. This result illustrates that predictive TRANSP calculations can provide a time-dependent constraint on global equilibrium parameters within the NSTX-U simulation framework.

### ***Inductive Startup Calculations***

NSTX-U and MAST-U will employ a similar direct induction scheme to initiate the plasma discharge. Both devices require the development of flexible and resilient startup scenarios in order to maximize the efficiency of operations. Similar to the transition from NSTX to NSTX-U, MAST-U requires a new startup scenario due to changes in the conducting toroidal structures, power supplies, and coil locations.

Prior to FY-18, LRDFIT was used to prepare direct induction scenarios for NSTX-U and evaluate direct induction results on NSTX, NSTX-U, and MAST. LRDFIT is capable of computing vacuum fields in the presence of toroidally conductive axisymmetric structures. The TokSys framework developed in FY-18 could be used to conduct similar calculations. Calculations completed prior to NSTX-U operations accelerated the development of startup over a range of OH precharge [R18-2-4]. Work completed in FY-17 made LRDFIT available for MAST calculations and validated the calculations against MAST results [R18-2-10].

FY-18 activities extended the LRDFIT model to include the MAST-U geometry in order to produce predictive startup calculations. MAST-U has unique limitations compared to NSTX-U; the most notable difference is the larger number of PF coil sets needed to generate a field null and field evolution that is comparable to NSTX-U.

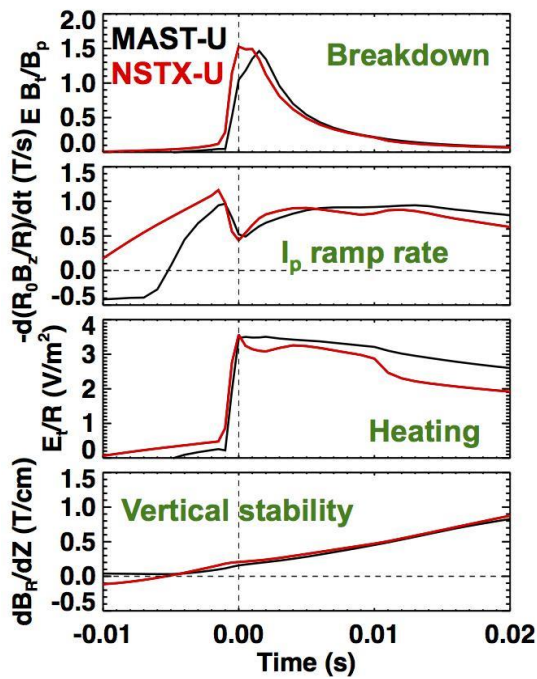


**Fig. R18-2.6:** Startup scenario metrics for a realized NSTX-U startup (red) and a MAST-U scenario designed to match the NSTX-U criteria (black).

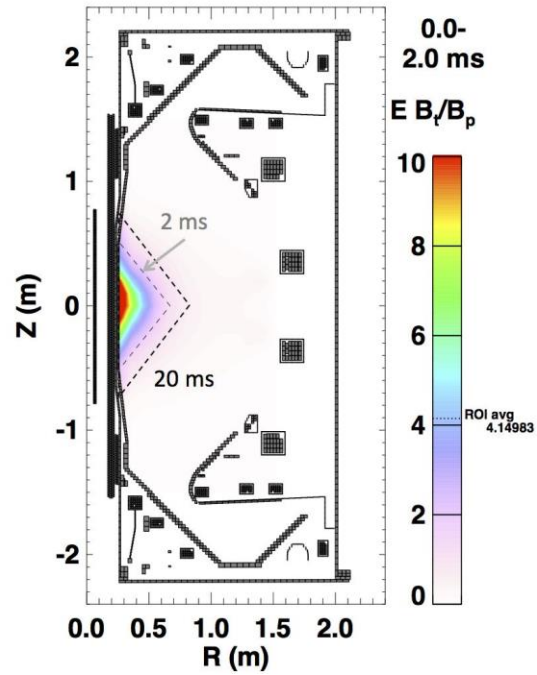


**Fig. R18-2.7:** Average Lloyd parameter over first 2 ms. Dashed lines show ROI evolution from 2 ms to 20 ms.

A set of four criteria was developed in order to make simple quantitative comparisons when developing and optimizing scenarios. Fig. R18-2.6 compares the four criteria between a startup scenario realized on NSTX-U ( $I_{TF} = 3.0$  MA,  $I_{OH} = 20$  kA/turn) and a possible startup scenario for MAST-U ( $I_{TF} = 2.4$  MA,  $I_{OH} = 22.5$  kA/turn) with  $V_{loop} = 4$  V. The criteria require that a region of interest (ROI) is defined in R,Z space. For both devices, the ROI is a triangle extending from the inboard limiter that grows in radius after 2 ms as shown in Fig. R18-2.7. Also, the criteria are derived assuming the current density  $J \sim 1/R$  and is constant with Z within the ROI (i.e. assume  $B_z \gg B_p$  and a zero- $\beta$  equilibrium).

The first criteria evaluates the Lloyd criteria equal to  $EB_t/B_p$  (kV/m), where larger values reflect an increased likelihood of realizing breakdown of a neutral gas along open magnetic field lines. This is computed via a surface average over the ROI and adds an offset of 10G to the computed poloidal fields to reflect the contribution of non-axisymmetric fields [R18-2-4]. The second criteria describe the rate of increase in the vertical field required for radial equilibrium as  $I_p$  increases. This is computed taking a surface average of  $R_0 B_z/R$ , where  $R_0$  is the current centroid of the ROI. The third criteria describe the spatially averaged heating of the plasma. Generally, the third criteria should scale with the second criteria since larger heating increases  $dI_p/dt$ , requiring the vertical field to increase at a larger rate. The final criteria describe the vertical stability of the plasma, where a larger positive number is more stable. This is computed by integrating  $dB_R/dZ$  over the top and bottom portions of the boundary.

The completed calculations demonstrate that MAST-U could achieve a startup scenario similar to NSTX-U at maximum OH precharge for the first run campaign. The MAST-U scenario satisfies the power supply constraints, machine force limits and the desire to minimize D-coil heating and stress. The LRDFIT model, combined with the described metrics, was used to develop an extensive startup procedure that addresses an array of operational contingencies on MAST-U (IS-ASC C.3).

The primary development of the simulation framework was the extension of LRDFIT to include the MAST-U geometry and establishing criteria for evaluating the vacuum field calculations. Resulting calculations have been the basis of the MAST-U startup procedure development and have motivated targeted studies on both ST devices to further quantify the operational limits in passive stability and the  $I_p$  ramp rate.

### ***Summary and Future work***

This research milestone advances the computational tools required to accelerate the realization of high-performance discharges on NSTX-U and MAST-U. The simulation framework focuses on the unique challenges of the ramp-up phase, however, the simulation tools can also be applied for optimizing the flattop and ramp-down phases of the discharge.

The primary accomplishment in FY-18 was developing and demonstrating a simulation framework where predictive calculations can be completed with closed-loop, real-time control simulations for NSTX-U. This framework was developed by building on the existing TokSys code and with assistance from personnel at General Atomics. The simulation can be driven by the plasma control system (PCS) or using control algorithms written within the TOKSYS environment. Many of the critical control algorithms in the NSTX-U PCS now have equivalent models added to the TOKSYS library.

A linear time-varying (LTV) plasma model was developed in order to use a fast, linear model that is valid in the ramp-up phase when the equilibrium is rapidly changing. The first closed-loop simulations using a non-linear plasma model (i.e. Grad-Shafranov solver) were completed in FY-18 and provide a higher-fidelity model for testing control algorithms. The FY-19 milestone will expand the capabilities of the model to complete fully-predictive simulations. For example, using reduced models and/or TRANSP models to constrain the evolution of the kinetic profiles of the equilibrium.

Analysis of predictive TRANSP calculations completed for this milestone have identified suitable choices of models and free-parameters that provide an avenue for driving the time-dependent kinetic equilibrium parameters within the simulation framework. Using a suitable choice of models and free parameters, some global parameters can be reproduced for NSTX-U discharges within 20% of the experimental values. Future work will focus on evaluating the agreement of the predictive calculations with the measured kinetic profiles and to increase the statistics of the comparisons. Predictive time-dependent calculations of the 1-D profiles will

provide an opportunity to evolve the equilibrium with higher-order constraints and evaluate the MHD and fast-ion stability of the ramp-up scenarios.

The startup modeling using LRDFIT was expanded in FY-18 in order to support MAST-U operations. Metrics developed for the startup scenario (equilibrium, stability, heating, and current drive) enable a comparison between the proposed MAST-U scenarios and startup on NSTX, NSTX-U, and MAST scenarios. The results have supported the operational procedures for the first experiments on MAST-U. Future plans include reproducing these results within the TokSys framework and expanding the calculations to self-consistently include the plasma response.

## References

[R18-2-1] D.A. Humphreys et al., "Development of ITER-relevant plasma control solutions at DIII-D", *Nuclear Fusion*, v 47, n 8, Aug. 2007, p 943-51.

[R18-2-2] Boyer, M. D. et al., Plasma boundary shape control and real-time equilibrium reconstruction on NSTX-U. *Nucl. Fusion* **58**, (2018).

[R18-2-3] Boyer, M. D. et al., Feedback control design for non-inductively sustained scenarios in NSTX-U using TRANSP. *Nucl. Fusion* **57**, 066017 (2017).

[R18-2-4] Battaglia, D. J. et al., Scenario development during commissioning operations on the National Spherical Torus Experiment Upgrade. *Nucl. Fusion* **58**, (2018).

[R18-2-5] Rafiq, T., Kritz, A. H., Weiland, J., Pankin, A. Y. & Luo, L. Physics basis of Multi-Mode anomalous transport module. *Phys. Plasmas* **20**, (2013).

[R18-2-6] Chang, C.S. and Hinton, F.L., Effect of finite aspect ratio on the neoclassical ion thermal conductivity in the banana regime. *Phys. Fluids* **25**, 1493 (1982).

[R18-2-7] Sauter, O., Angioni, C. & Lin-Liu, Y. R. Neoclassical conductivity and bootstrap current formulas for general axisymmetric equilibria and arbitrary collisionality regime. *Phys. Plasmas* **6**, 2834–2839 (1999).

[R18-2-8] Guttenfelder, W. et al., Progress in simulating turbulent electron thermal transport in NSTX. *Nucl. Fusion* **53**, (2013).

[R18-2-9] Kaye, S. M. et al., Scaling of electron and ion transport in the high-power spherical torus NSTX. *Phys. Rev. Lett.* **98**, 1–4 (2007).

[R18-2-10] FY17 NSTX-U Annual report.

### **R(18-3): Validate and further develop reduced transport models for electron thermal transport in ST plasmas.**

*Description: The design of next generation spherical tori (STs) will be influenced by the scaling of energy confinement. While ion thermal transport is often near neoclassical levels in H-modes in ST plasmas, gyro-kinetic simulations have indicated a number of potential drift wave turbulence mechanisms that can influence electron thermal transport. Reduced transport models that capture the key physics and scaling of the computationally expensive first-principles gyro-kinetic simulations are required to more thoroughly validate the modeling against experimental data, which can then be used to infer the key physics that determines the overall energy confinement. A variety of reduced transport models based on drift wave turbulence have been developed and tested extensively for conventional tokamaks. These models encompass much of the physics expected to be important in STs, although they have been tested much less rigorously for ST parameters (low aspect ratio, high beta, strong flow). In order to improve the fidelity of reduced transport models (like TGLF, RLW and MMM), experimental NSTX, MAST and NSTX-U data will be used to examine predictions based on these models to assess their suitability for ST plasma. The physics accuracy of these fluid-based models will also be qualified by comparing directly to first-principles gyro-kinetic simulations over a range of conditions. The dependence of electrostatic ITG and TEM instabilities on aspect ratio will be evaluated by comparing L-mode cases to established conventional aspect ratio conditions. Validation with high beta H-mode data will push the limits of the available reduced models to recover electromagnetic instabilities like MTM and KBM. A key outcome of this milestone will be to determine the ST physics regimes in which further model development is required. The first-principles gyro-kinetic simulations based on ST parameters will form the basis for enhancements of the TGLF reduced model.*

Progress of the R18-3 milestone was made in multiple areas. Comparisons between multiple models and first-principles gyrokinetics were performed for specific cases that helped to clarify where future model upgrades or new developments are required. Particular emphasis was given to microtearing modes, electron temperature gradient/multi-scale turbulence, and energetic particles modes/kinetic ballooning modes. Work is continuing through the end of FY-18 and beyond to address these issues.

#### **1. Testing model predictions over a database of NSTX discharges**

A series of TRANSP runs were performed to study how well various transport models (predominantly H-modes) reproduced NSTX conditions over a range of beta and collisionality. The results of these benchmark comparisons are critical for defining directions in which these models need to be further developed in order to produce a comprehensive predictive capability. Data were taken from a beta scan (6.75 to 14.3%) at fixed collisionality and from collisionality scans at three different beta values: 5 to 6.5% (collisionality from 0.024 to 0.160), 6.5 to 7.5% (collisionality from 0.039 to 0.182), and 7.5-9.5% (collisionality from 0.028 to 0.224). For these benchmarks, only  $T_e$  was predicted. The models used were Rebut-Lallia-Watkins (RLW) [1,2], Multi-Mode 7.1 (MMM) (see [3] and references therein), and the 2016 version of TGLF (see [4] and references therein). MMM has been updated to with a microtearing mode model (MMM7.2) [5], and initial tests of this model were performed as well.

The results of the benchmarking indicated that RLW showed more agreement with the experimental data at high collisionality as expected - where microtearing is important. This is

also true for MMM7.2. However, neither RLW nor MMM7.2 contains the appropriate collisionality dependence that would suppress the microtearing mode as collisionality is reduced. TGLF does not do a good job in describing NSTX discharges in any region of parameter space. This model does not take electromagnetic effects fully and appropriately into account. (This is true also at standard aspect ratio.) This in part is reflected by very high Kinetic Ballooning Mode fluxes that the code computes. This occurs because the TGLF model computes much lower KBM critical gradients than the Te gradients observed in the experiment. This indicates that TGLF needs further development in the area of computing heat fluxes produced by electromagnetic turbulence. More detailed comparisons are made below that highlight some of the issues that have been investigated that motivate continued future work.

## 2. Lehigh MTM model predictions (MMM7.2)

Previous gyrokinetic validation efforts have shown that electron thermal transport caused by electromagnetic microtearing mode turbulence [6-8] may be responsible in part for setting the favorable dimensionless energy confinement scaling,  $B\tau_E \sim \nu_e^{-0.8}$  observed in NSTX and MAST H-modes [9-11]. While slab theory has provided some insight into the nature of MTM turbulence, there has not been a physics-based MTM transport model capable of reproducing the trends predicted by first principles gyrokinetic simulations.

Recently, a new unified fluid/kinetic model for microtearing modes (MTM) has been developed by the Lehigh group [5] and incorporated into Multi-Mode Model version MMM7.2. The Lehigh MTM model makes improvements to older slab theory by treating arbitrary electron collisionality and including magnetic curvature effects. As a result, the model has been found to reproduce many of the linear gyrokinetic results predicted in NSTX discharges [12], such as the variation of real frequency and growth rates with poloidal wavenumber (example shown in Fig. R18-3.1), beta, and electron temperature and density gradients [13]. A particularly important result is that the model recovers the non-monotonic dependence of linear MTM growth rate with collision frequency. It fails, however, to reproduce a similar non-monotonic dependence on safety factor and magnetic shear due to a simplified treatment of the parallel mode structure. Future work will explore using a more complicated dependence of the parallel wavenumber ( $k_{||}$ ) to improve the linear model predictions.

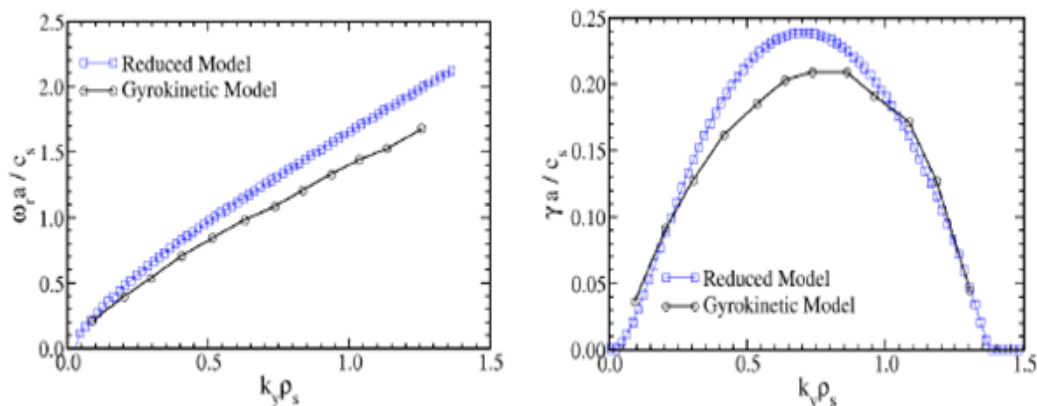


**Fig. R18-3.1:** (left) Real frequencies and (right) linear growth rates from Rafiq MTM model compared to gyrokinetic predictions using GYRO.

In addition to linear stability, the Lehigh MTM model solves a nonlinear dispersion relation that self-consistently determines an estimated saturated magnetic fluctuation amplitude,  $\delta B/B_0$ . Using this saturated amplitude with a Rechester-Rosenbluth like stochastic transport model [14] provides the basis for the electron thermal transport model. A comparison of the predicted  $T_e$  profiles using this model is shown for two NSTX H-mode discharges in Fig. R18-3.2. The model is found to agree with experiment at high collisionality but overpredicts transport at low collisionality, predicting  $T_e$  far too low.

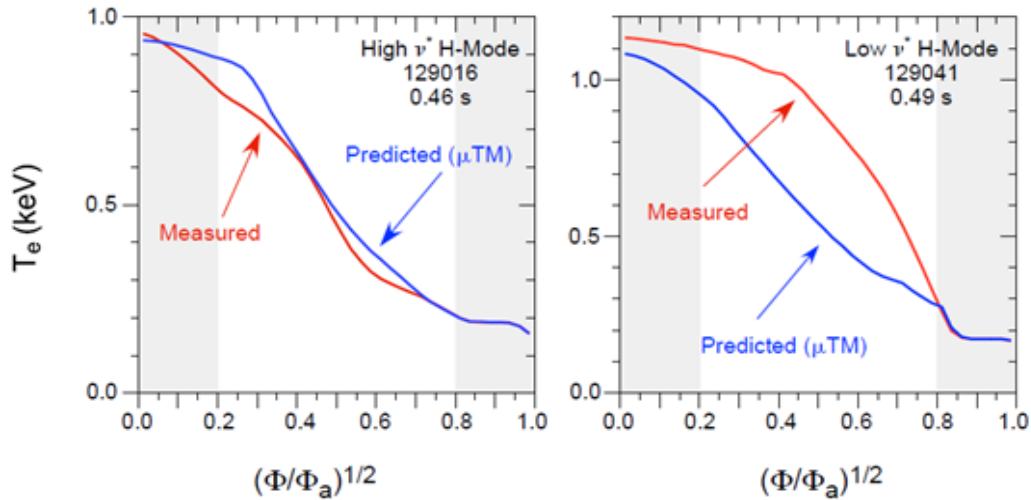


**Fig. R18-3.2:** Measured electron temperature profiles compared with predictions using the Lehigh MTM model for (left) high collisionality and (right) low collisionality NSTX H-mode discharges.

While the MTM model was found to reproduce the linear growth rate scaling with collision frequency, a few ways to improve the modeled transport have been identified that should improve agreement in the lower collisionality discharges. First, the expression for electron thermal diffusivity originally employed was based on the collisional form of the stochastic transport Rechester-Rosenbluth model,  $\chi_e = v_{TE}^2 / \nu_{ei} |\delta B/B|^2$ . However, this is only applicable in the limit of  $\lambda_{mfp} < qR$ , and will give unphysically large values of  $\chi_e$  as collisionality is reduced. The more general form of Rechester-Rosenbluth is given by  $\chi_e = D_m v_{TE} = |\delta B/B|^2 L_c v_{TE}$ , where the magnetic diffusivity  $D_m$  depends on the magnetic correlation length  $L_c$ , which is estimated to be  $L_c = \min[\lambda_{mfp}, qR]$  depending on collisionality [14]. A more general transport expression can be

written to account for this [7]:

$$\chi_{e,MTM} = \min \left[ 1, \frac{1}{\epsilon^{3/2} \nu_{*e}} \right] q R v_{Te} \left| \frac{\delta B^2}{B^2} \right|$$

The expression for electron diffusivity also relies on a single value for saturated magnetic fluctuation amplitude,  $\delta B/B$ . This is determined in the Lehigh MTM model by solving the nonlinear dispersion relation for a single poloidal mode number. However, the nonlinear gyrokinetic simulations predict a spectrum of modes that can contribute to transport [7], each of which can exhibit slightly different parametric scalings. To account for this, a simple Lorentzian function has been fit to the nonlinear gyrokinetic spectrum of  $\delta B(k_y)$  that in the future will be incorporated into the MTM saturation model. Once these updates are included, the model predictions will be re-validated over the range of collisionality investigated above to test the limits of applicability.

### 3. ETG / multi-scale model predictions

Electron scale ( $k_{\theta}\rho_s \gg 1$ ) turbulence due to the electron temperature gradient (ETG) instability has been hypothesized to play a role in numerous NSTX discharges. Model ETG transport has been investigated in both NSTX L-mode and H-mode.

#### L-mode

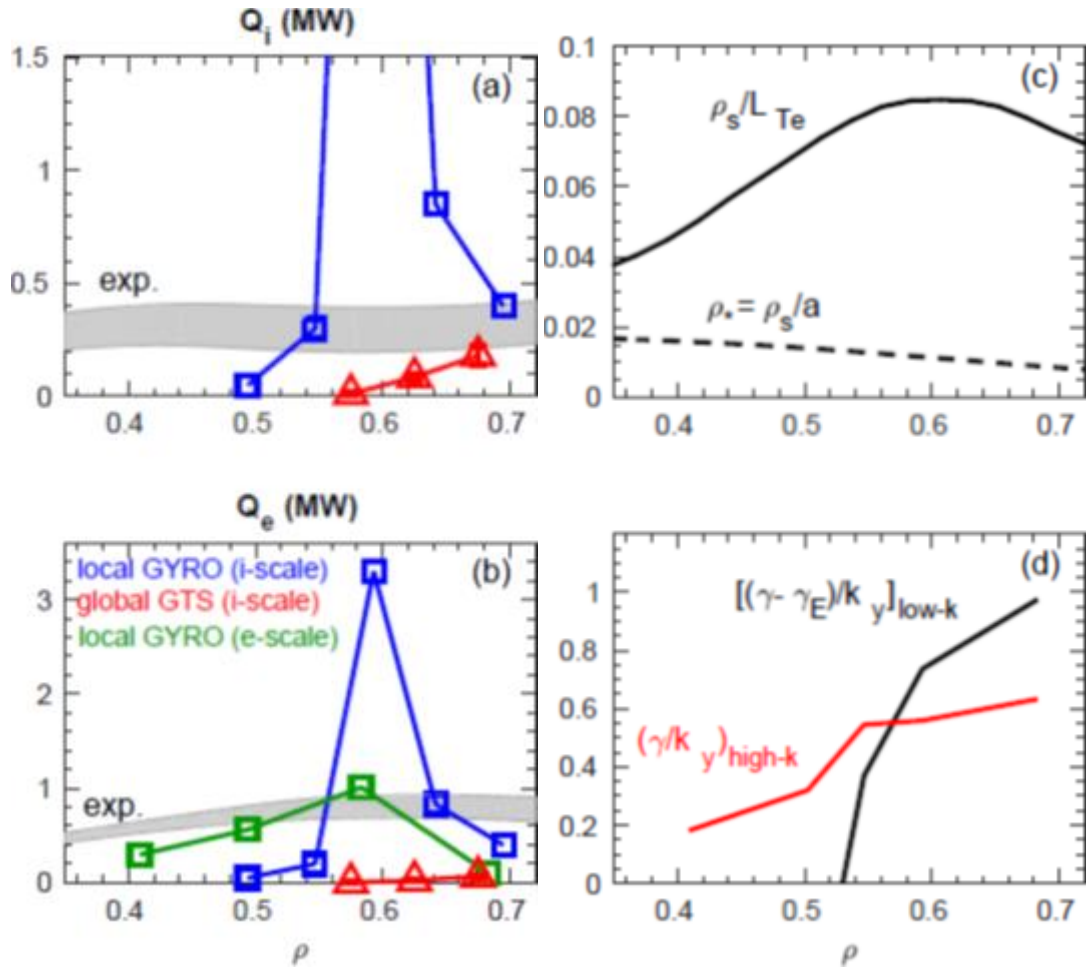


**Fig. R18-3.3:** Comparison of simulated and experimentally inferred (a) ion and (b) electron thermal heat fluxes. (c) Profile of locality parameters,  $\rho_* = \rho_s/a$  and  $\rho_s/L_{Te}$ . (d) Ratio of gyrobohm-normalized growth rate to poloidal wavenumber for maximum growth rate for ion scale ( $k_y = k_{\theta}\rho_s < 1$ ) and electron scale ( $k_y > 1$ ).

Previous local, nonlinear gyrokinetic simulations run for an NSTX L-mode [15] using GYRO predict ion-scale transport that peaks at very large values around  $\rho=0.6$  (Fig. R18-3.3a-b). However, there is a rapid reduction in transport on either side of this peak due to ExB shearing rates becoming larger than linear growth rates towards the core and a reduction in the gyrobohm coefficient  $Q_{GB} \sim T^{5/2}$  towards the edge. Global nonlinear ion scale simulations using GTS [16,17] predict a much smoother variation of transport as a consequence of profile shearing effects at the relatively large values of  $\rho_* = \rho_s/a$  (or  $\rho/L_{Te}$ ) (Fig. R18-3.3c). When added to neoclassical transport, the global simulations reproduce ion thermal transport comparable to experiment. However, predicted electron heat flux in the global simulations is negligible

indicating that some physics is still missing. Linear analysis predicts ETG modes are also unstable in this discharge, so we have recently run local, nonlinear ETG simulations in the same region using numerical grids that resolve only electron-scale turbulence ( $[L_x, L_y]=[6,4]\rho_s=[360,240]\rho_e$ ,  $[n_x, n_y]=[192,48]$ ,  $[18,19]$ ). As seen in Fig. R18-3.3b, the ETG simulations predict significant transport around the mid-radius ( $\rho=0.4-0.6$ ), approaching experimental levels [20]. However, given the similarity in electron heat flux at electron scales and ion heat flux at ion scales from global simulations ( $Q_{e,high-k} \sim Q_{i,low-k}$ ), cross-scale coupling effects cannot be ruled out. The potential importance of multiscale effects is further illustrated by noting that the ratio of maximum  $(\gamma/k_y)$  predicted from electron scale instability is comparable to or exceeding the same ratio from ion scale instability (Fig. R18-3.3d). This metric has recently been put forth as a criterion for indicating the potential importance of multi-scale effects [4]. Profile predictions using the reduced model TGLF within TGYRO have also been validated against measured profiles.

Fig. R18-3.4 shows the predicted  $T_e$  profiles for the original saturation model “SAT0” significantly overpredict the temperatures. However, using the recently updated “SAT1” saturation model that accounts for cross-scale coupling [4] provides an increase in electron thermal transport that brings the predicted  $T_e$  profiles into much better agreement with the experiment. The agreement between the TGLF-SAT1  $T_e$  predictions and the experiment lend additional motivation to pursue full, multi-scale gyrokinetic simulation (that simultaneously simulate ion-to-electron scales) to directly predict the importance of cross-scale coupling. We note, however, that TGLF is a local model. Given the obvious impact of non-local effects on the ion-scale turbulence predicted in the gyrokinetic simulations (Fig. R18-3.3a), it is possible that a combination of global plus multiscale would be required to predict the complete ion and electron thermal transport profiles. (Similar implications are found for both NSTX-U L-modes [21] and recent NSTX H-mode analysis [22,23].) The feasibility of such simulations is unclear and will require careful future exploration as computational resources increase. In addition, a standard framework for modeling the non-local effects in reduced models such as TGLF has not yet been developed, although some guidance can be taken from previous systematic gyrokinetic investigations (e.g. [24]).

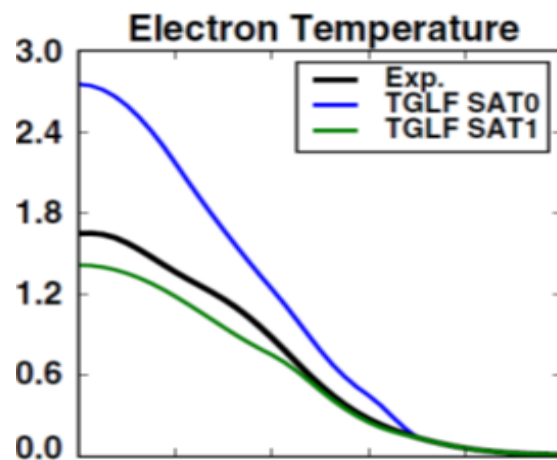


**Fig. R18-3.4:** Comparison of measured and predicted  $T_e$  for NSTX L-mode plasma. The predicted profiles use TGLF with two different saturation models.

## H-mode

The TGLF model was also tested in an H-mode discharge where previous analysis found ETG could provide significant transport near the mid-radius [8]. Fig. R18-3.5 shows that the predicted  $T_e$  profiles for this discharge agree around the mid-radius, but only when using the “SAT1” model (bottom). Using the original “SAT0” model (top) significantly overpredicts  $T_e$ , indicating the enhanced ETG transport represented by the “SAT1” model is critical for agreement. However, the model still underpredicts transport deeper into the core, illustrating missing transport. For this particular plasma, including electromagnetic effects in the model makes little difference to the predicted transport inside  $\rho < 0.7$ .

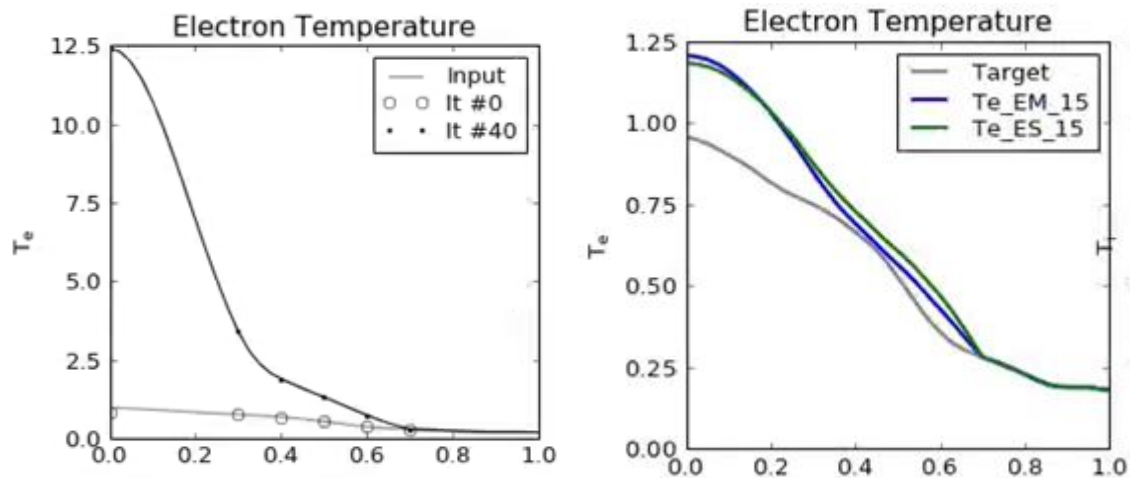


**Fig. R18-3.5:** Comparison of measured and predicted  $T_e$  profiles for NSTX H-mode plasma. The predicted profiles use TGLF with two different saturation models: (top) SAT0, (bottom) SAT1.

To further test the importance of ETG transport in the model prediction and validate that the model captures the correct underlying physics, we compare flux-gradient relationships at the mid-radius ( $\rho \sim 0.5$ ,  $r/a \sim 0.6$ ). Nonlinear, electron-scale gyrokinetic simulations predict ETG transport for this case can be rather stiff (R18-3.6, left; from [8]), producing experimental levels of electron heat flux ( $\sim 2$  MW) with marginal variation in the temperature gradient. The TGLF1 model predicts a similar level of stiffness but only when using the SAT1 model with enhanced ETG transport. Including electromagnetic effects change the results, but to a smaller degree than the change in saturation model. These results give confidence that the TGLF ETG model may be sufficient for modeling electron-scale transport in spherical tokamaks.

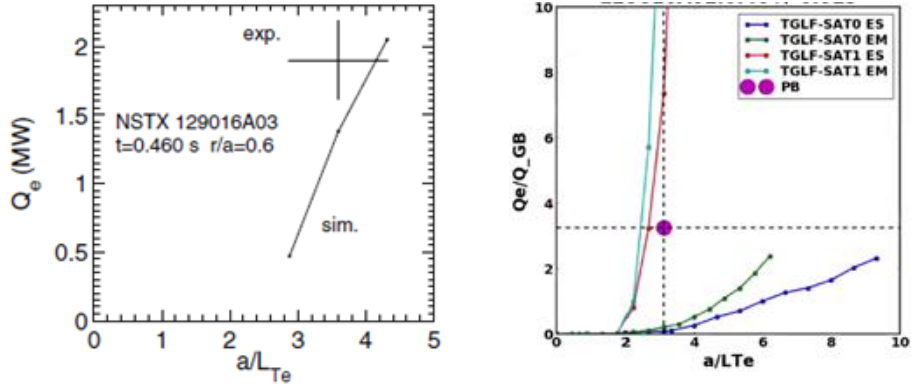


**Fig. R18-3.6:** (left) Electron heat flux vs. electron temperature gradient predicted by nonlinear gyrokinetic simulations. The experimental values are shown by the cross-hairs (right). Electron heat flux (in gyrobohm units) vs. electron temperature gradient from TGLF predictions using various model assumptions. The experimental value is given by the magenta dot.

Inspecting TGLF model predictions further out in radius indicates more complicated behavior when including electromagnetic effects, as illustrated in Fig. R18-3.7 at  $\rho=0.7$  for the same discharge. For the electrostatic model a monotonic flux-gradient relationship is predicted similar to  $\rho=0.5$ . However, when including electromagnetic effects the flux-gradient relationship becomes erratic, giving a non-monotonic dependence of flux up to extremely large values. (Note the logarithmic scale.) This wild variation in flux-gradient relationship challenges transport solvers like TRANSP or TGYRO to obtain converged solutions, limiting the location of the outer boundary condition in the predictive simulations above (Fig. R18-3.5). As noted in the first section, attempts to predict profiles for even higher beta discharges using TGLF often fail to converge or give wild results, likely due to similar irregular flux-gradient model behavior. To address these issues, a number of potential upgrades to TGLF have been discussed with G. Staebler (General Atomics). However, these upgrades will likely necessitate development of a newer version of the model which is outside the scope of the FY-18 milestone activity.

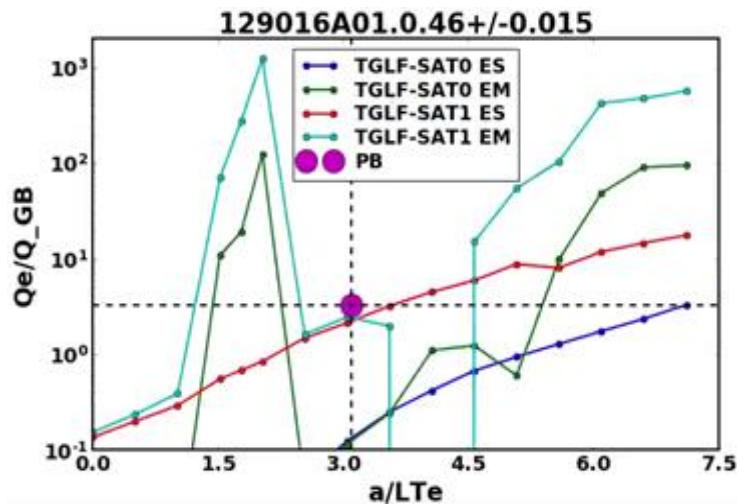


**Fig. R18-3.7:** Gyrobohm-normalized electron heat flux vs. electron temperature gradient predicted by TGLF at  $r=0.7$  using different model assumptions.

#### 4. KBM/EPM Threshold Predictions.

As NBI heating increases in NSTX H-modes it is commonly observed that, while the profile is broadened overall, the on-axis electron temperature is limited to  $T_e \leq 1$  keV. An example of this is seen in the low collisionality discharge in Fig. R18-3.2. Understanding the core profile response in high-power, high-beta discharges is important for achieving high non-inductive current fraction required for high performance steady-state scenarios envisioned for future ST devices [25, 26].

In the deep core region ( $\rho < 0.5$ ), thermal gradients are typically too small to drive drift wave instabilities, and other mechanisms must be considered to account for the flattened  $T_e$  profile. One hypothesis is that global and compressional Alfvén eigenmodes (GAE/CAE), driven by the increased energetic ion population, can lead to stochastic electron orbits and enhanced electron thermal transport [27, 28]. Additionally, CAEs couple to kinetic Alfvén waves (KAW) near the mid-radius, and it is possible they transfer a fraction of energy outside the core region ( $\rho \sim 0.5$ ) reducing the energy deposited by beam slowing down [29].

However, it is also possible that the increased energetic ion population can also contribute to drift wave instability drive, leading to an energetic particle mode (EPM), the fast-ion-driven analog of the kinetic ballooning mode (KBM). In some papers this mode is also referred to as the beta-induced Alfvén eigenmode, BAE, e.g, [30] with reference to KBM/BAE theory [31]. Linear stability calculations in the deep core of such NSTX H-modes that include some model of energetic particle drive have not previously been reported. To investigate this, we have run linear CGYRO simulations using a high- $\beta_{pol}$  discharge ( $\beta_{pol}=2$ ) that exhibited the lowest achieved surface voltage in NSTX H-mode ( $V_{surf}=130$  mV) and a corresponding high, non-inductive current fraction ( $f_{NI}=65\%$ ) [32]. Scenarios like this have been used as the basis for NSTX-U projections [25].

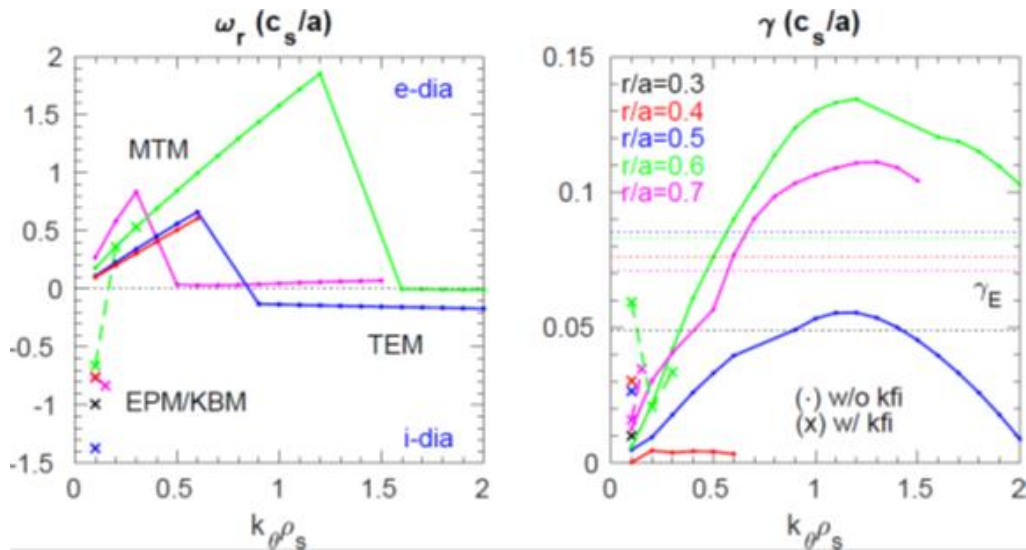


**Fig. R18-3.8:** Real frequencies (left) and linear growth rates (right) at multiple radii in a high- $\beta_{pol}$  NSTX H-mode discharge. Simulations without kinetic fast ions are shown by solid lines with dots, while simulations including kinetic fast ions are shown by crosses with dashed lines. Corresponding ExB shearing rates are shown by the dotted lines.

Fig. R18-3.8 shows the real frequencies and linear growth rates from the simulations at multiple radii. Electromagnetic microtearing modes at  $k_{\theta}\rho_s < 1$  are found to be unstable at many radii, illustrated by large real frequencies in the electron diamagnetic (e-dia) drift direction. There is also a spectrum of electrostatic trapped electron modes predicted at increasing wavenumber,  $k_{\theta}\rho_s > 1$ . Inside  $r/a \leq 0.5$  both MTM and TEM modes are likely to be suppressed by the large ExB shearing rates ( $\gamma_E > \gamma_{lin,max}$ ), shown by the dotted lines. However, if a kinetic fast ion species is included in the simulations (using a simple Maxwellian background approximation with  $T_{fast} = 2/3 E_{fast}$  calculated by TRANSP/NUBEAM), unstable EPM/KBM are found at very low  $k_{\theta}\rho_s \sim 0.1$  (shown by crosses). They are distinguishable in Fig. R18-3.8 by real frequencies strongly in the ion diamagnetic (i-dia) drift direction.

The EPM modes predict relatively large quasi-linear fluxes in the energetic ion channel. To determine the effect they have on regulating the electron temperature profile will require nonlinear simulations beyond the scope of this milestone. However, a simple first model would be to assume that very large transport occurs in all channels above the EPM/KBM threshold so that the profiles are likely limited to be near the onset of the modes. (This is similar to the approach applied in EPED to describe transport in the H-mode pedestal [33].)

To determine how close the core profile is to the EPM/KBM limit, simulations were performed varying electron beta in Ampere's equation. Results are shown in Fig. R18-3.9. If kinetic fast ion effects are neglected (solid lines), the KBM threshold is  $\sim 50\%$  higher than the experimental value of electron beta (vertical dotted lines). However, when including the kinetic fast ions (dashed lines), the EPM/KBM threshold is much closer to the experimental value, hinting at their importance in setting the ultimate pressure limit. Additional scans varying electron temperature gradient (not shown) indicate similar onset behavior, although the key parameter determining stability for the EPM/KBM modes is  $\alpha_{MHD} = -q^2 R \nabla P_{tot} \cdot 2\mu_0 / B^2$ . Indeed, the growth rate variations with different parameter scans ( $\beta_e, a/L_{Te}, \dots$ ) are found to overlay when plotted vs.  $\alpha_{MHD}$ .

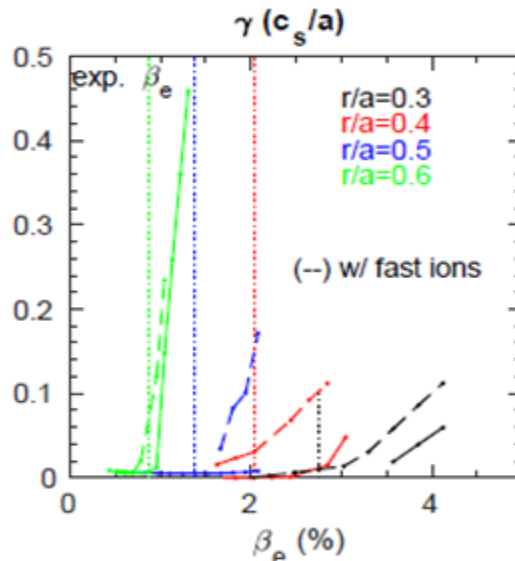


**Fig. R18-3.9:** Linear growth rates vs. electron beta at multiple radii without and with kinetic fast ions. The experimental value of electron beta is given by the vertical dotted lines.

The above analysis highlights the need for a model of KBM/EPM transport to include in predictive simulations, especially for the high beta scenarios envisioned for large non-inductive current fractions. TGLF has recently been used to perform similar predictions in high- $\beta_{\text{pol}}$  DIII-D discharges [34], but required careful retuning of model choices (beyond default settings) to achieve meaningful results. Similar analysis will be pursued in the future for the NSTX case above.

## References

- [1] P.H. Rebut, M. Brusati, Plasma Phys. Control. Fusion **28**, 113 (1986).
- [2] P.H. Rebut, P.P. Lallia, M.L. Watkins, IAEA-FEC, Nice, France (1988).
- [3] T. Rafiq et al., Phys. Plasmas **20**, 032506 (2013).
- [4] G.M. Staebler et al., Nucl. Fusion **57**, 066046 (2017).
- [5] T. Rafiq et al., Phys. Plasmas **23**, 062507 (2016).
- [6] W. Guttenfelder et al. Phys. Rev. Lett. **106**, 155004 (2011).
- [7] W. Guttenfelder et al., Phys. Plasmas **19**, 056119 (2012).
- [8] W. Guttenfelder et al., Nucl. Fusion **53**, 093022 (2013).
- [9] S.M. Kaye, et al., Phys. Rev. Lett. **98**, 175002 (2007).
- [10] M. Valovic, et al., Nucl. Fusion **51**, 073045 (2011).
- [11] S.M. Kaye et al., Nucl. Fusion **53**, 063005 (2013).
- [12] W. Guttenfelder et al., Phys. Plasmas **19**, 022506 (2012).
- [13] T. Rafiq et al., IAEA-FEC, Ahmedabad, India (2018).
- [14] A.B. Rechester, M.N. Rosenbluth, Phys. Rev. Lett. **40**, 38 (1978).
- [15] Y. Ren et al., Nucl. Fusion **53**, 083007 (2013).
- [16] W.X. Wang et al., Nucl. Fusion **55**, 122001 (2015).
- [17] W.X. Wang et al., Phys. Plasmas **22**, 102509 (2015).
- [18] W. Guttenfelder, J. Candy, Phys. Plasmas **18**, 022506 (2011).
- [19] Y. Ren et al., Phys. Plasmas **19**, 056125 (2012).
- [20] S.M. Kaye et al., IAEA-FEC, Ahmedabad, India (2018).
- [21] W. Guttenfelder, AAPPS-DPP invited talk, Chengdu, China (2017).
- [22] J. Ruiz-Ruiz et al., APS-DPP oral, Milwaukee (2017).
- [23] J. Ruiz-Ruiz et al., US-TTF, San Diego, CA (2017).
- [24] R.E. Waltz, J. Candy, Phys. Plasmas **12**, 072303 (2005).
- [25] S.P. Gerhardt et al., Nucl. Fusion **52**, 083020 (2012).
- [26] J.E. Menard et al., Nucl. Fusion **56**, 106023 (2016).
- [27] D. Stutman et al., Phys. Rev. Lett **102**, 115002 (2009).
- [28] N. Gorelenkov et al, Nucl. Fusion **50**, 084012 (2010).
- [29] E. Belova et al., Phys. Rev. Lett **115**, 015001 (2015).
- [30] J. Citrin et al., Plasma Phys. Control Fusion **57**, 014032 (2015).
- [31] F. Zonca et al., Plasma Phys. Control Fusion **38**, 2011 (1996).
- [32] S.P. Gerhardt et al., Nucl. Fusion **51**, 073031 (2011).
- [33] P.B. Snyder et al., Nucl. Fusion **51**, 103016 (2011).
- [34] G.M. Staebler et al., Phys. Plasmas **25**, 056113 (2018).

## R(18-4): Optimize energetic particle distribution function for improved plasma performance

*Description: The improved neutral beam injection (NBI) capabilities that are available on NSTX-U enable a flexible tailoring of the fast ion distribution function resulting from NBI. In collaboration with DIII-D and MAST-U, this milestone will explore the use of different NBI sources and timing of NB injection to improve plasma performance and reproducibility by affecting fast ion-driven instabilities, e.g. through their mitigation or suppression. A main focus of this study is the current ramp-up/early flat-top phase, during which strong fast ion-driven activity can be destabilized (cf. NSTX-U shots from the FY-16 experimental campaign). Instabilities include toroidal and reversed-shear Alfvénic modes (TAE/RSAE) as well as energetic particle modes and fishbones. Sawteeth during the stationary phase of L-mode NSTX-U discharges will also be included. All these instabilities have the potential to cause substantial fast ion redistribution, thus affecting the overall efficiency of NB heating and current drive. If not properly accounted for in simulations, the effects of fast ion driven instabilities make the discharge evolution difficult to predict. Work within the Energetic Particle TSG will leverage and contribute to scenario development activities by the Advanced Scenarios and Control TSG, including the planned collaboration with MAST-U in FY17-18. Once a suitable target scenario is identified, AE and fishbone stability will be assessed. The analysis will include exploration of different NBI combinations (e.g. on- vs. off-axis) and timing in time-dependent simulations to identify the optimum NB mix and resulting safety factor and current profiles that lead to reduced mode activity. Scenario development will rely on the TRANSP code. TRANSP analysis will be assisted by results from the NOVA/NOVA-K and ORBIT codes and from reduced models such as the ‘kick’ and Resonance-Broadening Quasi-linear (RBQ) models to infer the mode stability. Validation of the ‘kick model’ for scenarios with unstable fishbones will be conducted in collaboration with MAST-U. In collaboration with DIII-D, a recently developed criterion to predict the nonlinear behavior of Alfvénic instabilities (e.g. quasi-stationary vs. bursting/chirping) will be validated to gain further confidence in predictions of the fast ion transport instabilities can cause. Test particle simulations of fast ion scattering by plasma turbulence will be performed using the GTS code to assist the validation of the theoretical criterion for instability chirping.*

Optimization of the NB injection scheme requires a detailed knowledge of the behavior of the resulting energetic particle (EP) population, especially when EP behavior departs from (neo) classical predictions. Instabilities driven by the EPs – such as Alfvénic modes (AEs) - are one of the main causes of non-classical behavior. Work in FY-18 has focused on improving analysis and modeling tools to achieve high-fidelity simulations of NB-heated plasmas, including the effects of instabilities.

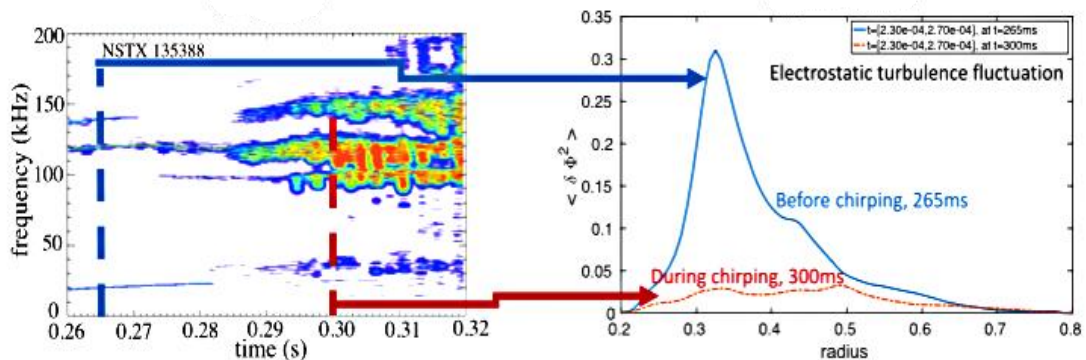


**Fig. R18-4.1:** Left: spectrum of magnetic fluctuations in the TAE range of frequency showing the transition of modes with quasi-stationary frequency to bursting/chirping modes after  $t \sim 290$ ms. Right: radial profile of electrostatic turbulence fluctuations at two times from the GTS code. (Adapted from [R18-4-2].)

Considerable progress has been made in the development of an improved criterion to predict the specific regime of unstable AEs based on the characteristic of the background thermal plasma [R18-4-1]. More specifically, AEs are usually observed in two different regimes characterized by either constant mode frequency and slowly varying amplitude or bursting amplitude with rapid (~1ms time scale) frequency variations (or *chirps*). Each regime can lead to substantially different effects on the EP population, from weak redistribution to convective, explosive transport. The improved criterion builds upon previous theory of wave-particle interaction near marginal stability by extending the treatment to realistic mode structures and values of EP scattering (e.g. by thermal plasma fluctuations). Fig. R18-4.1 shows an example for an NSTX discharge with unstable TAEs transitioning in time from quasi-stationary to bursting/chirping [R18-4-2]. The GTS code is used to compute thermal plasma fluctuations, which provide an estimate for the enhanced EP scattering rates. The criterion successfully recovers the observed AE regime transition as time evolves. Similar validation work on DIII-D plasmas [R18-4-1] gives confidence in the predictions, which have then been applied to ITER

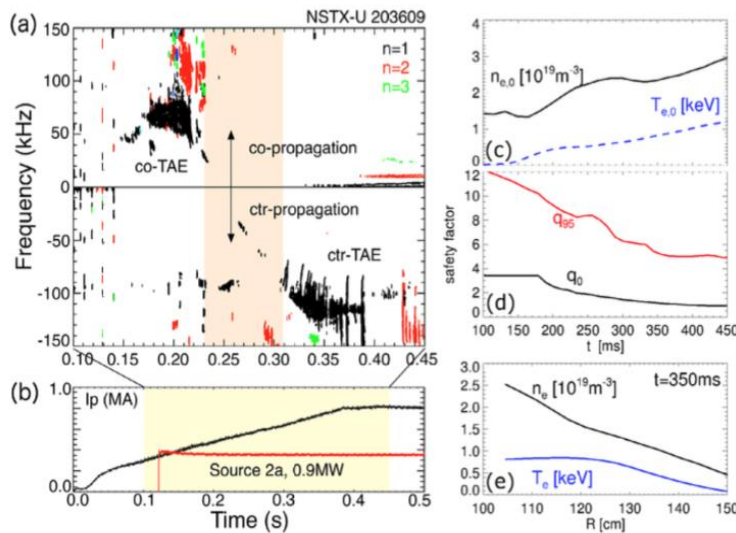


**Fig.R18-4. 2:** (a) Magnetic fluctuation spectrum showing the transition from co-propagating TAEs to counter-TAEs. (b) Waveforms of plasma current and injected NB power. (c) Evolution of central electron density and temperature. (d) Evolution of central and minimum values of the safety factor. (e) Electron density and temperature profiles at  $t=350ms$ . (From [EP-18-4-6]).

scenarios. The criterion suggests that ITER plasmas may be prone to bursting/chirping AEs. Work is ongoing to compare results from the improved AE chirping criterion to numerical modeling of the formation of EP phase-space structures (*holes* and *clumps*) through wave-particle interaction, which is postulated to be at the origin of the insurgence of the AE chirping regime [R18-4-3].

Knowing the expected AE regime is crucial to assess the validity of different EP transport models. For instance, the effects of AE in the bursting/chirping regime may not be accurately reproduced by quasi-linear theory. The development, implementation and validation of a reduced EP transport model known

as Resonance-Broadened Quasi-Linear (RBQ [R19-4-9]) model has been a major focus of EP research in FY-18. The main results are summarized in the final report for the FY-18 Joint Research Target (JRT18) milestone. For the R18-4 milestone, most modeling work has instead involved the reduced “kick model” implemented in TRANSP [R18-4-4] and the hybrid MHD code HYM [R18-4-5] for high-frequency AEs.

An example of NBI optimization to improve performance through reduction of EP transport is provided by NSTX-U scenarios that feature co- and counter-propagating TAE instabilities [R18-4-6]. An example is shown in Fig. R18-4.2. AE stability is first investigated through the kick model in TRANSP, resulting in a satisfactory agreement in terms of unstable AE spectrum and

timing of the instabilities. Based on those results, numerical experiments are performed through TRANSP to add short pulses with different NB sources than in the original discharge. The goal is to perturb regions of phase space where wave-particle interactions take place and possibly alter the AE drive from fast particles to reduce the mode activity. In TRANSP simulations, this approach is successful in reducing the drive for counter-TAEs [R18-4-6]. Dedicated experiments on NSTX-U are needed to confirm the predictions.

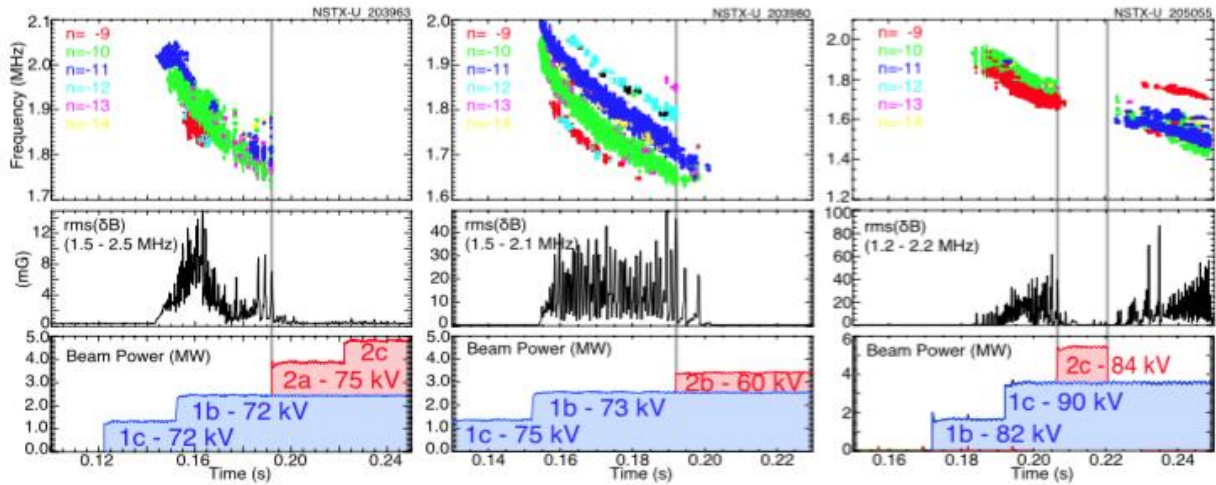


**Fig. R18-4.3:** Examples of suppression of GAE instabilities through injection from the NSTX-U tangential NB sources. (From [R18-4-7]).

Activity of high-frequency Global AEs (GAEs) is also sensitive to details of the fast ion distribution function. In this case, direct experimental evidence has been collected from NSTX-U demonstrating the complete suppression of GAEs in discharges utilizing the new, more tangential NB sources available on NSTX-U [R19-4-7] (see Fig. R18-4.3). The results have been interpreted based on an earlier theory for GAE drive, which distinguishes between drive and damping contributions of fast ion with different value of the  $k_{\perp}r$  product ( $k_{\perp}$ : perpendicular wavenumber;  $r$ : Larmor radius of resonant fast ion). In addition, exhaustive simulations with the HYM hybrid-MHD code [R-18-5] have been performed and show good agreement with the experiment in terms of spectrum of unstable modes as well as their stabilization following NB injection from the more tangential sources.

In addition to Alfvénic modes, the effect of NBI mix on the stability of lower-frequency instabilities such as fishbones and kink modes has been investigated in FY-18 [R18-4-8]. For this purpose, the “kick model” in TRANSP has been extended to handle instabilities characterized by rapid frequency variations such as fishbones. Initial analysis for NSTX and NSTX-U discharges with dominant fishbone activity shows promising results. Simulations can reproduce the experiment - e.g. in terms of measured neutron rate drops - for reasonable values of mode amplitude  $\delta B/B \sim 10^{-3}$ . (No direct internal measurements of the mode amplitude are available for a direct comparison.) Similarly to the TAE analysis, TRANSP simulations enable an assessment of the expected response of the modes to different NB injection geometries. For instance, injection from the 2<sup>nd</sup> NB line is predicted to be beneficial in reducing the fishbone drive, which is mostly attributed to resonances between the mode and trapped fast ions.

However, simulations do not predict a complete suppression, since passing fast ions can also contribute to the drive. Future work will include the effects of a self-consistent calculation of the

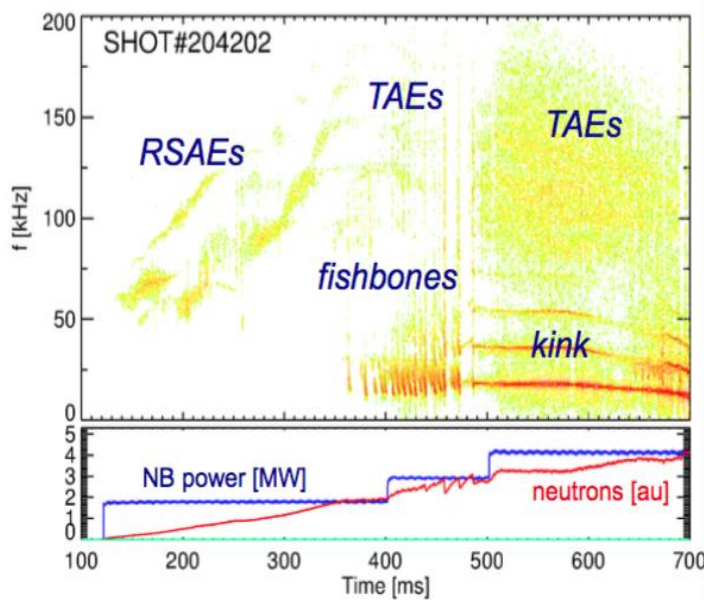


**Fig. R18-4.4:** Top: magnetic fluctuation spectrum showing the coexistence of several types of instabilities, including Alfvénic modes and lower-frequency fishbones/kinks. Bottom: waveforms of injected NBI power and measured neutron rate.

q-profile evolution, as the NB source mix is varied to identify regimes with improved fishbone stability.

Finally, work has started to combine the results from scenarios that are characterized by the presence of a single class of instabilities to the more general case of multiple types of instabilities that present simultaneously. An example of such scenarios from NSTX-U is shown in Fig. R18-4.4. For this case, the analysis is complicated by the potential synergy of instabilities affecting the fast ion distribution in different regions of phase space. For instance, fast ion transport induced by fishbones is expected to affect predominantly trapped particles. Some of the transported particles can turn into passing particles, which will then affect TAE (and possibly GAE) stability. In fact, initial analysis of the discharge

shown in Fig. R18-4.4 doesn't show the same clear results discussed previously for TAE/GAE or fishbones-only cases. The main limitation, at present, is the lack of truly time-dependent, self-consistent calculations of the mode properties within TRANSP, which would require a dedicated MHD module that is presently unavailable.

#### References:

- [R18-4-1] V. N. Duarte et al., 2017 *Nucl. Fusion* 57 054001.
- [R18-4-2] V. N. Duarte et al., 2018 *Nucl. Fusion* 58 082013.
- [R18-4-3] B. J. Q. Woods et al., 2018 *Nucl. Fusion* 58 082015.
- [R18-4-4] M Podestà et al., 2017 *Plasma Phys. Control. Fusion* **59** 095008.
- [R18-4-5] E. Belova et al., 2017 *Physics of Plasmas* **24** 042505.
- [R18-4-6] M. Podestà et al., 2018 *Nucl. Fusion* **58** 082023.
- [R18-4-7] E. D. Fredrickson et al., 2018 *Nucl. Fusion* **58** 082022.
- [R18-4-8] M. Podestà, US Transport Task Force (TTF) Meeting, San Diego CA 2018.
- [R19-4-9] N. N. Gorelenkov et al., 2018 *Nucl. Fusion* **58** 082016.

# NSTX-U Research Results - Additional Research Highlights

## I. Boundary Science

### A. Pedestal Structure and Control

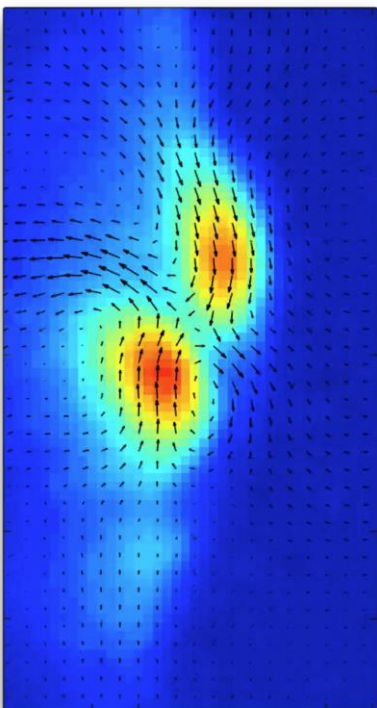


**Fig. PSC-1:** Sample output from novel velocimetric algorithm, for NSTX GPI data with 2 counter-propagating blobs.

The pedestal group is responsible for developing an understanding of the pedestal structure and devising the means to control this structure for maximum fusion performance.

#### ***Low-to-high confinement***

Velocimetry is increasingly used to infer velocities from diagnostic movies like gas-puff imaging (GPI) on NSTX (Fig. PSC-1), as well as beam emission spectroscopy (BES) and other methods, with growing application for flow-turbulence interactions; e.g. in Low to High (L-H) transitions. However, the technique is inherently uncertain because of the so-called “aperture effect.” T. Stoltzfus-Dueck derived averaging techniques that annihilate the invisible part of velocity for the relevant case of incompressible flow ( $\nabla \cdot v = 0$ ). Furthermore, he developed and implemented a novel algorithm for velocimetry of divergence-free flows that compares favorably to earlier codes and allows application of averaging techniques. The new algorithm has been applied to NSTX data during FY-18 for L-H transition studies (Ahmed Diallo, APS-DPP invited, 2017), with further testing, benchmarking, and application expected for FY-19.

#### ***Beam emission spectroscopy using carbon***

The University of Wisconsin beam emission spectroscopy (BES) group had planned to explore the modification of BES detectors on NSTX-U for Carbon and other low-Z impurity measurements. In April 2018, the Wisconsin University group installed optical filters to observe carbon-V charge-exchange (CX) emission at 529 nm, and the first carbon CX measurements with the DIII-D BES detection system were obtained. Fig. PSC-2a shows that the Carbon CX emission signal is about 20% of the neutral beam (NB) D-alpha emission signal. Fig. PSC-2b shows the Alfvén-time scale evolution of an edge-localized mode (ELM) event across the pedestal and scrape-off-layer (SOL) with both NB D-alpha emission and Carbon CX emission. Notably, the NB D-alpha emission and the carbon CX emission exhibit different evolution dynamics following the ELM event. This extension of BES measurement capabilities opens new scientific opportunities for multi-field 2D measurements of turbulence, instabilities, and fast impurity transport. The U. Wisconsin BES collaboration is ready to use the new measurement technique on NSTX-U for impurity research.

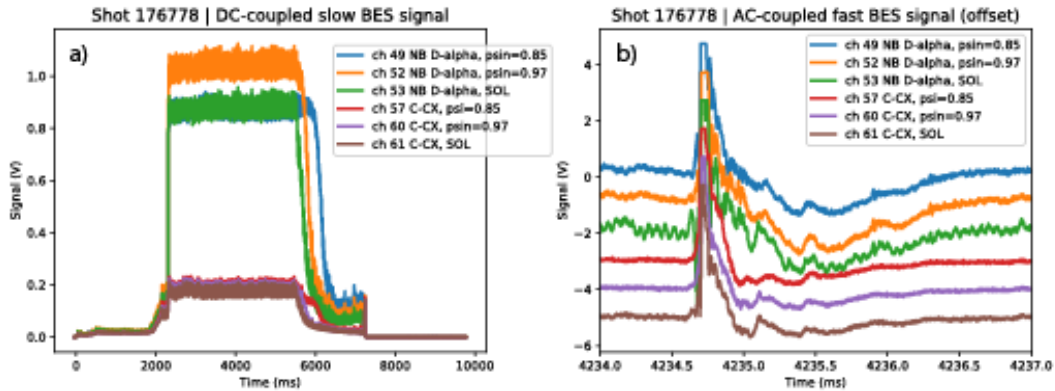


**Fig. PSC- 2:** a) Carbon charge- exchange emission signal. b) Evolution of ELM event across the pedestal and SOL.

### Enhanced Pedestal Physics

The Enhanced Pedestal (EP) H-mode [PED-1, PED-2, PED-3] on NSTX features the development of a wider H-mode pedestal with a significant increase in the carbon temperature (TC) and rotation gradients ( $v_e$ ) in an ELM- and MHD-free period following a large ELM. These discharges achieve improved energy and momentum confinement with a beneficial decrease in the impurity accumulation relative to a standard ELM-free H-mode regime. Analysis completed in FY-18 suggests that the increased  $\nabla T_i$  observed in EP H-mode is consistent with the scaling of the neoclassical ion thermal transport at low ion collisionality.

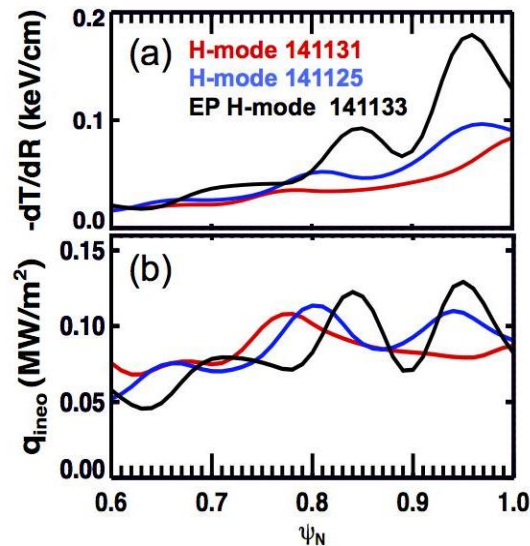


**Fig. PSC-3:** (a) Measured carbon temperature gradient and (b) approximation of the ion neoclassical flux for three discharges. Red and blue traces are ELM-free H-modes while black trace is an EP H-mode discharge.

One element of the recent analysis identified matched H-and EP H-mode discharges for evaluating the changes in transport leading to the larger edge  $\nabla T_i$ . Fig. PSC-3a shows a comparison of the edge  $\nabla T_i$  measured with the CHERs diagnostic for similar H-mode (red and blue) and EP H-mode (black) discharges. The increased edge temperature gradient in the EP H-mode discharge is consistent with the scaling of the leading terms of the neoclassical energy flux [PED-4]:

$$q_{ineo} = -0.68 \frac{\epsilon^{-3/2} q^2 \rho_i^2}{\tau_i} (1 + 0.48\epsilon^{1/2}) n \frac{dT_i}{dr} \sim \frac{-\sqrt{T_i}}{Z_{eff} n_e n_i} \frac{dT_i}{dr} \quad (\text{Equation 1})$$

Rewriting equation 1 gives:

$$-\frac{dT_i}{dr} \sim q_i \frac{\epsilon^{3/2} B^2}{Z_{eff} n_e n_i} \frac{\sqrt{T_i}}{q^2 (1 + 0.48\epsilon^{1/2})} \sim q_i \left( \frac{Z_{eff} n_e n_i}{I_p^2 \sqrt{T_i}} \right)^{-1} \quad (\text{Equation 2})$$

Fig. PSC-3b illustrates the neoclassical energy flux (Equation 1) is similar for the three matched discharges despite the differences in the temperature gradients. This implies that the edge ion temperature gradient increases in the EP H-mode discharge in order to maintain a similar level of energy loss through the ion channel.

When the denominator of Equation 2 is small (i.e. low  $Z_{eff}$ , density and  $q$ ), small changes in the edge density can lead to large changes in the temperature gradient and the global energy confinement. This is demonstrated using a reduced transport model with a simplified neoclassical ion energy transport, anomalous electron energy transport, and ion-electron coupling formulation. Fig. PSC-4a shows the density profiles that serve as an input to the model. A number of self-consistent calculations are performed with successive shifts in the radial position of the density pedestal and a fixed heating profile. The relatively small shift of the density pedestal (1.5 cm total or about 3% of the minor radius) leads to a large change in the ion temperature profile (Fig. PSC-4c) and the ion temperature gradient (Fig. PSC-4d) when the pedestal is in a regime with low edge density. The red points show the profiles measured for EP H-mode discharge 141133 as a reference. The edge pressure profile (Fig. PSC-4b) is slightly shallower within the temperature pedestal ( $R > 1.39$  m) and much steeper inside the top of the temperature pedestal. One active topic of investigation is understanding how the peeling-ballooning stability evolves in EP H-mode discharges such that the recovery from an ELM leads to a stable pressure pedestal with larger width and height.

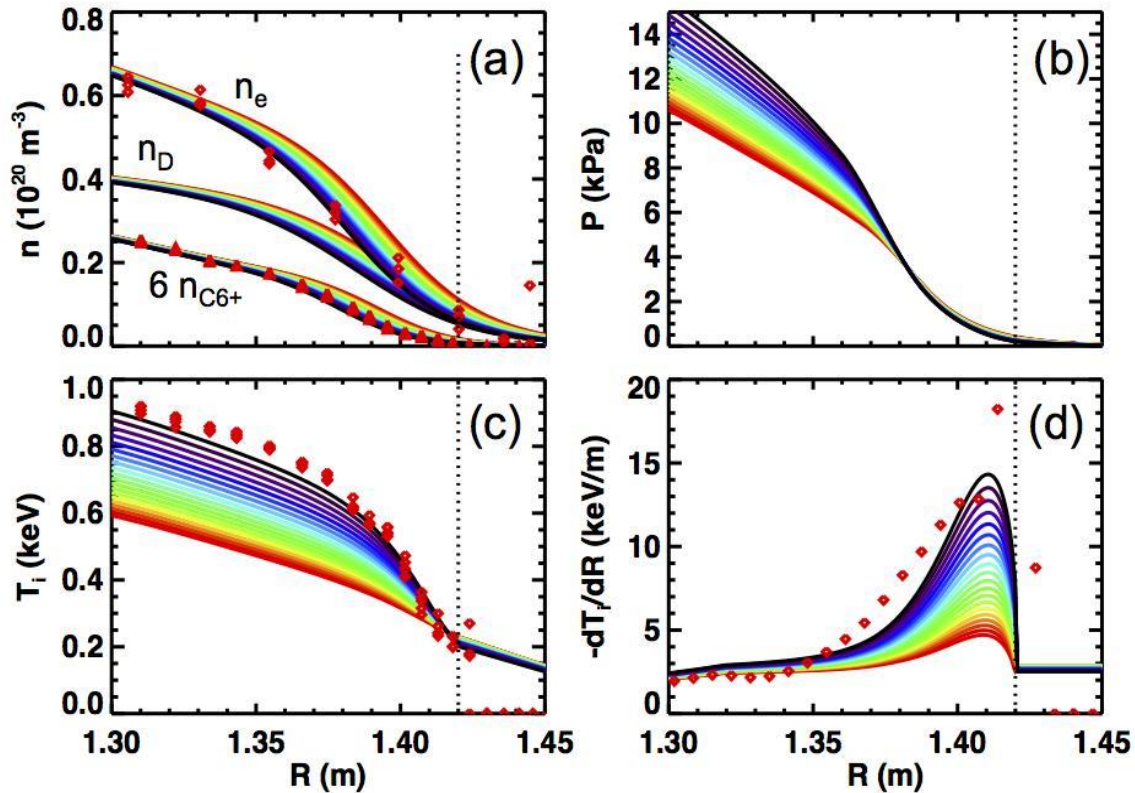


**Fig. PSC-4:** (a) Density profiles input into simple 1D transport model. Each color represents a different calculation where the density pedestal is shifted inwards from red to black. The (b) pressure, (c) ion temperature and (d) ion temperature gradient computed for each different density profile.

The second element of the new analysis developed a database of  $T_i$  profiles in NSTX H-modes to examine the experimental conditions favorable for accessing EP H-mode. The results supported the thesis that EP H-mode is accessed at low edge ion collisionality. Fig. 5a and 5b illustrate that the largest local ion temperature gradients (y-axis) are accessed in regions with low carbon (Fig. PSC-5a) and electron (Fig. PSC-5b) density. The contours convey the occurrence rate within the database, where each color represents a factor of two increase (black = 1, red > 128). The horizontal dashed line at  $dT_i/dR = 0.12$  keV/cm is a general criteria for identifying EP H-mode discharges where about 10% of the profile database have gradients above this threshold. Fig. PSC-5c shows the gradient database plotted against the logarithm of the leading terms of the neoclassical ion gradient. The light dotted lines represent contours of constant heat flux ( $q_i$ ). The red triangles show the database entries for EP H-mode discharge 141133. The points generally follow these contours, connecting the most common regime for H-mode operations (orange region) to the EP H-mode regime at lower density.

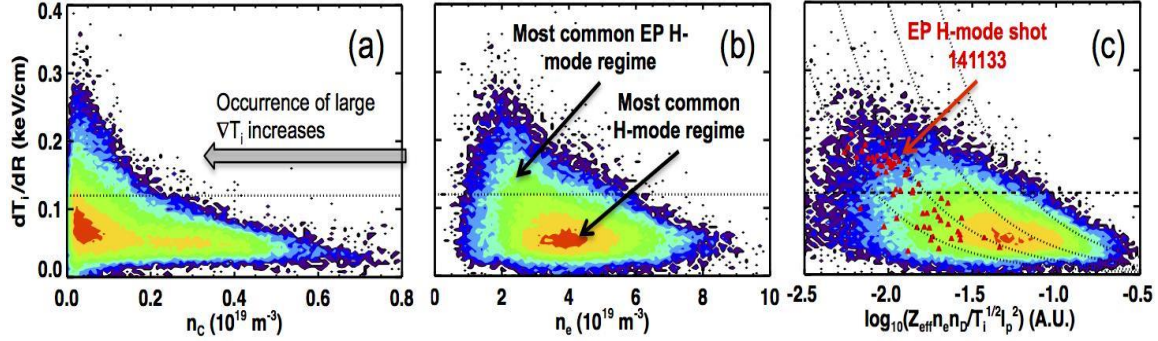


**Fig. PSC-5:** Database for the maximum measured  $dT_i/dR$  in H-mode profiles on NSTX. Red indicates a large number of entries, black is a single entry. The profiles with a gradient exceeding 0.12 keV/cm occurs at (a) small carbon density, and (b) small electron density. (c) The maximum gradient is consistent with the scaling described in equation 2 where the dotted lines represent a constant  $q_i$ .

The large ion temperature gradients achieved in EP H-mode surpass the maximum gradients predicted from neoclassical codes such as NCLASS and GTC-NEO. Future work will use multi-species global delta-f (GTC-NEO) and full-f (XGC0) neoclassical codes to investigate the source of this discrepancy. The present analysis supports that the increased gradients in the edge temperature is consistent with the scaling derived from the leading terms of neoclassical transport theory, even if the quantitative agreement between theory and measurements has yet to be established.

A common observation of H-mode discharges with reduced neutral recycling is that the density pedestal quickly recovers after an ELM, but the pedestal is briefly shifted inwards relative to the time prior to the ELM. Presumably, this temporary shift in the density pedestal is due to a reduction of the turbulence driving particle transport while the temperature gradient is recovering more slowly. As a result, a period of reduced collisionality can occur during the ELM recovery where the ion temperature pedestal briefly “overshoots” the pre-ELM levels. An active area of research is to identify the salient mechanisms that reinforce the low collisionality and inward shift of the density pedestal driving a positive feedback loop toward improved energy confinement.

One possible mechanism driving the feedback is the reduction of the neoclassical impurity pinch with lower collisionality and larger temperature screening. A smaller impurity pinch leads to an inward shift of the impurity density profile, reinforcing the lower collisionality by reducing  $Z_{\text{eff}}$ . Another possible mechanism is a reduction in the electron thermal and particle transport with larger ion temperature gradient scale length ( $\nabla T/T$ ), as shown with GS2 calculations [PED-3]. A reduction in the electron thermal transport impacts the ion transport via a reduction in the energy loss to ion-electron coupling, especially near the bottom of the pedestal.

A common characteristic of EP H-mode discharges is reduced neutral fueling via wall conditioning (such as larger lithium depositions or recent boronization) and efficient gas fueling.

The largest gradients achieved in an H-mode discharge were produced in a unique experiment with strong wall pumping from lithium wall conditioning and efficient fueling using the supersonic gas injector [PED-2]. The favorable positive feedback in the pedestal structure that is initiated by accessing lower edge ion collisionality motivates the continued focus on developing actuators for controlling the edge pedestal collisionality that are compatible with large core density and heat flux mitigation on NSTX-U.

## References

[PED-1] Maingi, R. et al., The enhanced pedestal H-mode in the National Spherical Torus experiment. *J. Nucl. Mater.* **390–391**, 440–443 (2009).

[PED-2] Maingi, R. et al., Triggered Confinement Enhancement and Pedestal Expansion in High-Confinement-Mode Discharges in the National Spherical Torus Experiment. *Phys. Rev. Lett.* **105**, 135004 (2010).

[PED-3] Gerhardt, S. P. et al., Progress in understanding the enhanced pedestal H-mode in NSTX. *Nucl. Fusion* **54**, 83021 (2014).

[PED-4] Wesson J 2011 Tokamaks 4th Edition (Oxford: Oxford University Press).

## B. Divertor and Scrape-off Layer

### Edge turbulence

Turbulence at the edge of NSTX or NSTX-U is important since it affects plasma transport across the edge, and so controls to some extent the width of the high heat flux region at the divertor plate. Contrary to our usual intuition about tokamak turbulence, it would be *good* to have a higher level of turbulent transport in the edge to reduce the peak heat load at the divertor plate. This turbulence can be mathematically described by a two-dimensional cross-correlation function, which measures its spatial structure perpendicular to the magnetic field. A new paper was published in FY2018 on the two-dimensional turbulence cross-correlation functions in the edge of NSTX [1], which analyzes in great detail previous measurements made on NSTX using a gas puff imaging diagnostic. Typical results, as illustrated in Fig. DSOL-1, show a rather complex pattern in which the correlation function varies with the radial location in the plasma (varying from left-to-right from 6 cm inside the separatrix to 6 cm outside the separatrix), and with the specific plasma conditions (varied from the top to the bottom row). These are among the most detailed measurements of this kind ever made in a tokamak. Although the interpretation of these results in terms of both edge turbulence theory and turbulent transport is not yet clear, we believe that these results can be used to validate theoretical simulations presently under development, such as the XGC-1 code at PPPL.

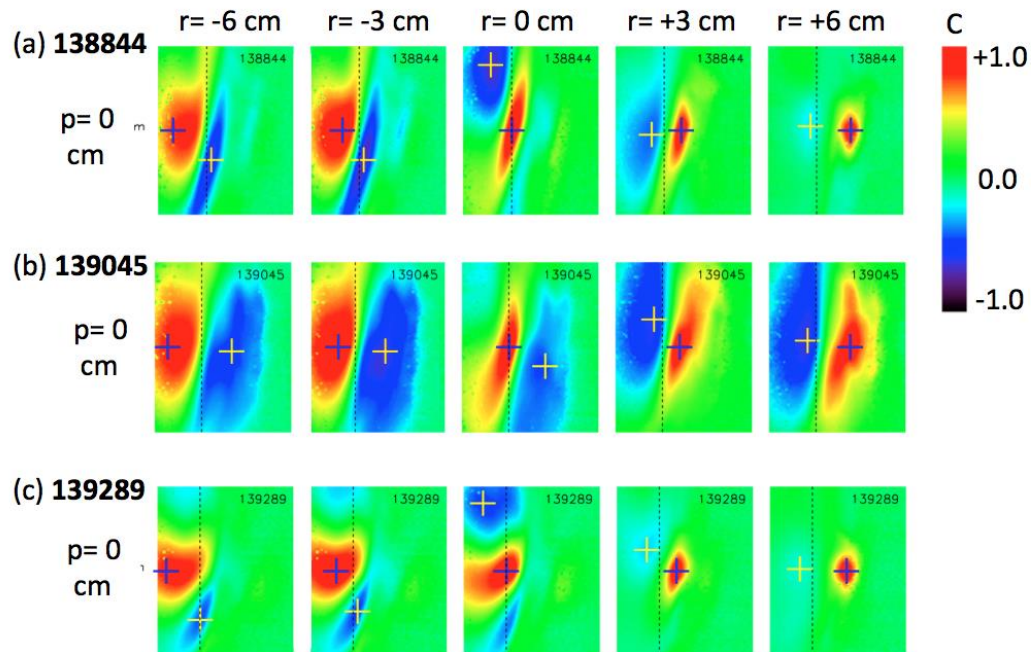


**Fig. DSOL-1:** Two-dimensional turbulence cross-correlation functions over 24 cm radial (i.e. horizontal) by 30 cm poloidal (vertical) region at the edge of NSTX. The magnitude of the correlation is shown in color (legend at right), where red indicates a high correlation with respect to the dark crosses, and blue indicates a negative correlation region. Each frame shows the correlation function at a given radius (varying from left-to-right) and for a given shot (varying from top to bottom). The separatrix location is shown by the vertical dotted line in each frame.

### ***Blob-hole correlation model***

As discussed above, edge turbulence, which is potentially beneficial for mitigating high heat fluxes on the divertor target plates, has been studied experimentally in NSTX and NSTX-U using a two-dimensional cross-correlation technique [1]. Motivated by the experimental findings, modeling studies of blob-hole correlations in the edge plasma have been carried out and a report has been prepared and published [2]. In the new work, the evidence for inward propagation of holes was investigated in detail. “Holes” are negative-going density perturbations left behind when positive-going “blobs” are formed in the edge plasma. The recent 2-D cross-correlation analysis of NSTX GPI data [1] showed consistent negative regions which are now qualitatively explained by the new blob-hole model. The expected inward radial motion of holes is also qualitatively consistent with the measured inward direction of the minima in normalized GPI images. Quantitative comparison awaits large discharge-specific simulations. In addition to improving our understanding of edge and scrape-off layer turbulence in general, inward hole propagation may be of interest to understand possible turbulence spreading from the separatrix region into the pedestal and inward transport of impurities.

### ***Filamentary instabilities in the edge, SOL and divertor legs***

Filamentary instabilities in typical NSTX, NSTX-U and MAST plasma shapes have been studied using the ArbiTER eigenvalue code. This work has explored the 3-D structure of edge/SOL turbulence to determine the conditions under which filamentary turbulent structures can be expected to connect turbulence at the midplane to the divertor target in an ST geometry. It is expected to be relevant to turbulent spreading of the particle and heat flux exhaust channels in the SOL. Calculations over a range of values of temperature and density show quantitative agreement with analytical theory in two limiting cases. In the non-connected case, mode structure is dominated by parallel resistivity, resulting in a mode structure that depends on  $nT^{-3/2}$ . In the connected case, the mode structure is dominated by sheath resistivity resulting in mode structure that depends on  $nT^{-1/2}$ . This work and analytical theory have been applied to understand GPI measurements in NSTX and NSTX-U which show midplane-target disconnection near the separatrix in the resistive X-point regime. [3] In separate but related work, modeling of filamentary instabilities in the inner and outer divertor legs with the ArbiTER eigenvalue code has begun [4].

### ***Connection of midplane turbulence to divertor target plate in NSTX L-mode discharges.***

The connection between midplane turbulence and the divertor target can be important to understand heat flux width scaling, to interpret divertor measurements and transport (usually based on average quantities) and more in general to understand the 3D structure of SOL turbulence. As reported in the 2016 NSTX-U end of the year report, a decrease in the divertor fluctuation level, estimated from fast camera imaging of neutral lithium emission, was observed approaching the outer divertor strike point in NSTX Ohmic L-mode discharges. The region with reduced fluctuations coincided with the region with reduced correlation with midplane turbulence, as estimated from the zero-delay cross correlation between GPI and divertor imaging. The radial profile of the correlation is shown in Fig. DSOL-2(a). Large correlation

( $\sim 0.7$ ) was observed in the far SOL and progressively decreased approaching the separatrix. Recent work examined the divertor turbulence characteristics in the disconnected region, in terms of turbulence spatial scales and motion, correlation with midplane blobs and comparison with analytical models for mode disconnection.

Midplane and divertor target turbulence correlation lengths and motion were evaluated from zero-delay and time-delayed 2D cross correlation maps, respectively, in five repeated Ohmic L-mode discharges. Midplane radial and poloidal correlation lengths were on the order of 4 cm and 6-7 cm, respectively. No change in the midplane turbulence correlation lengths was observed across the divertor-disconnected region. Radial turbulence velocities were between 0.5-1 km/s while poloidal turbulence velocities were  $\sim 1$ -3 km/s (poloidally downward). The radial region showing turbulence disconnection  $\psi_N \sim 1.00$ -1.08 coincided with the minimum in the radial velocity and the largest negative poloidal velocity. Comparison between divertor and midplane turbulence motion showed generally very good agreement in both poloidal and radial motion of the filaments across the entire connected region. Divertor radial correlation lengths were in agreement with midplane correlation lengths in the far SOL. A reduction in the divertor radial correlation length was observed in the disconnected region as shown in Figure DSOL-2(b). Poloidal correlation lengths were a factor of  $\sim 2$  larger in the divertor than at midplane across the entire radial profile.

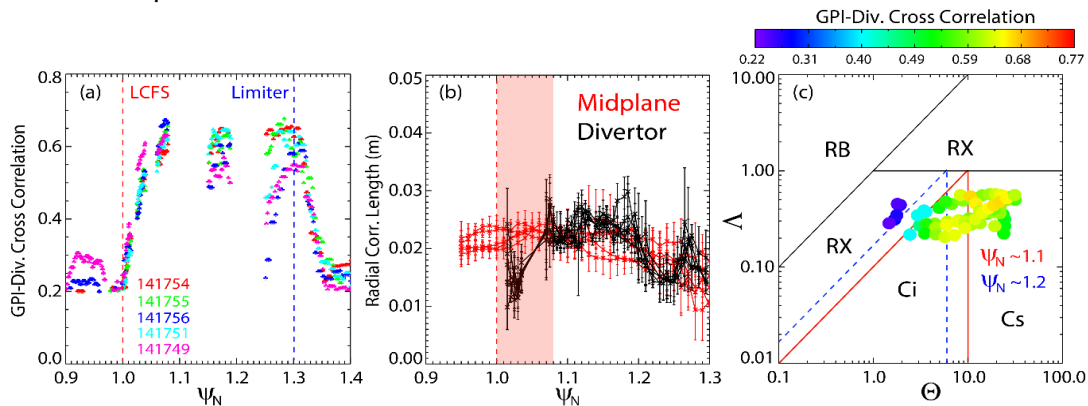


**Fig. DSOL-2 (Left to Right):** (a) Cross correlation between midplane and divertor turbulence, (b) midplane and divertor correlation lengths, (c) midplane to divertor turbulence cross correlation mapped onto blob regime diagram.

The experimental observations of turbulence disconnection were compared with the electrostatic two-region model [Myra, PoP 13, 112502 (2006)] and are summarized in Fig. DSOL-2(c). Here, experimental values of the turbulence correlation between midplane and divertor are plotted in the blob regime diagram as a function of normalized blob size ( $\Theta$ ) and normalized collisionality ( $\Lambda$ ) for five repeated L-mode discharges. In the blob regime diagram, experimental regimes ranged from the sheath-connected regime (Cs) in the far SOL to the connected ideal-interchange (Ci) and resistive X-point (RX) regimes. From the far SOL to the separatrix, the blob regime changed due to a change in normalized blob size with an approximately unchanged normalized collisionality. The color of each experimental point corresponds to the measured cross correlation. Blob disconnection is observed transitioning from the Cs regime to the Ci and RX regimes, confirming the role of X-point geometry and collisionality for the disconnection of midplane instabilities from the divertor target. The

observed decrease in the turbulence radial velocity approaching the separatrix is also expected from the same theory as the X-point shear provides the short circuiting of the polarization charge driving the filament radial motion.

### ***Divertor detachment optimization in an unfavorable open geometry horizontal target divertor configuration in NSTX and NSTX-U***

Analysis of the divertor geometry effects in NSTX relevant to high-triangularity NSTX-U divertor configurations continued. The analysis of the NSTX experiment that compared several standard lower single null divertor geometries differing mainly by the outer divertor leg length and orientation with respect to the divertor plate was summarized in the PSI 2018 conference presentation [5]. Fig. DSOL- 3 shows the configurations compared.

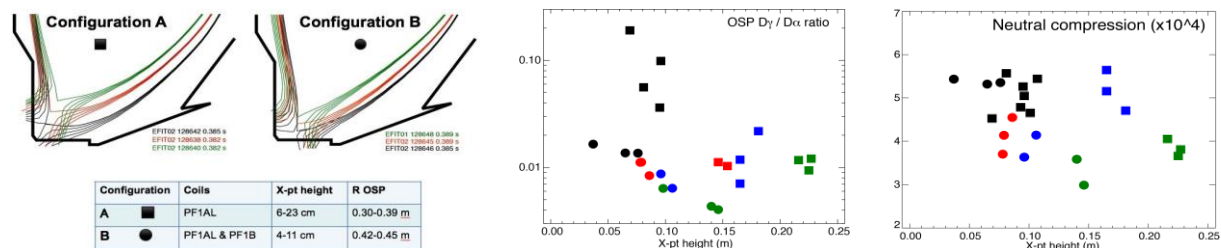


**Fig. DSOL-3:** Divertor configurations studied in the NSTX experiment, as well as outer strike point  $D_y / D_\alpha$  line intensity ratios and divertor neutral compression as functions of the X-point height for the two types of configurations.

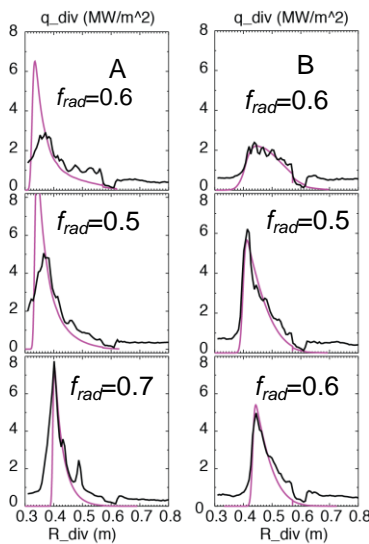


**Fig. DSOL-4:** A comparison of divertor heat flux profiles measured in Configurations A and B at different X-point heights (ref. to Fig. 1) and the profiles predicted by the JEMv3 model.

The divertor poloidal leg length variation resulted in several effects, as some divertor configurations were characterized by: longer connection length (hence more parallel/perpendicular dissipation and different parallel gradients), higher degree of

divertor plasma “plugging efficiency” (hence higher divertor neutral compression at lower X-point height), and higher poloidal flux expansion (resulting in much reduced deposited peak heat flux). The divertor poloidal leg orientation affected the poloidal angle at which magnetic field lines hit the divertor plate. The configurations with the angle less than 90 degrees directed recycling neutrals toward the separatrix, led to enhanced recycling and eventually to enhanced volumetric losses (“the vertical target plate” effect). In other configurations with the angle higher than 90 degrees, the neutrals were recycled toward the outer SOL and did not contribute to ionization within the divertor. Re-ionization of recycling neutrals in the divertor chamber termed “flux amplification” is an essential feature of the high-recycling divertor regime. As the recycling is increased, the divertor density increases, the

divertor temperature further decreases, leading to an increase in the  $P_{rad}$  and pm loss factors, loss of parallel pressure balance, and a transition to detachment. The experimental scans were compared to two models: the two-dimensional multi-fluid plasma model with charge state

resolved carbon impurity implemented in the UEDGE code, and a reduced heat flux model JEMv3 used for divertor heat flux estimated in NSTX-U divertor analysis. Both models suggested that divertor configurations with the “vertical target effect” (Conf. A above) had higher energy dissipation and hence were closer to detachment.

In summary, the standard divertor configurations with lower X-point height, higher connection length and low poloidal separatrix angle in NSTX appeared favorable for divertor detachment: inherently high flux expansion led to reduced peak heat flux, and plasma plugging and higher recycling lead to lower divertor temperature and higher density. Such configurations overcome unfavorable effect created by open horizontal plate divertor configuration. These configurations are naturally created in NSTX and NSTX-U with the existing (and planned) divertor coil layout.

### ***M3D-C1 / TRIP3D modeling of divertor strike point splitting due to error fields***

Divertor strike point splitting in NSTX-U in the presence of error fields has been calculated. M3D-C1 was used to calculate the perturbed equilibrium, and TRIP3D was used to integrate the magnetic fields in those equilibria to calculate footprint splitting. Splitting due to misalignments in poloidal field coils is found to be small, but splitting up to 10 cm is found to be possible for 5 mm / 5 mrad misalignment of the TF inner leg.

Nonaxisymmetric magnetic field perturbations due to error fields produce complex 3D edge magnetic topologies that alter the properties of the heat and particle flux distributions on the target plates. The M3DC1 code is used to simulate the perturbed equilibria due to the shift and tilt of poloidal and toroidal field coils and the field line tracing code TRIP3D is used to estimate their impact on the footprints.

While the effect the misalignment of several poloidal field coils separately has on the footprint is negligible for shifts up to 5 mm and tilts up to 5 mrad, a rigid 5 mm shift of the toroidal field coils is found to result in a 10 cm spread footprint on each of the outer divertor plates (Fig. DSOL- 5). A combination of shift and tilt of the toroidal field coils produces larger or smaller footprints than shift alone depending on the phasing between the two (Fig. DSOL-6). These results will be used to inform the precision needed to install poloidal and toroidal field coils in NSTX-U.

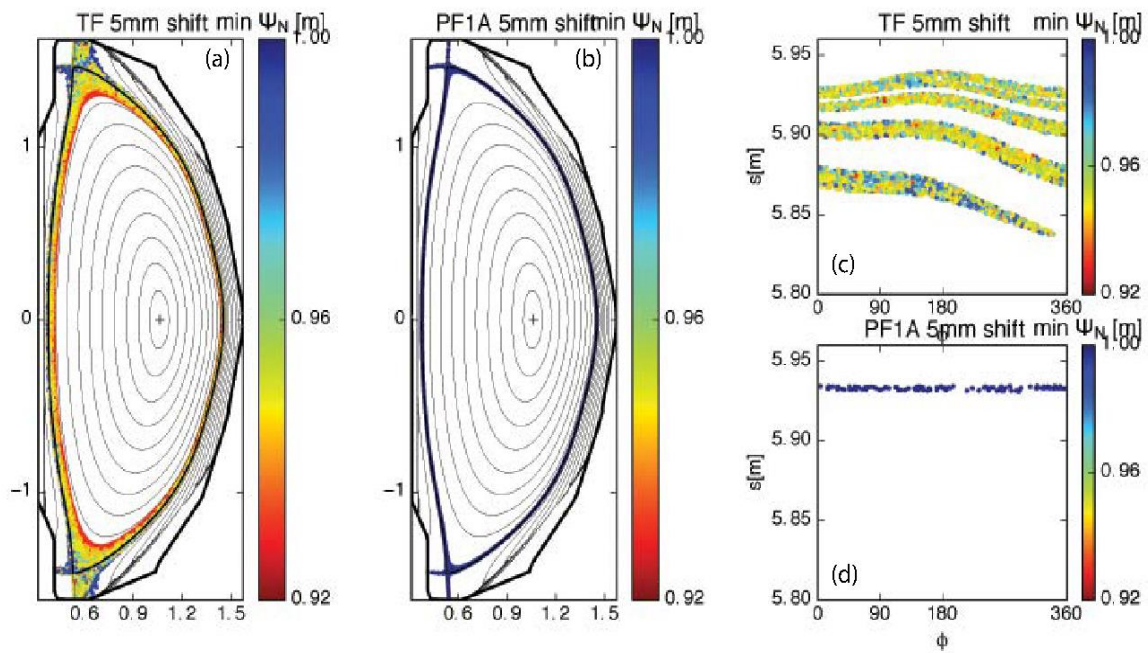


**Fig. DSOL-5:** Poincare plot of the magnetic field lines that hit the wall due to a 5mm shift of the toroidal field coils (a) and of the poloidal field coil 1A (b). (c) and (d) their footprints on the low outer divertor. The colors represent the minimum  $\psi_N$  reached by the field line.

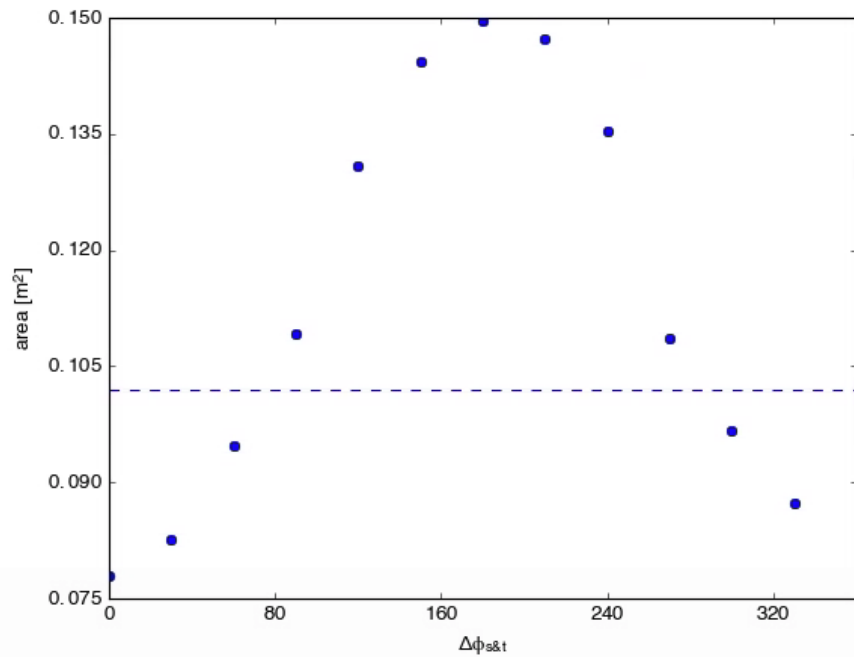


**Fig. DSOL-6:** Footprint area in the top outer divertor as function of the phasing between a 5 mm shift and a 5 mrad tilt of the toroidal field coils. The dashed line corresponds to the area of the footprint due to a 5 mm shift only.

## References

- [1] S.J. Zweben, D.P. Stotler, F. Scotti and J.R. Myra, "Two-dimensional turbulence cross-correlation functions in the edge of NSTX," *Phys. Plasmas* **24**, 102509 (2017).
- [2] J. R. Myra, S. J. Zweben and D. A. Russell, "Blob-hole correlation model for edge turbulence and comparisons with NSTX gas puff imaging data," *Plasma Phys. Control. Fusion* **60**, 075015 (2018).
- [3] F. Scotti, V. Soukhanovskii, S. Zweben, D. Baver and J. Myra, "SOL and near-separatrix intermittent filaments in the NSTX and NSTX-U divertor," 2018 PSI Conference, Princeton USA.
- [4] D. A. Baver, J. R. Myra, F. Scotti and S. J. Zweben, "ArbiTER studies of divertor leg modes in spherical tokamaks," Transport Task Force Workshop, San Diego, California, May 8-11, 2018.
- [5] V. A. Soukhanovskii, O. Izacard, F. Scotti, R. Maingi, R. E. Bell, R. Kaita, S. Kaye, B. P. LeBlanc, J. E. Menard, R. Raman, "Divertor detachment optimization in an unfavorable open geometry horizontal target divertor configuration in NSTX and NSTX-U", Poster 479, 23rd International Conference on Plasma Surface Interactions in Controlled Fusion Devices June 18-22, 2018 Princeton, New Jersey, to be submitted to Nuclear Fusion.

## C. Materials and Plasma Facing Components

### ***Fundamental surface science of PFCs for improved plasma performance in NSTX-U***

We have continued to make progress during FY-18 on fundamental surface science studies of Li films related to Li and Li-coated PFCs for improved plasma performance in NSTX-U. In tokamak experiments, the presence of impurities and reactions with background gases inevitably creates Li compounds. Thus, it is important to understand the retention and sputtering dynamics of deuterium (D) in Li and Li compound (Li-O and Li-C-O) films in order to understand and most efficiently make predictions on plasma performance. Energetic  $D_2^+$  incident on thin Li films was shown to readily form LiD leading to a lower Li sputtering yield than the sputtering yield of pure Li. Measured sputtering yields for thin LiD films agreed with previous simulations and bulk erosion measurements. The  $He^+$  sputtering yield of pure Li was 2-3 times higher than the sputtering yield of  $D_2^+$  on LiD. Incident 1000-1200 eV/ $D_2^+$  sputtered Li-O films at a slower rate than  $D_2^+$  on LiD and Li-C-O films [BPR-MP-1].

Deuterium retention in pure Li and composite Li-O and Li-C-O films was also studied as a function of time after these films were exposed to 450 eV  $D_2^+$  ion irradiation. The amount of D retained in both Li and Li-O films at 300 K decreased at the same rate by 45% after 16 hours. The amount of D retained in Li-C-O films was found to be independent of time up to 3 days. Increasing the temperature of pure Li films to 420 K increased this rate of decrease by 50%, while increasing the thickness of the lithium film from 3 to 16 atomic layers had no effect on the rate of retention decrease [BPR-MP-2].

In addition to ultrathin film studies, Anurag Maan, a UTK graduate student under the supervision of Prof. David Donovan (UTK), has been working with PPPL to perform D retention experiments on thick pure and oxidized lithium samples. These samples were characterized by high-resolution X-ray photoelectron spectroscopy (HR-XPS) and Rutherford backscattering spectrometry (RBS), and are relevant to the results for thick films formed by repeated Li evaporation on PFCs over the course of experimental campaigns. These experiments used our lab-based plasma source to irradiate samples under controlled conditions and nuclear reaction analysis (NRA) analysis of these samples exposed to a  $D_2^+$  fluence on the order of  $10^{21} \text{ m}^{-2}$ . [BPR-MP-3]

Tokamak PFCs have surface roughness that can cause microscopic spatial variations in erosion and deposition and hence influence material migration, erosion lifetime, dust and tritium accumulation, and plasma contamination. However, high spatial resolution measurements of deposition on the scale of the surface roughness have been lacking to date. In collaboration with Dr. Charles Skinner (PPPL) and others, we have obtained elemental images of graphite samples from NSTX-U and DIII-D DiMES experiments performed in our lab with a Scanning Auger Microprobe (SAM) at sub-micron resolution that show strong microscopic variations in deposition and correlate this with 3D topographical maps of surface irregularities. The NSTX-U samples were boronized and exposed to deuterium plasmas, and the DiMES samples had localized Al and W films and were exposed to dedicated helium plasmas. Topographical maps of the samples were performed with a 3D confocal optical microscope and compared to the elemental deposition pattern. The results revealed localized deposition concentrated in areas shadowed from the ion flux, incident in a direction calculated (for the DiMES case) by taking account of the magnetic pre-sheath [BPR-MP-4].

### ***Alternative PFC Concepts***

Liquid metal plasma-facing components (PFC) have potential application as divertor and first wall surfaces in fusion reactors. One particular embodiment of a liquid metal PFC is one constrained by a porous substrate as to stabilize the surface against electromagnetic body forces or surface shears. Numerous approaches have been reported in the literature for different methods of optimizing the porous layer including wire meshes, flame-sprayed surfaces, laser-texturing, and chemical-vapor infusion lattices. Given the range of options for producing these porous layers, it is necessary to consider the pathways to optimization one may take.

Recent theoretical treatments of the porous material indicate optimization is possibly through use of a permeability-enhanced Hartmann number. These calculations, however, do not account for the impact of finite saturation on the wicking behavior if the liquid is in the porous substrate. The simplest expression of capillary pressure,  $P_c$ , is as follows:  $P_c = 2 \sum \cos(\gamma) / r_p$  where  $\sum$  is the surface tension of the liquid,  $\gamma$  is the contact angle, and  $r_p$  is the pore radius. It is known in other porous systems that the capillary pressure varies as a function of the saturation of the material from values exceeding the simple expression at near-zero saturation to zero capillary pressure once fully saturated. The actual capillary pressure relative to the nominal pressure in the equation above is often determined empirically and is referred to as the Leverett

J-function. One example J-function for compacted sands indicates the capillary pressure can be less than 30% of the nominal value for a range of 50-100% saturation which reduces sorptivity of the media and would impact passive replenishment rates.

If a liquid metal PFC is to operate with non-zero capillary pressure, as during passive replenishment, then a saturation of less than 100% is required. However, incomplete saturation implies the possibility of exposed substrate. This exposed substrate would be subjected to plasma bombardment and its destruction through plasma bombardment would defeat one of the main features of a liquid PFC. To explore the effect of finite saturation, we conducted particle bombardment on a novel, porosity-enhanced flame-spray material in the IGNIS experimental device at the University of Illinois. The composition of a liquid-metal infused, porous substrate surface is analyzed with high-resolution, *in-situ* XPS and LEISS before and after bombardment of the surface at energies between 250-500 eV/amu. The rate of passive recovery of a protective layer will be examined in both hydrogen and helium environments using *in-operando* LEISS, monitoring the appearance of Li and Mo [BPR-MP-5].

### ***Whole Machine Transport Processes***

The National Spherical Torus Experiment Upgrade (NSTX-U) operated in 2016 with graphite plasma facing components, periodically conditioned with boron to improve plasma performance. Following each boronization, spectroscopic diagnostics generally observed a decrease in oxygen influx from the walls, and an *in-vacuo* material probe (MAPP) observed a corresponding decrease in surface oxygen concentration at the lower divertor. However, oxygen levels tended to return to a pre-boronization state following repeated plasma exposure. This deconditioning occurred on a faster time scale when conditioning with less boron. This behavior is interpretively modeled using the WalldYN mixed-material migration code, which couples local erosion and deposition processes with plasma impurity transport in a non-iterative, self-consistent manner that maintains overall material balance and has recently been applied to ITER [BPR-MP-6]. A new model for spatially inhomogeneous thin films has been developed for WalldYN, which allows for the differentiation between conditioning films of different thickness. This new capability improves model agreement with observed spectroscopic data. Plasma backgrounds representative of NSTX-U conditions are reconstructed from a combination of NSTX-U and NSTX datasets. Likely mechanisms driving the observed evolution of surface oxygen are examined, as well as remaining discrepancies between model and experiment and potential improvements to the model [BPR-MP-7].

### ***In vacuo material characterization with MAPP***

The Materials Analysis and Particle Probe (MAPP) was installed in NSTX-U and used for the first time during the FY 2015 experimental campaign. MAPP is an *in vacuo* materials diagnostic facility designed to measure PFC chemistry on a day-to-day or shot-to-shot basis, using X-ray Photoelectron Spectroscopy (XPS) and other accompanying techniques.

Although all of the data gathered during the campaign was on a daily basis, by the end of the campaign, the shot-to-shot analysis was possible. This was achieved by integrating on-line the remote operation of MAPP's analysis tools plus the insertion and retraction of the samples holder via remote control. The data provided daily by MAPP in combination with visible light spectroscopy, and in particular the atomic concentrations of elements on the surfaces, suggests that plasma performance in NSTX-U is strongly affected by the concentration of oxygen on the walls. An increased concentration of this element on the walls seems to increase its presence as an impurity in the plasma, hence decreasing plasma performance.

An example of this can be seen below, in Fig. MPF-1 a and b. Fig. MPF-1a shows the evolution of the atomic concentration of an ATJ graphite sample in MAPP. Shot 203935 is chosen to represent "before boronization," as the previous one had been five days prior. 203971 is after boronization, and 203991 is after a day of high-performance operations. Fig. MPF-1b shows that shot 203971 has better performance compared to 203935. The duration increased from 325 ms to over 500 ms, the confinement time tripled, the store energy doubled, and the maximum electron density almost tripled, all with the same Neutral Beam Injection (NBI) power. Figure 1b also shows a reduction in ELMs in shot 203971. This suggests better performance following boronization. Shot 203991 took place following another day of high-performance discharges. The performance of this shot decreased to almost what was observed prior to boronization in shot 203935, which is correlated with an increase in oxygen concentration at the surface of the ATJ sample as measured by MAPP.

After FY2015 experimental campaigns, offline experiments have been performed since at the IGNIS facility at UIUC. These experiments support trends observed with MAPP: with increased deuterium irradiation, oxygen concentration at the surface increases. Further irradiation, however, causes a decrease in the atomic concentration at the surface of both oxygen and boron due to sputtering of boron oxides. This indicates a need for repeated boronizations, which was observed in operations as well. Post-mortem analysis was performed on cored samples of NSTX-U tiles during FY 2018. XPS depth profiles were performed on three different samples taken from different locations in NSTX-U: the center stack, lower inboard divertor, and lower outboard divertor. The center stack and lower outboard divertor (i.e. near the strike points) show similar chemistries to the MAPP samples. However, the boron and oxygen concentration was higher in the lower outboard divertor. This is possibly due to a lower deposition of boron during boronization, which in turn would bind less oxygen. Additional experiments will be performed on cored samples to investigate hydrogen retention on graphite surfaces with both boron and lithium films in FY19.

In early 2018, MAPP was removed from the NSTX-U test cell for transport to UIUC, where it is currently being reassembled. In Illinois, the analyzer will be improved in order to have better energy resolution in the data, and the chamber will be upgraded in order to allow for more diagnostics to be added. These diagnostics include low-energy ion scattering spectroscopy (LEISS), using both forward and backward scattered ions. In a reconfigured chamber, the forward-scattered ions could also be used for direct recoil spectrometry (DRS), a technique that can directly measure hydrogen isotopes at the surface.

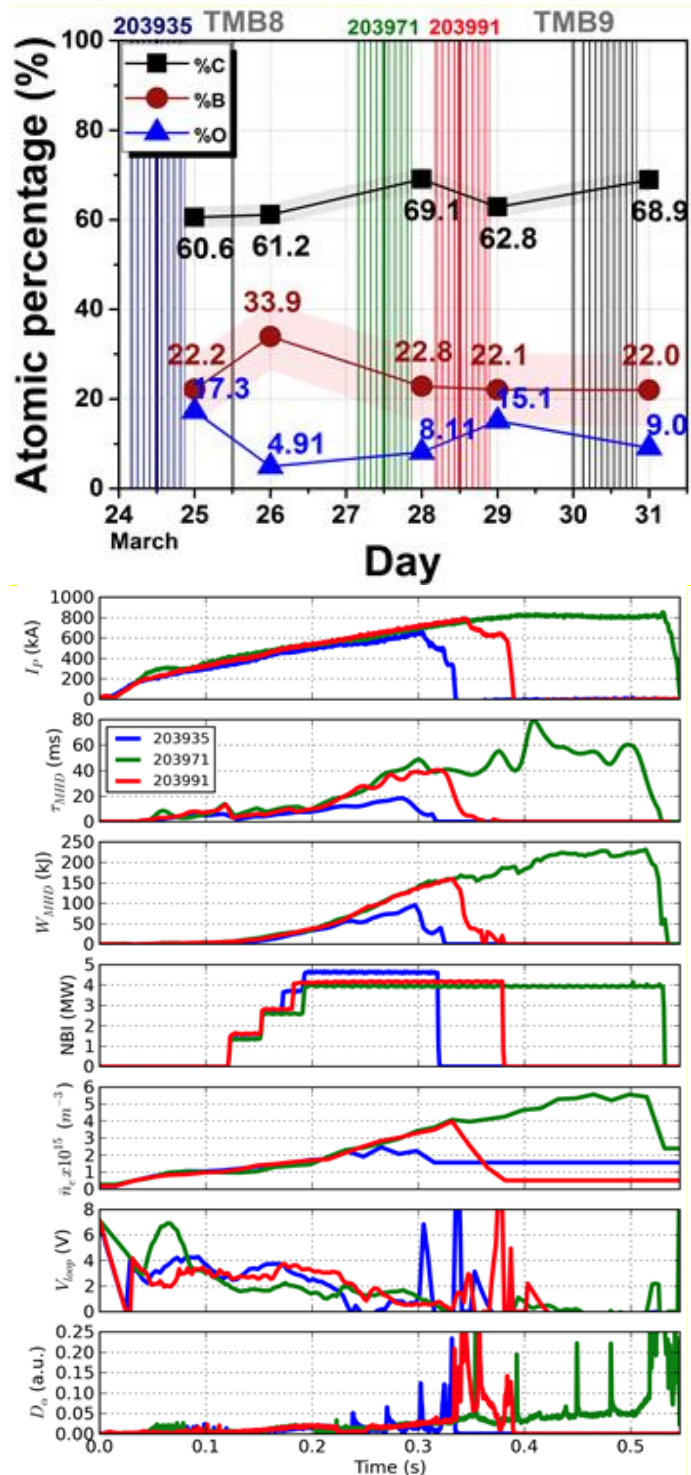


**Fig. MPF- 1a):** Atomic concentrations of ATJ sample obtained with data from a). The vertical lines mark the plasma shots shown in b. **Fig. MPF-b):** Relevant plasma parameters of three different shots on March 25th (203935, in blue), 28th (203971, in green), and 29th (203991, in red).

## References

[BPR-MP-1] L. Buzi, Y. Yang, A.O. Nelson, R. Kaita, P.S. Krstić and B.E. Koel, “Sputtering of lithium and lithium compound films under deuterium and helium ion bombardment”, *Nucl. Mater. and Energy* (2018), submitted.

[BPR-MP-2] Y. Yang, L. Buzi, A.O. Nelson, R. Kaita and B.E. Koel, “Post exposure time dependence of deuterium retention in lithium and lithium compounds”, *Nucl. Mater. and Energy* (2018), submitted.

[BPR-MP-3] A. Maan, R. Kaita, D. Elliott, D.P. Boyle, R. Majeski, D. Donovan, L. Buzi, B.E. Koel, T.M. Biewer, “Investigation of deuterium retention in thick lithium oxide films on high-Z plasma-facing components”, *Nucl. Mater. and Energy* (2018), submitted.

[BPR-MP-4] C.H. Skinner, R. Bell, C.P. Chrobak, R. Kaita, B.E. Koel, W.R. Wampler, “Elemental and topographical imaging of microscopic variations in deposition on NSTX-U and DIII-D samples”, *Nucl. Mater. and Energy* (2018), submitted.

[BPR-MP-5] M.A. Jaworski, A. Kapat, J.P. Allain, “Effects of Finite Saturation in Porous Surfaces During Particle Bombardment”, *Nucl. Mater. and Energy* (2018), to be submitted.

[BPR-MP-6] K. Schmid, et al., *Nucl. Fusion* 55 (2015) 053015.

[BPR-MP-7] J.H. Nichols, M.A. Jaworski, C.H. Skinner, F. Bedoya, F. Scotti, V.A. Soukhanovskii, K. Schmid, “Global modeling of wall material migration following boronization in NSTX-U” *Nucl. Mater. and Energy* (2018), submitted.

## II. Core Science Research Highlights

The Core Science group consists of three topical science groups (TSGs) including: (A) macroscopic stability, (B) transport and turbulence, and (C) energetic particles. Each of these TSG areas is covered as a sub-section in the core science report below.

### A. Macroscopic Stability TSG Research Highlights

Macroscopic stability research at NSTX-U in FY2018 was aimed at further development and application of predictive simulation tools to understand various global and local MHD phenomena observed in NSTX/NSTX-U and other devices through collaboration, thereby improving the control and avoidance of MHD instabilities and disruptions in tokamaks. The resonant and non-resonant effects by error fields on various NSTX-U scenarios were investigated to develop physics requirements and error field correction strategies to avoid low  $m/n$  locked mode instabilities or rotational braking. The halo currents, forces, and instabilities induced by vertical displacement events were successfully predicted by non-linear M3D-C1 simulations. DECAF code was extended to produce disruptivity diagrams in various parametric spaces. The island power balance model adopted in DECAF offered a predictive guidance for the density limit similarly to the Greenwald limit. DECAF can also automatically identify rotating MHD instabilities, their bifurcation, and locking. The many physics models in DECAF can together provide an assessment of the chain of events leading to disruption, and an understanding that the plasma state can evolve significantly from more usual high performance parameters to the point at which the disruption actually occurs. Tearing modes saturated in small-island regimes in NSTX were identified and successfully explained by resistive DCON for the thresholds, and M3D-C1 showed that the saturation may be due to the rotation shear. MARS-K applications showed the benefits of top and bottom sensor arrays in measuring high  $n$  RMP plasma response in NSTX-U. Resistive M3D-C1 MHD simulations with the proposed NCC 3D coils have shown that the internal island structure bifurcates before they overlap with neighboring islands, with new sets of X- and O-points that result in an internal island stochastization and alteration of the heat and particle transport across the islands prior to the onset of global stochasticity. The collaborations with other domestic/international tokamaks were also continued on various MHD topics. The collaboration with COMPASS and other devices on error fields yielded a combined  $n=1$  and  $n=2$  resonant error field threshold scaling for ITER and tokamaks based on single mode approximation, although error fields from high-field-side generally require consideration of multi-modes corrections. A collaboration with KSTAR is producing a unique long-pulse, high  $\beta$ , and high non-inductive current fraction dataset to inform the DECAF development process; for example, by testing no-wall and tearing stability calculations.

#### 1. Error Field Correction in NSTX-U

The misalignments of primary magnets can degrade tokamak performance and often lead to disruptive magnetohydrodynamic (MHD) events. This was one of the reasons why the H-mode access was relatively limited in the previous NSTX-U operations [MS-1] and thus has been investigated as a part of NSTX-U recovery. The previous studies of error fields have been

extended to produce physics recommendations of the magnet alignments in the future assembly. The focus was made on the shifts and tilts that can produce the most dangerous  $n=1$  field penetration, in the experimental L-mode targets as well as the projected H-mode scenarios. Both resonant and non-resonant field effects were examined by the IPEC and M3D-C1 codes per each poloidal field (PF) and toroidal field (TF) coil shift/tilt, or in the worst-case scenarios by adding them in phase. The study yielded 4 physics recommendations (PRs) [MS-2], which were used in the context of physics and operational goals to determine requirements for the global alignments. The PRs are based on the standard physics criteria, in particular the single  $2/1$  mode approximation for the resonant parts. Further investigations of error field effects on NSTX-U discharges show that  $1/1$  field penetration can also potentially be critical in sawtoothed plasmas.

### (a) Predicted Resonant and Non-resonant Error Field Effects

The effects of each coil misalignment on the  $2/1$  resonant fields were estimated on various L and H-mode scenarios using the IPEC and M3D-C1 codes. Based on the linear calculations, the  $m=2$  and  $n=1$  resonant fields ( $\delta B_{21}$ ) were used to represent the drive of the error field penetration and the disruptive locked modes. Fig. MS-1 shows the filamentary representation of PF and TF coils used in IPEC, and Fig. MS-2 shows each of  $\delta B_{21}$  estimated by IPEC per 1mm shift or 1mrad tilt of each individual coil, assuming the full kA-turns except 100A RWMEFC coils.

Several conclusions can be quickly made from Fig. MS-2; Shifts and tilts of the TF inner legs are problematic, especially in L-mode plasmas. Shifts and tilts of individual PF-4 and PF-5 coils are also highly problematic. This is especially true in H-mode, where plasma response effects enhance the perturbation. Shifts and tilts of the TF outer legs are not significant, and also shifts and tilts of the divertor coils (PF-1a/1b/1c and PF-2) are not significant for global MHD studies. (Note that the misalignments of the divertor coils are quite significant for PFC heat loading, as described in the boundary section of this report).

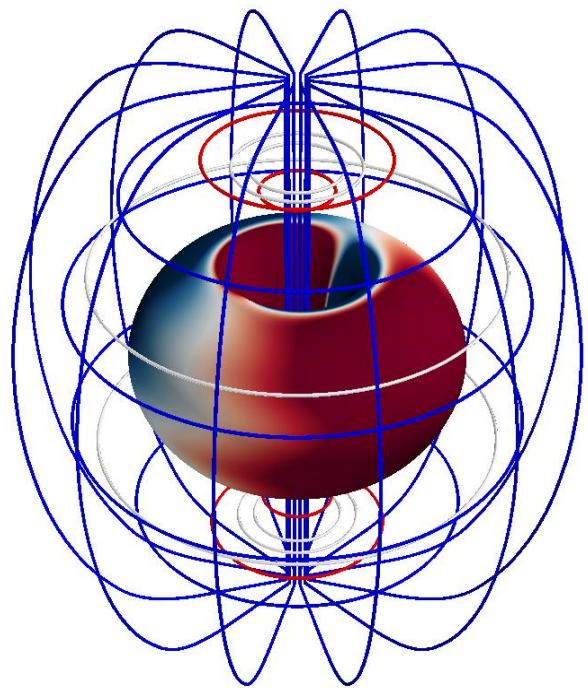


**Fig. MS-1:** Filamentary models for PF and TF coils used in IPEC. 3D contour shows distribution of normal magnetic fields by actual TF errors.

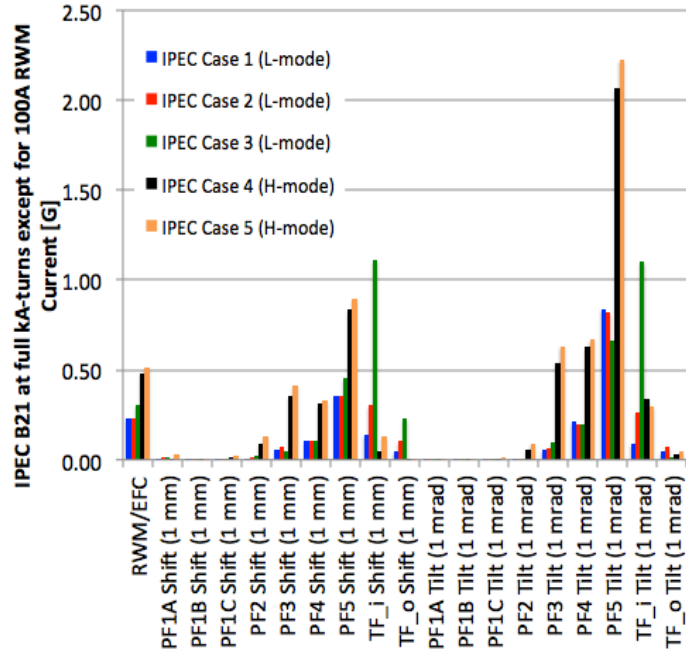


**Fig. MS-2:** Dependence of  $dB_{21}$ , for full coil kA-turns on the TF and PF coils and 100A on the RWM coils, on individual coil tilts and shifts using IPEC. TF\_i and TF\_o are the inner and outer legs of TF.

The detailed information for each L and H-mode target plasmas used here in IPEC (or M3D-C1) corresponding to Case 1-6 can be found in [MS-2]. A similar analysis was done with the M3D-C1 code. For example, Fig. MS-3 shows the results of the L-mode discharge Case 1&3 on the left and also of a new H-mode target (Case 6). Case 6 is a high performance target with  $\beta_N=5.5$ , which is beyond no-wall limit and thus could not be quantitatively simulated by IPEC.

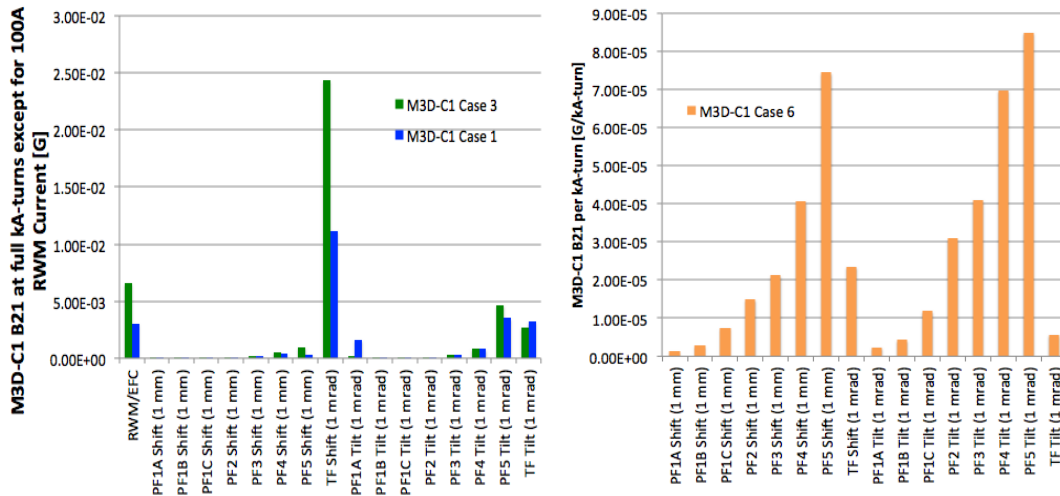


**Fig. MS-3:** Dependence of  $dB_{21}$ , for full coil kA-turns on the TF and PF coils and 100A on the RWM coils, on individual coil tilts and shifts using M3D-C1, for two L-mode cases on the left as well as a high  $\beta$  case on the right.

M3D-C1 and IPEC both predict that the TF and PF5 coils are the dominant source of error fields. Also, the importance of TF perturbations relative to PF5 perturbations decreases when moving to H-mode. This trend is, however, much stronger in IPEC than M3D-C1. A part of this disagreement is due to the fact that the M3D-C1  $\delta B_{21}$  and IPEC  $\delta B_{21}$  are not directly comparable quantities. The IPEC  $\delta B_{21}$  is an inferred value based on what would be present if the ideal resonant currents dissipated and is, therefore, essentially a measure of the magnitude of the resonant currents. On the other hand, the M3D-C1  $\delta B_{21}$  is the total resonant field in a resistive-MHD response model, and is therefore a measure of the tearing response of the plasma. Other numerical differences between the codes might also influence these results. In particular, neither code can properly handle a pure shift or tilt of the plasma, since this violates the boundary conditions at the magnetic axis in IPEC and the outer conducting wall in M3D-C1. This is expected to be important in calculating the response to the TF error field, which is dominantly 1/1 in nature.

NTV calculations with a combined NTV formulation based on IPEC solutions [MS-3] have also been completed for the H-mode Case 4 and 5. (L-mode NTV is negligibly small.) Note that the NTV torque will scale as  $T_{NTV} = \alpha_{NTV} N^2 I^2 \delta^2$ , where  $N$  is the number of coil turns,  $I$  is the coil current,  $\delta$  is the perturbation in mm or mrad, and  $\alpha_{NTV}$  is a coefficient. The NTV torque for full coil currents is given in Fig. MS-4. The NTV is clearly dominated by tilts and shifts of the outer

PF5 coils, with tilts and shifts of the inner-TF the second strongest effect. Displacements of the outer-TF coils are less significant. Note that NTV cannot be simply added, due to the quadratic dependence on field components. Also note that NTV is a profile effect, as the examples are shown in Fig. MS-5 for the TF displacements and PF-5 radial variations observed during the FY-16 run (the measured PF-5U tilt is not included in this calculation). The NTV profiles by the RWM coils are also shown, with a magnitude selected to match that from the PF-5 perturbation. It is clear that the NTV can be from the outer-PF perturbation, can be matched, and therefore cancelled by the RWM coils. However, the NTV from the TF perturbations has a completely different profile and is not well matched by the EFC coils. Therefore, it will be difficult or impossible to eliminate the NTV effects of a large TF perturbation with the EFC coils.

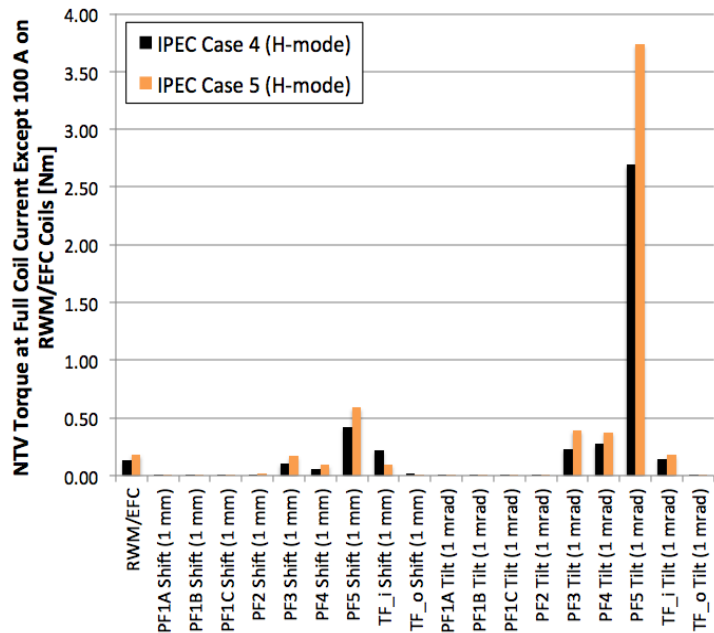


**Fig. MS-4:** Dependence of  $T_{NTV}$ , for full coil kA-turns on the TF and PF coils and 100 A on the RWM coils, on individual coil tilts and shifts using IPEC.

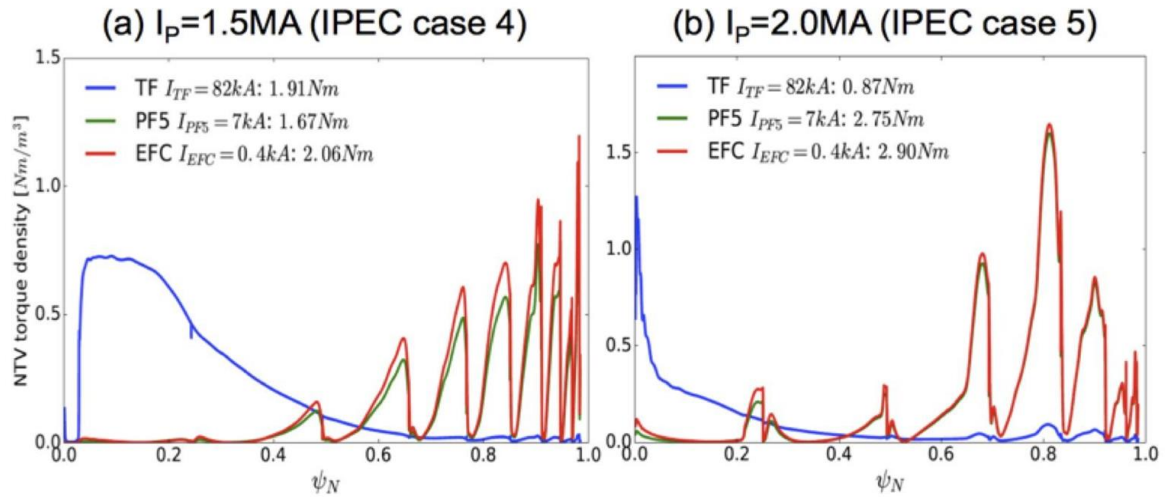


**Fig. MS-5:** Profiles of the NTV torque density by TF and PF5 error fields in NSTX-U for the two H-mode cases studied by IPEC.

### (b) Physics Recommendations for Coil Alignments

The analyses and data shown in the previous section were used to develop physics recommendations (PRs) as follows:

- (PR1) Full IPEC  $\delta B_{21}$  EF from TF tilt/shift should be reduced to  $<0.7\text{G}$  in L-mode.
- (PR2) Full IPEC  $\delta B_{21}$  EF from PF-5 tilt/shift should be  $<1.35\text{G}$  in L-mode and  $<3\text{G}$  in H-mode.
- (PR3) TF EF NTV should be reduced to  $0.9\text{Nm}$ .
- (PR4) The resonant M3D-C1  $\delta B_{21}$  fields should be correctable with  $1\text{kA}$  RWMEFC coil currents.

PR1&2 are required to control the 2/1 field below a half of the projected thresholds in various scenarios including low density cases. The error field threshold scaling used for the two PRs is:

$$\frac{B_{2,1}}{B_T} = 0.96 \times 10^{-4} (n_e [10^{19} m^{-3}])^{1.1 \pm 0.07} (B_T [T])^{-1.4 \pm 0.09} (R [m])^{-0.6 \pm 0.16}$$

based on IPEC  $\delta B_{21}$  which has also been used for ITER [MS-4]. PR3 is to maintain NTV torque sub-dominant compared to NBI torque, specifically 1/5 values of the expected  $6\text{Nm}$  NBI torque using 4 sources. Lastly, PR4 is developed to make error fields correctable perfectly with 1/3 capability of RWMEFC coils, as the error field threshold scaling also contains deviations and errors. These PRs are all combined, to define the envelope of TF and PF5 coil distortions over which one of PR criteria is violated, as shown in Fig MS-6. Find [MS-2: NSTX-U-DOC-101-01, Unreleased] to see justifications and descriptions in full detail.

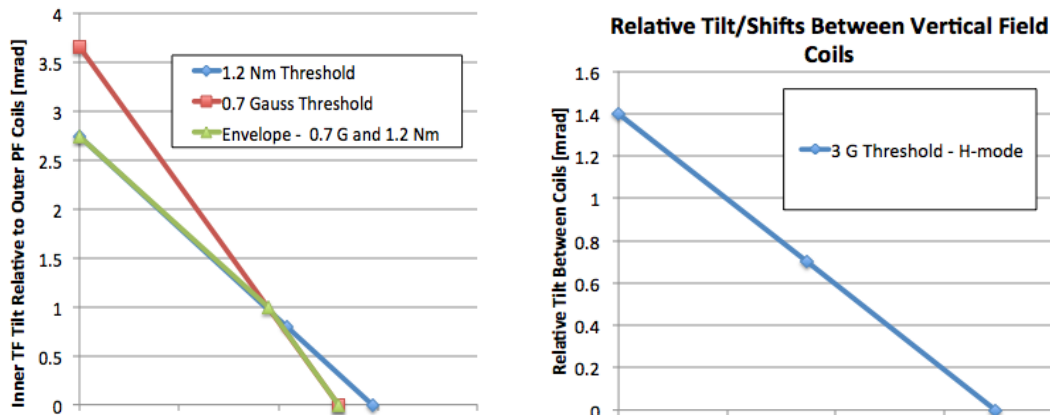


**Fig. MS-6:** Allowed envelop of tilts and shifts of the TF relative to the outer-PF coils (left) and one PF-5 relative to the other (upper vs. lower, right).

**(c) Investigation of TF Error Field Effects**

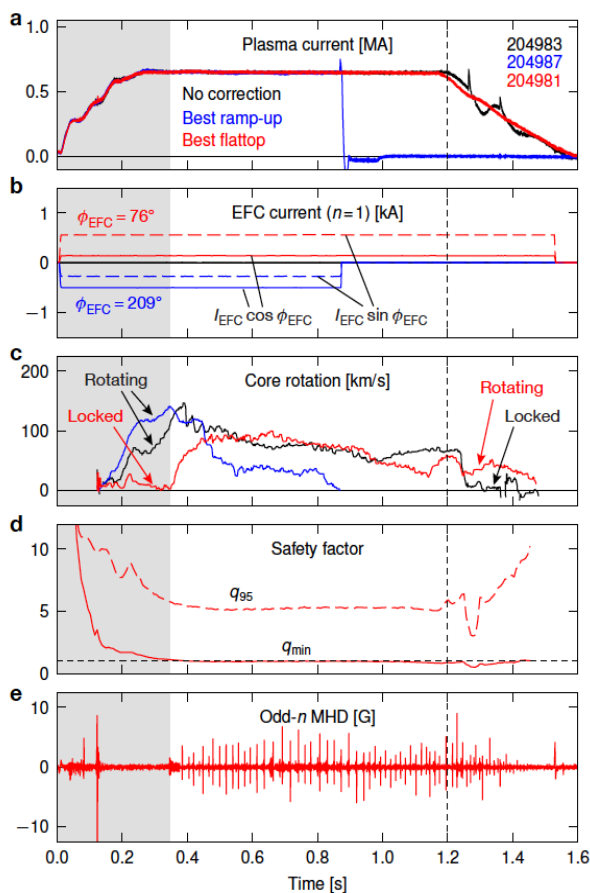


**Fig. MS-7:** Time traces of “best ramp-up” (blue) and “best flattop” (red) error field correction cases relative to reference discharge (black).

The metrology of the coils and simulations in FY16-17 indicated that NSTX-U had a significant error field dominated by the  $n=1$  misalignment of inner TF bundle. This TF error produced complicated plasma response, especially in terms of its toroidal phase when it is inferred from the optimal correction phase. Fig. MS-7 shows the example of the correction phase variations [MS-5]. One can see that the best correction (blue) during the ramp-up (gray shadow, before  $t=0.35s$ ) maintains strong rotation but quickly locked to the error field after the short flat-top. On the other hand, the nearly worst correction (red) during the ramp-up shows the best performance in the flat-top. The  $q_{min}$  trace in Fig. MS-7d, which is extracted from magnetic equilibrium reconstructions of the plasma, indicates that the key change at  $t=0.35s$  is the existence of the  $q=1$  surface and thus the strong interaction with the large  $1/1$  resonant field ( $\delta B_{11}$ ), possibly from the TF-bundle misalignment. Also note that the superior performance of the best flattop case is maintained during the ramp down, indicating the  $1/1$  interaction may continue to dominate the overall plasma response.

The structure of the 1/1 mode that locks the plasma is further investigated, with the temporal evolution of spatial rotation and  $T_e$  profiles. For example, Fig. MS-8 shows radial  $T_e$  profiles acquired before, during, and after the mode locking event. Prior to locking, the plasma exhibits periodic sawtoothing behavior, confirming the location of the  $q=1$  surface determined from magnetic equilibrium reconstructions. At the onset of locking, the  $T_e$  profile deviates sharply from its sawtoothing behavior and reveals the structure of the 1/1 mode (red) with a large magnetic island, at the location of  $q=1$  surface on the inboard side of the plasma. Once mode locking is complete, the  $T_e$  profile settles into a new equilibrium with the entire flattening across the core of the plasma.

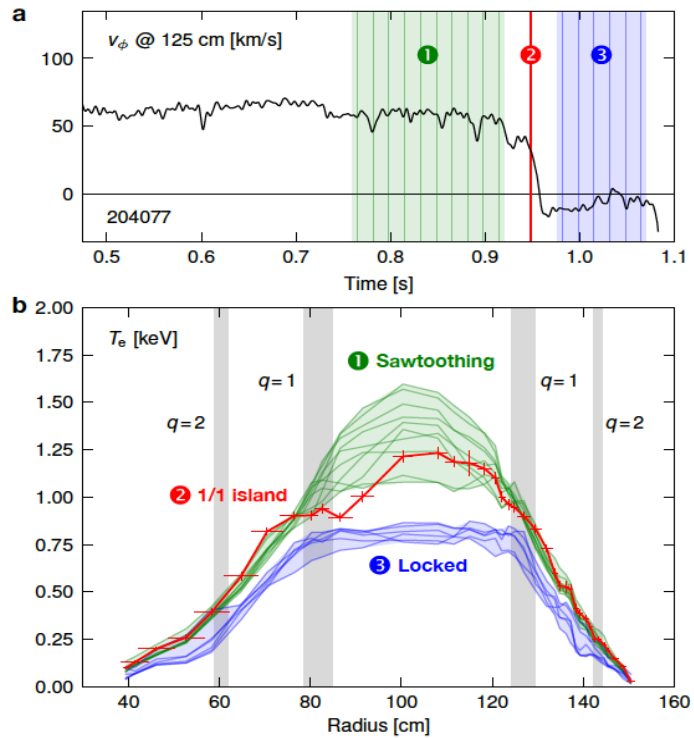


**Fig. MS-8:** Evolution of (a) core rotation and (b) spatial profiles of electron temperature in a sawtoothing discharge which is later locked by 1/1 mode.

This direct 1/1 locking results imply that one may have to consider the minimization of intrinsic 1/1 error fields in addition to the conventional 2/1 error fields, especially in a scenario operated in the sawtoothing regime, including ITER. An important question is why this 1/1 direct mode locking is particularly pronounced in the NSTX-U. One possibility is that the large high-field-side (HFS) error fields generated by the misaligned TF bundle interact with the plasma in a way that substantially increases its sensitivity to 1/1 perturbations. Another is that the low aspect ratio of NSTX-U makes it more vulnerable to 1/1 perturbations than conventional-aspect-ratio tokamaks. These possibilities motivate dedicated HFS error field experiments in a conventional-aspect-ratio tokamak, which will be introduced in section 7. The NSTX-U results also highlight the need for more accurate modeling of the plasma response to 1/1 resonant fields in the sawtoothing regime.

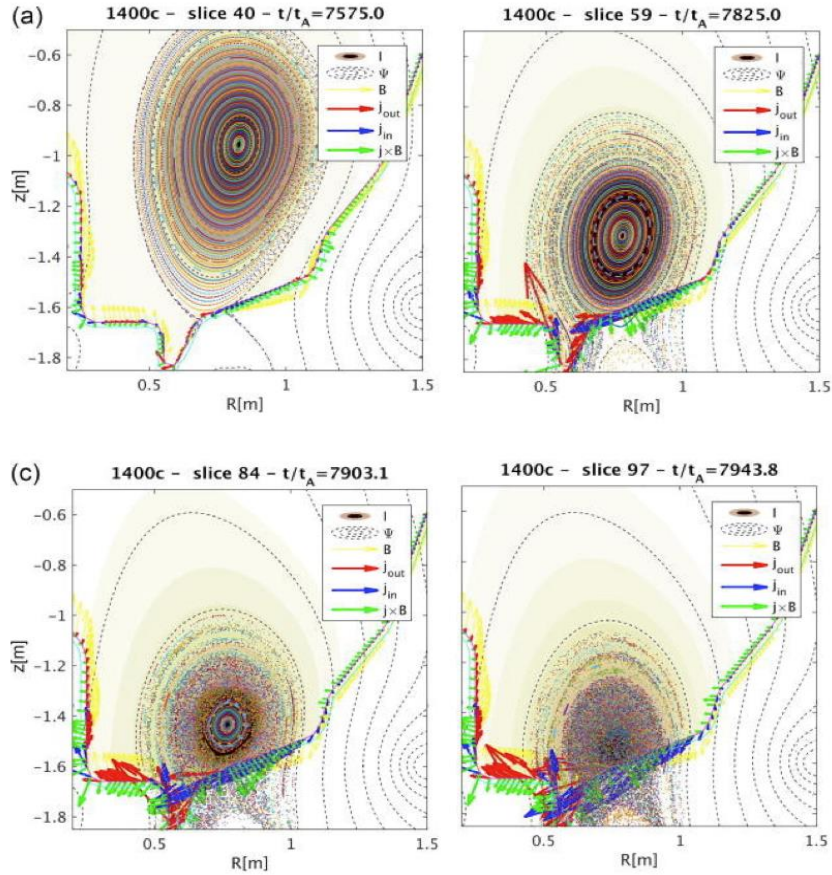


**Fig. MS-9:** Poincaré plots at a sequence of times in a 3D M3D-C1 simulation of a VDE in NSTX. Red and blue arrows show halo currents into and out of the wall, respectively. Green arrows show the direction of the poloidal electromagnetic force density on the wall.

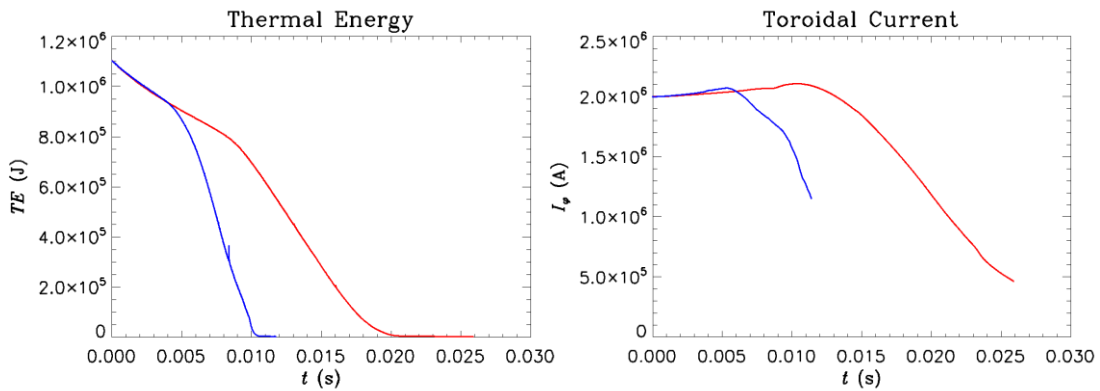


**Fig. MS-10:** The thermal energy (left) and the toroidal current (right) in two M3D-C1 simulations of a vertical displacement event in NSTX-U model discharge. Blue and red lines show cases in which the drift time is  $\sim 10$  ms and  $\sim 20$  ms, respectively.

## 2. Simulations of Vertical Displacement Events in NSTX-U

Three-dimensional simulations of a vertically unstable NSTX discharge were carried out using M3D-C1 in order to investigate the formation of non-axisymmetric halo currents during a nominally axisymmetric event [MS-6]. This work was also intended to inform the development of future halo current diagnostics on NSTX-U. These simulations were initialized with a vertically unstable equilibrium reconstruction of NSTX discharge 139536. In both the discharge and the simulation, the plasma control system was disabled to observe the evolution of the VDE under the condition of fixed coil currents. Disruption mitigation was not applied, so the plasma remains hot and essentially axisymmetric as it drifts vertically toward the wall. As shown in Fig. MS-9, the simulations show that the plasma remains stable to non-axisymmetric modes until well after it makes contact with the wall. Once contact is made, the edge plasma is scraped off while the core plasma remains hot. While the low resistivity in the core causes the safety factor profile there to remain fixed, the contraction of the plasma current due to the scraping-off gives rise to strong skin currents at the edge which eventually become unstable, first at moderate toroidal mode numbers ( $n \sim 5$ ), and then to lower toroidal mode numbers. The non-axisymmetric halo currents due to these instabilities show a similar pattern of forming first at moderate  $n$  and coalescing to lower  $n$ . These instabilities stochasticize the edge, leading to a fast thermal quench due to parallel heat losses.

Axisymmetric M3D-C1 simulations were also carried out for an NSTX-U model equilibrium with  $I_p = 2$  MA in order to assess forces on coils during VDEs. These calculations were initialized with a vertically unstable model NSTX-U equilibrium. Two cases were considered: one with a drift time of  $\sim 10$  ms, and the other with a drift time of  $\sim 20$  ms. The drift time was changed by scaling

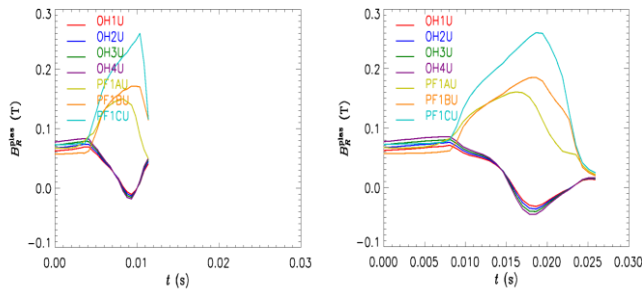


**Fig. MS-11:** The axisymmetric radial field at the centroid of upper OH and PF1 coils during a simulation of an upward-moving NSTX-U VDE, for cases where the drift time is  $\sim 10$  ms (left) and  $\sim 20$  ms (right).

the resistivity of the wall in M3D-C1. The ensuing VDE was simulated without introducing any disruption mitigation, in order to present a "worst-case" scenario. The thermal energy and toroidal current are plotted as a function of time for these simulations in Fig. MS-10.

It was found that the VDE generated excess radial field at on the order of 0.1 T for coils in the polar region towards which the plasma displaces, with the largest excess fields at the PF1C location, in this

case (see Fig. MS-11). The maximum excess field in these simulations was found to be largely independent of the drift time for the cases considered; therefore, the expected impulse to each coil is expected to scale approximately linearly with the drift time, if the coil currents were held fixed over this time. In reality, the drift times considered here significantly exceed the current ramp-down time of the coils, and therefore ramping down the coil currents at the onset of the disruption is expected to be an effective measure for avoiding sudden forces during these events.

### 3. Disruption Event Characterization, Forecasting, and Related Physics Analysis

#### (a) Disruptivity and General Event Diagrams from DECAF analysis

The plasma current in tokamak confinement devices is subject to disruptions due to instabilities that are the result of chains of physical events. Disruption prediction and avoidance research has expanded in several ways. The disruption event characterization and forecasting (DECAF) code [MS-7] has produced analysis of large databases for NSTX, MAST, and KSTAR for a small set of disruption characterization events. Access includes full coverage of the plasma discharge, rather than a limited period as would be available from a disruption database. Access to the full discharge data is shown later to be critical to fully understand the evolution of the plasma toward the plasma current quench. Thousands of shot seconds are available in the databases, with upwards of one half million tested sample times per database).

Analysis of the disruption current quench event has now produced the equivalent of “disruptivity diagrams.” The code’s many separate physical event modules provide warnings and declare occurrences of key events leading to disruption. The DECAF code includes the ability to make diagrams showing the probability of a DECAF event occurring within a given parameter space of tokamak operation. Most commonly the time of disruption, or DIS event, is used. An example is shown in Fig. MS-12, for a database of 10,432 NSTX discharges from the range of shot number 120000–142524 (only good plasma discharges with the necessary EFIT equilibrium reconstruction data are kept in the database).

Unlike standard disruptivity plots, DECAF can provide additional insight by illustrating where in parameter space these DECAF events other than DIS happen. For example, the DECAF event VSC detects the loss of vertical stability control in a tokamak. When plotted in the parameter space of elongation,  $\kappa$ , vs  $I_i$ , it becomes quite clear that vertical stability in NSTX shows a strong dependence on these parameters (Fig. MS-13).

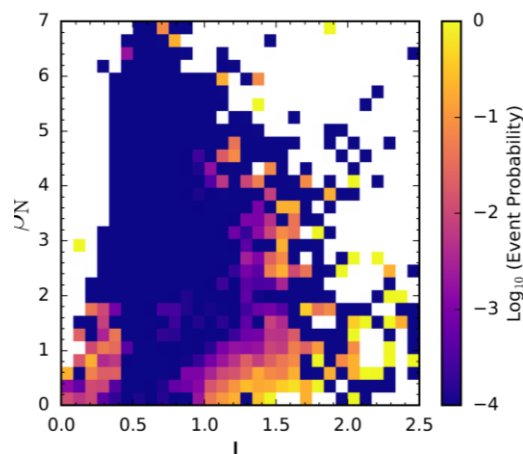


**Fig. MS-12:** Disruptivity diagram of a database of NSTX discharges in  $\beta_N$  vs  $I_i$  parameter space, with the colors showing the probability of the DIS event occurring within a segment of that space.

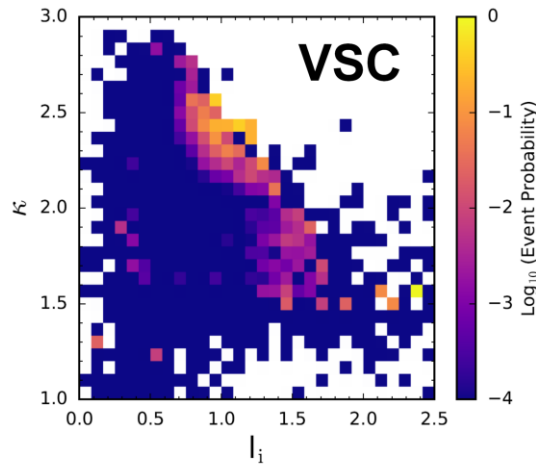


**Fig. MS-13:** Event probability diagram of a database of NSTX discharges in  $\kappa$  vs  $I_i$  parameter space, with the colors showing the probability of the VSC event occurring within a segment of that space.

Since the foundation of DECAF analysis, it has been accepted that accurate and extrapolable disruption prediction would require the analysis of data from several different tokamaks. DECAF analysis has now begun for large databases of multiple devices. DECAF generated disruptivity plots for MAST and KSTAR in addition to NSTX (Fig. MS-14) continue to support the previously observed but relatively unknown conclusion that plasma disruptivity does not increase with  $\beta_N$ . Indeed, a dedicated experiment was conducted during NSTX operation that measured the plasma stability using active MHD spectroscopy and produced a consistent result [MS-8]. As will be shown later, the high beta regions are, in fact, areas for forecasting algorithms to monitor for events that can *lead* to disruptions, however.

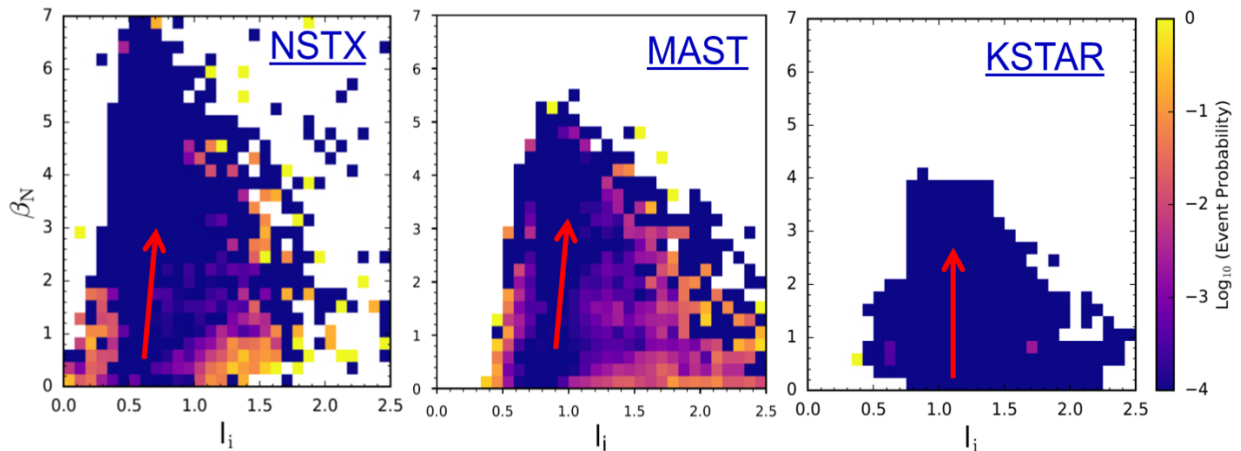


**Fig. MS-14:** Event probability diagram of DECAF full current quench disruption event DIS showing that the probability of this event does not have to increase as the plasma normalized beta is increased based on large databases from three tokamaks: NSTX, MAST, and KSTAR.

## (b) Local Island Power Balance Theory for Density Limit

Recently several theories have been developed to explain the observed global Greenwald limit in tokamaks, including a ballooning stability limit at the separatrix [MS-9] and a local density limit theory [MS-10]. The framework of the DECAF code represents an opportunity to test these theories, and work has begun to test the local island power balance limit theory. In this theory, power balance in an island between input Ohmic heating and radiated power loss results in maximum local density that scales with local current density [MS-11]. If the density at the island exceeds the limit, or alternatively if the radiated power at the island exceeds the input power ( $P_{loss} > P_{input}$ ), then the island grows and can lead to disruption of the plasma. The limit derived in this way can be written either in a form which mimics the global Greenwald density limit, but in a local form, or one that mimics a radiated power fraction, but again, localized to the magnetic island surface. In order to test this theory and implement it as a warning algorithm, the necessary inputs were imported to the DECAF code [MS-7]. These include: the radiated power profile, the resistivity profile, and the current density profile.

The radiated power profile ( $P_{loss}$ ) can either be measured and imported directly or can be estimated from density profiles and calculated cooling rates of deuterium and impurities such as carbon, which depend on electron temperature [MS-12]. Figure MS-15 shows both the measured and calculated profiles for NSTX discharge 134020. The calculated profile is calculated assuming that carbon is the only impurity and will be used in subsequent analysis here with the understanding that it may be somewhat less than the measured value.  $P_{loss}$  is calculated from:  $P_{loss} = n_e \sum n_Z L_Z$ , where the species  $Z$  considered are limited to deuterium and carbon and the cooling rates  $L$  in  $\text{Wm}^3$  are given for deuterium by  $L_D = 5.35 \cdot 10^{-37} T_e^{1/2}$  with electron temperature in keV [MS-9], and for carbon by tabulated formulae listed in Ref. [MS-10].

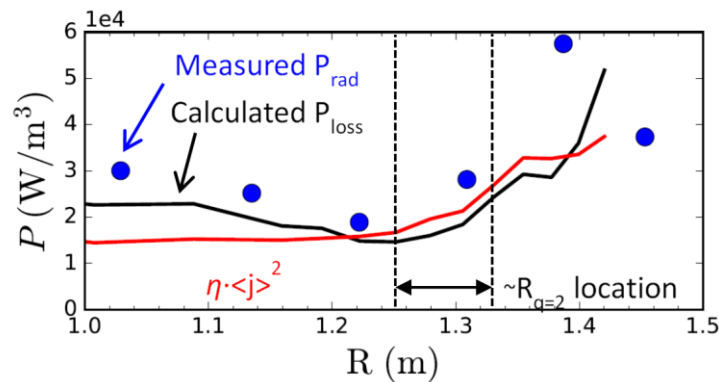


**Fig. MS-15:** Profiles of calculated (deuterium and carbon) and measured total radiated power density and calculated input power density for NSTX discharge 134020 at 0.60s.

The input power profile which  $P_{loss}$  is compared to in Fig. MS-15 is calculated from  $P_{input} = \eta j^2$ . The resistivity profile,  $\eta$ , is calculated based on electron temperature and the effective charge  $Z_{eff}$  (the formula appears in Ref. [MS-9]), which themselves are measured by Thomson scattering and charge exchange recombination spectroscopy (again assuming carbon is the only impurity). The current density profile used here is the total of surface-averaged current

density profiles from various sources (Ohmic, bootstrap, beam-driven), which are imported from the TRANSP code [MS-13]. The latter is an expansion of DECAF capability as previously no external code has been used to import calculated quantities (besides those from equilibrium reconstructions). This represents an opportunity but one that must be used cautiously as TRANSP calculations are not universally available for database studies, nor will they be in future real-time applications.

The power balance model is a local condition for island growth, so we must determine whether  $P_{loss} / P_{input} > 1$  at the location of the island of concern. For example, one can see from Fig. MS-15 that at a time just before the low frequency MHD onset in NSTX discharge 134020, the calculated  $P_{input}$  is still just slightly larger than the calculated  $P_{loss}$  at the location of the  $q = 2$  surface. The MHD activity that arises at the end of these discharges which may be associated with island growth has toroidal mode number  $n = 1$ , and the lowest order rational surface in the plasmas is  $q = 2$ , so  $m/n = 2/1$  activity is the most likely candidate, and we will evaluate the local criterion at the radial location of the  $q = 2$  surface. This presents a challenge, however, because equilibrium reconstructions (magnetics only, or partial kinetic) can give a radius of the  $q = 2$  surface, but it usually has some error and is somewhat noisy in time, which means the resulting calculated power limit fraction can also be noisy. To combat this, we approximate the radius of the  $q = 2$  surface as a smooth, linear function in time during the discharge (usually increasing slightly in time). For each discharge this function is determined from the noisier post-discharge equilibrium reconstructed location, which means that our evaluation of this data set is not set up at present for real-time application, but one could imagine using a prescribed  $q = 2$  location for a planned discharge or a moving average from real-time equilibrium reconstruction. This also means that the calculation is not necessarily exactly local to the island location, though it should be quite close. Additional assumptions of the present model evaluation include the TRANSP calculation of the current density, which is surface averaged and also performed a posteriori, and the assumption that carbon is the only impurity. Future improvements of the model implementation are possible.

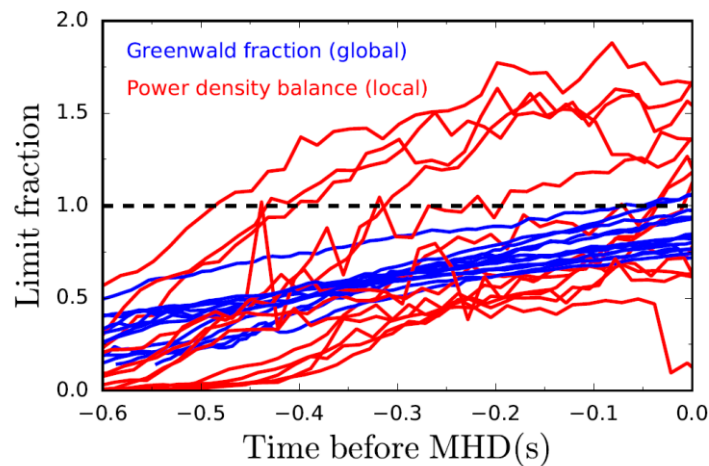


**Fig. MS-16:** Greenwald fraction and local power limit fraction for 13 NSTX discharges vs. time leading up to the onset of low frequency MHD activity.

Nevertheless, the model was applied to the aforementioned set of 13 NSTX discharges, and the results, of  $P_{loss}/P_{input}$  vs. time leading up to the time of the end of shot MHD onset, is shown in Fig. MS-16. Also shown in this figure is the Greenwald fraction for each discharge. One can see that, because of the rising density in these discharges, both criteria tend to rise with time towards the end of the discharge, towards, or surpassing, the theoretical limit of unity. The criteria are obviously correlated since both depend on the rising density, but it is clear that the Greenwald limit is more consistent than the local power balance model. The Greenwald fraction has a range of about 0.75 to 1.05 at the time of MHD onset, and actually somewhat higher at the time of disruption which comes within a few hundred milliseconds thereafter, while the power limit fraction has a range of about 0.60 to 1.65. This is not really surprising; with the Greenwald limit being a global calculation, while the power balance calculation is a local one with all the potential error that entails. Further work is required, then, to determine both whether the local power balance model represents a good physical explanation for the Greenwald limit, and whether it is a useful criterion to monitor for disruption avoidance purposes.

### **(c) Discrimination of Rotating MHD Instabilities and Related Disruption Forecasting by DECAF**

The DECAF code development has now produced significantly increased capability by automatically identifying rotating MHD instabilities, their bifurcation, and locking. Toroidal mode number is now also automatically discriminated for an arbitrary number of modes occurring simultaneously. The capability has been generalized to operate on any tokamak data available to DECAF. The information analyzed for these modes along with plasma rotation profile and other plasma measurements (15 criteria presently used for analysis of NSTX) produces predictive warning signals for the modes, along with a total MHD event warning signal showing initial success as a disruption forecaster. These capabilities are illustrated for an NSTX disruption in Fig. MS-17. In the shot analyzed, rotating MHD instabilities thought to be non-linearly saturated and slowly evolving resistive modes are found using a generalized phase matching algorithm in DECAF using an array of toroidal magnetic probes. The code discriminates the toroidal mode number,  $n$ , of the instabilities and tracks all modes greater than a specified amplitude, including modes that occur simultaneously. The modes that approach the disruption are indicated by the chevrons in the diagram (which show the mode  $n$  number). Further key DECAF events based on the mode evolution are also shown, including the bifurcation of the modes (BIF-n1,2) (loss of torque balance leading to rapid loss of mode rotation), and events marking the locking of the modes (LTM-n1,2). A single “total” MHD warning signal that varies with time is also shown. This warning was created by a set of criteria and can be used a disruption predictor. A significant part of DECAF analysis is determining the best sets of criteria to choose to create a predictive DECAF warning signal. The warning model shown in Fig. MS-17 is comprised of 15 separate criteria, also shown in the figure displayed as a heat map. This summary of model criteria provides a very useful illustration of how the total warning level reaches high values, indicating a disruption. For the present model, a total warning level of 4 indicates close proximity to the disruption. The heat map also gives us an understanding of what is happening in the plasma to create dangerous plasma states approaching the disruption. For example, early in the discharge, MHD modes are found, and core plasma rotation is low as the plasma starts up and typically transitions from counter-NBI

rotation to co-NBI rotation. However, the mode frequencies are relatively high at this time, which is generally a safe condition. Later, near  $t = 0.25\text{s}$ , the MHD warning level again increases as modes are again found with decreased and decreasing rotation frequency. However, these frequencies are not critically low (no mode bifurcations are found) and plasma rotation is not low, so the warning level remains low. However, after  $t \sim 0.6\text{s}$  the heat map shows more negative criteria occurring simultaneously including an increased mode amplitude, decreasing mode frequencies, and decreasing plasma rotation across the profile. Near  $t \sim 0.7\text{s}$  more negative criteria occur: mode frequencies are below past computed bifurcation frequency levels, the modes drop to very low frequency, and core plasma rotation is critically low. Late in the evolution toward the disruption ( $t \sim 0.8\text{s}$ ), a critical level of locked mode amplitude occurs. Such a locked mode detector signal is typically used to predict a possible disruption, but this indication occurs very late in the evolution. We see here that the DECAF code starts to show a significant change in the MHD warning level about 200 ms earlier, providing far better advanced notice of the potential disruption. Additionally, and of critical importance, the DECAF analysis provides to us a physical understanding of the negative evolution of the plasma state as it moves toward the disruption.

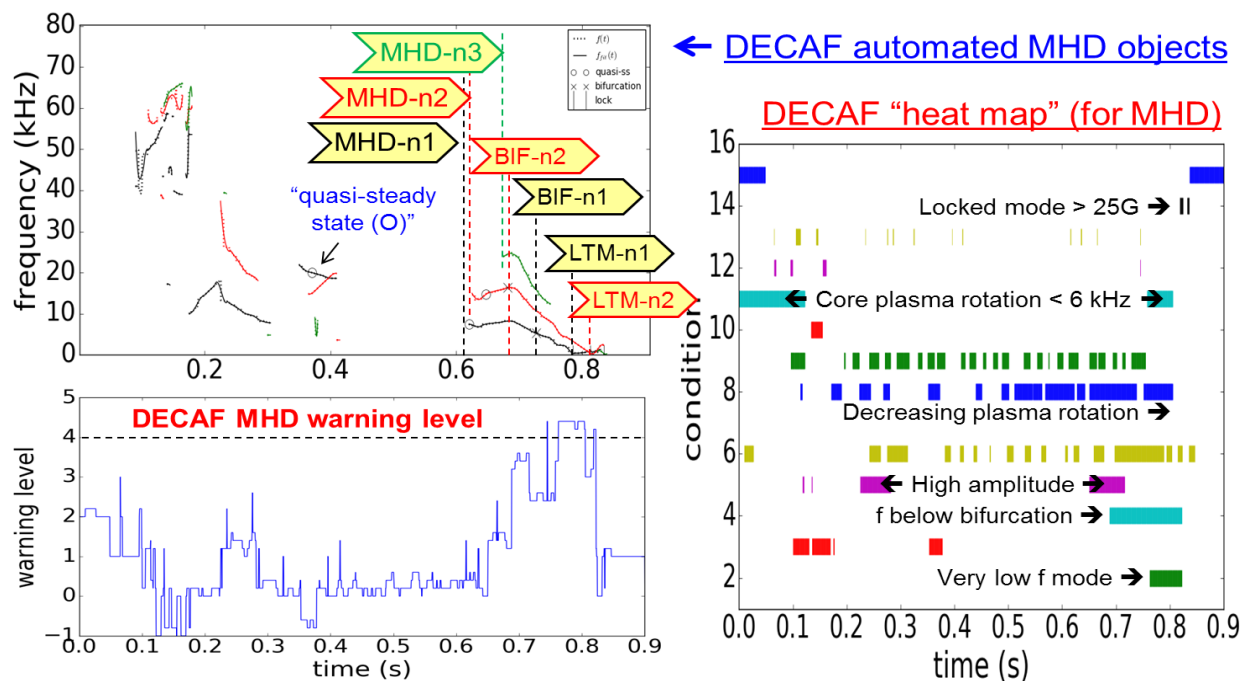


**Fig. MS-17:** Expanded rotating MHD mode discrimination capabilities in DECAF. The upper left frame shows the mode discrimination and decomposition into DECAF events. The lower left panel shows a total MHD warning level that increases as the disruption is approached. The right panel shows a heat map illustration of 15 event criteria that comprise the total MHD warning level.

#### (d) DECAF analysis of extended disruption event chains forecasting disruption

DECAF event characterization and event chain analysis of NSTX plasmas shows that disruption forecasting analysis should generally start during plasma states that would otherwise be overlooked. This is illustrated using the NSTX disruptivity database plot shown earlier, with new

overlays shown in Fig. MS-18. The left frame of this figure shows by red ellipses the regions of highest disruptivity as would be determined by human inspection. However, an apparent problem is that the region of high disruptivity at low normalized beta,  $\beta_N$  and mid-range plasma internal inductance,  $l_i$ , is not thought to be a dangerous operational region. The enigma is resolved by understanding that the plasma state can evolve significantly from more usual high performance parameters to the point at which the disruption actually occurs. This fact is completely missed, for example, by disruption database studies that only process data near the time of the actual disruption. Even worse, such studies may parameterize disruptive limits based on these misguided terminal states. Next, consider the middle frame of Fig. MS-18. The straight lines shown are a cartoon schematic of how a black box machine learning algorithm may start to divide the database into hyperplanes along the lines of disruptive vs. non-disruptive regions. In stark contrast, DECAF disruption event chain analysis of two discharges in this database that disrupt (flagged by the “DIS” event in DECAF, marked by red and green X’s in the figure) show that the *start* of the event chain appears in the region indicated by the red and green circles – which is far from what would be expected by the other analysis techniques described in the first two panels of the figure. The disruption event chain for the green arrow shown in Fig. MS-18 is shown in Fig. MS-19 along with the DECAF MHD mode decomposition and total MHD warning level. As before, we see the total MHD warning level rising toward a critical value as the disruption is approached. The DECAF mode decomposition adds additional information showing that the mode evolution toward lower rotation frequencies is relatively slow. This is one reason why the plasma disrupts quite far from the plasma state where the event chain starts.

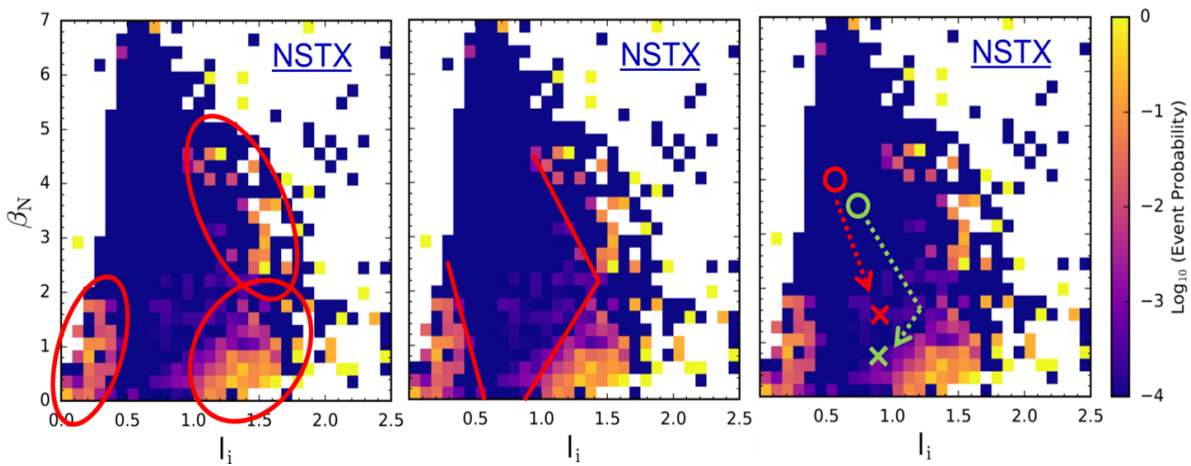


**Fig. MS-18:** DECAF analysis shows unexpected regions of interest in disruptivity plots: (left) the red ellipses indicate where a human analyzes may target plasma conditions for disruption, (middle) red lines indicate how the separation of regions might occur by a black box machine learning algorithm, (right) DECAF event chain analysis of two discharges that eventually disrupt (X’s) have event chains that start near the circles on the frame – deep in a low disruptivity portion of the diagram that might otherwise be neglected.

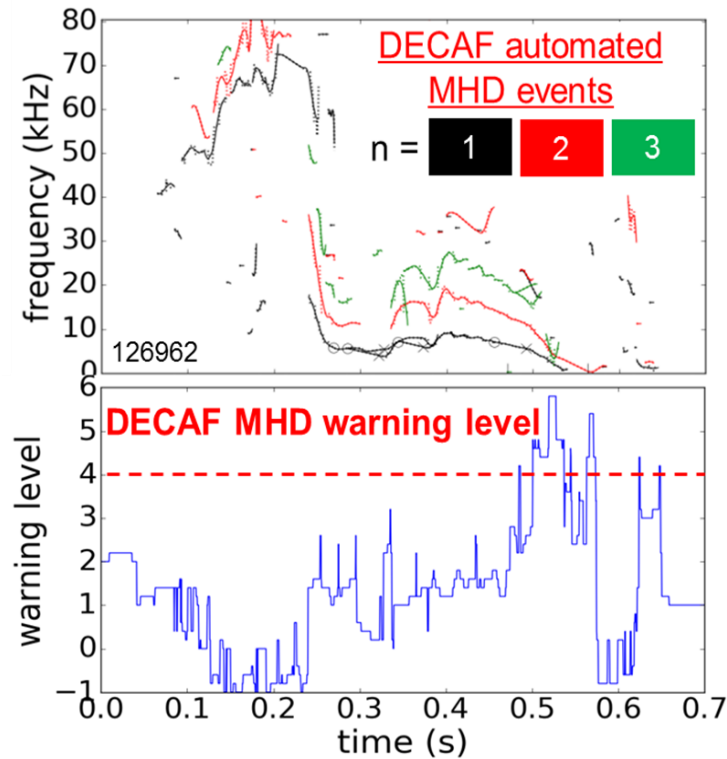


**Fig. MS-19:** (top to bottom) DECAF decomposition of rotating MHD in a relatively slow evolution toward disruption; total MHD warning signal; DECAF event chain leading to disruption.

The DECAF event chain in Fig. MS-19 provides a wealth of information. First, we see a critical warning for the individual  $n = 1$  rotating MHD mode (MHD-n1) as a starting point for the chain. Note from the top frame that the low frequency  $n = 1$  mode itself was detected far earlier – near  $t \sim 0.22$ s. However, the warning level for the activity was not determined to be sufficiently high then. This event could have therefore been flagged earlier if the warning sensitivity was set lower. The desire for an earlier warning of the  $n = 1$  mode is also indicated by the mode bifurcation (BIF-n1) occurring only 5 ms later. The mode locks (LTM-n1) 45 ms after the bifurcation. Then, a different dynamic occurs, as DECAF finds a PRP event 23 ms later. This warning literally flags that the pressure peaking factor is exceedingly high. For NSTX, that indicates that an H-L back-transition has occurred, the H-mode pedestal is lost, and the neutral beams are driving increasing peakedness of the plasma pressure. The plasma can then no longer match the plasma current requested by the control system (5ms after PRP) and simultaneously the plasma is making a close approach to the vessel wall (wall proximity control (WPC) event). Finally, the plasma disrupts 4 ms after the WPC event. It is also interesting that the plasma vertical displacement event warning occurs 3 ms after DIS. Usually the events are reversed in time. This indicates that the plasma remains mainly on the midplane during this evolution, uncharacteristic of many NSTX disruptions.

#### 4. Spontaneous tearing modes in small island regimes

Resistive MHD activity in NSTX is analyzed and compared with preliminary results from NSTX-U. Tearing-type modes with  $n = 1, m = 2$  helicity are identified. As previously observed, soft X-ray measurements indicate coupling to a core-localized  $n = 1, m = 1$  perturbation, which eventually leads to flattening of the rotation profile from the core to the  $q = 2$  surface [MS-7]. In the discharges studied, the magnetic mode amplitude grows smoothly from the Mirnov array noise floor width (Fig. MS-20, lower panel). Coincidentally, this noise floor corresponds to a tearing mode island width comparable to the ion gyro-radius. The gradual mode onset is indicative of a so-called ‘spontaneous’ mode [MS-14], as opposed to the paradigmatic ‘neoclassical tearing mode’ onset [MS-15] (in which the mode is metastable and is triggered instantaneously at finite amplitude by an exogenous magnetic perturbation). Intriguingly, prior to the emergence of the mode amplitude definitively above the noise floor, a faint precursor fluctuation is seen in many cases (Fig. MS-21). It is not yet clear whether this represents turbulent excitation of a marginally-stable mode, or a mode which is linearly unstable but saturated at very low amplitude. The physics of the tearing mode in the small-island regime (width comparable to ion gyro-radius and consequently to drift wave turbulence scales) is still uncertain, with many possible effects at play [MS-16].

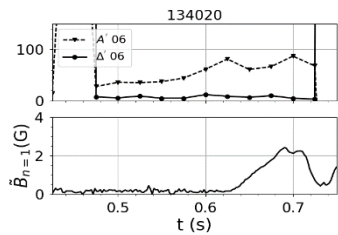


**Fig. MS-20:** (top) Stability parameters from RDCON for NSTX discharge 134020. (bottom) Magnetic  $n=1$  mode amplitude. NBI power stepped down at 0.7 sec to decrease beta.

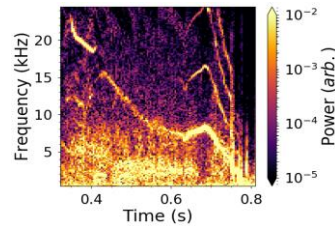


**Fig. MS-21:** Spectrogram of  $n=1$  magnetic amplitude for the same discharge.

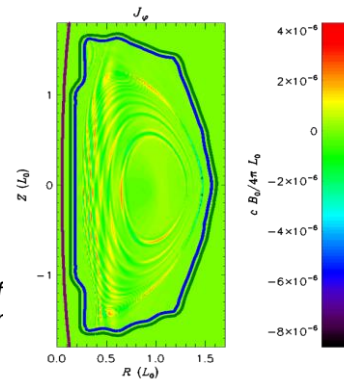


**Fig. MS-22:** Mode structure from M3D-C1 linear simulation for the same discharge

Similar  $n=1$  tearing mode behavior is observed in NSTX-U plasmas with higher toroidal field, more neutral beam heating power for similar high normalized beta, and higher electron temperature for a longer resistive diffusion time. Linear M3D-C1 simulations indicate an instability which comprises multiple poloidal harmonics, consistent with strong toroidicity-induced coupling at low aspect ratio. In these simulations, the mode is suppressed by inclusion of the measured plasma rotation profile, presumably due to shear. Resistive DCON stability calculations yield positive tearing stability index  $\Delta'$  well before and during the mode onset in all discharges studied (Fig. MS-22, upper panel). The stabilizing Glasser-Green-Johnson (GGJ) effect (due to field line curvature and pressure gradient) is thought to counteract the destabilizing  $\Delta'$ . The GGJ effect increases at lower aspect ratio  $R/a$ , and is therefore expected to be more advantageously significant in NSTX/NSTX-U than standard-aspect tokamaks such as DIII-D [MS-17]. However, the expansion of the center column in NSTX-U should weaken this stabilizing effect over that in NSTX; this is something which needs further dedicated experiments in NSTX-U to confirm.

## 5. Study of Non-ideal and Kinetic Plasma Response to 3D Fields

### (a) Magnetic Sensors for Kinetic 3D Plasma Response

Aiming at a more complete measurement of the non-axisymmetric 3D magnetic field in NSTX-U, a conceptual design for an extension of the NSTX-U magnetic diagnostic system was performed. The existing system of magnetic probes to measure 3D field is found to be sufficient to resolve toroidal harmonics up to  $n=5$  in the LFS and up to  $n=4$  in the HFS. However, the poloidal distribution is found insufficient to resolve local poloidal wavenumbers on either the LFS or HFS of the device.

MARS-F/K simulations were carried out to investigate the poloidal structure of the plasma response to magnetic perturbations with toroidal periodicity from  $n=1$  to  $n=3$  applied with the NCCs in two different plasmas, one at  $\beta_N \sim 5.5$  and one at  $\beta_N \sim 2.5$ . In all the cases the strongest field at the wall due to the plasma response is found to be in the LFS, with a change in wavelength between the HFS and LFS. These results, combined with the hardware limitations, suggest 6 poloidal positions where measuring the magnetic field would be relevant. The results are shown in Fig. MS-23.

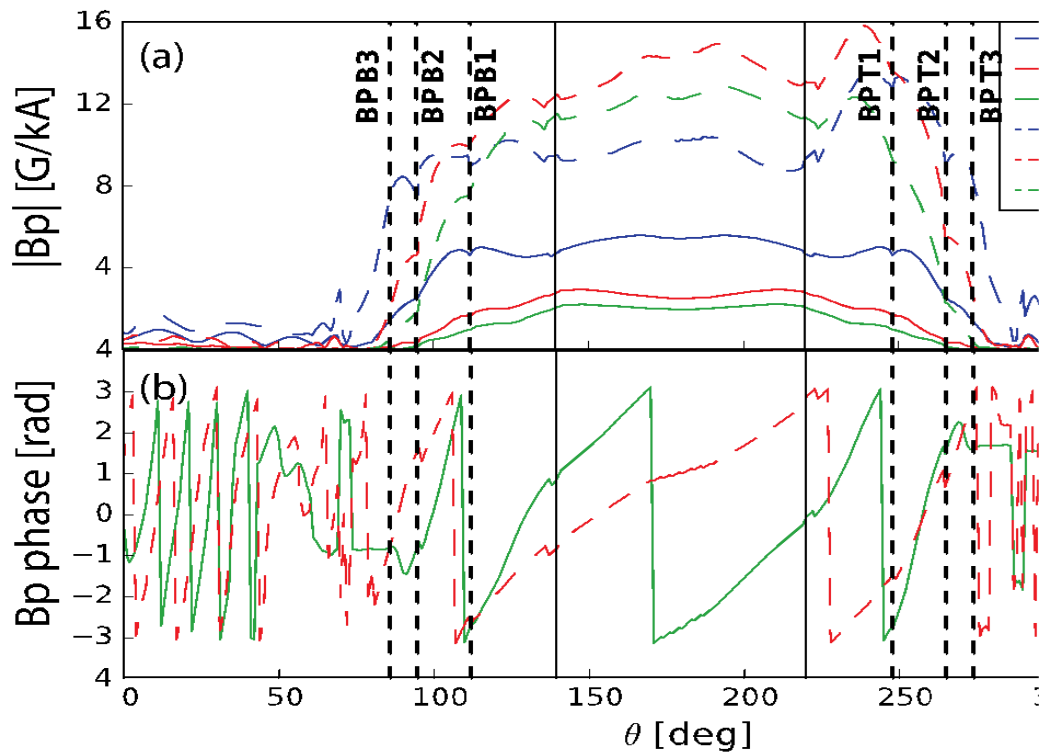


**Fig. MS-23:** Amplitude (a) and phase (b) of the poloidal component of the plasma response at the wall for different cases analyzed. In (b) only the highest and lowest amplitude case are reported. The vertical solid lines correspond to the existing probes, the dashed lines to the suggested ones. The phase between the NCC coils in the different cases is the one that produces the maximum response, so it varies case by case. A toroidal array is present also at  $\theta=0$ .

Further MARS-F/K simulations were performed to test the capability of the system beyond the required one:

- The system is found to be adequate to measure the plasma response to perturbations up to  $n=6$
- The system is found to be adequate to measure the multimodal plasma response (Fig. MS-24) It is found that adding one toroidal array at one of the suggested poloidal location would be enough to identify it, although not enough to have an adequate poloidal description of the different modes.
- The location of the probes with respect to the conductive structures surrounding the plasma is found adequate to detect the plasma response to perturbations with a frequency up to  $\frac{\omega_{RMP}}{\omega_A} = 10^{-4}$  and probably higher.

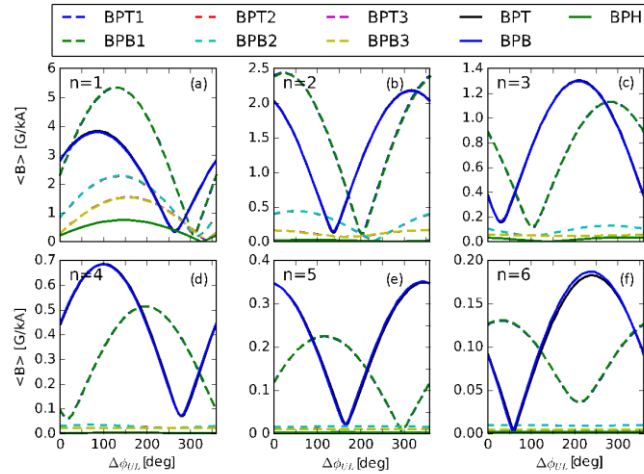


**Fig. MS-24:** Multimodal plasma response for the low  $\beta_N$  case as function of the NCC coils phasing. Each panel corresponds to a different toroidal perturbation applied, different line style and color used to identify different toroidal arrays.

- Assessment of the tradeoff in poloidal length of the probes for mode numbers  $n \leq 6$ , with shorter lengths yielding more precise resolution of the poloidal structure and longer lengths providing a larger signal, leads to an optimal probe length between 10 cm and 30 cm.

A Monte Carlo study identified optimized connections of the existing and proposed toroidal arrays in differential pairs, for simultaneous detection of toroidal mode numbers  $1 \leq n \leq 3$ . Several cases were considered, including new connections for the existing arrays to improve condition number of detection, additional pairs to improve the redundancy of the LFS arrays, new pairs for the HFS array, and possible sparse configurations for new arrays that would allow detection of  $n=1$  or  $n=2$  or  $n=3$  using a small number of probes and connections.

### (b) Observations of Internal Magnetic Island Bifurcations in Resistive MHD Simulations

An interesting new type of internal magnetic island bifurcation has been identified in M3D-C1 resistive MHD simulations. It is found that single harmonic,  $n = 3$ , magnetic perturbations applied to NSTX-U kinetic equilibria with  $\beta_N$  of 5.5 and 7.6 result in an amplification of the radial  $\delta b_{mn}$  eigenmode response as the current in a non-axisymmetric perturbation coil (NCC) is increased. This produces a smooth, continuous, deformation and stretching of the flux surfaces in the vicinity of each rational surface, which affects the evolution of the internal structure of magnetic islands.

As shown in Fig. MS-25, for a representative  $q = 3$  island located on the high-field side ( $\theta \sim 180^\circ$ ) of the  $\beta_N = 5.5$  equilibrium, dramatic changes in the internal island structure are observed as the coil current is increased from 1 kA to 16 kA. In this  $\beta_N = 5.5$  case, internal island bifurcations occur at 3.48 kA and 14.68 kA while in the  $\beta_N = 7.6$  case only one bifurcation is observed at 4.23 kA as the NCC current is scanned to a maximum value of 30 kA. This difference in the critical island bifurcation current is consistent with a larger  $\delta B_{mn}$  eigenmode amplification in the  $\beta_N = 5.5$  case than in the  $\beta_N = 7.6$  case. For example, the peak  $\delta B_{9,3}$  eigenmode amplitude in the  $\beta_N = 5.5$  case is a factor of 4.9 larger than that of the  $\delta B_{9,3}$  eigenmode in the  $\beta_N = 7.6$  case. In addition, since the island widths are small compared to the distance between resonant surfaces,  $\sigma_{\text{chir}} < 1$ , the internal flux surfaces become stochastic prior to the onset of global stochasticity due to island overlap  $\sigma_{\text{chir}} > 1$ . (See Fig. MS-25 at 16 kA.)

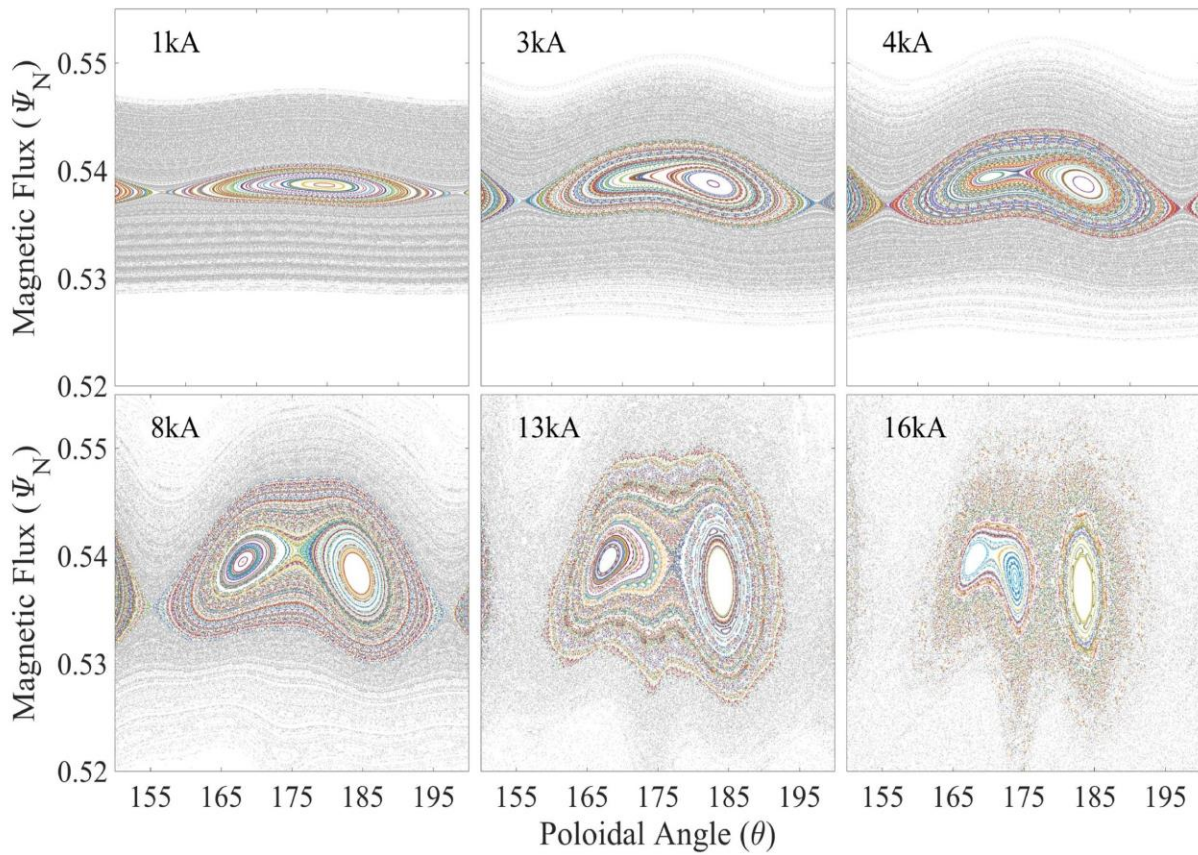


**Fig. MS-25:** Evolution of a representative  $q = 3$  magnetic island with increasing NCC current in a NSTX-U  $\beta_N = 5.5$  equilibrium showing a starching of the internal flux surfaces that results in bifurcations, which create new sets of internal X- and O-points.

## 6. Progress with the Electromagnetic Particle Injector (EPI)

The shattered pellet injector now being considered for ITER uses the MGI valve to propel the frozen pellet. This will limit its velocity to only about 200-300 m/s, and because it will be located many meters away from the plasma, its response time is further slowed. The penetration depth of the shattered fragments into ITER grade plasmas is unknown. The Electromagnetic Particle Injector (EPI) on the other hand has the potential for delivering the radiative payload composed of micro spheres of B, BN or Be, inside the  $q = 2$  surface on a 3-4 ms time scale, much faster and deeper than what can be

achieved using present methods. To address this important issue, a novel system based on the rail-gun concept was designed, and an initial test system fully assembled and tested. Experimental tests on the proto-type system have been able to verify the primary advantages of the EPI concept over other disruption mitigation concepts for a tokamak. These are the rapid response time and the capability to attain the high projected required speeds in this fast time scale. In preparation for a tokamak/NSTX-U test of the concept, a much-improved compact system has been built. Compared to the initial test version, this system employs 2T magnetic field augmenting coils to substantially reduce the current through the system to attain the required velocity. Capability for radiative payload deposition in the core provides a means to suppress the formation of the runaway current. With EPI, one can precisely calculate the injection parameters needed for deep penetration into any plasma, including the ITER plasma, giving confidence that simulation capabilities validated with present tokamak experiments can be used to reliably project its performance to ITER. During FY-19, the new EPI system will be nearly fully tested to establish its operating parameters, and work will begin on the details and requirements for an EPI installation on a tokamak. NSTX-U, DIII-D and KSTAR are all potential candidates for this first tokamak test. A paper summarizing the results from the first version of the EPI system has been submitted to Nuclear Fusion. Results from the EPI experiments will also be presented at the 2018 IAEA Fusion Energy Conference.

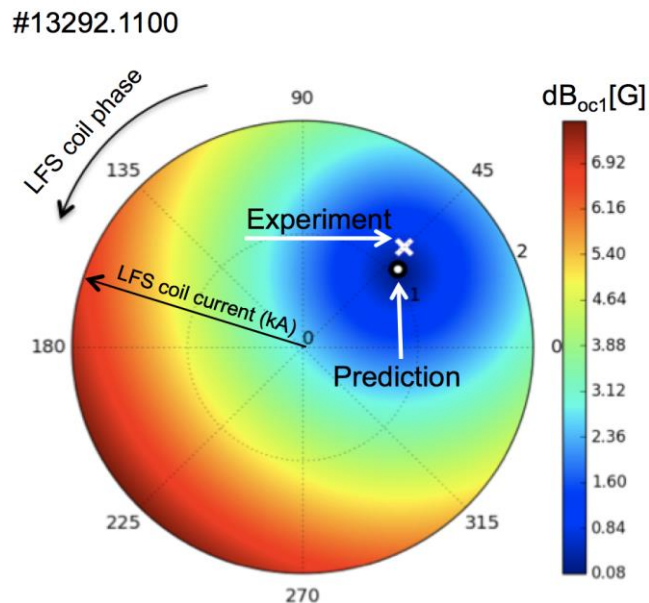


**Fig. MS-26:** Comparison of the empirically determined optimum correction and the prediction based on IPEC overlap resonant field in COMPASS using LFS coils against HFS proxy error.

## 7. Collaborations for error field physics

### (a) Effects of high-field-side error fields

The previous studies in NSTX-U showed that a high-field-side (HFS) error field by TF can be subjected to a complex phase rotation of resonant  $m/n$  fields and higher sensitivity on equilibrium changes. The collaboration with COMPASS has been continued using its unique HFS 3D coils to understand these effects. The HFS coils in COMPASS were used to induce locked modes, and the LFS coils were used to compensate such a proxy error field. It is shown that the empirically optimal amplitude and phase for LFS correction against HFS error is highly consistent with the predicted optimum based on  $2/1$  IPEC resonant fields, even if the correction increases other  $m/n$  resonant fields due to their different toroidal phases. The level of agreement is illustrated in Fig. MS-26. Note that the metric used here to estimate the resonant drive of locking is the overlap resonant field for core, which is nonetheless essentially identical to the  $2/1$  resonant field here since there is only  $q=2$  resonant surface included in the overlap field calculations. A surprising aspect is that this combination of LFS+HFS fields leaves substantial residual errors in the plasma (Fig. MS-27) while minimizing a component that can cause locked modes. The results confirm that the conventional single mode approximation still works for HFS error fields, as far as the locked mode avoidance is concerned.

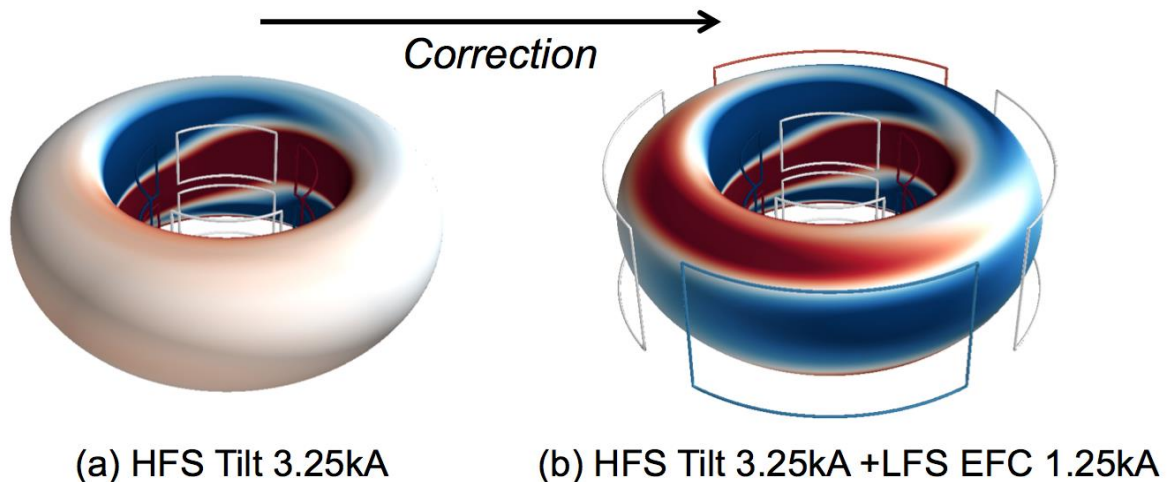


**Fig. MS-27:** Perturbed magnetic fields by HFS proxy error field (a) without correction and (b) with LFS coil correction on plasma boundary surface of COMPASS tokamak.

The conclusion above is quite different from one made from the NSTX-U TF error field studies. The single-mode approximation based on the  $2/1$  or the overlap field for the core offered the explanation of the optimal correction only for the ramp-up phase, not at all for the flattop or the ramp-down phase. The difference came from the interaction with  $1/1$  modes later in time which is shown to be strong in NSTX-U but is not clear in COMPASS. A multi-mode effect in COMPASS comes rather from higher  $m/n$  modes, such as  $3/1$  or  $4/1$ , rather than  $1/1$ . The experiments show that the residual error fields after LFS+HFS can strongly affect the stability of L-H transition, and the MARS simulation indicates that  $3/1$  may be the key component to explain the observation [MS-18]. In the end, recent NSTX-U and COMPASS error field studies both indicate the stronger multi-mode aspects of HFS error fields.

## (b) Error field threshold scaling for n=1 and n=2

The n=2 resonant error field can also cause a disruptive locking event, as first pointed out in [MS-19]. As a preparation of error field correction in the future NSTX-U, a dedicated effort to understand the parametric dependency of the n=2 locking threshold on density and toroidal field was made in FY17 through the national DIII-D campaign. This study has been further extended

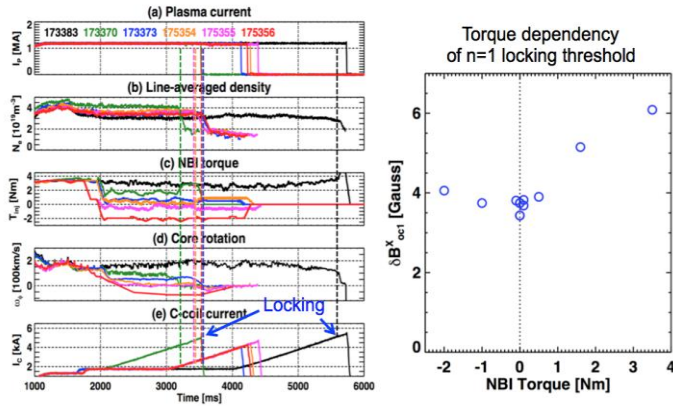


**Fig. MS-28:** Torque and rotation scan in DIII-D using the balanced NBIs (left), and the measured n=1 locking threshold dependency on torque in H-mode target plasmas (right).

D balanced NBIs. It is clear that the locking threshold increases with the torque or rotation, but the dependency observed in these H-mode cases is not as strong as reported in the previous DIII-D L-mode studies [MS-19] or NSTX H-modes [MS-20].

These new data obtained from DIII-D are combined with the error field threshold database across other devices and scenarios to see the general trends. A unified threshold scaling between n=1 and n=2 was also attempted for the first time, using the overlap resonant field representation. The regression analysis on the database yields

$$\frac{B_{oc1}^x}{B_T} = 0.99 \times 10^{-4} (n_e [10^{19} m^{-3}])^{1.1 \pm 0.08} (B_T [T])^{-1.3 \pm 0.11} (R [m])^{-0.83 \pm 0.13} \left(\frac{\beta_N}{l_i}\right)^{-0.70 \pm 0.06} \left(\frac{\omega_\varphi}{\omega_{De}}\right)^{0.20 \pm 0.07}$$

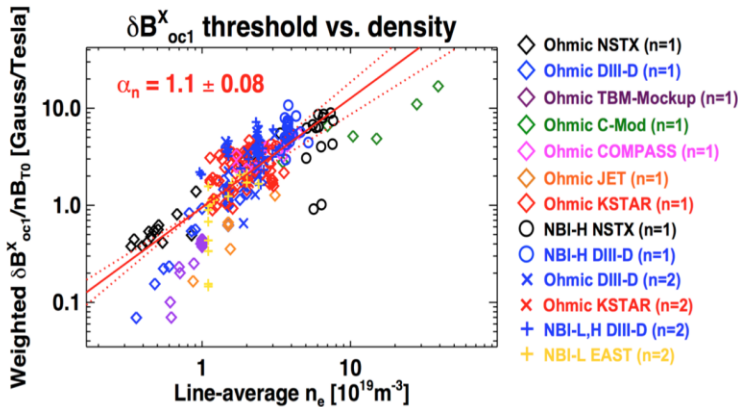


**Fig. MS-29:** Density correlation of n=1+2 locking threshold across Ohmic, L-, H-mode scenarios in various devices including NSTX, DIII-D, C-Mod, COMPASS, JET, KSTAR, and EAST.

in FY-18, as also a part of the ongoing ITPA activities for MHD to develop the reliable error field correction strategies for ITER, which was also reported in the FY17 annual report. In particular a focus was made to study the injected torque (and ultimately rotation) effects on the error field thresholds, including n=1 as well as n=2, and also on both L-mode and H-mode targets. Fig. MS-28 shows the examples of the torque scans, by utilizing the unique torque control capabilities of the DIII-

Here,  $\delta B_{oc1}^x$  is the overlap resonant field,  $\frac{\beta_N}{l_i}$  is a macroscopic stability index, and  $\frac{\omega_\varphi}{\omega_{De}}$  is the normalized toroidal rotation with respect to the electron diamagnetic rotation. The density correlation, as shown in Fig. MS-29, is again almost linear and more robust than the other parametric dependencies. This new scaling is however not yet ready for use and must be improved particularly for the following two aspects. First, the stability index

scaling is necessary to use overlap resonant field [MS-21] as a metric since it is an external field

representation and thus the resonant field amplification (RFA) effect [MS-22] is essentially missing. However, the RFA can be a more complicated function of the stability index, or even rotation [MS-23], than what the simple power index scaling can represent. As an example, its limiting behavior to a zero- $\beta$  plasma is pointing to an indefinitely large threshold and this is clearly misleading. Secondly, the rotation scaling is not yet reliable with a significant standard deviation relative to the mean value. The normalization to electron diamagnetic rotation could be another issue here. A critical assumption behind this rotation scaling is  $\frac{\omega_{\varphi}}{\omega_{De}}=1$  for Ohmic plasmas, where rotation diagnostics is mostly missing. It is entirely possible that the ion diamagnetic rotation can play more important role depending on the regimes [MS-24], and thus the rotation scaling can be also subjected to more complicated functional forms than the power law scaling. The dependencies of locking thresholds on RFA and rotation should be further investigated and thoroughly examined in both theory and experiment.

## **8. Collaboration with KSTAR on Ideal, Kinetic, and Resistive Stability Analysis Supporting DECAF**

The collaboration with KSTAR on disruption prediction and avoidance is producing a unique long-pulse, high beta, and high non-inductive current fraction (over 75% at present based on our TRANSP interpretive analysis) dataset to inform the DECAF development process. DECAF analysis is fueled by multi-device coordinated research that continues to validate/develop physics models for the code, thereby increasing the understanding of the events detected by the code and to improve the disruption forecasting capability of the code.

This KSTAR research has produced steady evolution of both linear ideal and resistive MHD analysis for long-pulse KSTAR plasmas. A critical part of this analysis has been extensive kinetic equilibrium reconstruction analysis including motional Stark effect (MSE) data, producing robust reconstructions for all plasmas having full diagnostic coverage. The analysis concludes that the classical resistive  $\Delta'$  does not accurately describe the experimental plasma stability. This indicates that neoclassical terms in the modified Rutherford equation will be required at a minimum to reproduce the KSTAR experimental results.

Figures MS-30 and MS-31 show a summary of two KSTAR plasmas that were formed from the same target plasma but with altered plasma current and toroidal field. The plasma shown in Figure MS-29 operates at higher  $\beta_N \sim 3.5$  compared to the one shown in Fig. MS-30 operating at higher toroidal field  $B_T = 2T$ . The shot with higher normalized beta suffers a strong  $m/n = 2/1$  tearing mode which decreases the plasma beta significantly. The shot at reduced  $\beta_N \sim 2$  does not show tearing mode activity. The frames of the two figures show that both plasma have about 70% non-inductive current, but that the profiles of this current is considerably different in the two shots. The lower  $\beta_N$  shot in Fig. MS-31 shows a broader bootstrap current profile. The  $q$  profiles as determined from the kinetic equilibrium reconstructions with MSE for each shot show a significantly different evolution. The high  $\beta_N$  shot shows a low  $q$  shear region forming due to the high non-inductive current. By the time of the  $2/1$  tearing mode onset at  $t \sim 4s$ , the figure shows that the low  $q$  shear region occurs near the minimum in  $q$ . In contrast, the  $q$  profile evolution of the  $\beta_N \sim 2$  shot in Fig. MS-31 has a low  $q$  shear region but farther out on the profile

and at a far higher  $q$  value (about near  $q = 4$ ). This difference might be a significant difference leading to the very different experimental tearing mode stability between the two discharges. An experiment has been scheduled for the 2019 KSTAR run campaign to determine if this hypothesis is correct.

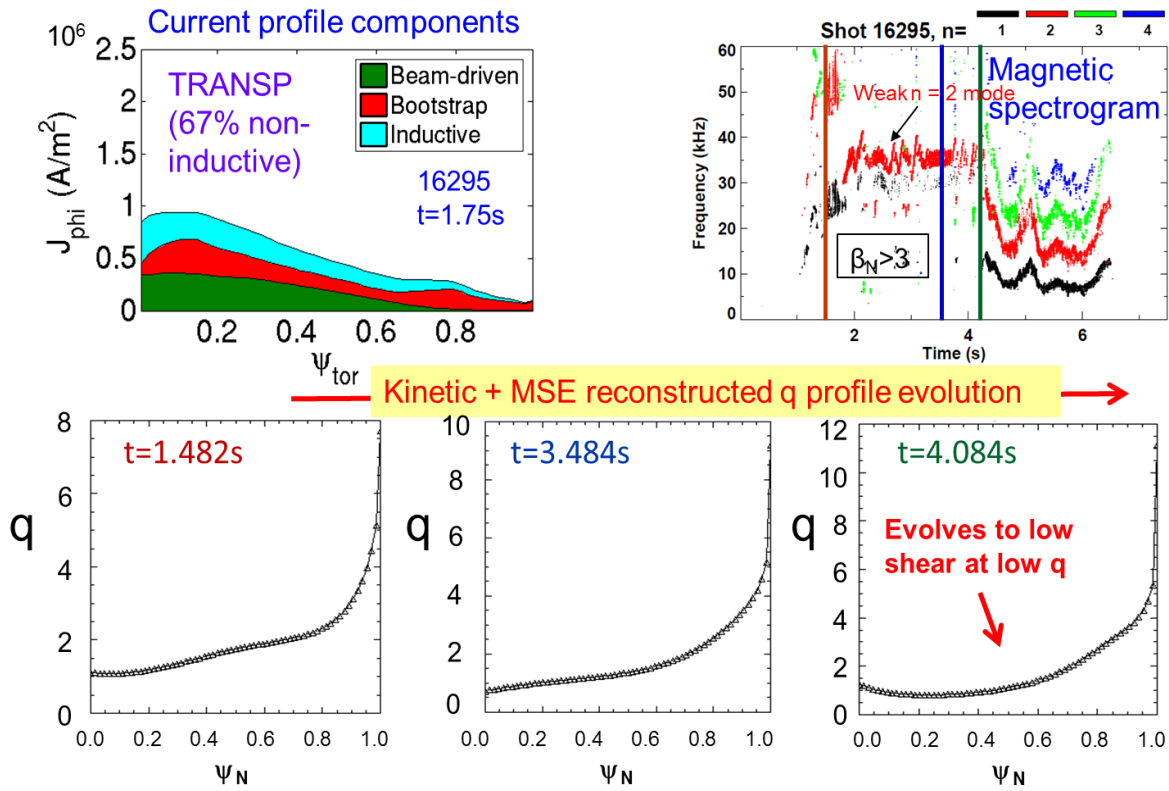


**Fig. MS-30:** Non-inductive current profiles, magnetic spectrogram of toroidal probe array, and  $q$  profile evolution of kinetic equilibrium reconstructions with MSE data for  $\beta_N \sim 3.5$  plasma in KSTAR.

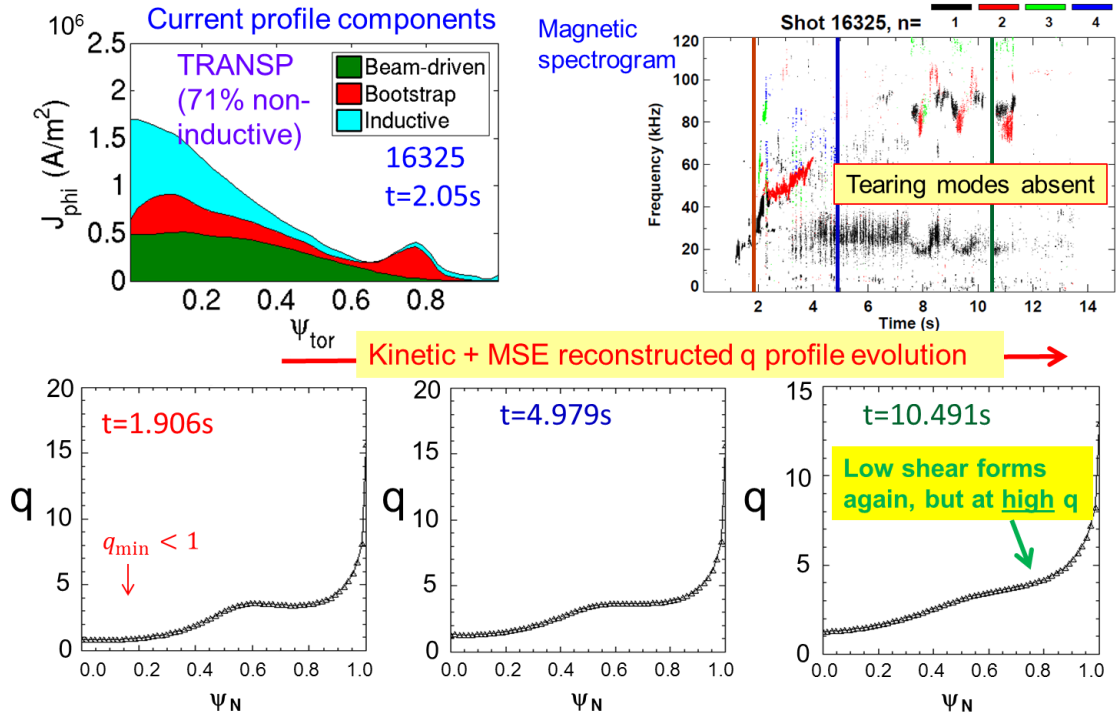


**Fig. MS-31:** Non-inductive current profiles, magnetic spectrogram of toroidal probe array, and  $q$  profile evolution of kinetic equilibrium reconstructions with MSE data for  $\beta_N \sim 2$  plasma in KSTAR.

The high quality of the kinetic equilibrium reconstructions has allowed relatively smooth evolution of both linear ideal and resistive stability computations using the DCON code. This is a required first step in the evaluation of MHD stability criteria for KSTAR to be used in the DECAF code. Fig. MS-32 the computation of the ideal  $n = 1$  no-wall stability functional  $\delta W$  for the KSTAR shot with  $\beta_N \sim 2$ . Other than a few time points with relatively high convergence error, the computation produces a smooth evolution of the criterion.

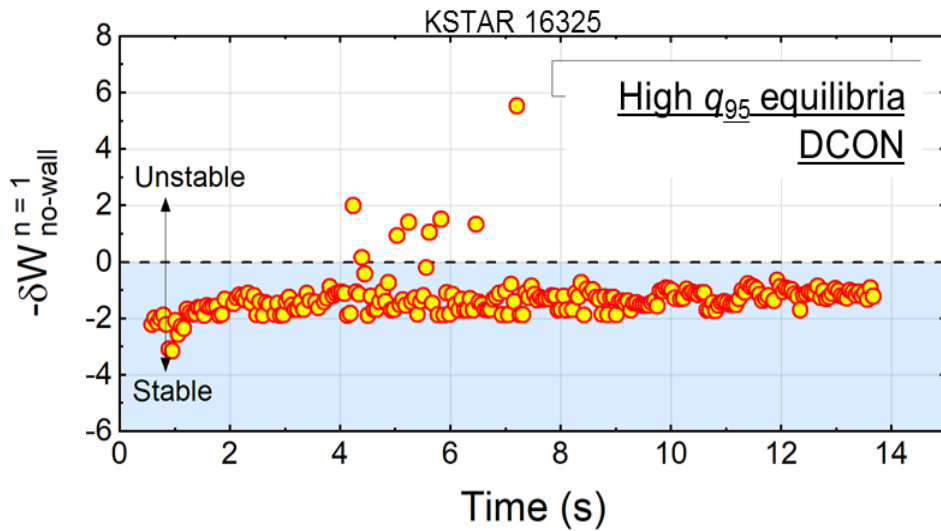


**Fig. MS-32:** Computation of ideal  $n = 1$  no-wall stability functional using DCON code for the  $\beta_N \sim 2$  plasma in KSTAR.

Linear resistive stability computation of the classical  $\Delta'$  stability criterion is notoriously very highly sensitive to the equilibrium input for evaluation. Our kinetic equilibrium reconstructions with MSE are now of sufficient quality and robustness to support relatively low analysis noise in the stability evaluation. The  $\Delta'$  calculation is shown for both the  $\beta_N \sim 3.5$  and  $\beta_N \sim 2$  plasmas in Fig. MS-33. The computations show a clear trend and sign of  $\Delta'$  as the plasmas evolve. The sign of  $\Delta'$  in theory determines the classical linear resistive stability.

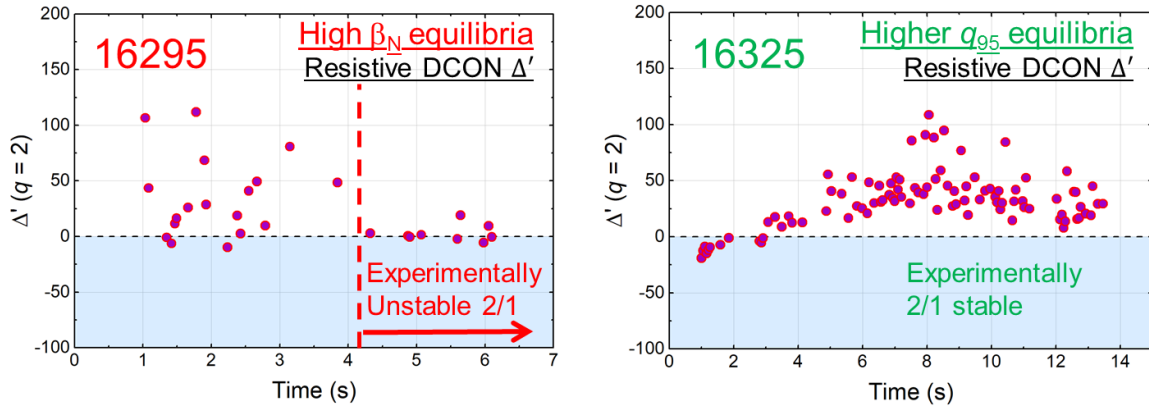


**Fig. MS-33:** Computation of resistive  $\Delta'$  calculation using the DCON code for  $\beta_N \sim 3.5$  and  $\beta_N \sim 2$  plasmas in KSTAR.

However, Fig. MS-33 shows that the theoretically computed  $\Delta'$  does not reproduce what is found in the KSTAR experiments. In the  $\beta_N \sim 3.5$  case, the trend in  $\Delta'$  is from positive to near zero, theoretically indicating greater stability as the plasma evolves, while experimentally the plasma becomes 2/1 tearing mode unstable. A similar incompatibility is found for the  $\beta_N \sim 2$  case. In this case, the  $\Delta'$  clearly evolves to be positive, theoretically showing that the 2/1 tearing mode should be unstable, which is not observed in the experiment. These results indicate that we will at least need to include the neoclassical terms of the modified Rutherford equation to attempt to reproduce the experiment. That alteration may or may not be sufficient to reproduce the experimental findings.

Kinetic MHD analysis of global MHD modes (resistive wall modes) using the MISK code does find stability of high beta KSTAR plasmas, consistent with experiment. To date, we have computed KSTAR high  $\beta_N$  plasmas to exceed the ideal  $n = 1$  no-wall stability limit, yet resistive wall modes have not yet been found on KSTAR. The kinetic calculations show that the modes are stabilized by kinetic effects. The addition of energetic particles to these calculations show greater stabilization due to their influence.

## References

- [MS-1] D. Battaglia et al., Nucl. Fusion **58**, 046010 (2017).
- [MS-2] S. P. Gerhardt et al., NSTX-U-DOC-101-01, Unreleased (2018).
- [MS-3] J.-K. Park et al., Phys. Rev. Lett. **102**, 065002 (2009).
- [MS-4] J.-K. Park et al., ITER IDM#UMLSUM (2017).
- [MS-5] C. E. Myers et al., submitted to Phys. Rev. Lett. (2018).
- [MS-6] Pfefferlé et al., Phys. Plasmas **25**, 056106 (2018).
- [MS-7] J. W. Berkery et al., Phys. Plasmas **24**, 056103 (2017).

- [MS-8] J. W. Berkery et al., Phys. of Plasmas **21**, 156112 (2014).
- [MS-9] T. Eich et al., Nucl. Fusion **58**, 034001 (2018).
- [MS-10] D. A. Gates et al., Phys. Rev. Lett. **108**, 165004 (2012).
- [MS-11] Q. Teng et al., Nucl. Fusion **56**, 106001 (2016).
- [MS-12] D. E. Post et al., Atomic Data and Nuclear Data Tables **20**, 397 (1977).
- [MS-13] R. Budny et al., Nucl. Fusion **32**, 429 (1992).
- [MS-14] J. E. Menard et al., Nucl. Fusion **45**, 539 (2005).
- [MS-15] R. J. La Haye et al., Nucl. Fusion **38**, 987 (1998).
- [MS-16] R. J. La Haye et al., Phys. Plasmas **13**, 055501 (2006).
- [MS-17] C. C. Hegna, Phys. Plasmas **6**, 3980 (1999).
- [MS-18] T. Markovic et al., EPS conference on Plasma Physics (2018).
- [MS-19] M. Lanctot et al., Phys. Plasmas **24**, 056117 (2017).
- [MS-20] J.-K. Park et al., Nucl. Fusion **52**, 023004 (2012).
- [MS-21] J.-K. Park et al., Nucl. Fusion **51**, 023003 (2011).
- [MS-22] A. H. Boozer, Phys. Rev. Lett. **22**, 5059 (2001).
- [MS-23] H. Reimerdes, Phys. Rev. Lett. **106**, 215002 (2011).
- [MS-24] R. Fitzpatrick, Plasma Phys. Control. Fusion **54**, 094002 (2012).

## B. Transport and Turbulence

In addition to the R18-3 milestone activity, additional transport and turbulence research in FY-18 proceeded on multiple fronts. Nonlinear simulations were run and validated using NSTX-U L-mode data as well as NSTX H-mode data. Simulation of microtearing turbulence was initiated in complementary high-beta Pegasus H-mode discharges, and analysis of DIII-D FY17 NSTX-U Campaign experiments have also progressed.

### *NSTX-U L-mode modeling*

Local, single-scale nonlinear gyrokinetic simulations have been run to predict transport in NSTX-U L-mode plasma [TT-1]. At radii outside  $\rho > 0.6$ , ion temperature gradient (ITG) turbulence dominates the predicted transport at ion scales ( $k_{\theta}\rho_s < 1$ ) providing  $\sim 0.5\text{-}0.7$  MW of electron heat flux, which is about half the experimental value (Fig. TT-1, black circles). The predicted ion heat flux varies dramatically, increasing to values much larger than the experiment when moving outward. The increase of predicted ion heat flux occurs as the  $E \times B$  shearing rate drops to values much smaller than the linear growth rates [TT-2]. Inside  $\rho < 0.6$  microtearing modes (MTM) dominate at the ion scales, with nonlinear simulations predicting  $\sim 1\text{-}2$  MW of electron heat flux comparable to experiment (not shown). Additional simulations, however, are required to verify that the MTM simulations are sufficiently resolved numerically.

We note that the local ion-scale simulations use numerical grids that are  $\sim 100 \rho_i$  wide. However, the width of the region under investigation ( $\rho = 0.5\text{-}0.75$ ) is only  $\sim 30 \rho_i$  wide due to the relatively large value of  $\rho^* = \rho_i / a \sim 1/150$  in these plasmas. Therefore, non-local effects are very likely important to predicting the correct quantitative transport, as has been noted for NSTX L-mode analysis [TT-3-TT-5]. (See additional discussion in the R18-3 milestone summary.)

In addition to ion-scale turbulence, electron-scale simulations ( $k_{\theta}\rho_s > 3$ ) of electron temperature gradient (ETG) turbulence also predict significant transport around the mid-radius ( $\rho = 0.4\text{-}0.6$ ), which approaches experimental levels. Given the similarity in electron heat flux as predicted separately from both electron scale and ion scale ( $Q_{e,\text{high-}k} \sim Q_{i,\text{low-}k}$ ), cross-scale coupling effects cannot be ruled out [TT-6]. Similar implications are found for NSTX-U L-modes (see R18-3 Milestone summary) and the recent NSTX H-mode analysis. In addition, with the importance of non-local effects at ion scales, it is possible that a combination of global plus multiscale would be required to predict the complete ion and electron thermal transport profiles. The feasibility of such simulations is unclear and will require careful future exploration as computational resources increase.

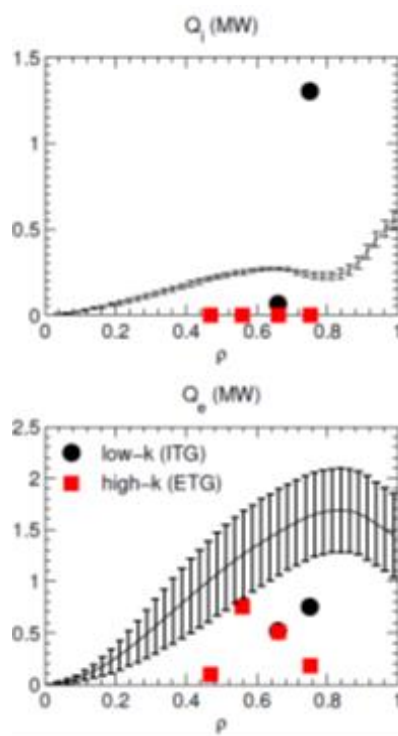


**Fig. TT-1:** (top) Ion and (bottom) electron thermal transport profiles. Experimentally inferred profiles with uncertainties are given by the lines. Symbols show predicted transport from either ion scale (black circles) or electron scale (red squares) simulations.

## **NSTX H-mode analysis and modeling**

### ETG simulations and high-k synthetic diagnostic

In collaboration with MIT graduate student J. Ruiz-Ruiz and Professor A. White, work has continued on validating nonlinear gyrokinetic simulations for an NSTX H-mode discharge. This includes the use of a new synthetic diagnostic for comparison with high-k scattering measurements. The discharge exhibits two states where electron-scale turbulence (electron temperature gradient, ETG) is expected to contribute substantially to transport, identified as either “high-ETG” or “low-ETG” drive. The low-ETG drive case shows reduced fluctuations and ETG stabilization due to increased density gradient that resulted from a programmed current ramp-down [TT-7]. Extensive linear and nonlinear single-scale gyrokinetic simulations using the GYRO code [TT-8] have been run, varying inputs within experimental uncertainties in an attempt to match experimental fluxes and measured high-k fluctuation amplitudes.

Linear simulations indicate the main instabilities present for both conditions are trapped electron modes (TEM) at ion scales and ETG at electron scales. However, TEM linear growth rates are smaller than the  $E \times B$  shearing rate for the “high-ETG” cases, with a corresponding suppression of transport predicted in nonlinear ion-scale simulations. On the other hand, nonlinear electron-scale ETG simulation are found to match experimental electron heat fluxes when temperature and density gradient are varied within experimental uncertainty, identifying ETG as the origin of anomalous electron thermal transport in this case.

For the “low-ETG” drive case, transport predicted by electron scale simulations also approach the experimental level when density and temperature gradients are adjusted within uncertainties. However, ion scale simulations predict very large transport when using the same scaled gradients. Additional gradient scans show the ion scale transport is very close to marginal and possibly in the nonlinearly-upshifted zonal flow regime (or “Dimits shift regime” [AD]). Therefore, cross-scale coupling cannot be ruled out for the low ETG condition [TT-6], and it is likely that multiscale simulation will be required to resolve this validation case.

To further validate the simulation results, a new 2D synthetic diagnostic for the NSTX high- $k$  scattering system has been fully implemented. The new implementation in real space differs from past work by F. Poli [TT-9, TT-10] which employed an implementation in wavenumber space. While both strategies have been shown to be analytically equivalent, the implementation in real space is the more natural, straightforward approach and allows easier implementation in other codes. In addition, it is easily expandable to a 3D implementation; analytic foundations have been recently developed in collaboration with J. Candy at General Atomics. A draft manuscript outlining the synthetic diagnostic approach and initial tests has been written and will be submitted as part of the thesis work.

Very large, nonlinear simulation domains were required to apply the synthetic diagnostic for wavenumbers equivalent to the experimental measurements [TT-11]. These so-called ‘hybrid-scale’ simulations (requiring  $\sim 1\text{M}$  CPU-hrs/simulation on NERSC Edison) are fundamentally electron scale but also capture significant ion contributions that span over two orders in wavenumber,  $k_{\theta}\rho_s = 0.3\text{-}65$  ( $\sim 3\text{x}$  the electron scale wavenumber range,  $k_{\theta}\rho_s \sim 1\text{-}65$ ).

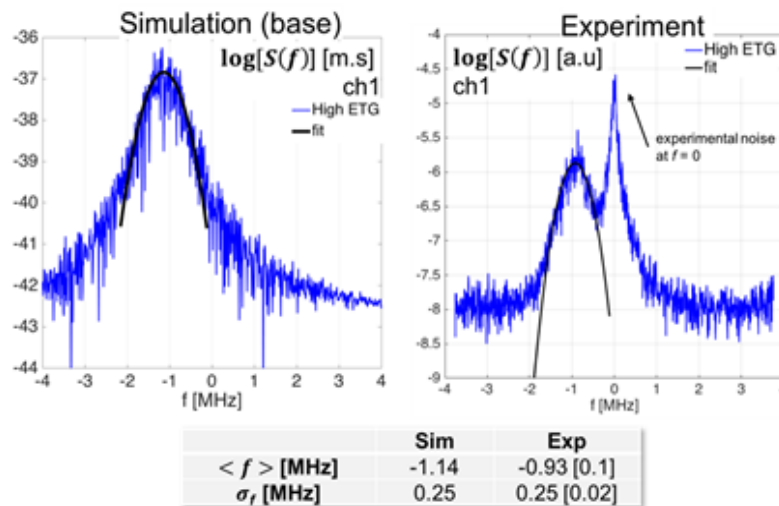


**Fig. TT-2:** High- $k$  turbulence frequency spectrum from simulation (left) and experiment (right), applied to channel 1 of the high- $k$  scattering system (high ETG conditions). A Gaussian envelope is fit to both spectra to the mean frequency  $\langle f \rangle$  and the spectral width  $\sigma_f$ . The synthetic frequency spectrum reproduces  $\langle f \rangle$  and  $\sigma_f$  from experiment.

Fig. TT-2 shows a comparison of a single synthetically-generated frequency spectrum to experimental data for the “high ETG” drive case. The detected turbulence frequency in the lab

frame is dominated by Doppler shift, and is not a critical constraint on simulation. The width of the frequency spectrum, however, is a main probe into the intrinsic turbulence characteristics and is found to be in good agreement with the experiment. This gives further confidence that ETG turbulence may account for transport and turbulence in the “high-ETG” drive case.

Fig. TT-3 shows a comparison of the frequency-integrated wavenumber power spectrum from both experimental cases that was rescaled by an arbitrary constant as they are not absolutely calibrated. Also shown are the equivalent synthetic spectra based on electron-scale simulations that provided the best agreement with experimental transport fluxes. The synthetic spectra show similar changes in peak amplitude as the experimental measurements. The spectral shape for the high-ETG drive case, however, does not show the clear peak in middle wavenumber. Sensitivity studies of the synthetically generated spectra will be compared as part of the thesis work to demonstrate agreement in transport and turbulence quantities can be simultaneously demonstrated.

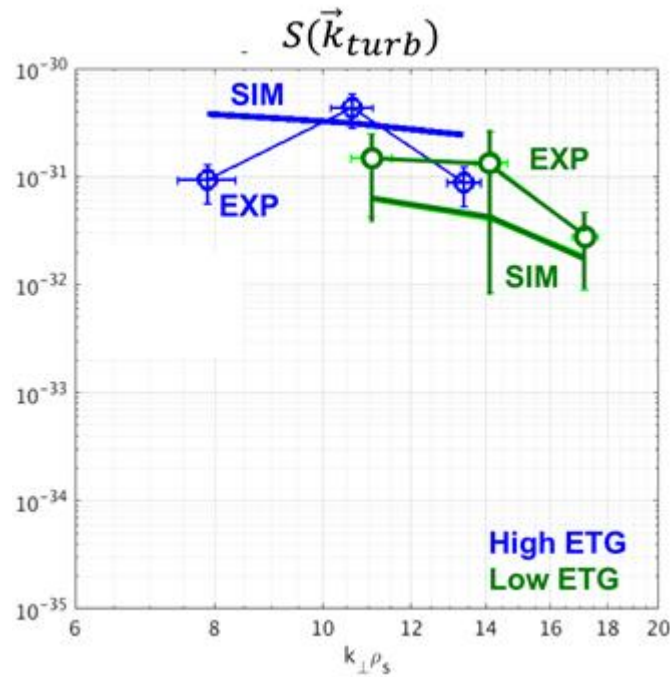


**Fig. TT-3:** Experimental and synthetic wavenumber spectrum of high- $k$  fluctuations applied to two different experimental plasma conditions (high and low ETG). Simulation can match the shape of the  $k$ -spectrum at low ETG (consistent with the  $Q_e$  agreement), but not at high ETG. Note the experimental absolute value has been rescaled by a constant (lack of absolute calibration).

### Impurity Transport Modeling

Previous analysis found that carbon density profiles in discharges with boronized wall conditions and natural ELMs were generally in agreement with neoclassical predictions [TT-12]. However, in lithium-conditioned ELM-free discharges, the neoclassical predictions (using NEO [TT-13]) predict a large inward carbon flux inside the top of the pedestal inconsistent with experiment. Recent analysis has shown that carbon profiles in similar lithium-conditioned discharges were

found to match neoclassical predictions when ELMs are triggered via externally applied 3D fields [TT-14]. Gyrokinetic simulations with CGYRO code [TT-15, TT-16] were performed to investigate whether turbulent carbon transport could account for the deviation from neoclassical transport observed in ELM-free lithium-conditioned discharges. The simulations predict that a mix of electrostatic ballooning modes and electromagnetic microtearing modes are unstable in the region of interest. To estimate the magnitude and direction of theoretical turbulent carbon flux, the ratio of quasi-linear fluxes predicted by CGYRO ( $\Gamma_c/Q_e$ ) were averaged over ion scale wavenumbers ( $k_\theta \rho_s = 0.1-1$ ) and then multiplied by experimental electron heat flux inferred from TRANSP. Figure TT-4 shows radial carbon fluxes from NEO and CGYRO for an ELM-free discharge (NEO black, CGYRO blue) and a discharge with ELMs triggered at 50 Hz (NEO red, CGYRO green). In the ELM-free discharge, for  $r/a=0.7-0.8$ , CGYRO predicted unstable ballooning modes producing outward radial carbon flux. Quasilinear carbon fluxes are on the order of  $2 \times 10^{20}$  ion/s. This outward flux only partially compensates the anomaly in the neoclassical predictions on the order of  $1-2 \times 10^{21}$  ion/s. (We note that the larger flux predicted by CGYRO at  $r/a \sim 0.6$  occurs where  $E \times B$  shearing rates are larger than linear growth rates and are expected to suppress transport.) Tests of centrifugal effects implemented in both NEO and CGYRO indicate their inclusion made little difference to the predicted fluxes in these cases. Further sensitivity studies and non-linear CGYRO simulations are envisioned in the near future.

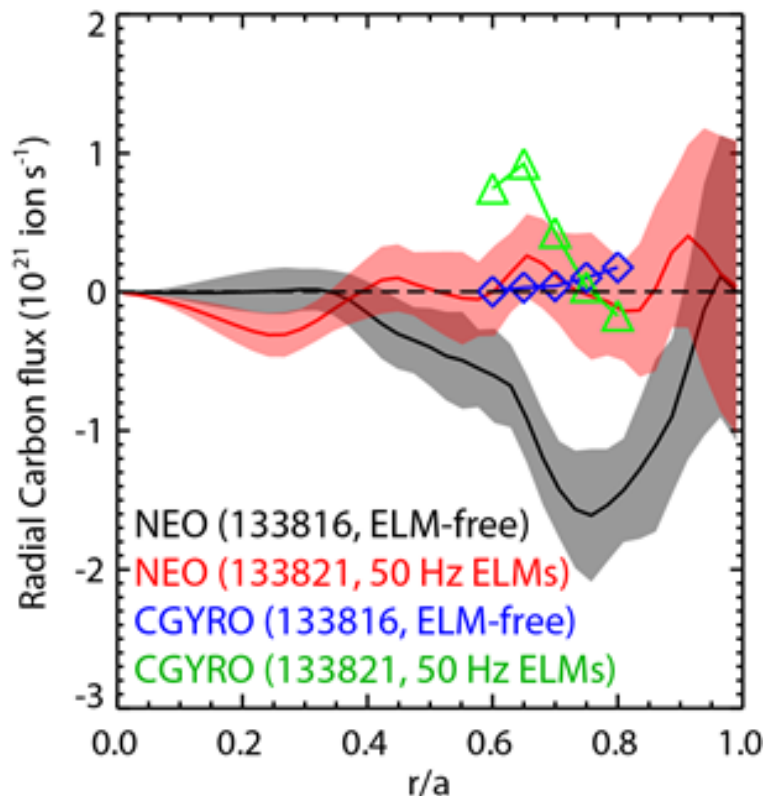


**Fig. TT-4:** Predicted carbon particle flux from NEO for two lithium-conditioned NSTX-H modes that are either naturally ELM-free or with triggered ELMs. Also shown are the estimated anomalous fluxes using the quasi-linear ratio  $\Gamma_c/Q_e$  from linear CGYRO simulations multiplied by the experimentally inferred electron heat flux from TRANSP.

## Collaborations

### Pegasus H-mode modeling

The Pegasus ST device complements NSTX-U capabilities with ELMy H-mode operation at lower aspect ratio ( $A$ ), higher  $\beta$ , and higher normalized current ( $I_N$ ). A diamagnetic well ( $\nabla B$  reversal) was routinely observed during near-unity- $\beta$  operation of the Pegasus ST [TT-17], and the magnetic topology may afford novel, favorable characteristics affecting turbulent transport. Previous work showed large  $\nabla p$  reduced magnetic drifts responsible for drift wave instabilities [TT-18], so  $\nabla B$  reversal at high  $\beta$  in Pegasus motivates an investigation of  $\nabla B$  and  $\nabla p$  drift terms that influence turbulence and microstability.

Given the emphasis on ST collaborations during the NSTX-U recovery and the close association between the University of Wisconsin BES group and the Pegasus team, the groups, along with P. Terry from University of Wisconsin and M.J. Pueschel from UT-Austin, began investigating the gyrokinetic stability properties of the diamagnetic observed in Pegasus. As shown in Fig. TT-5, GENE linear flux-tube calculations at the maximum  $\nabla B$  reversal in the near-unity  $\beta$  scenario indicate two varieties of microtearing modes are unstable at  $k_y \rho_i \approx 0.2$  and  $0.8$ . The modes are more unstable in a comparable monotonic  $|B|$  configuration, so  $\nabla B$  reversal is an overall stabilizing influence. Additionally in Fig. TT-5, the microtearing modes at  $k_y \rho_i \approx 0.2$  are insensitive to the  $\nabla p$  term in the  $\nabla B$  drift, which is typical for drift wave turbulence in low- $\beta$  tokamaks. In contrast, the microtearing modes at  $k_y \rho_i \approx 0.8$  are highly sensitive to the  $\nabla p$  term in the  $\nabla B$  drift. Investigation of microstability properties of  $\nabla B$  reversal in the Pegasus ST continues, and nonlinear GENE simulations with challenging numerical resolution requirements are in progress on NERSC computing systems.

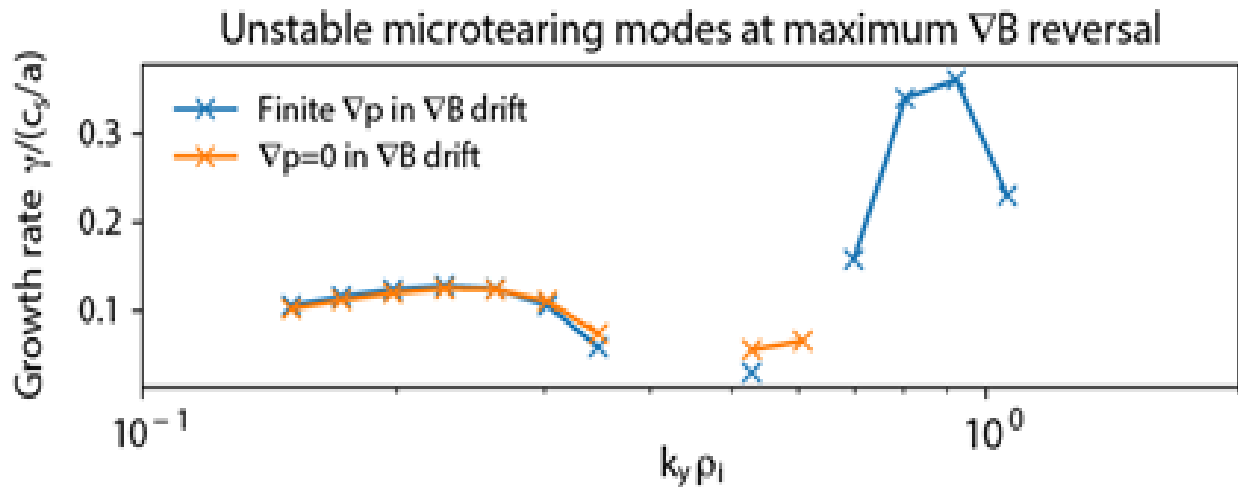


**Fig. TT-5:** Linear growth rate spectra for unstable microtearing modes predicted in the diamagnetic well region in a high beta Pegasus H-mode. The microtearing modes at  $k_y \rho_i \approx 0.2$  are insensitive to the  $\nabla p$  term in the  $\nabla B$  drift, but the  $k_y \rho_i \approx 0.8$  modes are highly sensitive to the  $\nabla p$  term.

### DIII-D “NSTX-U” Campaign Analysis

Analysis continued for two DIII-D transport experiments lead by NSTX-U team members that were chosen to run as part of the FY17 “NSTX-U Campaign” established following the unplanned NSTX-U outage.

#### ***Study of collisionality dependence of ion- and electron-scale turbulence in advanced inductive hybrid scenario with ST-relevant $q_{95}$ on DIII-D***

The strong inverse collisionality dependence of normalized energy confinement time ( $B\tau_E \sim \nu_e^{-1}$ ) observed in NSTX [TT-19] and MAST [TT-20] is a unique feature of spherical tokamak (ST) plasmas and was found to be determined by the electron channel [TT-19]. If such a confinement scaling can extend to even lower collisionalities in STs, it can lead to cheaper and more compact future fusion reactors than those based on conventional tokamak design. Thus, this energy confinement scaling is the primary motivation for NSTX-U. On the other hand, energy confinement of conventional tokamaks may have a collisionality dependence as well. Although the present ITER confinement scaling shows weak dependence on collisionality, an analysis of a DIII-D H-mode data set has shown a stronger collisionality dependence, i.e.  $B\tau_E \sim \nu_e^{-0.5}$  [TT-21]. In order to investigate the mechanisms underlying the above observed collisionality dependence, an experiment entitled “study of collisionality dependence of ion- and electron-scale turbulence in advanced inductive hybrid scenario with ST-relevant  $q_{95}$  on DIII-D” was carried out on DIII-D as a part of the DIII-D/NSTX-U national campaign. The aim was to measure ion- and electron-scale turbulence in a well-controlled, dimensionless electron collisionality scan, in a DIII-D advanced inductive scenario, with an ST-relevant  $q_{95}$  and with other dimensionless quantities (e.g.  $\rho^*$ ,  $\beta$ ,  $T_e / T_i$ ,  $q$ ) kept approximately constant. The collisionality scan was achieved experimentally by varying  $B_T$  and  $I_p$  together with  $B_T/I_p$ . Plasma density was kept constant (with fixed plasma shape), and electron temperature,  $T_e$ , varied as  $T_e \sim B^2$  by changing heating power (NBI and ECH), which led to  $\nu_e \sim T_e^{-2} \sim B^{-4}$ . In the experiment, discharges with four different  $B_T$  values (1.3, 1.5, 1.65 and 2.1 T) - i.e. four different collisionalities - have been achieved with  $\nu_e$  varied by a factor of about 5.6 at  $\rho=0.5$  and by a factor of about 9.2 at  $\rho=0.7$  with  $q_{95} \approx 6.5$ , where  $\rho$  is the square root of normalized toroidal flux. Matching different plasma profiles for different collisionalities is essential to keep other dimensionless quantities constant. Reasonable profile matching was also achieved in this experiment. Furthermore, confinement scalings, i.e.  $B\tau_E \sim \nu_e^{-0.48}$ ,  $B\tau_E \sim \nu_e^{-0.48}$  and  $B\tau_E \sim \nu_e^{-0.47}$  were found using collisionality values at  $\rho=0.5$ , 0.6 and 0.7, respectively, and was consistent with what was found for DIII-D H-mode plasmas [TT-21]. The density fluctuation wavenumber spectra measured at  $\rho \sim 0.55-0.65$  by a Doppler Back Scattering (DBS) system on DIII-D [TT-22] showed that measured spectral power clearly decreases at lower wavenumbers, i.e.  $k\theta_{ps} < 2$ , as  $B_T$  increases (collisionality decreases), consistent with the observed confinement scaling dependence on collisionality. Kinetic equilibrium reconstruction and transport analysis was carried out with OMFIT by coupling a time-dependent tokamak transport and data analysis code (TRANSP) [TT-23] and EFIT. It was found that electron thermal transport was dominant in determining the energy confinement scaling with electron channel being the dominant heat-loss channel for the three lower  $B_T$  cases (electron and ion heat fluxes are comparable for the  $B_T=2.1$  T case).

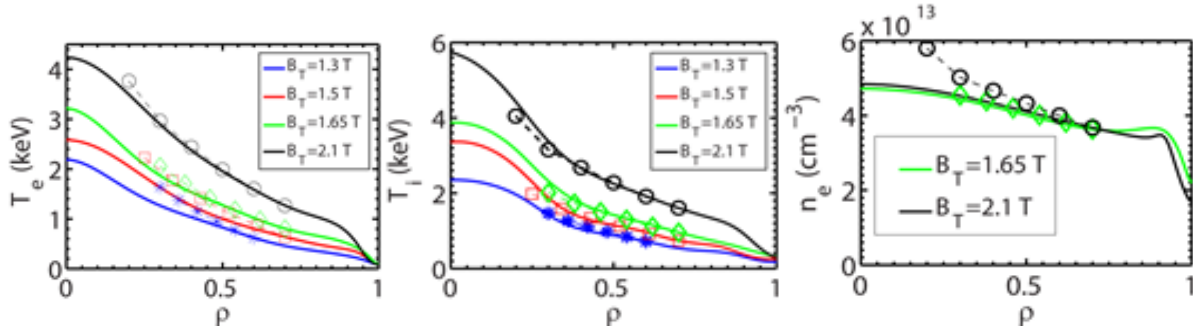


**Fig. TT-6:** Left: electron temperature profiles; Middle: ion temperature profiles; Right: electron density profiles. Experimental profiles are shown as solid lines and TGLF-predicted profiles are shown as symbols with dashed lines. Colors of the solid lines and symbols denote different  $B_T$  cases for both experimental and predicted profiles: (blue solid lines and asterisks: 1.3 T, red solid lines and open squares: 1.5 T, green solid lines and open diamonds: 1.65, black solid lines and open circle: 2.1 T.) Note that the radial ranges of the TGLF-predicted profiles, e.g.  $\rho$  from 0.35 to 0.6 for the  $B_T=1.3$  T case, are not the same for different cases. For each case, a different radial simulation domain was chosen in order to achieve a converged solution. Also note that simultaneous evolution of  $T_e$ ,  $T_i$  and  $n_e$  was only successful for the two higher  $B_T$  cases.

In order to understand these experiment observations, numerical modeling has been carried out with a reduced trapped gyro-Landau fluid model (TGLF) with the original saturation rule (TGLF-SAT0) [TT-24], using TGYRO transport solver and with global gyro-kinetic code GTS [TT-25]. Figure TT-6 compares TGLF-predicted  $T_e$  (left),  $T_i$  (middle) and  $n_e$  (right) profiles with experimental profiles. It can be seen that while TGLF does a decent job predicting  $T_i$  profiles for all four  $B_T$  cases and  $T_e$  profiles for the two higher  $B_T$  cases, it significantly over-predicts  $T_e$  for the two lower  $B_T$  cases, meaning that TGLF significantly under-predicts electron thermal transport with experimental profiles for these two cases. The above results also mean that TGLF modeling is not able to explain the experimentally observed confinement scaling. In addition, density profile predictions were only achieved for the two higher  $B_T$  cases, where the prediction for the  $B_T=1.65$  T case is much better than that for the  $B_T=2.1$  T case. The inability to achieve converged solutions with  $n_e$  evolution for the two lower  $B_T$  cases is also due to the under-prediction of electron thermal transport by TGLF with experimental profiles. Since for the two lower  $B_T$  cases TGYRO calculation will need to increase  $T_e$  gradient significantly to match experimental electron heat flux, the enhanced  $T_e$  gradient drives negative particle flux, which makes simultaneously matching experimental particle flux (always positive due to NBI fueling) impossible. We note that the TGLF-SAT0 saturation rule used in the presented simulations does not include cross-scale coupling. However, as shown in Fig. TT-6, reasonable predictions for the two higher  $B_T$  cases by TGLF using the TGLF-SAT0 saturation rule suggest that cross-scale coupling may not be important for these two cases. Although the cross-scale coupling might be important for the two lower  $B_T$  cases, it was found to be difficult to obtain converged solutions for these plasmas with the TGLF-SAT1 saturation rule, which includes the cross-scale coupling.

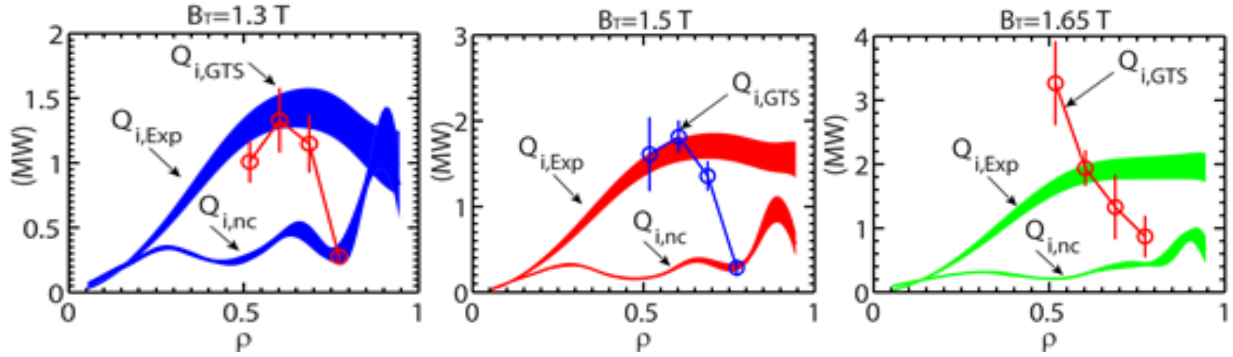


**Fig. TT-7:** Comparisons between experimental ion heat flux,  $Q_{i,Exp}$ , ion neoclassical heat flux,  $Q_{i,nc}$  (colored bands) and GTS-predicted ion energy flux,  $Q_{i,GTS}$ , (open circles) for different  $B_T$  cases: left:  $B_T=1.3$  T; middle:  $B_T=1.5$  T; right:  $B_T=1.65$  T. The vertical width of the colored bands denotes the experimental uncertainty.  $Q_{i,nc}$  is calculated with NCLASS neoclassical code.

The comparisons between experiments and GTS simulations in ion thermal transport are presented in Fig. TT-7. These global ion-scale GTS simulations have a simulation domain from  $\rho=0.05$  to  $0.9$  with buffer regions at  $\rho < 0.25$  and  $\rho > 0.8$ . The size of grids on poloidal planes is about local ion gyro-radius, and 80 particles per cell-species are used with kinetic electrons and collisions; no impurity species included. It is clear that the GTS-predicted ion energy flux plus neoclassical contribution is in reasonable good agreement with experimental ion heat flux for the two lower  $B_T$  cases at three radial locations (consistent with the TGYRO modeling), although the small value of  $Q_{i,GTS}$  at  $\rho \sim 0.77$  may be due to the influence of the outer buffer region ( $\rho > 0.8$ ). The agreement is worse for the  $B_T=1.65$  T case, where  $Q_{i,GTS}$  shows very different radial trend compared to the experiment. We note that GTS predicts no unstable ion-scale mode for the  $B_T=2.1$  T case. Thus, for the two higher  $B_T$  cases, GTS predictions are very different from the TGYRO modeling shown in Fig. TT-6, which certainly requires further investigation. We note that the neoclassical contribution becomes more important at larger radius for all three cases as seen in Fig. TT-7. Particularly for the  $B_T=1.3$  T case, the neoclassical contribution dominates at  $\rho > 0.85$ . Thus, the trend seen in GTS simulations ( $Q_{i,GTS}$  decreasing towards larger radius) is possibly consistent with the trend in neoclassical contribution. To confirm this, the inner boundary of the outer simulation buffer needs to be moved to  $\rho=0.9$ , which will be carried out in the next-step analysis. We also note that these ion-scale GTS simulations predict negligible electron thermal transport, which is very different from TGLF predictions shown in Fig. TT-6. Further linear and nonlinear simulations will be carried out to address this discrepancy.

### **Validating electromagnetic effects in high performance plasmas**

Initial analysis of the DIII-D QH-mode discharges indicated that the ratio of scattered powers measured in the deep core ( $\rho \sim 0.4$ ) by cross polarization scattering (CPS, expected to be proportional to  $\sim \delta B$  [TT-26, TT-27]) and Doppler backscattering (DBS, proportional to  $\sim \delta n$  [TT-22]) increased with increasing beta, as expected from theory [TT-28, TT-29]. Significant follow-on analysis has been performed with OMFIT including profile fitting, TRANSP analysis, and kinetic equilibrium reconstructions to eventually enable a direct comparison between the measurements and turbulence simulations. The transport analysis is complicated by observed

relatively large impurity content as the QH-modes were run ~6 weeks after a boronization. As a consequence, impurity radiation signals (iron, nickel, etc.) measured by SPRED were significantly larger than the target discharge originally run immediately following boronization. To account for the large impurity content in the transport analysis, the impurity transport code STRAHL was used to calculate the density of multiple iron charge states by constraining to both soft x-ray and bolometer measurements. The results indicated very large impurity content with  $Z_{\text{eff}} \sim 8\text{-}12$  on-axis. The dominant charge state (Fe24) was then included in TRANSP analysis to produce transport and equilibrium solutions the most consistent with neutron and stored energy measurements. These will provide the basis for future gyro-kinetic simulations to predict transport and fluctuation spectra where the DBS and CPS measurements were obtained.

## References

- [TT-1] W. Guttenfelder, AAPPs-DPP invited talk, Chengdu, China (2017).
- [TT-2] W. Guttenfelder, APS-DPP oral, San Jose, CA (2016).
- [TT-3] Y. Ren et al., Nucl. Fusion **53**, 083007 (2013).
- [TT-4] W.X. Wang et al., Nucl. Fusion **55**, 122001 (2015).
- [TT-5] W.X. Wang et al., Phys. Plasmas **22**, 102509 (2015).
- [TT-6] N.T. Howard et al., Nucl. Fusion **56**, 014004 (2016).
- [TT-7] J. Ruiz-Ruiz et al., Phys. Plasmas **22**, 122501 (2015).
- [TT-8] J. Candy, R.E. Waltz, J. Comp. Physics **186**, 545 (2003).
- [TT-9] F.M. Poli et al., Phys. Plasmas **17**, 112514 (2010).
- [TT-10] F.M. Poli et al, APS-DPP, Chicago (2010).
- [TT-11] J. Ruiz-Ruiz et al., APS-DPP oral, Milwaukee (2017).
- [TT-12] F. Scotti et al., Nucl. Fusion **53**, 083001 (2013).
- [TT-13] E.A. Belli, J. Candy, Plasma Phys. Control. Fusion (2008).
- [TT-14] F. Scotti et al., IAEA-FEC, Kyoto, Japan (2016).
- [TT-15] J. Candy et al., J. Comp. Physics, **324**, 73 (2016).
- [TT-16] E.A. Belli, J. Candy, Phys. Plasmas **25**, 032301 (2018).
- [TT-17] D. Schlossberg et al., Phys. Rev. Lett. **119**, 035001 (2017).
- [TT-18] C. Bourdelle et al., Phys. Plasmas **10**, 2881 (2003).
- [TT-19] S. M. Kaye, et al., Phys. Rev. Lett. **98**, 175002 (2007).
- [TT-20] M. Valovic, et al., Nucl. Fusion **51**, 073045 (2011).
- [TT-21] T. Luce, et al., Plasma Phys. Controlled Fusion, **50**, 043001 (2008).
- [TT-22] T.L. Rhodes et al., Rev. Sci. Instrum., **81**, 10D912 (2010).
- [TT-23] R.J. Hawryluk, 1981 Physics of Plasma Close to Thermonuclear Conditions (New York: Pergamon).
- [TT-24] G. M. Staebler, J. E. Kinsey, and R. E. Waltz, Phys. Plasmas, **14**, 055909 (2007).
- [TT-25] W.X. Wang et al., Phys. Plasmas, **13**, 092505 (2006).
- [TT-26] T.L. Rhodes et al., Rev. Sci. Instrum. (2014); Rev. Sci. Instrum. (2016).
- [TT-27] K. Barada et al., RSI (2016).
- [TT-28] W. Guttenfelder et al., APS-DPP, Milwaukee, WI (2017).
- [TT-29] W. Guttenfelder et al., US-TTF, San Diego, CA (2018).

## C. Energetic Particles

NSTX-U Energetic Particle research in FY-18 made progress in four main areas: improvements of numerical tools for EP research, development of reduced EP transport models for comprehensive time-dependent integrated simulations, analysis of Alfvénic instabilities in NSTX/NSTX-U plasmas, and assessment of EP transport by low-frequency MHD instabilities. Progress in each area is summarized in the following sections. Additional work addressing the R18-4 Milestone is discussed previously in this report as are collaborative activities fulfilling the JRT-18 Milestone led by NSTX-U/PPPL. A complete report will be submitted to FES at the end of FY18.

### *Improvements To Energetic Particle Analysis And Modeling Tools*

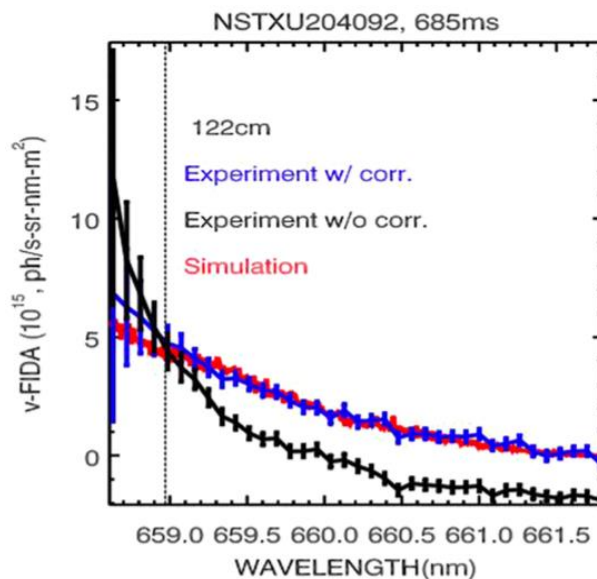


**Fig. EPM-1:** Experimental spectra without (black) and with (blue) corrections for scattered light. The red line shows the spectrum predicted by the FIDAsim code. (From [EP-1]).

Previous analysis of data from the NSTX-U Fast-ion D-alpha (FIDA) diagnostics has suggested that emission from the cold  $D_\alpha$  line contaminates the measured FIDA spectrum [EP-1]. The scattered light can be compared to the FIDA emission, thus making the interpretation of the measured signals difficult and prone to large uncertainties. In these cases, a correction for the scattered light is required to extract useful FIDA results. Two methods that relate the scattered light contamination to the intensity of the cold  $D_\alpha$  line have been developed. The first method uses laboratory measurements with a calibration lamp to infer the amount of contamination measured by the diagnostic. The second method uses data acquired during plasma operation, which are then processed through a singular value decomposition analysis to

infer the required corrections. Based on NSTX-U data, both the FIDA spectra and spatial profile are in better agreement with theoretical predictions after applying the corrections (Fig. EPM-1).

On the modeling side, the processing of experimental and simulation data used to compute the inputs for the fast ion transport “kick model” in TRANSP has been considerably streamlined. The procedure requires analysis through the ideal MHD code NOVA-K based on experimental profiles, followed by analysis via the ORBIT particle-following code based on the eigenmodes produced by NOVA-K. The procedure has been improved, for example, by developing a multi-processor version of ORBIT that is specifically optimized for the calculations required by the kick model. The optimization resulted in a considerable reduction in the time required to compute the

kick model inputs from several hours down to 5-30 minutes based on the number of modes being analyzed. This improvement is important in view of the planned development of a module in TRANSP/NUBEAM to update the kick model inputs self-consistently during a TRANSP runs; for instance, to account for variations of the background plasma parameters or modification in the radial structure of the instabilities included in the simulation.

In parallel with improvements to the kick model, good progress has been made in developing a different approach based on quasi-linear theory, which is at the basis of the Resonance-broadened Quasi-linear model (RBQ1D [EP-2]). During FY-18, developments of the RBQ1D code have resulted in the implementation of self-consistent multimode simulation capabilities. An important development is the capability to describe transport induced by multiple Alfvénic modes acting simultaneously on the fast ion population. The formulation for this work has been developed as a generalization of the earlier Quasi-linear approach originally proposed by the Institute for Fusion Studies group at Austin [EP-3]. RBQ1D now incorporates each of the marginally unstable RSAE or TAE modes into its framework and follows each mode dynamics separately. All eigenmodes contribute to define the diffusion coefficients in velocity space, which are summed together to infer the evolution of the whole system. It was found by the RBQ1D code that the initial growth and damping rates values are very important for the evolution of the system as well as how the resonance broadening is defined. At the moment, the broadening is computed in RBQ1D by three independent physics mechanisms including eigenmode amplitude (via phase space islands), pitch angle scattering, and the instantaneous growth rates. Additional work has been conducted [EP-4] to verify the resonance broadening assumptions from quasi-linear theory against simulations with the ORBIT code and to assess under which conditions the quasi-linear theory may break down.

### ***Development of Reduced Models for Energetic Particle Transport***

First-principles calculations of the interaction between fast ions and Alfvénic eigenmodes are numerically expensive for modeling realistic tokamak configurations. It can, therefore, be convenient to exploit reduced models for experimental situations in which highly nonlinear effects such as wave chirping or three-wave coupling are not present. The RBQ1D [EP-2] is capable of evolving the fast ion distribution function while self-consistently evolving the amplitude of modes. The code is presently under development in its one-dimensional version, with the distribution function relaxation happening along the toroidal canonical momentum. (Note that resonant wave-particle interactions are instead resolved in terms of the three constants of motion defining the fast ion phase space, namely energy, canonical angular momentum, and magnetic moment.)

RBQ1D is interfaced with the linear ideal MHD and stability codes NOVA/NOVA-K, which provide radial mode structure, damping rate, and resonant surfaces for candidate unstable modes. Development and verification of the diffusion solver used in the RBQ1D code have been completed. Numerical outputs from RBQ1D have been verified against known analytical solutions of the pitch angle scattering operator for simplified test cases. Both the resonant and the collisional diffusive operators within the code were verified. For example, the distribution function calculated by the code is compared with the analytical result for the case when the

diffusion coefficient is a constant in Fig. EPM-2. Using a grid spacing of 0.01 for the canonical momentum  $P_\phi$  and a (normalized) time step 0.0001, the maximum accumulated error is less than 2%. Conservation laws are also verified in the model problem. RBQ1D has now been coupled with TRANSP using the same infrastructure previously developed for the kick model, which makes it easier a direct benchmark between the two approaches.

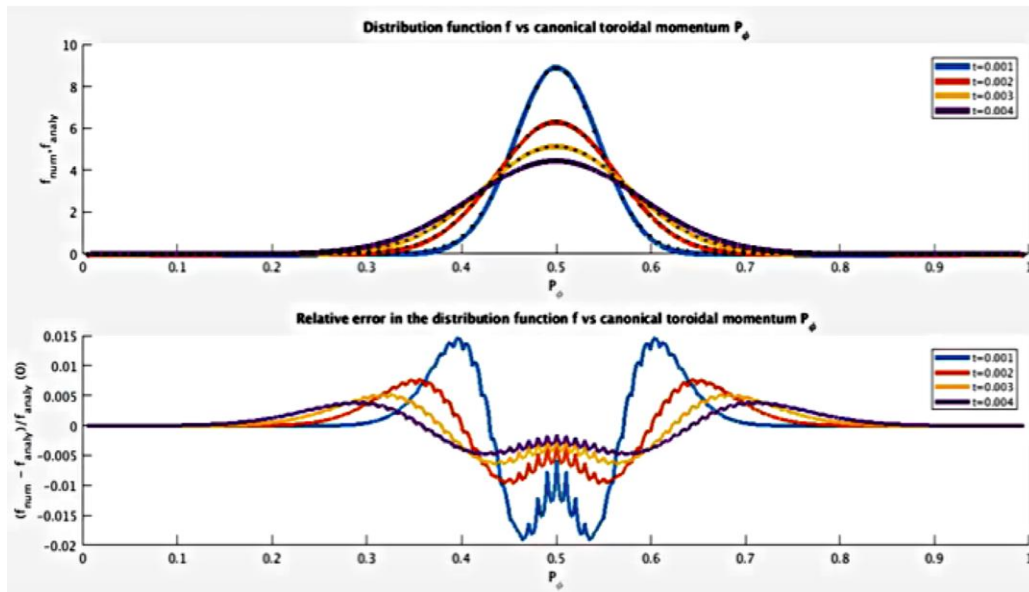


**Fig. EPM-2:** Top: evolution of a test distribution function vs time from RBQ1D (solid) and analytical diffusive solution (dotted). Bottom: relative error of RBQ1D vs analytical solution as a function of time.

### **Analysis of Alfvénic Instabilities on NSTX and NSTX-U**

During the FY-16 campaign, NSTX-U achieved operations at a higher toroidal field than was possible on NSTX, as well as more flexible NB injection parameters in terms of injection geometry and resulting fast ion distribution functions. The broader range of experimental conditions has enabled a first assessment of the characteristics and scaling properties of high-frequency Alfvénic instabilities such as Global Alfvén Eigenmodes (GAEs) [EP-5], as well as a comparison with theory on GAE destabilization [EP-6]. The experimental scaling of the GAE frequency and toroidal mode numbers with toroidal field (see Fig. EPM-3) is qualitatively consistent with the predictions of the analytic theory. In particular, the postulated mechanisms for mode destabilization via Doppler-shifted ion cyclotron frequency resonances could be successfully validated [EP-5]. The observed suppression of GAEs – cf. summary of the R18-4 Milestone activities - has also been reproduced in simulations with the hybrid ideal stability code HYM [EP-7], giving confidence in the physics included in the code and in its application for the analysis of AEs in the ion cyclotron range of frequency. Simulations have confirmed that fast ions with higher pitch (ratio of parallel to total velocity) from the 2<sup>nd</sup> NB line installed on NSTX-U are very effective in suppressing GAE modes, which opens the way to scenario optimization through selective NB injection.

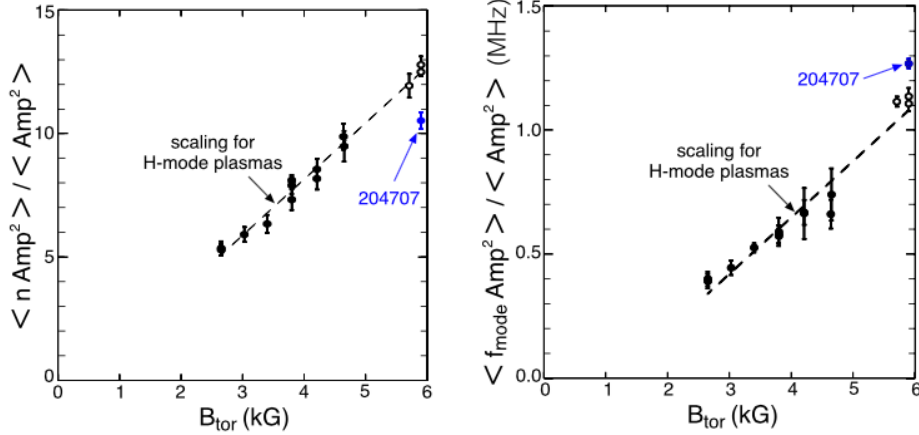


**Fig. EPM- 3:** Left: Scaling of the average GAE toroidal number, weighted by the square of the amplitude, with toroidal field for an ensemble of NSTX and NSTX-U discharges. Solid circles are from NSTX, open circles from NSTX-U. Right: Scaling of the amplitude-weighted GAE frequency. Solid circles are NSTX, open circles are from NSTX-U shots. Dashed lines are a simple linear fit to the data. Blue points refer to L-mode scenarios. (From EP-5).

The experimental characterization of GAEs has been complemented by numerical simulations with the HYM code [EP-8]. These simulations have investigated how properties of high-frequency AEs (e.g. mode frequency) vary as a function of properties of the fast ion distribution that makes the modes unstable. The fully self-consistent HYM simulations have revealed

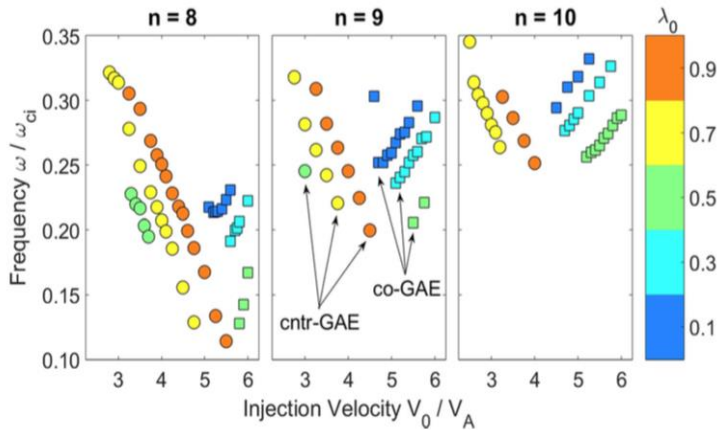


**Fig. EPM-4:** Variations of mode frequency for GAEs with different toroidal mode number as the NB injection velocity is varied in HYM simulations. Colors indicate different values of the pitch value at the injection velocity. (From [EP-8].)

strong energetic particle modifications to GAEs modes for NSTX-like scenarios. Key parameters defining the fast ion distribution function - such as the injection velocity (normalized to the Alfvén velocity) the central pitch – have been varied in order to study their influence on the characteristics of the excited modes.

It is found that the frequency of the most unstable mode changes significantly and continuously with beam parameters, in accordance with the Doppler-shifted cyclotron resonances which drive the modes

(Fig. EPM-4). The most substantial dependence is on the injection velocity. This unexpected result is observed for both counter-propagating GAEs, which are routinely excited in NSTX, and high frequency co-GAEs, which have not been previously studied. Large changes in frequency without clear corresponding changes in the mode structure are signatures of an “energetic particle mode,” referred to here as an energetic-particle-modified GAE. Additional simulations conducted for a fixed MHD equilibrium demonstrate that the GAE frequency shift cannot be explained by the equilibrium changes due to energetic particle effects.

As NSTX-U operations resume, internal measurements of CAE and GAE radial structure (as demonstrated in [EP-9]) will be crucial for the validation of codes such as HYM that simulate the mode linear and nonlinear dynamics. Comparison of results obtained from NSTX-/NSTX-U and larger aspect-ratio devices such as DIII-D is also planned to strengthen the code validation. An experiment was performed in 2017 as part of the NSTX-U/DIII-D National Campaign to investigate CAE stability and structure at high aspect ratio in DIII-D and exploiting the flexible DIII-D beam injection system. New analysis was performed in 2018 using reflectometer measurements from the experiment to obtain CAE mode structure for a case of particular interest for the validation of HYM. HYM has shown that CAEs are excited only when beam density exceeds a threshold set by damping processes. The experimental modes were observed during a beam current ramp at constant voltage and were excited only above particular threshold in current. Singular value decomposition analysis of the reflectometer measurements shows modes with  $f \sim f_{ci} / 2$  that have broad radial structure, peaking near the mid-radius  $R \sim 2$  m. (The magnetic axis and edge are at  $R = 1.76$  and  $2.34$  m, respectively.) Future work will focus on the comparison between experimental results and HYM prediction.

### ***Energetic Particle Transport by Low-Frequency MHD***

Low-frequency MHD instabilities can be as effective – if not *more* effective – than Alfvénic instabilities in enhancing fast ion transport and losses. Based on typical scenarios from NSTX and complemented by new experimental data from NSTX-U, work in FY-18 has focused on understanding the interaction of NB ions with kink, fishbones, and sawteeth instabilities. In parallel, work is progressing to develop and validate reduced models to describe the fast-ion response to those instabilities and include the effects of instabilities in integrated simulations (e.g. TRANSP).

Work on kinks and fishbones [EP-10] has been part of NSTX-U Milestone R18-4 and is summarized earlier in this annual report. The following paragraphs summarize the main achievements from the study of fast ion transport by sawteeth on NSTX-U. An example of the sawtoothing scenario is shown in Fig. EPM-5. Repetitive drops in neutron rate are observed at each sawtooth event, which suggests fast ion redistribution or loss in addition to redistribution of thermal plasma as a result of the flux reconnection.

The solid-state neutral particle analyzer (SSNPA) and fast ion D-alpha (FIDA) diagnostics on NSTX-U were available to infer fast ion transport by sawteeth. Both systems have a tangentially-viewing instrument and a radially- or vertically-viewing instrument, which are mainly sensitive to passing and trapped fast ions, respectively. It has been observed on both diagnostics that passing particles are strongly expelled from the plasma core to the edge during

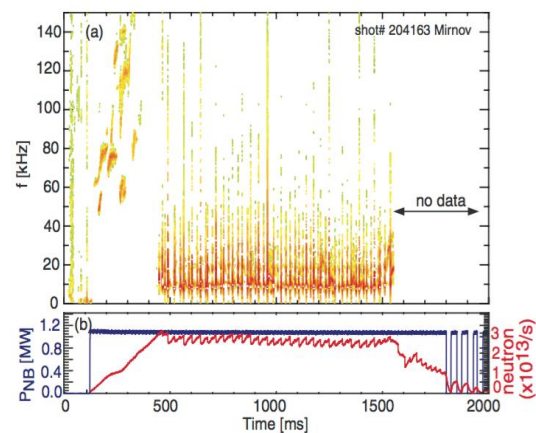


**Fig. EPM-5:** (a) Magnetic fluctuations for NSTX-U sawtooth discharge #204163. (b) Waveforms of injected NB power and measured neutron rate.

sawtooth crashes, while trapped fast ions are weakly affected. The tangentially-viewing SSNPA observes large signal spikes at the sawtooth crashes because fast ions move to the edge and charge exchange with edge neutrals. The radially-viewing SSNPA data suggest that there is a small drop of trapped particles in the core. The tangentially-viewing FIDA (t-FIDA) system observes a depletion as large as 25% in the region inside the inversion radius, while an increase at the outer region (Fig. EPM-6a-b). There is almost no change in the signals of the vertically-viewing FIDA system. The neutron emission can drop as much as 15% at the sawtooth crashes, accompanied by an increase of edge  $D_\alpha$  light.

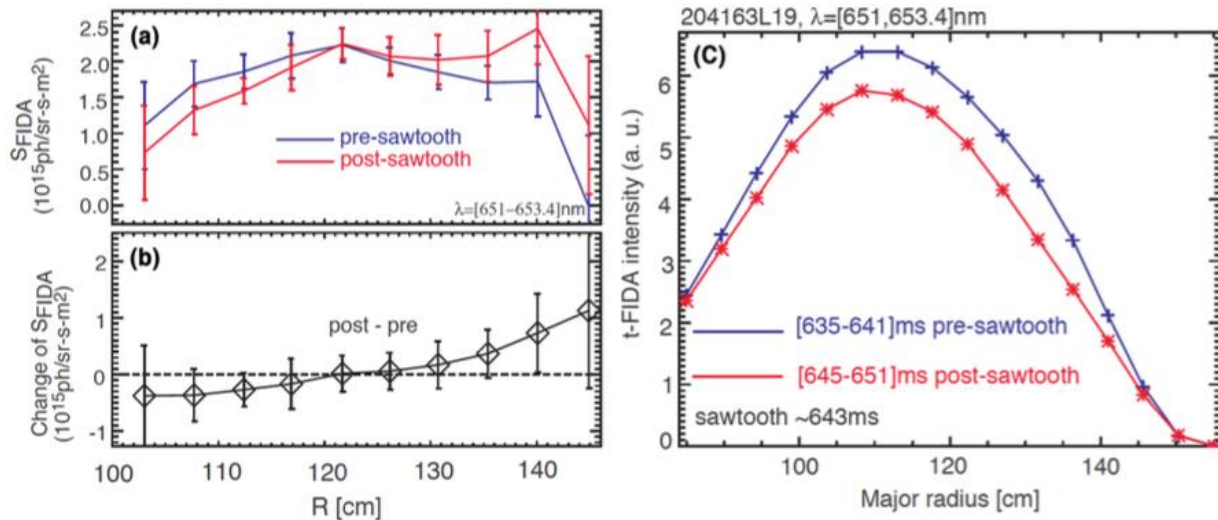


**Fig. EPM-6:** (a) Comparison of t-FIDA spatial profiles before and after sawtooth crashes. (b) Relative change of t-FIDA radiance before and after sawtooth crashes. (c) Predicted FIDA profiles before/after a sawtooth crash based on TRANSP simulations with full reconnection sawtooth model and FIDAsim post-processing to generate the synthetic FIDA profiles. (From IEP-111.)

TRANSP simulations with the Kadomtsev and Porcelli sawtooth models have been performed and compared with the experiment. The Kadomtsev model, which assumes full reconnection of the flux inside the  $q=1$  surface, overestimates the neutron rate drop at each sawtooth crash. When tuning the sawtooth model input parameters, the partial reconnection Porcelli model can qualitatively reproduce the neutron rate drop and t-FIDA signal drop in the core, but it fails to predict the t-FIDA signal increase at the edge as shown in Fig. 6c. The comparison between experimental measurements and TRANSP simulations suggests that the models presently implemented in TRANSP may be too simple to capture details of the variation of the fast ion distribution induced by sawteeth. In particular, introducing energy selectivity for sawtooth induced fast ion redistribution may be required to improve the agreement between experimental and simulated quantities. The particle-following code ORBIT has been used to characterize the redistribution of fast particles as a function of their parameters such as energy, pitch and radial location [EP-12]. In ORBIT, the perturbation amplitude is determined by comparison with experimental measurements of the neutron rate drop. The characteristics of fast ions with different orbit types (e.g. trapped vs. passing) have been investigated in phase and real space. Due to a sawtooth crash, fast ion energy and angular momentum are modified resulting in the redistribution in phase space and orbit type change. As expected, the redistribution of fast ions in real space shows that the sawtooth instability brings different effect on fast particles with

different orbit types as observed in experiments [EP-11]. Initial interpretative TRANSP simulations using the “kick model” based on the ORBIT modeling results show features in the fast ion redistribution before/after a sawtooth crash that resemble the experimental data, as shown in Fig. EPM-6.

#### References:

- [EP-1] G. Hao et al., 2018 *Rev. Sci. Instrum.* **89** 063507.
- [EP-2] N. N. Gorelenkov et al., 2018 *Nucl. Fusion* **58** 082016.
- [EP-3] H. L. Berk et al., 1996 *Phys. Plasmas* **3** 1827.
- [EP-4] G. Meng et al., 2018 *Nucl. Fusion* **58** 082017.
- [EP-5] E. D. Fredrickson et al., 2018 *Nucl. Fusion* **58** 082022.
- [EP-6] N. N. Gorelenkov et al., 2003 *Nucl. Fusion* **43** 228.
- [EP-7] E. Belova et al., 2017 *Physics of Plasmas* **24** 042505.
- [EP-8] J. B. Lestz et al., 2018 *Physics of Plasmas* **25** 042508.
- [EP-9] N. A. Crocker et al., 2018 *Nucl. Fusion* **58** 016051.
- [EP-10] M. Podestà, 2018 US Transport Task Force (TTF) Meeting, San Diego CA.
- [EP-11] D. Liu et al., 2018 *Nucl. Fusion* **58** 082028.
- [EP-12] D. Kim et al., 2018 *Nucl. Fusion* **58** 082029.

### III. Integrated Scenarios

The integrated scenarios group is tasked with understand the following elements within the NSTX-U program:

- ST startup & ramp-up,
- HHFW heating and current drive,
- neutral beam current drive,
- axisymmetric plasma control,
- fully non-inductive plasma scenarios, including non-inductive ramp-up, and,
- integration of the above elements amongst themselves, and with the scientific understanding achieved in the other science groups.

The science group is divided into three topical science groups (TSGs), as follows in the list below. This leadership is the same as in FY-17.

- A. The **Solenoid Free Plasma Startup** (SFPS) TSG is tasked with understanding solenoid free startup-up and ramp-up.
- B. The **Wave Heating and Current Drive** (WHCD) TSG is tasked with understanding the physics and technology of HHFW, ECH, and potentially EBW, in the unique plasma conditions and geometry of the ST.
- C. The **Advanced Scenarios and Control** (ASC) TSG is tasked with understanding axisymmetric plasma control, scenarios with very high non-inductive current fraction or very long pulse, and discharge scenario development in general.

#### A. Solenoid-Free Start-up and Ramp-up

##### ***A.1 CHI Experiment on QUEST and related Theory/Modeling***

Due to considerable transient CHI physics progress on NSTX, we have been investigating reactor applications for CHI. In support of this activity, a new electrode configuration that is much easier to implement in a reactor configuration is being developed. In support of a future conceptual design for such an electrode configuration for NSTX-U, active experimental work is in progress on the QUEST-ST in Japan, which employs this new biased electrode configuration. A paper that describes the experimental results obtained from CHI studies on QUEST was submitted to Plasma Physics and Controlled Fusion. It describes results that show that transient CHI startup in the alternate electrode configuration used on QUEST is indeed possible. Reliable gas breakdown was achieved, and toroidal currents up to 45 kA were generated.

A paper describing results from TSC simulations of the QUEST CHI concept was published in the journal: Plasma and Fusion Research,

[http://www.jspf.or.jp/PFR/PFR\\_articles/pfr2018/pfr2018\\_13-3402059.html](http://www.jspf.or.jp/PFR/PFR_articles/pfr2018/pfr2018_13-3402059.html). These simulations indicate that lowering the CHI electrode plate closer to the existing divertor coils on QUEST would allow for the generation of a much narrower injector flux footprint width that is important for increasing the closed flux fraction in transient CHI discharges. Alternatively, as a short-term measure, the simulations suggest that energizing a lower inboard coil would also be helpful for reducing the injector flux footprint width in the present electrode configuration. This new scenario will be experimentally studied during the next CHI campaign on QUEST.

In support of these activities, conditions needed for gas breakdown in CHI discharges on NSTX was analyzed in detail and a paper related to this was published in Nuclear Fusion (Nucl. Fusion 58 (2018) 016013). The paper describes the use of the Townsend avalanche theory to model and interpret plasma initiation in NSTX by Ohmic heating and coaxial helicity injection. The model is informed by spatially resolved vacuum calculations of electric field and magnetic field line connection length in the poloidal cross-section. Adapting the model to discharges initiated by CHI offers insight into the causes of upper divertor (absorber) arcs in cases where the discharge fails to start in the lower divertor gap. Upper and lower limits were established for vessel gas fill based on requirements for breakdown and radiation. It is predicted that CHI experiments on NSTX-U should be able to use as much as four times the amount of prefill gas employed in CHI experiments in NSTX. This should permit access to a wider range of injector flux conditions, such as with a higher ratio of the injector flux to toroidal field, that are suitable for transient CHI start-up. Since all tokamaks and ST will operate at a specified value of the toroidal field, and it is the magnitude of the injector flux that is proportional to the closed flux current in transient CHI plasmas, the future trend in transient CHI studies is to increase this parameter to the highest possible levels. The work is now being extended to understand conditions required for a CHI configuration in ST and AT reactor configurations, and is the subject of an Invited Talk (by K.C. Hammond) at the 2018 APS DPP Conference.

During FY-19 we will conduct studies aimed at generating closed flux surface and conduct an initial test of heating this plasma with ECH. We will also conduct an initial scoping study that examines the feasibility of such an electrode configuration that could be installed in the upper divertor region of NSTX-U. Also, in support of full non-inductive start-up and ramp-up studies, we will design a biased divertor configuration for a high-field test on the PEGASUS ST. Next-step ST devices will see an increase in both the toroidal flux and the injector flux capability in relation to the physical device size. The injector flux would be generated by the divertor coils. In supporting TSC simulations in the NSTX-U, QUEST, and PEGASUS configurations the capability for poloidal flux injection in different geometries is being studied. Initial scoping studies for a biased divertor CHI configuration for Pegasus were conducted, and the power supply requirements identified. These studies would also provide an initial estimate of the maximum toroidal and closed flux currents a transient CHI discharge can generate on NSTX-U.

Three-dimensional MHD simulations, however, are critical and essential for prediction and accessibility to the regimes of maximum start-up with increased toroidal and injector fluxes in larger STs. The NIMROD simulations conducted as part of this activity explored a reduced set of TSC simulations in the NSTX-U geometry to understand if any physical limits exist to the

amount of open injector flux that could be usefully converted to closed flux. Earlier nonlinear resistive MHD simulations in the absence of three-dimensional fluctuations have demonstrated a large volume of closed flux surfaces with narrow injector flux footprint during transient CHI in the NSTX-U configuration. Calculated total plasma current in the closed flux region was shown to be about 228 kA. Our simulations also suggested that plasmoid-mediated reconnection may be the leading mechanism for fast flux closure observed during the experiments. We now examine whether maximum closure during transient CHI is feasible in the presence of non-axisymmetric 3-D magnetic fluctuations. We have extended our simulations to numerically investigate two major effects: 1) the role of three-dimensional magnetic fluctuations on the plasmoid-mediated flux closure and, 2) the effect of toroidal field on the 3-D stability during transient CHI.

We investigated the growth and saturation of both axisymmetric plasmoids and non-axisymmetric instabilities during both the injection and decay phases of transient CHI. Similar closed flux current of about 220kA and large-volume flux closure were obtained even in the presence of non-axisymmetric edge magnetic fluctuations. Depending on the saturated amplitudes of the non-axisymmetric fluctuations, it was shown that their effects on the flux closure are minimal during the decay phase. We then performed simulations to explore the effect of toroidal field on the reconnection process as well as the 3-D stability for maximum flux closure during transient CHI. We adjusted the injector voltage to obtain the same CHI-generated current of 220 kA for two toroidal fields of 1.2 and 2.8T. The 3-D physics response was shown to be drastically different. Complete stabilization of non-axisymmetric fluctuations were obtained at higher toroidal flux (paper in preparation). Further simulations will be carried out for prediction and accessibility to the regimes of maximum start-up with increased toroidal and injector fluxes in larger STs.

## References

[IS-CHI-1] K. Kuroda, R. Raman, K. Hanada, M. Hasegawa, T. Onchi, M. Ono, B. A. Nelson, T. R. Jarboe, M. Nagata, O. Mitarai, K. Nakamura, H. Idei, J. Rogers, S. Kawasaki, T. Nagata, A. Kuzmin, S. Kojima, C. Huang, O. Watanabe, A. Higashijima, Y. Takase, A. Fukuyama, S. Murakami, Initial results from solenoid-free plasma start-up using Transient CHI on QUEST, Plasma Physics and Controlled Fusion (accepted for publication August, 2018).

[IS-CHI-2] K. Kuroda, R. Raman, S.C. Jardin, et al., TSC simulation of transient CHI in new electrode configuration on QUEST, Plasma and Fusion Research **13**, 3402059 (2018).

[IS-CHI-3] K.C. Hammond, R. Raman, F.A. Volpe, Application of Townsend avalanche theory to tokamak start-up by CHI, Nucl. Fusion **58** (2018) 016013.

[IS-CHI-4] K. Kuroda, R. Raman, K. Hanada, et al., Current Start-up using the new CHI system, Plasma and Fusion Research: Rapid Communication, **12**, 1202020 (2017).

## B. Wave Heating and Current Drive

### B.1: Initial Modeling on the Impact of Hydrogen Species on High Harmonic Fast Wave Performance

The NSTX-Upgrade (NSTX-U) project consists of two main elements: a new and more powerful center-stack, and a tangentially-aimed second NBI system. NSTX-U will double the toroidal field from  $\sim 0.5$  T to 1 T, the plasma current from  $\sim 1$  MA to 2 MA, and the NBI heating and current drive power up to 10 MW. Beyond these new capabilities, NSTX-U retains the previous 6 MW High-Harmonic Fast Wave (HHFW) system for heating and current drive. For a magnetic field of 1 T, the first and second harmonics of hydrogen (H) are located at the high-field side and in the core plasma, respectively. As a consequence, part of the HHFW injected power can be absorbed by the H population. This condition might open up new HHFW scenarios, which in turn can also be relevant for the initial ITER experiments with 10 MW of ICRH during the hydrogen plasma phase. Therefore, it is important to investigate the impact of the H species on HHFW performance in NSTX-U plasmas. First of all, the injected power absorbed by H species can affect the electron and/or the fast-ion heating with respect to the “standard” HHFW performance in NSTX. Second, the presence of the H species might have some positive effects: the presence of the second cyclotron harmonic of hydrogen in the core plasma can cause a localized H power absorption, which in turn might modify the ion temperature. In addition, due to the high-energy (non-Maxwellian) tail of the H distribution function (caused by the acceleration of H species by HHFW), part of the H absorbed power could be transferred to electron heating (beyond the direct electron Landau damping) to the “standard” HHFW performance.

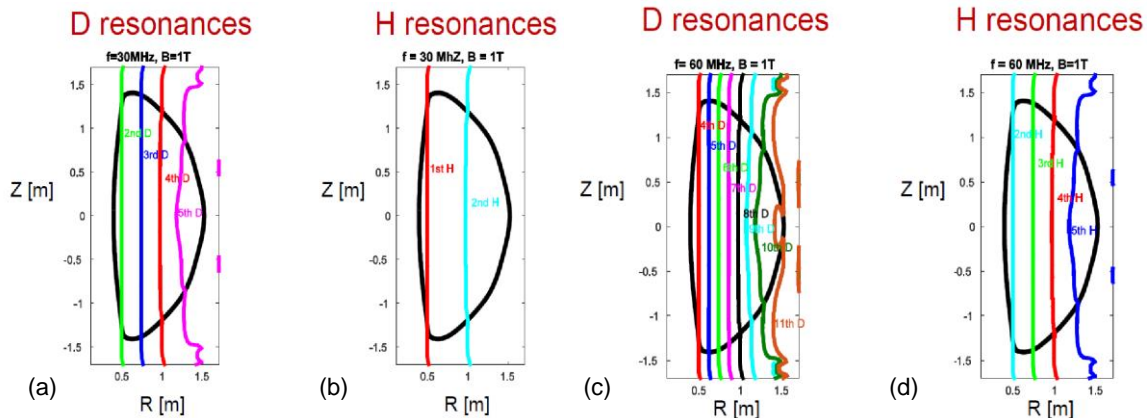


**Fig. IS-WHCD-1:** Deuterium (D) and hydrogen (H) cyclotron resonances for an NSTX-U  $B=1$  T plasma assuming  $f = 30$  MHz (a & b) and 60 MHz (c & d).

For these reasons, we have analyzed some NSTX/NSTX-U scenarios by the use of the full wave code AORSA. Initial full wave simulations have been performed for NSTX-U  $B=1$ T plasma with different H concentrations (from 2% to 10% H concentration) with and without NBI [IS-WHCD-1, IS-WHCD-2]. Furthermore, two wave frequency regimes have initially been considered (30 MHz, which corresponds to the frequency of the current HHFW heating system,

and 60 MHz) that have different D & H cyclotron resonances in the plasma (see Fig. IS-WHCD-1). In particular, for a  $B=1$  T plasma, doubling the present wave frequency would reproduce a scenario already adopted in NSTX (at least, in terms of H & D cyclotron resonances in the plasma) but with doubling of the wave parallel phase velocity for a given antenna phasing. Fig. IS-WHCD-2a shows the contour plot of the H absorbed power for  $f = 30$  MHz and 10% H concentration evaluated by AORSA while figure 2b shows the absorbed power profiles for all species considered in the simulations. One can clearly see a localized H absorption around the 2<sup>nd</sup> cyclotron H harmonic unlike an on-axis power deposition for electrons and fast ions (D-NBI). Fig. IS-WHCD-3 shows the total HHFW absorbed power to each plasma species (without NBI) as labeled as a function of different toroidal wave number ( $n_\phi = -5, -12, -21$ ), which represent the dominant  $n_f$  components of the HHFW antenna for three different antenna phases. In this case the H concentration is again 10%.

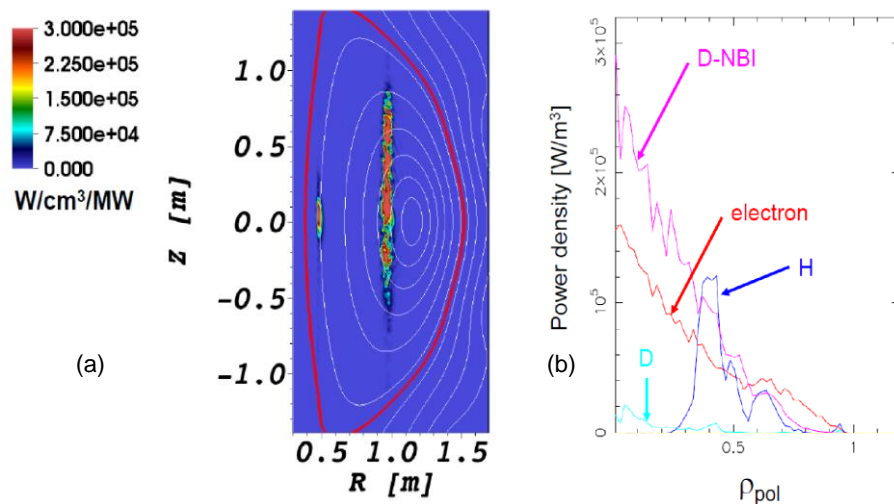


**Fig. IS-WHCD-2:**(a) Contour of the H power deposition for NSTX-U  $B=1$ T assuming 10% of H concentration and  $n_\phi=-12$ . (b) Flux surface averaged power density power deposition of all plasma species (D, H, D-NBI, and electron) as a function of the square root of the normalized poloidal flux,  $\rho_{pol}$ .

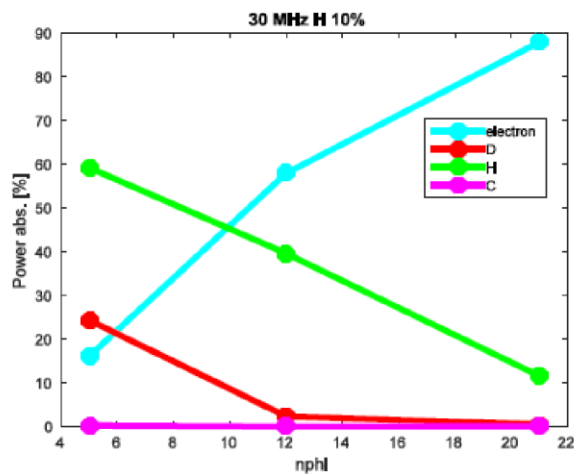
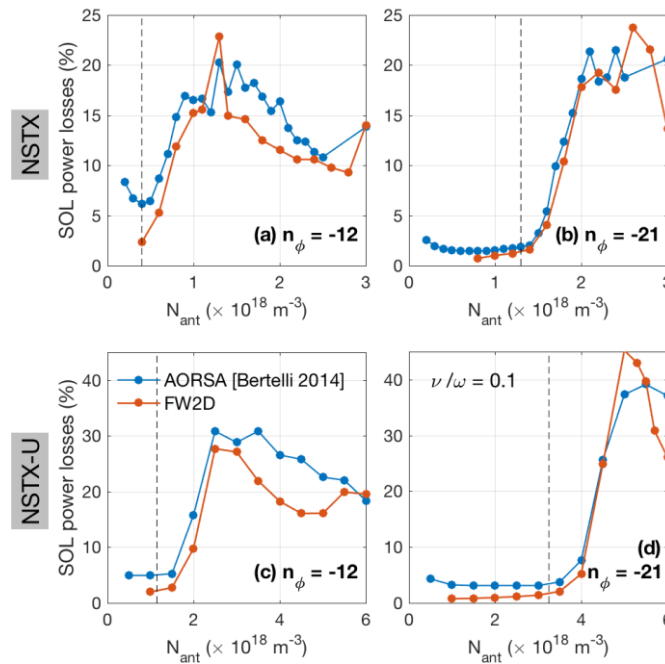


**Fig. IS-WHCD-3:** Absorption of electrons, thermal deuterium (D), hydrogen (H), and carbon (C) as a function of  $n_f$  for an NSTX-U  $B=1$ T plasma obtained from AORSA simulations assuming H concentration = 10%.

For larger  $n_f$  the electron damping is dominant; however, H species plays an important and significant role in the power partitioning. Similar results have been obtained considering NBI. Generally, a dominant electron and fast ion absorption are obtained when NBI are present. So far, the numerical analysis has been performed assuming a Maxwellian plasma. The present results will be reported in the upcoming 2018 IAEA conference. In FY-19, we expect to include non-Maxwellian effects in the H and fast ions species by making use of the Fokker-Planck code CQL3D.

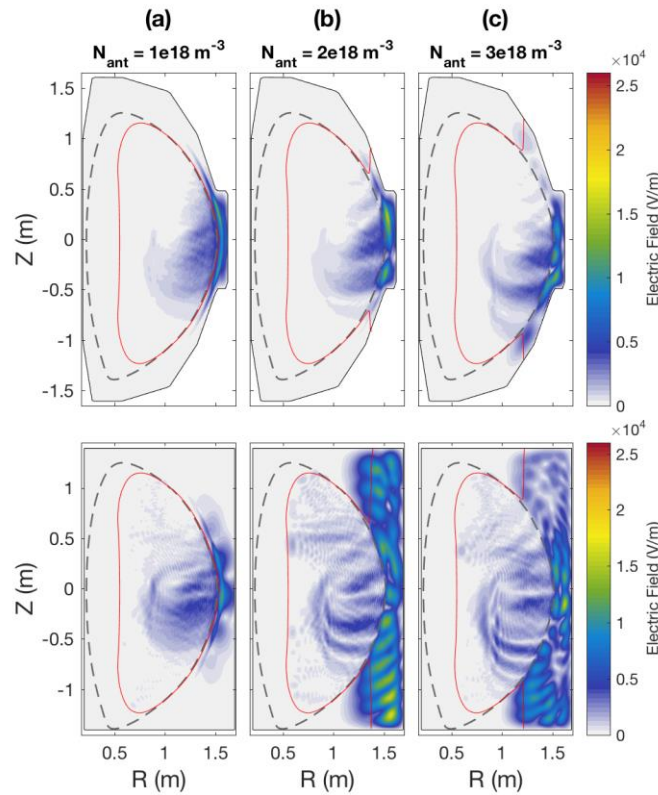
### **B.2: Modeling on RF Edge Losses in NSTX/NSTX-U Plasmas by a Finite Element Code FW2D**

After completing a comparison between the finite element code FW2D [IS-WHCD-3] and AORSA [IS-WHCD-4] in terms of the wave electric field propagation, during FY-18 we mainly focused on two aspects: the evaluation of the HHFW losses in the FW2D code, and the impact of the realistic vacuum vessel boundary conditions on the wave propagation in the SOL, including the evaluation of SOL losses [IS-WHCD-5, IS-WHCD-6, IS-WHCD-7]. Regarding the wave field propagation between AORSA and FW2D with a rectangular numerical domain, an excellent agreement has been found. For FW2D code, because it adopts a cold plasma approximation, power losses in the plasma core and SOL have been calculated by adopting artificial collisional effects, which cause all incoming wave power to be absorbed in the plasma. On the other hand, the AORSA code includes the plasma kinetic effects. Therefore, the power absorption in the plasma core is evaluated by the Landau damping and transit-time magnetic pumping. Artificial collisions, however, have been implemented in AORSA as well to estimate the power losses in the SOL plasma [IS-WHCD-8, IS-WHCD-9].



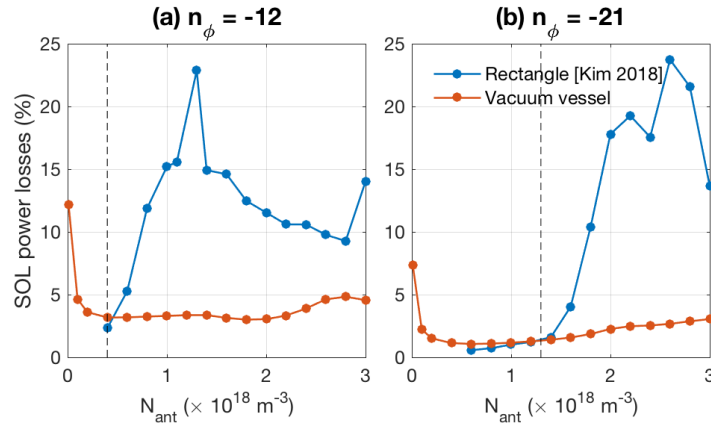
**Fig. IS-WHCD-4:** Fraction of power lost to the SOL ( $P_{abs}$ ) of (a-b) NSTX and (c-d) NSTX-U calculated by FW2D and AORSA as a function of the density in front of the antenna ( $N_{ant}$ ) for  $n_f = -12$  and  $-21$ . The vertical lines represent the critical density at which the cutoff starts to moving in front of the antenna.

Fig. IS-WHCD-4 shows the predicted HHFW power losses ( $P_{\text{abs}}$ ) using FW2D and AORSA as a function of the density in front of the antenna ( $N_{\text{ant}}$ ) assuming  $v/\omega = 0.01$  for NSTX (a-b) and NSTX-U (c-d). Despite the discrepancy of methodology to calculate  $P_{\text{abs}}$  between AORSA and FW2D codes, the results show very good agreement. A comparison between the actual NSTX/NSTX-U vacuum vessel geometry and simplified rectangular boundaries in the numerical domain has been performed. Such numerical study shows that wave propagation in the SOL strongly depends on the boundary shape and the density in front of the antenna. (See Fig. IS-WHCD-5). In particular, wave solutions with the two boundaries are significantly different when the FW cutoff is moved in front of the antenna. For vacuum vessel boundary cases, even though the FW cutoff is moved in front of the antenna due to higher density in front of antenna, the region between the last closed flux surface (LCFS) and the vacuum vessel is still narrow. As a consequence, the wave electric field can be still localized near the antenna.



**Fig. IS-WHCD-5:** Total electric field amplitude in NSTX shot 130608 using (a-c) realistic vacuum vessel and (d-f) rectangular vessel for different density values in front of antenna (shown in plots) with toroidal mode number  $n_{\phi} = -12$ .

On the contrary, for rectangular boundary case the SOL region is artificially wider and, as a result, FWs propagate in the SOL as soon as the FW cutoff is moved in and standing mode structure occur. We also predicted the fraction of power losses in the SOL as shown in Fig. IS-WHCD-6. The  $P_{\text{abs}}$  gradually increases as the density in front of the antenna increases in the vacuum vessel boundary while  $P_{\text{abs}}$  tends to be steeper when the FW cutoff is moved in the rectangular domain. The dependence of  $P_{\text{abs}}$  on the SOL size and the magnetic field strength is also examined as shown in Figure IS-WHCD-7.



**Fig. IS-WHCD-6:** Fraction of power lost to SOL ( $P_{abs}$ ) of NSTX calculated by FW2D as function of density in front of antenna ( $N_{ant}$ ) for (a)  $n_\phi = -12$  and (b)  $-21$ . The blue and red lines indicate  $P_{abs}$  for rectangular and vacuum vessel boundaries. Vertical lines represent critical density ( $N_{ec}$ ) at which the cutoff starts to be moving in front of the antenna.

For calculation, we adopt equilibrium for NSTX shot 120752 at 0.23 – 0.275 seconds. The distance ( $\Delta$ ) between the LCFS and the antenna at the mid plane in this case decreases in time from 7.5cm to 2.5cm as shown in Fig. IS-WHCD-7(a). Fig. IS-WHCD-7(b) shows the calculated  $P_{abs}$  from FW2D code as a function of  $N_{ant}$  and time. The results clearly show that  $P_{abs}$  increases with increasing density of the antenna showing consistency with NSTX experiments. These modeling results will be submitted to the Physics of Plasmas [IS-WHCD-6, IS-WHCD-7].

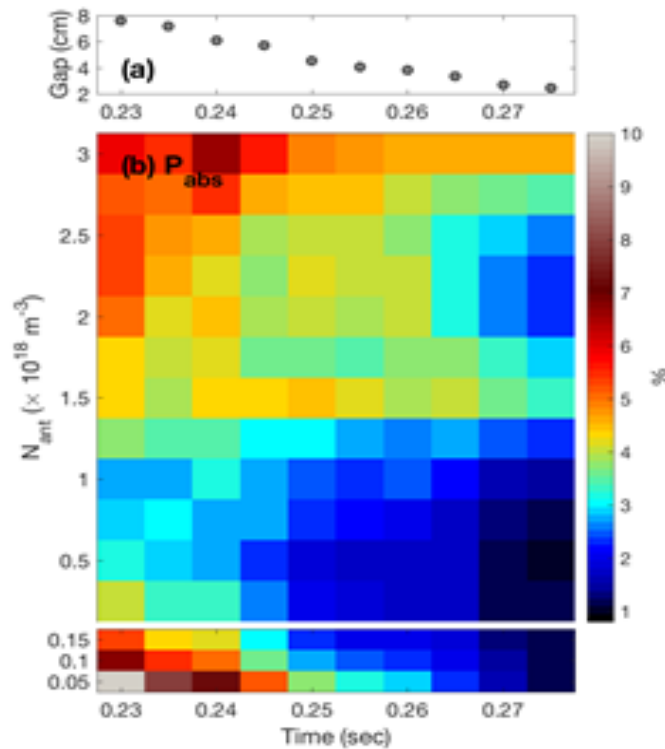


**Fig. IS-WHCD-7:**(a) Distance between LCFS and antenna for NSTX 120752 at 0.23-0.275 seconds and (b) Fraction of power lost to the SOL ( $P_{abs}$ ) as a function of  $N_{ant}$  and time (i.e., distance between the LCFS and the antenna).

### ***B.3: RF studies on LAPD Device***

RF rectification is a sheath phenomenon important in the fusion community for impurity injection, hot spot formation on plasma-facing components, modifications of the scrape-off layer, and as a far-field sink of wave power. The latter is of particular concern for the NSTX, where substantial fast-wave power is lost to the divertor along scrape-off layer field lines. To assess the relationship between rectified currents and rectified voltages, detailed experiments have been performed on the Large Plasma Device (LAPD), where an electron current is measured flowing out of the antenna and into the limiters, consistent with RF rectification. The scaling of this current with RF power had been presented the APS-DPP and US-Japan Workshop meetings. The limiter is also floated to inhibiting this DC current; the impact of this change on plasma-potential and wave-field measurements has been demonstrated. Comparison to data from divertor probes in NSTX will be made. These experiments on a flexible mid-sized experiment will provide insight and guidance into the effects of HHFW/ICRF on the edge plasma in larger fusion experiments.

### ***B.4: ICRF Collaboration with EAST: ICRF Interactions with the SOL***

Tokamak heating using waves in the ion cyclotron range of frequencies (ICRF) is known to interact strongly with the scrape-off layer (SOL) plasma, potentially limiting ICRF performance. As part on an ICRF collaboration with the Experimental Advanced Superconducting Tokamak (EAST), which has two ICRF antennas and twelve megawatts of ICRF source power in support of high-power and long-pulse operation, we studied the effect of ICRF heating on triple-probe signals. Applying time-resolved magnetic mapping to the divertor probe arrays enables detailed sensing of the spatial structure of the SOL modifications. We observe a sharp transition in floating potential from negative to positive over a length scale of a centimeter at a major radius just inboard of the ICRF antenna. The largest changes in floating potential are observed not for probes connecting to the active ICRF antennas but rather to the main limiter or limiters for inactive lower-hybrid launchers. Ion saturation current can be greatly reduced for probes mapping just in front of an antenna. Comparison to results from HHFW operation on NSTX are made; in both cases, probes which do not connect to the antenna but whose field lines pass just in front of it experience a negative shift in floating potential, which is consistent with RF rectification occurring in the divertors. A manuscript was prepared and is being submitted to a journal [IS-WHCD-10].

### ***B.5: EC/EBW Simulations on QUEST***

Graduate student Ryota Yoneda from Kyushu University worked in collaboration with N. Bertelli and M. Ono on EC/EBW modelling for QUEST plasmas employing ray tracing. Ray tracing simulations were performed for 28 GHz EC system in QUEST plasma and for 8.2 GHz EC high field side launcher for possible future X-B experiments. This work led to a publication recently accepted in *Plasma and Fusion Research* [IS-WHCD-11].

Numerical simulations of high energy electrons by mean of the Fokker-Planck code CQL3D coupled to the ray tracing code GENRAY have also been performed and presented at the

annual QUEST workshop. A comparison among different ray tracing codes (GENRAY, TRAVIS, and another independent ray tracing code termed RT-4 at PPPL) has also been done showing good agreement. From this activity we can conclude that even the 3<sup>rd</sup> and 4<sup>th</sup> harmonics can have a significant absorption; for 1 keV plasma the single-pass absorption can increase significantly; the X-mode polarization provide a dominant power absorption with respect the O-mode polarization.

Furthermore, we developed a grid-based start-up code where plasma parameters, generated plasma currents, and resulting poloidal magnetic fields are evolved from the vacuum fields. Initially, 2nd harmonic electron cyclotron heating takes place with multi-pass ECH absorption as the single-pass absorption is relatively small at low temperature. The current generated in this stage is purely pressure driven since the launched wave phase and polarization information is likely lost quickly. This is consistent with the lack of hard x-ray at this stage. The grad-B drift driven current, together with the processional currents, can then create a closed flux surface configuration and then the bootstrap current in a closed configuration can further enhance the plasma current. The ECH heating efficiency increases with plasma current since the confinement is increased and the resulting electron temperature rise would further increase the ECH absorption and plasma currents. Once the plasma temperature becomes sufficiently high (~ 1 keV), a single-pass absorption can rise sufficiently to transition to the ECCD phase. The entire start-up process is therefore a self-amplifying non-linear problem where a very rapid spontaneous plasma current rise can be expected. An important point to note is that two-component distribution (hot minority and colder bulk electrons) is highly advantageous for hot electron generation for efficient ECCD as observed in the QUEST startup experiment. The analysis shows that the QUEST experiment was able to generate energetic electrons by heating small hot component ~ 3% to minimize the collisional drag. Once heated to ~ 10 keV, the hot component could be sustained even with the subsequent density rise to  $3-4 \times 10^{12} \text{cm}^{-3}$ . The modeling results will be presented at the US-Japan RF Physics Workshop in Sept. 2018 [IS-WHCD-12].

#### ***B.6: RF SciDAC: “Center for Simulation of Fusion Relevant RF Actuators”***

In 2018, N. Bertelli served as the PPPL Principle Investigator of the RF-SciDAC project. This project is a collaboration of FES and ASCR participants from DoE laboratories, universities, and private companies. The main scientific objectives are: develop an integrated simulation for quantitative prediction of the antenna + sheath + scrape-off-layer + core plasma system which fully utilizes leadership class computing; validate this predictive capability on appropriately diagnosed experiments including dedicated RF test stands, linear devices, and existing tokamaks. Main activities on FY2018 were:

- Modeling on RF edge losses in NSTX/NSTX-U plasmas by a finite element code FW2D [IS-WHCD-5 - IS-WHCD-7].
- Initial work with the finite element code PETRA-M developed by MIT. This work will continue in FY-19.

- Verification of RF kick operator in NUBEAM Monte-Carlo particle code [IS-WHCD-13]. Part of this work will continue in FY19.
- Initial work on comparison between the 1D Fokker-Planck code FPP implemented in TRANSP and the CQL3D code. This work will continue in FY19.

## References

- [IS-WHCD-1] N. Bertelli, et al., *AIP Conf. Proc.* **1580** (2014) 310
- [IS-WHCD-2] N. Bertelli, et al., *59<sup>th</sup> APS-DPP Conference*, October 23–27, 2017; Milwaukee, Wisconsin. <http://meetings.aps.org/link/BAPS.2017.DPP.PP11.61>
- [IS-WHCD-3] E.-H. Kim, et al., *Geophys. Res. Lett.* **42** (2015) 5147
- [IS-WHCD-4] E. F. Jaeger, et al., *Phys. Plasma* **8** (2001) 1573
- [IS-WHCD-5] E.-H. Kim, et al., *EPJ Web of Conferences* **157**, 02005 (2017)
- [IS-WHCD-6] E.-H. Kim, et al., “Two-dimensional full-wave simulations of waves in space and tokamak plasmas” to be submitted to *Phys. Plasmas* (2018).
- [IS-WHCD-7] E.-H. Kim, et al., “Two-dimensional full-wave simulations of high-harmonic fast wave in the scrape-off layer of NSTX and NSTX-U” to be submitted to *Phys. Plasmas* (2018).
- [IS-WHCD-8] N. Bertelli, et al., *Nucl. Fusion* **54**, 083004 (2014).
- [IS-WHCD-9] N. Bertelli, et al., *Nucl. Fusion* **56**, 016019 (2016).
- [IS-WHCD-10] R. Perkins, et al., “Resolving interactions between ICRF heating and the SOL plasma in EAST using divertor probes” to be submitted to PPCF.
- [IS-WHCD-11] R. Yoneda, et al.; “High Field Side RF Injection for Excitation of Electron Bernstein Waves” accepted to *Plasma and Fusion Research* (2018).
- [IS-WHCD-12] M. Ono, et al., “Modeling of 2<sup>nd</sup> Harmonic Electron Cyclotron Heating and Current Drive Solenoid-free Start-up Experiment in QUEST”, 2018 US-Japan Workshop on RF Heating Physics, Shizuoka, Japan, Sept. (2018).
- [IS-WHCD-13] N. Bertelli, et al., *EPJ Web of Conferences* **157**, 03004 (2017).

## **C. Advanced Scenarios and Control**

### ***C.1 Summary of R18-2 Milestone***

The milestone R18-2 “Develop simulation framework for spherical tokamak breakdown and current ramp-up” details a significant fraction of the ASC efforts for this fiscal year. Key highlights include:

- A simulation framework developed to perform predictive closed-loop simulations of the discharge ramp-up on NSTX-U in order to accelerate the realization of high-performance discharges when operations resume;
- The framework builds upon the TOKSYS framework maintained by General Atomics that contains the necessary description of the NSTX-U actuators and conducting structures. A control-oriented model reduction technique was used to simplify the conductor model from the EFIT description in order to increase computational speeds;
- The simulation framework has a “flight simulator” capability (Simulation Simulink) where the operational plasma control system (PCS) software is executed in a feed-forward or closed-loop simulation. Additionally, the PCS control algorithms are mirrored within the SIMULINK environment to enable rapid development and functional testing of new control schemes;
- The linear plasma model within TOKSYS was extended to a linear time-varying (LTV) model. This was a critical element for completing fast time-dependent simulations when the current distribution and plasma boundary are evolving, such as during ramp-up;
- The LTV model was employed to examine the vertical growth rates and the effectiveness of the vertical controller for the ramp-up phase on NSTX-U;
- Predictive TRANSP calculations completed for this milestone identified suitable choices of models and free-parameters that reproduced the evolution of the global equilibrium parameters for a range of different ramp-up scenarios realized on NSTX-U;
- Criteria were established to evaluate time-dependent vacuum field calculations of the magnetic field evolution during the startup phase. Calculations were completed using the LRDFIT code to develop and optimize startup scenarios for the MAST-U commissioning campaign.

### ***C.2 Real-time Capable Neural Network Modeling of NUBEAM for Use on NSTX-U***

One of the long-term goals of the ASC group is to develop feedback control of the spatial distribution of toroidal rotation and current on NSTX-U in order to optimize performance and avoid physics and operational constraints. The coupled nonlinear dynamics of equilibrium profiles and the complex effects of actuators on the equilibrium evolution motivates embedding physics-based and data-driven models within real-time control algorithms. Due to the important role of beam heating, current drive, and torque in establishing scenario performance and stability, a high-fidelity beam model suitable for use in real-time applications is desired.

Motivated by the successful application of neural networks for rapidly calculating transport and pedestal pressure [IS-ASC-1], a neural network model has been developed to enable rapid evaluation of the beam heating, torque, and current drive profiles based on measured equilibrium profiles [IS-ASC-2]. The training and testing database was generated from the NUBEAM calculations output from interpretive TRANSP analysis of shots from the 2016 NSTX-U campaign and augmented with scans of  $Z_{eff}$ , fast ion diffusivity, beam voltages, and beam modulation patterns. Neural network predictions made for the testing data demonstrated the ability of the model to generalize and accurately reproduce NUBEAM calculated profiles and scalar quantities. Results of processor-in-the-loop simulations of the model within the NSTX-U plasma control system demonstrated the suitability of the approach for real-time use and accelerated offline analysis.

### Database Development

The motivation for the neural network model developed in this work is to approximately reproduce the results of the NUBEAM code quickly enough to enable use in real-time control applications, between shots analysis, and scenario optimization on NSTX-U. Rather than attempting to create a model for the entire predictive range of NUBEAM, which would require generating a comprehensive dataset encompassing the complete physically possible range of all of the inputs to NUBEAM, focus was put on a subset of inputs with ranges defined by the operating space of the NSTX-U's first campaign in 2016.

To generate the dataset, the interpretive TRANSP runs that are automatically run between NSTX-U shots were resubmitted with increased NUBEAM fidelity (5ms time steps and 10000 particles). Furthermore, for each shot, a grid scan was defined for key parameters, including  $Z_{eff}$ , edge neutral density, anomalous fast ion diffusivity, and beam voltages. Rather than submitting runs for all permutations of parameters, a subset of roughly 1000 runs based on approximately 250 shots was selected at random. The database includes nearly 100,000 time samples. Eighty percent of the shots in the dataset were randomly assigned to be used for model training, ten percent were assigned to validation, and the final ten percent were reserved for testing. No NUBEAM results from the discharges assigned to the testing dataset were used to train models, while validation data was used to assess accuracy and generalization during hyper parameter tuning. Inputs to the model were chosen to be shaping parameters, beam powers, edge neutral density,  $Z_{eff}$ , electron temperature and density profiles, q profile, and fast ion diffusivity. The outputs to be predicted by the model were chosen to be the neutron rate, shine through, charge-exchange and orbit loss, and profiles of beam heating to ions/electrons, beam current drive and torque, and fast ion pressure.

### Reduction of profile data and beam slowing down time effects

Radially varying quantities are represented in TRANSP on a discrete grid of points in the normalized toroidal flux coordinate, typically using between 20 and 60 points. To reduce the number of inputs and outputs of the NN model, and therefore reduce the size of the datasets and time required for training and evaluation, the radially varying quantities were projected onto

a set of basis functions. The basis functions for each quantity were chosen by applying principal component analysis of the dataset and keeping only the most significant modes, typically between 4 and 10.

Due to the slowing down time of fast ions, the various effects of a beam on the plasma depend on the time history of the discharge. Therefore, it cannot be expected that a model trained only on instantaneous values of the inputs should accurately predict the output behavior (unless the dataset is only made up of steady-state results). While many approaches could be taken to include time history effects in the model, including recurrent neural networks, the simple but evidently effective approach taken here is to augment the inputs of the model with a set of causal, low-pass filtered versions of the individual beam powers. To account for the potential range of slowing-down times possible at different plasma conditions, the beam powers are filtered with time constants 0.02s, 0.05s, and 0.1s.

### Model topology selection and testing results

A fully connected neural network topology was chosen for the models developed in this work. The choice of the number of hidden layers, hidden-layer nodes, and the regularization weight on the  $L_2$ -norm of the model coefficients was chosen through scoring how well models generalized to the shots in the validation dataset in a grid scan of hyper-parameters.

To provide improved estimates and a sense of the uncertainty of the estimated values, an ensemble of 5 models was trained, each on a randomly selected subset of the training dataset and all using the same neural-network topology. The output of the ensemble is taken to be the average output of the models, and the standard-deviation and range of the model predictions are used to provide estimates of the uncertainty of the predicted output.

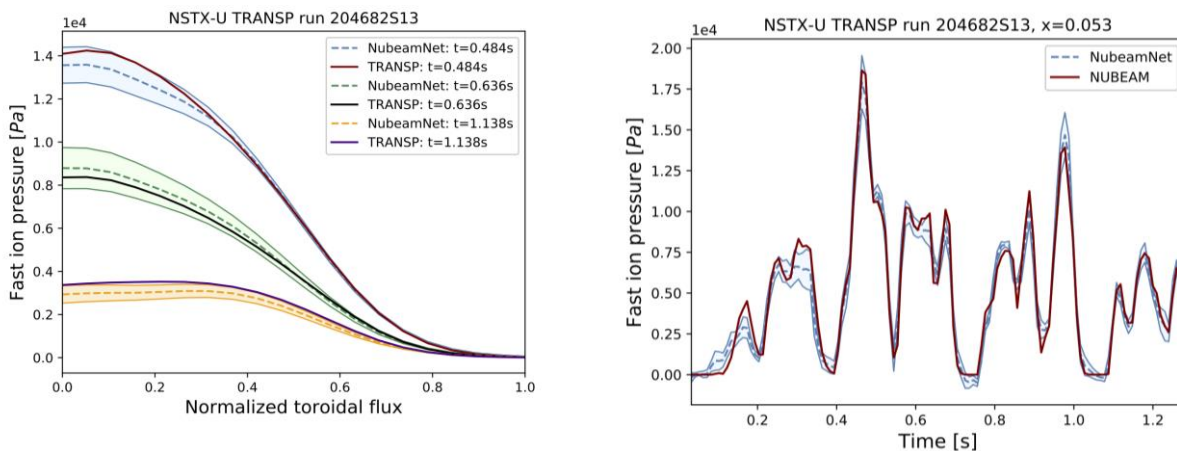


**Fig. 1S-ASC-1:** (Left) Comparison of NUBEAM and NubeamNet predicted fast ion pressure profiles at various times and (Right) comparison of time history near the magnetic axis.

Example comparisons of the NUBEAM calculation and NubeamNet estimation (with 3 layers of 125 nodes) for fast ion pressure are shown in Fig. IS-ASC-1 for TRANSP run 204682S13. The results show that the neural network is able to closely approximate the time behavior and prediction of profile shapes.

The neural network was implemented in the NSTX-U real-time computer, and a scan of model topology was conducted to assess the scaling of calculation time with model complexity. Results in Figure IS-ASC-2 show that models with complexity near that required to optimize the model fit can be run within the typical 200 microsecond cycle time of the NSTX-U control system. Recent advances in real-time PCIe-based internode communication in the NSTX-U control system [IS-ASC-3] will enable offloading calculations to a dedicated computer with enough cores to simultaneously calculate the models for uncertainty quantification, as well as calculation of the sensitivity of outputs to changes in inputs needed by real-time control and optimization algorithms.

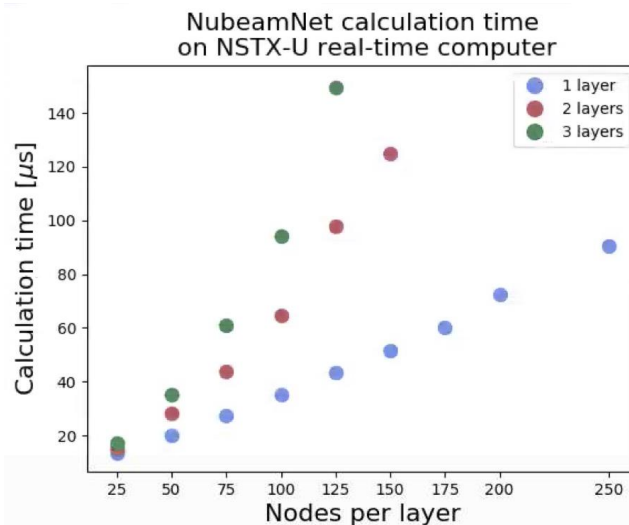


**Fig. IS-ASC-2:** Comparison of model execution time as a function of number of neural network layers and nodes per layer.

## Discussion

A neural network model for evaluating the beam heating, current drive, torque, and other effects of the NSTX-U neutral beam system on the plasma was developed. The model was trained on NUBEAM results calculated for the discharges in the first NSTX-U campaign. The speed of the resulting model makes it well-suited for many real-time applications on NSTX-U, including equilibrium reconstruction and profile control [IS-ASC-4,5]. Future work will include developing training sets and models based on predicted discharges to make the model useful for planning future NSTX-U campaigns that are not within the operating range explored in the first campaign. Alternative approaches to handling the time-history dependence, including recurrent neural networks, will be also be explored. Preliminary work has been done on developing similar models for the bootstrap current, resistivity, and geometric profiles required for evaluation of the magnetic diffusion equation, as well as for the plasma equilibrium. These will be further developed and integrated with the NUBEAM model to form a fast, high fidelity simulation capability for real-time control applications. Preliminary work has also been done to develop automated tuning of the hyper-parameters of the model (number of nodes, layers, etc.) through the use of genetic algorithms. The genetic algorithm exploits the PPPL computing cluster to evaluate many possible models in parallel (a generation), then combines aspects of the best models along with random mutations to produce a new generation for evaluation. Iterating through many generations results in an optimized model.

### C.3 Evolution of Wall Conditions on NSTX-U

The degradation of good wall conditions following a boronization occurred much faster on NSTX-U than NSTX [IS-ACS-6]. Consequently, the number and frequency of boronizations required to maintain good wall conditions was larger in the NSTX-U commissioning period compared to corresponding commissioning periods on NSTX. Analysis completed in FY-18 supports that the accelerated degradation of the wall conditions on NSTX-U was correlated with heating the horizontal section of the inboard divertor. These tiles were inadequately baked prior to operations due to large heat conduction to the PF1B coil support structures that were actively cooled to maintain the PF1B coil at a safe temperature. These results support the current effort to improve the bake of the divertor surfaces in the modification of the polar region design.

The fastest degradation of the wall conditions was observed following discharges with neutral beam heating above 1 MW and that ended in a vertical disruption event (VDE). This is illustrated in figure IS-ASC-3 where the evolution of wall condition metrics are shown for two consecutive days following a boronization during the final week of the commissioning period. The first ten discharges on June 22 were short ( $< 0.5$  s) H-mode discharges with  $P_{\text{NBI}}$  up to 6 MW; the remainder of the discharges on June 22 and 23 were longer duration (0.5 - 1.5 s) L-mode discharges with  $P_{\text{NBI}} = 1$  MW. The vertical dotted line indicates the transition from H-mode to L-mode experiments, while the vertical dashed line indicates the transition between separate run days. Both the H- and L-mode discharges had a similar LSN, low elongation shape that placed the outer strike point on the outboard divertor target during flattop. Thus, not much energy was conducted to the poorly baked plasma facing components (PFCs) during the course of the discharge unless the discharge ended in a vertical disruption.

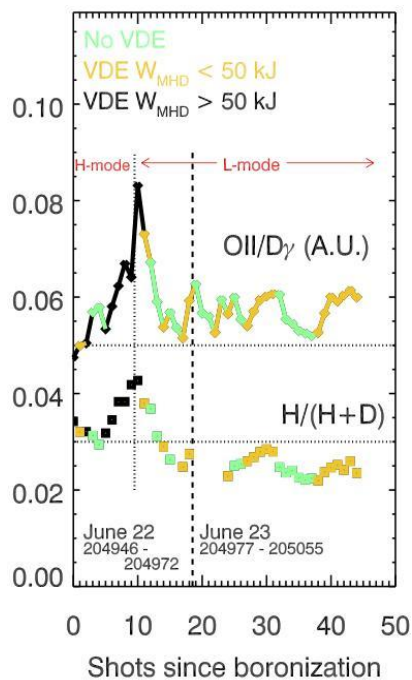


**Fig. IS-ASC-3:** Evolution of relative oxygen and hydrogen impurity content following a boronization. The evolution of the wall conditions depends on the heating of the inboard horizontal divertor PFCs due to VDEs.

The square data points in figure IS-ASC-3 show the relative concentration of neutral hydrogen compared to total neutral deuterium and hydrogen ( $H/(H+D)$ ) using data from the VIPS spectrometer by averaging the ratios for the upper and lower divertor views. The diamond data points show the ratio of the O II and  $D_\gamma$  signals from filter-scopes viewing vertically through the plasma toward the lower divertor. This ratio provides a relative metric of the oxygen content of the tile surfaces. Both ratios shown are the average values from 120ms – 180ms within each discharge, when the plasma is inboard limited and the details of the plasma are relatively independent of the experiment.

The lines connecting the diamonds in figure IS-ASC-3 illustrate that the details of the termination of a discharge impacted the wall conditions at the start of the next discharge. Discharges that ended with a vertical disruption event (VDE) generally led to a degradation of the wall conditions, especially when the stored energy lost in the disruption is above 50 kJ (black points). The green diamonds mark the discharges that ended without a VDE. The relative oxygen and hydrogen content is typically lower on the following shot. (The green lines slant downwards.) This lower value indicates that only heating the inboard limiter and outboard divertor targets (surfaces that were adequately baked) resulted in a net removal of impurities from those surfaces. The orange and black points indicate discharges that ended with a VDE. Generally, the impurity content is larger following these discharges and scales with the size of the stored energy ( $W_{MHD}$ ) lost during a VDE. The notable exceptions are the first two long L-mode discharges where the beneficial scrubbing of the outboard divertor and inner limiter by the plasma outweighs the detriment of the VDE.

Operations during the L-mode discharges demonstrate that avoiding heating the inner divertor by not placing a strikepoint on these surfaces and keeping the energy deposited in the divertor during a VDE below 50 kJ maintains plasma impurity content at a level comparable to the conditions achieved right after the boronization. The relative hydrogen content (squares) is reduced over the course of the L-mode discharges as they result in minimal heating of the inboard divertor tiles. The impurity content of discharges at the start of the second day (June 23) is similar to the last shot of the previous day. In addition, no concurrent rise in the nitrogen content was observed with the evolution of the hydrogen and oxygen content. This supports the thesis that the source of oxygen and hydrogen is not a leak in the vacuum vessel, but rather water trapped within material surfaces. The rapid increase in the oxygen and hydrogen content during the first ten discharges in figure IS-ASC-3 was consistently observed whenever a series of high-power discharges were conducted. The rise in the  $H/(H+D)$  ratio from 3% to 4% would have occurred over hundreds of discharges on NSTX, whereas it only required 10 - 20 discharges on NSTX-U. This presented an operational challenge when developing high-performance H-mode scenarios.

#### ***C.4 MAST-U Collaboration on Scenario and Control Development***

Collaboration on Scenario and Control development between MAST-U and NSTX-U continued in FY-18. The goal of the collaboration is to develop common tools and metrics for optimizing the performance on the two complimentary MA-class ST devices.

The activities completed toward this collaboration in FY-18 focused on the startup scenario modeling described in the R18-2 milestone report. The LRDFIT modeling framework was used to develop startup scenarios for a range of operational contingencies on MAST-U. For example, procedures were developed for startup in the event that some sets of coils are not available for operations or have more restrictive voltage and current limits than presently specified. This exercise retired some risk of delaying the start of the MAST-U commissioning period due to technical difficulties and helped identify the technical readiness required to meet the initial operational goals of MAST-U.

The NSTX-U ASC group also provided consultations on the real-time control hardware and software to the MAST-U team. Keith Erikson was asked to review the MAST-U plans for future PCS hardware investment and consult on the configuration and optimization of the NSTX-U real-time system. Devon Battaglia led a “Session Leaders Course” on startup for the MAST-U session leaders (equivalent to Physics Operators at NSTX-U). He also has reviewed and advised on the PCS software and GUI interface for MAST-U. The two devices use a similar PCS interface platform from General Atomics, and strive to foster collaboration through the mutual development of this platform.

Work began in FY-18 toward the development of matched scenarios between the two devices. Fig. IS-ASC-4 shows the comparison a potential matched shape at  $I_p = 1$  MA,  $B_T = 0.69$  T (at  $R = 0.936$  m) on the two devices. The coils (solid blocks), limiter surfaces (dashed lines) and plasma boundary (solid line) are colored red for MAST-U and black for NSTX-U. The rectangles inside the plasma boundary show the tangency radii of the neutral beams on the two devices. Producing matched shapes provides an opportunity to perform stability and transport studies that leverage differences in the designs of the two STs, such as the passive conductor structure, neutral beam location and divertor closure.

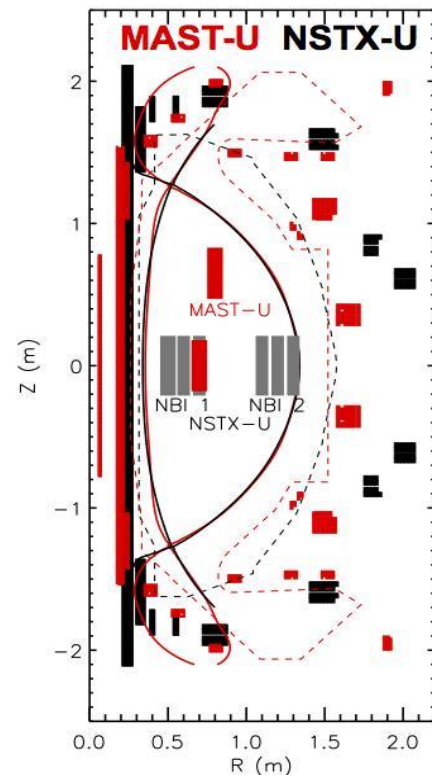


**Fig. IS-ASC- 4:** Comparison between NSTX-U (black) and MAST-U (red) plasma shapes at  $I_p = 1$  MA,  $B_T = 0.69$  T.

### C.5 Reflective Memory Supporting Future PCS Expansion

The current Plasma Control System (PCS) computers use 64 cores in a single host to support the real-time protection (DCPS) and control algorithms. Near-term plans for future PCS applications, such as real-time disruption forecasting, will exceed the growth curve of the processing that can fit into a single computer. Work was completed in FY-18 to complete a feasibility study of a new real-time communication design that enables coupling multiple 64-core nodes into a larger overall system of computers that can grow over time [IS-ASC-7].

DIII-D, KSTAR, and MAST-U have successfully used reflective memory in some fashion to incorporate multiple computing nodes in a real-time system. NSTX-U is now exploring a new technology to achieve similar functionality as these demonstrated solutions with highly deterministic results and peak performance. Dedicated tests performed with Dolphin Interconnect Solutions technology found the measured jitter of the reflective memory system was well within acceptable limits for the NSTX-U timing requirements, and in all cases, latency scaled linearly with payload size. Tests were completed using hardware consistent with the present (dated by a few years) NSTX-U real-time system, and the current generation of a PCIe serial bus boards. Fig. IS-ASC-5 shows the tests completed when connecting two serial bus boards presently employed on NSTX-U (AMD Gen2). The 1  $\mu$ s jitter satisfies the NSTX-U specifications; the latency scaling with payload size is promising and is most likely acceptable for expected payload sizes in future applications. The results with the PCIe serial bus demonstrates that upgrading to the newest serial bus technology would reduce the latency introduced by the reflective memory by a factor of two.

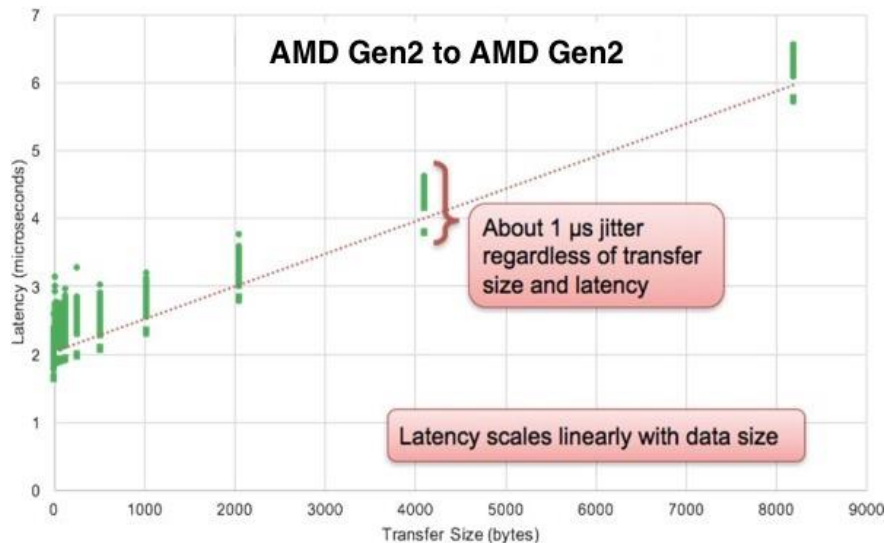


**Fig. IS-ASC-5:** Round-trip latency ( $\mu$ s) versus payload transfer size (bytes) with Dolphin reflective memory between two AMD Gen2 serial bus cards.

### C.6 Control System Design, Closed-Loop Simulation, Optimization for Snowflake Divertor

A promising heat flux mitigation strategy for NSTX-U is the snowflake divertor (SFD). Experiments on NSTX demonstrated a reduction of the peak divertor heat flux relative to the conventional divertor (from 5 to 1 MW/m<sup>2</sup>) due to favorable magnetic properties such as large poloidal flux expansion and longer X-point connection length [IS-ASC-8]. Significant progress has been made in FY-18 toward the development of a sophisticated, multiple-input-multiple-output algorithm for real-time feedback control of the SFD on NSTX-U [IS-ASC-9] to build upon prior work conducted on DIII-D [IS-ASC-10]. This work enables the SFD to be employed as a routine heat-flux mitigation tool on NSTX-U and DIII-D.

Control of the SFD is challenging due to the strongly nonlinear nature of the system dynamics. While magnetic control of the plasma shape and divertor configuration on tokamaks such as NSTX-U is traditionally accomplished with simple proportional-integral-derivative control algorithms with static gains, a physics-based, time-varying controller is required for the SFD to account for changes in the system response and coupling between poloidal field (PF) control coils. To this end, a simplified model of the time-response of the two X-points in the SFD to applied voltages on a set of PF coils, namely the PF1aL, PF1cL, and PF2L, was developed for use with modern model-based control design techniques. The primary components of the model are a set of coupled circuit equations describing the time-dynamics of the coil currents, a series approximation that models the response of an X-point to changes in poloidal field, and a linearized model of the plasma response to changes in the PF coil currents. The time-varying model of the SFD was then used with a standard control design algorithm known as the Linear-Quadratic-Regulator to design an optimal feedback controller given as input for a set of user-defined weights measuring the relative importance of each of the controlled variables. Due to the model-based nature of the control system, the controller gains may be updated during a discharge to account for evolving plasma conditions.

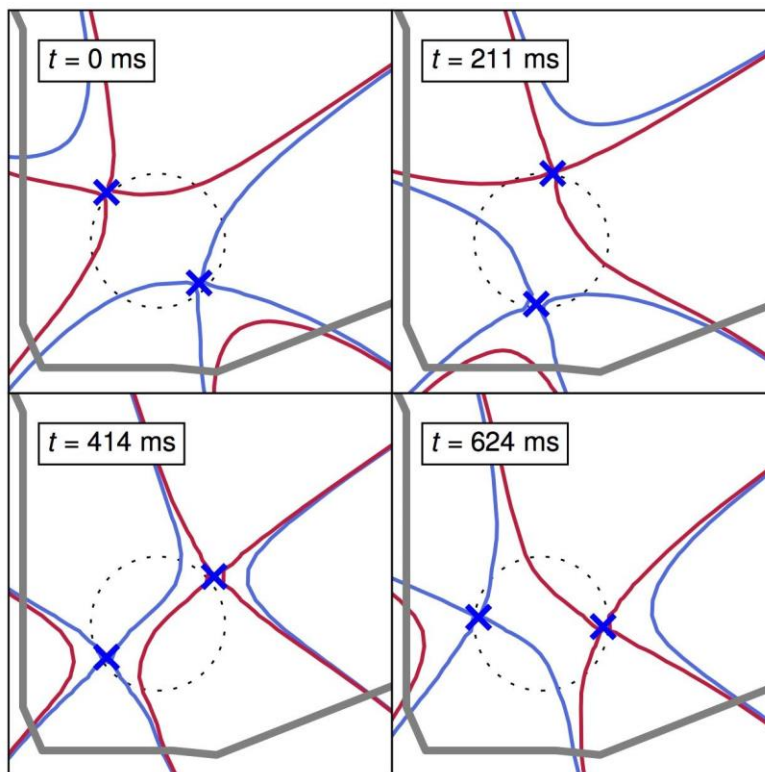


**Fig. IS-ASC-6:** Closed-loop simulation results depicting the primary (red) and secondary (blue) separatrix during a controlled transition of the snowflake divertor (SFD) configuration on NSTX-U from a low-field-side SFD-minus ( $t = 0$  ms) to a SFD-plus ( $t = 211$  ms) followed by a high-field-side SFD-minus ( $t = 414$  ms and  $t = 624$  ms) which was achieved by scanning the angular orientation of the primary and secondary X-points while maintaining a constant distance between the X-points. Dashed circles denote the target trajectory provided as input to the control algorithm during the simulation.

A control system simulator was developed for NSTX-U in MATLAB/Simulink which simultaneously evolves the PF coil and passive conductor currents and updates the plasma equilibrium by solving the free-boundary Grad-Shafranov problem. The nonlinear plasma model was operated in closed-loop with a simplified implementation of the ISOFLUX shape control algorithm used for plasma boundary and divertor control on NSTX-U. Voltage commands for the SFD control coils (PF1aL, PF1cL, and PF2L) were computed by the control algorithm as described in the previous paragraph, while voltages for the remaining coils were computed by ISOFLUX to maintain the boundary shape and upper X-point position. A series of simulations were performed using the control simulator to demonstrate the capabilities of the SFD controller. In Figure IS-ASC-6, the results of one such simulation are presented in which the algorithm was used to transition from a low-field-side SFD-minus ( $t = 0$  ms) to a SFD-plus ( $t = 211$  ms). This was followed by a high-field-side SFD-minus ( $t = 414$  ms and  $t = 624$  ms) by scanning the angular orientation of the primary and secondary X-points while maintaining a constant distance between the X-points. Optimal control system gains were re-computed every 5 ms to compensate for the significant variation in the divertor shape response that occurred as the equilibrium evolved. Additional simulations were performed in which the controller was used to scan the distance between the X-points at constant angular orientation in both the SFD-plus and SFD-minus configurations. The simulation scenarios demonstrate that the new control algorithm enables operations in a large variety of SFD equilibria of interest for future NSTX-U experiments.

The control algorithm as described was implemented in the NSTX-U Plasma Control System (PCS) with machine-independent code that is compatible with any device using the PCS software written by General Atomics. The PCS algorithm for SFD control, originally developed for use on NSTX-U, was successfully deployed in the DIII-D PCS and used during a SFD control development session on DIII-D in March 2018.

In addition to the design of the SFD control algorithm, recent work focused on the identification of optimal SFD configurations for power and particle exhaust on NSTX-U, with implications for both real-time control and scenario development. A simple analytical model was derived that describes the partitioning of scrape-off layer power and particle exhaust in the SFD due to diffusive transport to multiple activated strike points (SPs). The model was validated against simulation results from the multi-fluid edge transport code UEDGE and used to analyze a database of 70 SFD-minus equilibria. The heat flux profiles as computed by the simple model for three representative divertor configurations on NSTX-U are shown in Figure IS-ASC-7.

Based upon results of the SFD database analysis, the optimal SFD-minus equilibria for equal partitioning of either the integrated power fraction or peak perpendicular heat flux between SP2 and SP4 (as shown in Figure IS-ASC-7) were determined. Furthermore, the compatibility of the SFD configuration with a divertor cryo-pumping system was explored, which is a potential hardware upgrade for particle control on NSTX-U. The optimal location for the entrance to a cryo-pumping system was computed for enabling sufficient pumping performance in a variety of SFD-minus equilibria (77% of the SFD database). Pump placement at the optimal location was found to be advantageous as the large number of compatible equilibria reduces the precision

required of the SFD control system. The results of this work suggest future avenues for the development of real-time systems for SFD configuration control and heat flux mitigation. While many SFD equilibria are achievable with the divertor PF coil set on NSTX-U, the simple analytical model can be used to identify target configurations for the SFD control system based upon a set of power and particle exhaust requirements. Furthermore, simple modeling of SFD power and particle exhaust may facilitate improvements in real-time equilibrium reconstruction methods for advanced divertors by allowing for estimates of the magnetic configuration to be obtained from real-time divertor heat flux measurements.

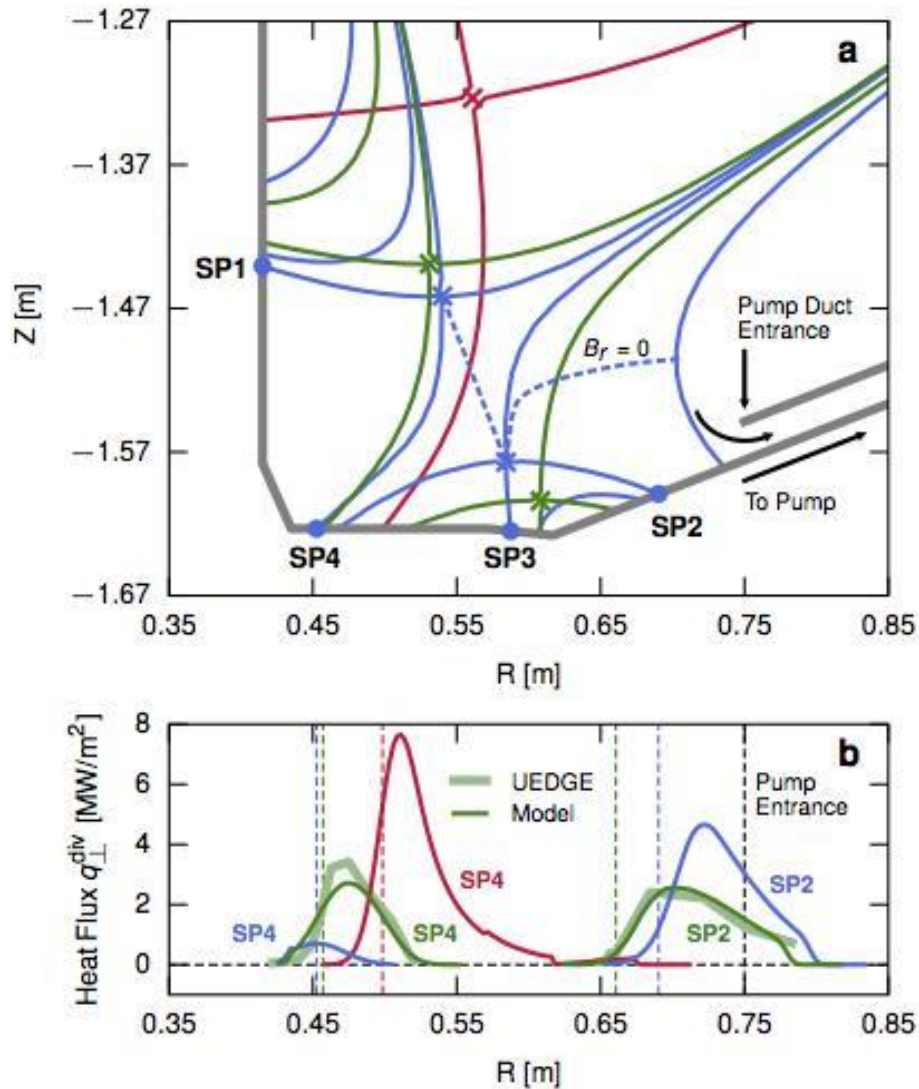


**Fig. IS-ASC-7:** Heat flux profiles (b) as computed by the simplified analytical model for three representative divertor configurations on NSTX-U, as shown in (a): large flux expansion single-null (red) as well as SFD-minus with large distance between X-points (green) and reduced distance between X-points (blue). Shown in (b) are the UEDGE predicted profiles for the green SFD-minus equilibrium. Shown also in (a) and (b) is the approximate location of the entrance to the divertor cryo-pump which was used for pump performance analysis.

## References

- [IS-ASC-1] Meneghini, O. et al., Self-consistent core-pedestal transport simulation with neural network accelerated models, *Nuclear Fusion* vol. 57, no. 8, p. 086034 (2017).
- [IS-ASC-1] Boyer, M.D. et al., Real-time capable neural network approximation of NUBEAM for use in the NSTX-U control system, 45th EPS Conference on Plasma Physics, P4.1084 (2018).
- [IS-ASC-3] Erickson, K.G. et al., NSTX-U advances in real-time deterministic PCIe-based internode communication, *Fusion Engineering and Design* vol. 133, pp. 104-109 (2018).
- [IS-ASC-4] Ilhan, Z.O. et al., Model predictive control with integral action for the rotational transform profile tracking in NSTX-U, *2016 IEEE Conference on Control Applications (CCA)*, pp. 623-628, (2016).
- [IS-ASC-5] Goumiri, I.R. et al., Simultaneous feedback control of plasma rotation and stored energy on NSTX-U using neoclassical toroidal viscosity and neutral beam injection, *Physics of Plasmas*, vol. 24, no. 5, p. 056101, (2017).
- [IS-ASC-6] Battaglia, D. J. et al., Scenario development during commissioning operations on the National Spherical Torus Experiment Upgrade. *Nucl. Fusion* **58**, (2018).
- [IS-ASC-7] Erickson, K. G., Boyer, M. D. & Higgins, D. NSTX-U advances in real-time deterministic PCIe-based internode communication. *Fusion Eng. Des.* **133**, 104–109 (2018).
- [IS-ASC-8] Soukhanovskii, V. A. et al., Snowflake divertor configuration studies in National Spherical Torus Experiment. *Phys. Plasmas* vol. 19, no. 8, p. 082504 (2012).
- [IS-ASC-9]. Vail, P. J., Kolemen, E., Boyer, M. D. and Welander, A. Control system development for the snowflake divertor on NSTX-U. Submitted to *Plasma Phys. Control. Fusion* (2018).
- [IS-ASC-10]. Kolemen, E., Vail, P. J. et al., Initial development of the DIII-D snowflake divertor control. *Nucl. Fusion* vol. 58, no. 6, p. 066007 (2018).
- [IS-ASC-11] Vail, P. J., Kolemen, E., and Izacard, O. Optimization of the snowflake divertor for power and particle exhaust on NSTX-U. Submitted to *Nucl. Mater. Energy* (2018).

# NSTX-U Publications

## Papers Published by NSTX-U Researchers (Oct. 2017 - Sept. 2018)

1. MENARD JE, Battaglia D, Bedoya F, et al.,  
[Overview of first operational and physics results from NSTX Upgrade](#)  
NUCLEAR FUSION **57** 102006 (October 2017)
2. ZWEBEN SJ, Stotler DP, Scotti F, et al.,  
[Two-dimensional turbulence cross-correlation functions in the edge of NSTX](#)  
PHYS. PLASMAS **24** 102509 (October 2017)  
*Copyright 2017 American Institute of Physics. This article may be downloaded for personal use only. Any other use requires prior permission of the author and the American Institute of Physics.*
3. DEN HARTOG DJ, Borchardt MT, Holly DJ, et al.,  
[A pulse-burst laser system for Thomson scattering on NSTX-U](#)  
JOURNAL of INSTRUMENTATION **12** C10002 (October 2017)
4. HOSEA J, et al.,  
[Development of slow and fast wave heating from the C-Stellarator to NSTX](#)  
EUROPEAN PHYSICAL JOURNAL Web of Conferences,  
22nd Topical Conference on Radio-Frequency Power in Plasmas **157** 02005 (Oct 2017)
5. KIM E-H, Bertelli N, Johnson J, et al.,  
[2D full-wave simulation of waves in space and tokamak plasmas](#)  
EUROPEAN PHYSICAL JOURNAL Web of Conferences,  
22nd Topical Conference on Radio-Frequency Power in Plasmas **157** 02005 (Oct 2017)
6. BERTELLI N, Gorelenkova M, Podesta M, et al.,  
[Self-consistent calculation of the effects of RF injection in the HHFW heating regimes on the evolution of fast ions in toroidal plasmas](#)  
EUROPEAN PHYSICAL JOURNAL Web of Conferences,  
22nd Topical Conference on Radio-Frequency Power in Plasmas **157** 03004 (Oct 2017)
7. LEE J, Wright J, Bertelli N, et al.,  
[A new quasilinear formulation for ICRF plasmas in a toroidal geometry](#)  
EUROPEAN PHYSICAL JOURNAL Web of Conferences,  
22nd Topical Conference on Radio-Frequency Power in Plasmas **157** 03028 (Oct 2017)
8. PERKINS R, Hosea J, Taylor G, et al.,  
[ICRF-Induced Changes in Floating Potential and Ion Saturation Current in the EAST Divertor](#)  
EUROPEAN PHYSICAL JOURNAL Web of Conferences,  
22nd Topical Conference on Radio-Frequency Power in Plasmas **157** 03039 (Oct 2017)

9. POLI, FM, Fredrickson E, Henderson MA, et al.,  
[EC power management in ITER for NTM control: the path from the commissioning phase to demonstration discharges](#)  
EUROPEAN PHYSICAL JOURNAL Web of Conferences,  
22nd Topical Conference on Radio-Frequency Power in Plasmas **157** 03041 (Oct 2017)
10. TAYLOR G, Bertelli N, Gerhardt SP, et al.,  
[Time-Dependent Simulations of Fast-Wave Heated High-Non-Inductive-Fraction H-Mode Plasmas in the National Spherical Torus Experiment Upgrade](#)  
EUROPEAN PHYSICAL JOURNAL Web of Conferences,  
22nd Topical Conference on Radio-Frequency Power in Plasmas **157** 03052 (Oct 2017)
11. KREBS I, Jardin SC, Gunter S, Lackner K, Hoelzl M, Strumberger E, Ferraro N.  
[Magnetic flux pumping in 3D nonlinear magnetohydrodynamic simulations.](#)  
PHYS. PLASMAS **24** 102511 (October 2017)
12. MOYER RA, Paz-Soldan C, Nazikian R, Orlov DM, Ferraro NM, et al.,  
[Validation of the model for ELM suppression with 3D magnetic fields using low torque ITER baseline scenario discharges in DIII-D](#)  
PHYS. PLASMAS **24** 102501 (October 2017)
13. ONO M, Majeski R, Jaworski MA, et al.,  
[Liquid lithium loop system to solve challenging technology issues for fusion power plant .](#)  
NUCLEAR FUSION **57** 116056 (November 2017)
14. PERKINS R, Hosea JC, Bertelli N, et al.,  
[Edge loss of high-harmonic fast-wave heating power in NSTX: a cylindrical model.](#)  
NUCLEAR FUSION **57** 116062 (2017)
15. ILHAN ZO, Barton JE, Schuster E, et al.,  
[Physics-based control-oriented modeling of the current density profile evolution in NSTX-Upgrade](#)  
FUSION ENG. DESIGN **123** 564 (November 2017)
16. BEIERSDORFER P, Lepson JK, Gu MF, et al.,  
[Plasma measurements of Fe XVII L-shell emission and blending with F VIII, F IX](#)  
ASTROPHYSICAL JOURNAL **850** 57 (November 2017)
17. BERKERY JW, Wang ZR, Sabbagh SA, Liu YQ, Betti R, and Guazzotto L  
[Application of benchmarked kinetic resistive wall mode stability codes to ITER, including additional physics](#)  
PHYS. PLASMAS **24** 112511 (November 2017)

18. GAN K,Ahn J-W, Gray TK, et al.,  
[ELM-free and inter-ELM divertor heat flux broadening induced by Edge Harmonic Oscillations in NSTX](#)  
NUCLEAR FUSION **57** 126053 (December 2017)
19. DUARTE VN, Berk HL, Gorelenkov N, et al.,  
[Theory and observation of the onset of nonlinear structures due to eigenmode destabilization by fast ions in tokamaks](#)  
PHYS PLASMAS **24** 122508 (December 2017)
20. KURODA K, Raman R, Hanada K, et al.,  
[Current start-up using the new CHI system](#)  
PLASMA AND FUSION RESEARCH **12** 1202020 (December 2017)
21. MIKKELSEN DR, Kessel CE, Poli FM, et al.,  
[Survey of heating and current drive for K-DEMO.](#)  
NUCLEAR FUSION **58** 036014 (January 2018).
22. SUN PJ, Li YD, Ren Y, et al.,  
[Experimental identification of nonlinear coupling between \(intermediate, small\)-scale microturbulence and an MHD mode in the core of a superconducting tokamak](#)  
NUCLEAR FUSION **58** 016003 (January 2018)
23. SUN PJ, Li YD, Ren Y, et al.,  
[Experimental Study of the Effect of 2/1 Classical Tearing Mode on \(Intermediate, Small\)-scale Microturbulence in the Core of an EAST L Mode Plasma](#)  
Plasma Phys. Control. Fusion **60** 025019 (January 2018)
24. POLI FM, Fredrickson ED, Henderson MA, et al.,  
[Electron cyclotron power management for control of neoclassical tearing modes in the ITER baseline scenario](#)  
NUCLEAR FUSION **58** 016007 (January 2018)
25. HAMMOND K, Raman R, Volpe, FA  
[Application of Townsend avalanche theory to tokamak startup by coaxial helicity injection](#)  
NUCLEAR FUSION **58** 016013 (January 2017)
26. WANG Z, Park J-K, Menard JM, et al.,  
[Drift kinetic effects on the plasma response in high beta spherical tokamak experiments.](#)  
NUCLEAR FUSION **58** 016015 (January 2017)
27. MYERS CE, Gerhardt SP, Eidietis NW, et al.,  
[A multi-machine scaling of halo current duration and rotation](#)  
NUCLEAR FUSION **58** 016050 (January 2017)

28. CROCKER NA, Kubota S, Peebles WA, et al.,  
[Density perturbation mode structure of high frequency compressional and global Alfvén eigenmodes in the National Spherical Torus Experiment using a novel reflectometer analysis technique](#)  
NUCLEAR FUSION **58** 016051 (January 2018)
29. POLI E, BOCK A, LOCHBRUNNER M, et al.,  
[TORBEAM 2.0, a paraxial beam tracing code for electron-cyclotron beams in fusion plasmas for extended physics applications.](#)  
COMPUTER PHYSICS COMMUNICATIONS 225 **36** (January 2018)
30. HAO GZ, Heidbrink WW, Liu D, et al.,  
[Measurement of the passive fast-ion D-alpha emission on the NSTX-U tokamak](#)  
PLASMA PHYS CONTROLLED FUSION **60** 025026 (February 2018)
31. MAINGI R, Hu JS, Sun Z, et al.,  
[ELM elimination with Li powder injection in EAST discharges using the tungsten upper divertor](#)  
NUCLEAR FUSION **58** 024003 (February 2018)
32. de VRIES PC, Luce TC, Bae YS, et al.,  
[Multi-machine analysis of termination scenarios with comparison to simulations of controlled shutdown of ITER discharges](#)  
NUCLEAR FUSION **58** 026019 (February 2018)
33. WELLER ME, Beiersdorfer P, Soukhanovskii VA, et al.,  
[Electron-density-sensitive Line Ratios of FeXIII–XVI from Laboratory Sources Compared to CHIANTI](#)  
ApJ **854** 102 (February 2018)
34. LUNSFORD R, Sun Z, Maingi R, et al.,  
[Injected mass deposition thresholds for lithium granule instigated triggering of edge localized modes on EAST](#)  
NUCLEAR FUSION **58** 036007 (March 2018)
35. BOYER MD, Battaglia DJ, Mueller D, et al.,  
[Plasma boundary shape control and real-time equilibrium reconstruction on NSTX-U](#)  
NUCLEAR FUSION **58** 036016 (March 2018)
36. GLASSER A, Kolemen E, Glasser AH  
[A Riccati Solution for the Ideal MHD Plasma Response with Applications to Real-time Stability Control](#)  
PHYS PLASMAS **25** 032507 (March 2018)

37. BATTAGLIA DJ, Boyer MD, Gerhardt S, et al.,  
[Scenario Development During Commissioning Operations on the National Spherical Torus Experiment Upgrade](#)  
NUCLEAR FUSION **58** 046010 (April 2018)
38. LAU C, Jaeger E, Bertelli N, et al.,  
[AORSA full wave calculations of helicon waves in DIII-D and ITER.](#)  
NUCLEAR FUSION 58, 066004 (April 2018).
39. LESTZ JB, Belova EV, Gorelenkov NN  
[Energetic-particle-modified global Alfvén eigenmodes](#)  
PHYS. PLASMAS **25** 042508 (April 2017)
40. POLI E, Bock A, Lochbrunner, et al.,  
[TORBEAM 2.0, a paraxial beam tracing code for electron-cyclotron beams in fusion plasmas for extended physics applications](#)  
COMPUTER PHYSICS COMM **225** 36 (April 2018)
41. PFEFFERLE D, Ferraro N, Jardin SC et al.,  
[Modeling of NSTX hot Vertical Displacement Events using M3D-C1](#)  
PHYS. PLASMAS **25** 056106 (May 2018)
42. WILCOX RS, Rhodes TL, Shafer MW, Sugiyama LE, Ferraro NM, et al.,  
[Helical variation of density profiles and fluctuations in the tokamak pedestal with applied 3D fields and implications for confinement](#)  
PHYS. PLASMAS **25** 056180 (May 2018)
43. LYONS BC, Paz-Soldan C, Meneghini O, et al.,  
[Predict-first experimental analysis using automated and integrated magnetohydrodynamic modeling](#)  
PHYS. PLASMAS **25** 056111 (May 2018)
44. ASHOURVAN A, Grierson B A, Battaglia D J, Haskey S R, and Stoltzfus-Dueck T,  
[Validation of the kinetic-turbulent-neoclassical theory for edge intrinsic rotation in DIII-D.](#)  
PHYS. PLASMAS **25** 056114 (May 2018)
45. LOPEZ N and Poli F  
[Regarding the optimization of O1-mode ECRH and the feasibility of EBW startup on NSTX-U](#)  
PLASMA PHYS. CONTROLLED FUSION **60** 065007 (June 2018)
46. HAO G, Heidbrink WW, Liu D, et al.,  
[On the scattering correction of fast-ion D-alpha signal on NSTX-U](#)  
REV. SCI. INST. 18 063507 (June 2018)

47. MYRA JA, Zweben SJ, Russell DA  
[Blob-hole correlation model for edge turbulence and comparison with NSTX gas puff imaging data](#)  
PLASMA PHYS. CONTROLLED FUSION **60** 075015 (July 2018)
48. PETRELLA J, Zatz I, Gerhardt S, et al.,  
[Forensic analysis of faulted NSTX-U inner poloidal field coil](#)  
IEEE Transactions on Plasma Science **46** 2653 (July 2018)
49. FREDRICKSON, ED, Podesta M,  
[Editorial: 15th IAEA Technical Meeting on Energetic Particles in Magnetically Confined Systems](#)  
NUCL. FUSION **58** 080201 (August 2018)
50. DUARTE VN, Gorelenkov NN, Schneller M, et al.,  
[Study of the likelihood of Alfvénic mode bifurcation in NSTX and predictions for ITER baseline scenarios](#)  
NUCL. FUSION **58** 082013 (August 2018)
51. GORELENKOV NN, Duarte VN, Podesta M, et al.,  
[Resonance broadening quasi-linear \(RBQ\) model for fast ion relaxation due to Alfvénic eigenmodes](#)  
NUCL. FUSION **58** 082016 (August 2018)
52. FREDRICKSON ED, Belova EV, Gorelenkov NN, et al.,  
[Global Alfvén eigenmode scaling and suppression: experiment and theory](#)  
NUCL. FUSION **58** 082022 (August 2018)
53. PODESTA M, Fredrickson ED and Gorelenkova M  
[Destabilization of counter-propagating Alfvénic instabilities by tangential, co-current neutral beam injection](#)  
NUCL. FUSION **58** 082023 (August 2018)
54. HEIDBRINK WW, Bardoczi L, Collins CS, et al.,  
[The phase-space dependence of fast-ion interaction with tearing modes](#)  
NUCL. FUSION **58** 082027 (August 2018)
55. LIU D, Heidbrink WW, Podesta M, et al.,  
[Effect of sawtooth crashes on fast ion distribution in NSTX-U](#)  
NUCL. FUSION **58** 082028 (August 2018)
56. KIM D, Podesta M, Liu D., et al.,  
[Orbit modeling of fast ion redistribution induced by sawtooth instability](#)  
NUCLEAR FUSION **58** 082029 (August 2018)

57. ERICKSON K, Boyer M. D., Higgins, D  
[NSTX-U advances in real-time deterministic PCIe-based internode communication.](#)  
 FUSION ENG. DESIGN **133** 104 (August 2018)
58. MUNARETTO S, Strait EJ, Wang Z  
[Conceptual design of extended magnetic probe set to improve 3D field detection in NSTX-U](#)  
 REV. SCI. INST. **89** 10J108 (2018)
59. CHU P, Wolfe B, Wang Z,  
[Measurement of incandescent microparticle acceleration using stereoscopic imaging](#)  
 REV. SCI INST. **89** 10K101 (2018)

### **Papers Recently Accepted for Publication**

1. REYMOND L, Diallo A , Vekselman V,  
 Using Laser-Induced Rydberg Spectroscopy diagnostic for direct measurements of the local electric field in the edge region of NSTX/NSTX-U: Modeling  
 Accepted for publication in REVIEW of SCI INST (2018)
2. YONEDA R, Hanada K, Elserafy H. et al.,  
 High Field Side RF Injection for Excitation of Electron Bernstein Waves.  
 Accepted for publication in PLASMA AND FUSION RESEARCH (The Japan Society of Plasma Science and Nuclear Fusion Research) (2018).
3. BARCHFELD R, Domier CW, Ren Y, et al.,  
 The High-k Poloidal Scattering System for NSTX-U  
 Accepted for publication in REVIEW of SCI INST (2018)
4. SOUKHANOVSII VA, Blanchard WR, Dong JK, et al.,  
 Supersonic gas injector for plasma fueling in the National Spherical Torus Experiment.  
 Accepted for publication in FUSION SCIENCE AND TECHNOLOGY (2018)
5. HASKEY S, Grierson B, Chrystal C, et al.,  
 Main ion and impurity edge profile evolution across the L- to H-mode transition on DIII-D  
 Accepted for publication in PLASMA PHYSICS AND CONTROLLED FUSION (July 2018)
6. PARK J.-K, Jeon Y, In Y, et al.,  
 3D Field Phase Space Control in Tokamak Plasmas  
 Accepted for publication in NATURE PHYSICS (July 2018)

# NSTX-U Presentations

## Invited / Oral Talks at Scientific Conferences (Oct. 2017 - Sept. 2018)

### 59<sup>th</sup> APS Division of Plasma Physics Meeting on Oct. 23-27, 2017 in Milwaukee, WI

A. Diallo (PPPL)	Energy Exchange Dynamics across L-H transitions in NSTX. (Invited)
E. Fredrickson (PPPL)	Suppression of Alfvénic modes through modification of the fast ion distribution. (Invited)
R. Goldston (PPPL)	A new scaling for divertor detachment. (Invited)
S.-H. Ku (PPPL)	Gyrokinetic simulation of fast L-H bifurcation dynamics in a realistic diverted tokamak edge geometry. (Invited)
D. Pfefferle (PPPL)	The ins and outs of modeling vertical displacement events. (Invited)
F. Poli (PPPL)	Integrated tokamak modeling: when physics informs engineering and research planning. (Tutorial)
T. Stoltzfus-Dueck (PPPL)	Parasitic momentum flux in the tokamak core. (Invited)
J. Menard (PPPL)	Status and plans for NSTX-U recovery.
L. Morton (GA)	A first look at resistive MHD stability differences between NSTX and NSTX-U high beta discharges.
G.Z. Hao (UC Irvine)	Simulation of the internal kink-like mode driven by the toroidal rotation in spherical tokamak.
J. Ruiz Ruiz (MIT)	Electron-scale turbulence and transport in an NSTX H-mode plasma using a synthetic diagnostic for high-k scattering measurements.
F. Scotti (LLNL)	Divertor-localized fluctuations in NSTX-U L-mode discharges.
F. Bedoya (U. Illinois)	Characterization of boronized graphite in NSTX-U and its effect on plasma performance.
C. Skinner (PPPL)	Elemental and topographical imaging of microscopic variations in deposition on NSTX-U and DIII-D samples.
D. Mueller (PPPL)	Improvement of vertical stabilization on KSTAR.

### RF workshop on. October 3-4, 2017, in Los Angeles CA

N. Bertelli (PPPL)	Understanding the interaction between RF wave fields and fast-ion populations in NSTX plasmas.
--------------------	--

### Workshop on High-Fidelity Boundary Plasma Simulations on Leadership Class Computers on Oct. 3-4, 2017 in Princeton, NJ

R. Maingi (PPPL)	Cutting edge boundary simulation calculations and validation opportunities for ITER and NSTX-U.
------------------	---

### **22nd MHD Stability and Control Workshop on Oct. 30-Nov. 1, 2017 in Madison WI**

- S. Sabbagh (Columbia U) Progress on disruption event characterization and forecasting in tokamaks (DECAF).
- M. Boyer (PPPL) Feedback control of stored energy and rotation on DIII-D using variable beam voltage and perveance.
- D. Kim (PPPL) Sawtooth period control experiments. (Invited)

### **FESAC Advisory Board Meeting on Feb. 1, 2018 in Gaithersburg, MD**

- R. Maingi (PPPL) Transformative Enabling Capabilities for Efficient Advance Toward Fusion Energy.

### **6th RIAM Workshop Kyushu University, Kasuga, Japan, 1-2 February 2018**

- N. Bertelli (PPPL) Initial Fokker-Planck simulations by using the CQL3D code for QUEST plasmas.
- L. Delgado-Aparicio (PPPL) Multi-energy SXR imaging and its applications to QUEST plasmas.
- M. Ono (PPPL) NSTX-U Plasma Start-up Research Program and Collaboration Strategy.

### **The KSTAR Conference 2018, Muju, South Korea, Feb. 21-23, 2018.**

- N. Bertelli (PPPL) Research plan in support of the helicon wave modeling in KSTAR.
- E.-H. Kim (PPPL) Full-wave simulations of high harmonic fast wave in the scrape-off layer of NSTX.
- D. Mueller (PPPL) Improvement of vertical stabilization on KSTAR.
- K. Erickson (PPPL) PPPL Real-time Advances Applicable to KSTAR.
- D. Boyer (PPPL) Real-time forecasting and feedback control algorithm design enabled by TRANSP.

### **US-Japan MHD Workshop: Toward development of integrated studies of 3D magnetic field effects in fusion devices” and “31st ITPA MHD Disruption and Control Topical Group on March 5-9, 2018 in Naka, Japan**

- S. Jardin (PPPL) Progress on disruption modeling
- J.-K. Park (PPPL) Summary for low-n and low-torque error field correction criteria.

### **Royal Society Meeting on March 26-27, 2018 in London UK**

- J. Menard (PPPL) Compact steady-state tokamak performance dependence on magnet and core physics limits.

### **National Academy of Science (NAS) Committee on a Strategic Plan for U.S. Burning Plasma Research on April 11-13, 2018 in Princeton NJ**

- J. Menard (PPPL) Options and Strategies towards Fusion Net-Electricity.
- S. Gerhardt (PPPL) NSTX-U: An Essential Science Facility for US Fusion Innovation.
- M. Jaworski (PPPL) First-wall, plasma-material interaction, and liquid metals for fusion.

**12th West Lake International Symposium on Plasma Simulation, Hangzhou (China) May 3-5, 2018**

E. V. Belova (PPPL) Numerical simulations of GAE stabilization in NSTX-U

**5th IAEA DEMO Workshop on May 7-10, 2018 in Daejeon, South Korea**

P. Titus (PPPL) Structural issues for large fusion magnets.

**U.S. Transport Task Force Meeting on May 8-11, 2018 in San Diego CA**

F. Poli (PPPL) Optimization of ramp-up current evolution for improved access sustainment of stable steady.

J. Ruiz Ruiz (MIT) Two synthetic diagnostics for quantitative comparisons between gyrokinetic simulation and experimental spectra of electron scale turbulence in NSTX plasmas.

N. Gorelenkov (PPPL) A Quasi-linear modeling of fast ion relaxation due to Alfvénic instabilities.

T. Stoltzfus-Dueck (PPPL) Towards Quantitative First-Principles Models for Intrinsic Rotation in Axisymmetric Devices (Invited, Plenary)

**9th US-PRC Magnetic Fusion Collaboration Workshop on June 5-7, 2018 in Xi'an, China**

R. Maingi (PPPL) Recent Progress on NSTX-U and Future Collaboration Opportunities.

R. Maingi(PPPL) Results from the US-PRC collaboration on PMI in EAST.

**23rd International Conference on Plasma Surface Interactions in Controlled Fusion Devices (PSI-23) on June 18-22, 2018 in Princeton NJ**

B. Koel (Princeton Univ.) Chemistry at the edge: surface science probes of plasma-materials interactions. (Tutorial)

R. Goldston (PPPL) SOL physics and heat dissipation (Tutorial)

R. Majeski (PPPL) The effect of lithium conditioning approaches for plasma-facing surfaces on the edge and core temperature and density profiles.

**45TH EPS Conf. of Plasma Physics Meeting on July 2-6, 2018 in Prague, Czech Republic**

J.-K. Park (PPPL) Phase Space Visualization and Validation of 3D Field Operating Windows for ELM Suppression in KSTAR. (Invited)

**6th Annual Theory and Simulation of Disruptions Workshop, Princeton Plasma Physics Laboratory, Princeton, New Jersey July 16-18, 2018**

S.A. Sabbagh (Columbia U.) Progress on Disruption Event Characterization and Forecasting (DECAF) in Tokamaks.

J.W. Berkery (Columbia U.) Disruptivity and Density Limits in MAST and other Tokamaks.

J.D. Riquezes (Columbia U.) Rotating MHD analysis for disruption event characterization and forecasting.

**Joint Varenna-Lausanne International Workshop on Theory of Fusion Plasmas, Varenna (Italy) Aug. 27-31, 2018.**

T. Stoltzfus-Dueck (PPPL)      Intrinsic rotation in Axisymmetric Devices. (Invited)

**US-JAPAN Workshop on RF Heating Physics, Gotemba, Shizuoka (Japan) Sept. 4-7, 2018.**

N. Bertelli (PPPL)                      The effect of the hydrogen species on the HHFW performance in NSTX/NSTX-U plasmas.

E.-H. Kim (PPPL)                      High harmonic fast wave propagation in the scrape-off layer of NSTX and NSTX-U.

M. Ono (PPPL)                      Modeling of 2nd Harmonic Electron Cyclotron Heating and Current Drive Solenoid-free Start-up Experiment in QUEST.

**4th European Microwave Conference, Nuremberg (Germany) Oct. 8-13, 2017**

N.C. Luhmann, Jr.  
(UC Davis)

Advances in Fabrication Technologies for Sub-Millimeter Wave and THz Applications at UC Davis.

## Seminars and Colloquia by NSTX-U Researchers

1. L. Delgado-Aparicio "Current trends in x-ray spectroscopy for fusion plasmas: Possible applications for QUEST (Kyushu U.) and JT60SA (QST)", Tokyo Japan, January 2018
2. S. Kaye "Containing a star on earth: the promise of fusion energy", Princeton NJ, January 2018
3. R. Perkins "Mitigating edge losses of high-harmonic fast-wave heating power on the National Spherical Torus Experiment", Irvine CA, March 2018
4. Y. Ren "Overview of high-k scattering diagnostics on NSTX and NSTX-U", ASIPP, China April 2018
5. E.-W. Kim "Recent research on wave modeling for tokamak and space plasmas", Dartmouth College, April 2018
6. M. Ono "NSTX-U Initial Operations and Solenoid-free Start-up Research Strategy", Kyoto Japan, April 2018
7. E. Belova "Onset and nonlinear relaxation of coherent current carrying edge filaments during transient events in tokamaks", Univ. Maryland, May 2018
8. M. Jaworski "Plasma Facing Components for the NSTX-U Recovery Project and Applications of Liquid Technologies to Conventional Energy Sources", DIFFER, Netherlands, May 2018
9. N. Bertelli "Thrust 1: Production of RF WDM components, interaction with AToM/TRANSP and thrust common development", VideoCon, June 2018
10. M. Ono "Roles and opportunities of the QUEST program for the Spherical Tokamak reactor development", Kyushu Japan, July 2018
11. W. Guttenfelder, "Intro to turbulence & concepts" PPPL Graduate Summer School, Aug. 2018
12. W. Guttenfelder, "Flavors of magnetized plasma turbulence" PPPL Graduate Summer School, Aug. 2018
13. W. Guttenfelder, "Modeling turbulence & transport" PPPL Graduate Summer School, Aug. 2018

# NSTX-U Awards and Leadership

## Major Awards by NSTX-U Researchers

- C.S. Chang (PPPL) Incite Award for 300 million hours of computing time
- N. Ferraro (PPPL) FES Early Career Award
- S. Jardin (PPPL) NERSC 2018-2019 ALCC of 40 million hours of NERSC computers
- D. Mueller (PPPL) Honorary Doctorate from MacMurray College
- T. Evans (General Atomics) 2018 APS-DPP John Dawson Award for Excellence in Plasma Physics.
- L. Delgado-Aparicio (PPPL) Chinese Academy of Sciences President's International Fellowship Initiative (PIFI)

## Hosted / Organized Meetings and Workshops

*NSTX-U researchers organized or co-organized the following meetings:*

1. TRANSP User's Group Meetings (APS-DPP 2017)
2. Fusion Facilities Coordinating Comm. meetings (Oct. 2017)
3. US Magnetic Fusion Research Strategic Directions Workshop (Dec. 2017)
4. NSTX-U Program Advisory Committee Meetings (Jan. 2018)
5. National Academy of Sciences Meeting (April 2018)
6. Plasma Surface Interaction Meeting (June 2018)

*NSTX-U Engineering organized:*

1. Low Heat Flux Plasma Facing Components Preliminary Design Review (September 29, 2017)
2. Torus Vacuum Pumping System Backing Pump and Pump Cooling System Preliminary Design Review (September 29, 2017)
3. High Heat Flux Plasma Facing Components Preliminary Design Review (November 15, 2017)
4. Heat Transfer Plate and Heat Transfer Tubing Preliminary Design Review (November 30, 2017)
5. High Temperature Helium Feedthrough Preliminary Design Review (December 1, 2018)
6. Inner PF Coil Preliminary Design Review (December 14, 2017)
7. Innerspace Pumping System Preliminary Design Review (December 20, 2017)
8. Plasma Facing Components Preliminary Design Review (January 4, 2018)
9. Gas Piping Preliminary Design Review (January 11, 2018)
10. Torus Vacuum Pumping System Backing Pump and Pump Cooling System Final Design Review (January 12, 2018)
11. Ex-Vacuum Vessel Heating System Preliminary Design Review (February 1, 2018)

12. DOE/SC Assessment of NSTX-U Recovery Plans, Phase 1 (February 6-8, 2018, with DOE/OPA)
13. NSTX-U Reassembly Peer Review (February 9th, 2018)
14. CAMAC Replacement Phase 1 and 2 Preliminary Design Review (February 16, 2018)
15. Vacuum Vessel Field Scope Preliminary Design Review (February 23, 2018)
16. PF-1b Power Circuit Preliminary Design Review (February 27, 2018)
17. Bakeout DC Connection Preliminary Design Review (April 5, 2018)
18. Outer PF Inspections Preliminary Design Review (March 13, 2018)
19. DOE/SC Assessment of NSTX-U Recovery Plans, Phase 2 (March 14-16, 2018, with DOE/OPA)
20. Machine Instrumentation Preliminary Design Review (March 22, 2018)
21. NSTX-U Project Advisory Committee (March 22-23, 2018)
22. Inner PF Coil Supports Preliminary Design Review (March 27, 2018)
23. Inner PF Coil Final Design Review (March 30, 2018)
24. TF/OH Bundle Reliability Preliminary Design Review (April 3, 2018)
25. Test Cell Shielding Preliminary Design Review (April 10, 2018)
26. Glow Discharge Cleaning Anode Preliminary Design Review (April 19, 2018)
27. Prototype Inner PF Coil Power Test Final Design Review (May 9, 2018)
28. Bakeout PLC Upgrade Preliminary Design Review (May 10, 2018)
29. Gas Delivery System Expansion Tank Burst Disk Preliminary Design Review (May 29, 2018)
30. Risk Registry Workshop (June 11-12, 2018)
31. CAMAC Replacement Pilot Phase 3 Final Design Review (June 6, 2018)
32. Passive Plate & Helium Line Conceptual Design Review (June 8, 2018)
33. CAMAC Replacement Pilot Phase 1 & 2 Final Design Review (June 26, 2018)
34. Passive Plate & Helium Line Preliminary Design Review (July 26, 2018)
35. Machine Reassembly PDR (August 1, 2018)
36. Polar Region Preliminary Design Review (August 2nd, 2018)
37. Test Cell Shielding Preliminary Design Review II (August 6, 2018)
38. Test Cell Radiation Annunciation and Oxygen Deficiency Monitor Preliminary Design Review (August 14, 2018)
39. NSTX-U Project Preliminary Design Review (August 15-16, 2018)
40. NSTX-U Project Director's Review and Independent Cost Evaluation (Sept 5-7, 2018)

*PPPL Theory organized:*

1. Boundary Physics Meeting (Oct. 2017)
2. Center for Tokamak Transient Simulations Satellite Meeting (Oct. 2017)
3. Center for Tokamak Transient Simulations Satellite Meeting (April 2018)
4. Exascale Computing Project Annual Meeting (April 2018)
5. SciDAC Fusion Machine Learning Workshop (June 2018)
6. Disruption Workshop (July 2018)
7. LWS Strategic Capabilities Meeting (August 2018)
8. Exascale Computing Project Fall team meeting & Advisory board meeting (Sept. 2018)

## **NSTX-U PPPL Employee FY18 Leadership in Venues Outside of PPPL**

1. Bertelli, N., PPPL PI of the RF SciDAC project
2. Boyer, M., Deputy Leader, USBPO Operations and Control Topical Group
3. Chang, C.S., US Chair for 2018 US-Japan Exascale Simulation of fusion plasmas
4. Delgado-Aparicio, L., Deputy Leader, USBPO Diagnostics Topical Group
5. Ferraro, N., Treasurer, Sherwood Executive Committee
6. Gerhardt, S. Leader, ITPA MDC WG-6
7. Gorelenkov, N., Leader, USBPO Energetic Particles Topical Group
8. Guttenfelder, W., Deputy Leader, U.S. BPO Transport & Confinement Topical Group
9. Guttenfelder, W., Co-Leader, Discussion Group 5, Austin MFE Strategies Workshop
10. Guttenfelder, W., Editor, US BPO eNews
11. Jaworski, M., Leader, USBPO Pedestal and Divertor Topical Group
12. Kaye, S., PI of TRANSP funding grant by DOE
13. Kaye, S., Coordinator, International H-mode Database Update Task (ITPA)
14. Kolemen, E., PSI Conference Local Organizer
15. Maingi, R., Chair, FESAC Transformative Enabling Capabilities (TEC) panel
16. Maingi, R., Chair, 23rd International Conference on Plasma Wall Interactions, Princeton, NJ, 18-22 June 2018, and member of the Program Committee
17. Menard, J., Co-chair, International Advisory Committee for China Fusion Engineering Test Reactor (CFETR)
18. Menard, J., Chair, U.S. DOE FES Fusion Facility Coordinating Committee
19. Menard, J., Co-chair, U.S. Magnetic Fusion Research Strategic Directions organization/workshops
20. Ono, M., Associate Editor, Journal of Fusion Energy
21. Park, J-K, MDC-19 Leader, ITPA MHD, Disruption and Control Topical Group
22. Park, J-K, Deputy Leader, MS Topical Science Group, NSTX-U Team
23. Poli, F., Leader, BPO Topical Group on Integrated Scenarios
24. Poli, F., Co-Leader, Discussion Group, Austin MFE Strategies Workshop
25. Poli, F., PI of ITER Task Agreement on EC modeling and application
26. Poli, F., PI of TRANSP funding grant by DOE
27. Poli, F., ITER Scientist Fellow
28. Ren, Y., Part-time Professor, Harbin Institute of Technology
29. Skinner, C., Chair, Local Organizing Committee, 23rd International Conference on Plasma Wall Interactions, Princeton, NJ, 18-22 June 2018
30. Skinner, C.H., Member, ITER Scientist Fellow
31. Wang, W. X., Secretary/Treasurer, Executive Committee of Sherwood Conference
32. Wang, W.X., Institutional PI of SciDAC TDS project
33. Wang, W.X., Visiting Professor, National Institute for Fusion Science, Japan
34. Wang, Z.R., Visiting Professor, Dalian University of Technology, China

## **NSTX-U PPPL Employee Membership and Participation in Scientific Groups and Meetings Outside of PPPL**

1. Bell, R., Expert, ITPA Diagnostics Topical Group
2. Belova, E., Editorial Board of Physics of Plasmas
3. Chang, C.S., Member, ITPA Pedestal and Edge Physics Topical Group
4. Diallo, A., Expert, ITPA Pedestal and Edge Physics Topical Group
5. Diallo, A. NSTX-U Representative for the JRT 2019 on Pedestal
6. Diallo, A. Member of the US Selection Committee for IAEA FEC 2018
7. Delgado-Aparicio, L., Member, ITPA Diagnostics Topical Group
8. Erickson, K., Member, MDSplus Developers Working Group
9. Ferraro, N., Expert, ITPA MHD Topical Group
10. Ferraro, N., Member, APS-DPP Women in Plasma Physics Committee
11. Fredrickson, E., Member, ITPA Energetic Particle Physics Topical Group
12. Gorelenkov, N., Member, ITPA Energetic Particle Physics Topical Group
13. Guttenfelder, W., Member, ITPA Transport and Confinement Topical Group
14. Guttenfelder, W., TTF Executive Committee
15. Jardin, S., Member, ITER Modeling Expert Group
16. Jardin, S., Member, ITPA MHD Topical Group
17. Kaye, S., Expert, ITPA Transport and Confinement Topical Group
18. Kaye, S., Member, U.S. Transport Task Force Steering Committee
19. Kaye, S., Member, U.S. Burning Plasma Organization Research Council
20. Kaye, S., Member, Fusion Advisory Board, UK
21. Kaye, S., Member, Culham Centre for Fusion Energy Advisory Committee
22. Kaye, S., Panel Member, National Academy of Sciences Burning Plasma Study
23. Kolemen, E., Member, ITER Plasma Control System design review committee
24. Lunsford, R., Expert, ITPA Pedestal and Edge Physics Topical Group
25. Maingi, R., Member, US DoE Fusion Energy Sciences Advisory Committee
26. Maingi, R., Member, ITPA Coordinating Committee
27. Maingi, R., Member, Executive Committee of the IEA TCP-CTP
28. Maingi, R., Member, Proto-MPEX Program Advisory Committee
29. Maingi, R., Member, Technical Program Committee of the H-mode Workshop
30. Maingi, R., Expert, ITPA Pedestal and Edge Physics Topical Group
31. Maingi, R., Expert, ITPA Divertor and SOL Topical Group
32. Maingi, R., Expert, ITPA Diagnostics Topical Group
33. Menard, J., Member, Executive Committee of IEA Implementing Agreement for Cooperation on Spherical Tori
34. Menard, J., Expert, ITPA MHD, Disruptions and Control Topical Group
35. Ono, M., U.S. Contact, US-Japan RF Workshop
36. Ono, M., International Visiting Professor, Kyushu University
37. Park, J.-K., Expert, ITPA MHD Topical Group
38. Park, J.-K., Committee Member, Workshop on MHD Stability Control
39. Park, J.-K., Lecturer, Princeton University
40. Podesta, M., Member, ITPA Energetic Particle Physics Topical Group

41. Podesta, M., Member, TTF Executive Committee
42. Podesta, M., Member of the Editorial Advisory Board of Review of Scientific Instruments
43. Poli, F., Member, US ITPA-IOIS Topical Group
44. Poli, F. Member, TTF Executive committee
45. Ren, Y., Expert, ITPA Transport and Confinement Topical Group
46. Ren, Y., Member, APS-DPP Program Committee
47. Stotler, D., Member, IAEA Technical Committee on Uncertainty Assessment and Benchmark Experiments for Atomic and Molecular Data for Fusion Applications
48. Taylor, G., Expert, ITPA Diagnostics Topical Group
49. Wang, W.X., Member, Scientific Program Committee of 12th West Lake International Symposium on Plasma Simulation
50. Wang, W.X., Member, Festival de Théorie (Aix-en-Provence, France, held biannually) International Scientific Committee

# NSTX-U Collaborator Institutions

Number	Institution	Country
1	College of William and Mary	USA
2	Columbia University	USA
3	CompX	USA
4	Florida International University	USA
5	General Atomics	USA
6	Idaho National Laboratory	USA
7	Johns Hopkins University	USA
8	Lawrence Livermore National Laboratory	USA
9	Lehigh University	USA
10	Lodestar Research Corporation	USA
11	Los Alamos National Laboratory	USA
12	Massachusetts Institute of Technology	USA
13	Nova Photonics, Inc	USA
14	Oak Ridge National Laboratory	USA
15	Old Dominion University	USA
16	Princeton University	USA
17	Purdue University	USA
18	Sandia National Laboratory	USA
19	Tech-X Corporation	USA
20	University of California - Davis	USA
21	University of California - Irvine	USA
22	University of California - Los Angeles	USA
23	University of California - San Diego	USA
24	University of California, Space Sciences Laboratory	USA
25	University of Colorado	USA
26	University of Illinois	USA

27	University of Maryland	USA
28	University of Rochester	USA
29	University of Tennessee	USA
30	University of Texas	USA
31	University of Washington	USA
32	University of Wisconsin	USA
33	University of Costa Rica	Costa Rica
34	Institute of Plasma Physics-Czech Republic	Czech Republic
35	Hiroshima University	Japan
36	Japan Atomic Energy Agency	Japan
37	Kyoto University	Japan
38	Kyushu University	Japan
39	NIFS National Institute for Fusion Science	Japan
40	Niigata University	Japan
41	University of Hyogo	Japan
42	University of Tokyo	Japan
43	FOM Institute DIFFER	Netherlands
44	ASIPP - Institute of Plasma Physics - Chinese Academy Of Sciences	P.R. China
45	Ioffe Physical-Technical Institute	Russia
46	TRINITI - Troitskii Institute of Innovative & Thermonuclear Research	Russia
47	KAIST - Korea Advanced Institute of Science and Technology	South Korea
48	NFRI - National Fusion Research Institute	South Korea
49	Seoul National University	South Korea
50	Ulsan Science Institute of Science & Technology	South Korea
51	Institute for Nuclear Research-National Academy of Science	Ukraine
52	Culham Centre for Fusion Energy	United Kingdom
53	Tokamak Energy	United Kingdom
54	University of York	United Kingdom